

Part 1 – The Lightcraft Technology Demonstration Program

Franklin B. Mead, Jr.

**AFRL/RZSP
10 E. Saturn Blvd.
Edwards AFB CA 93524-7680**

November 2007

Final Report

APPROVED FOR PUBLIC RELEASE; DISTRIBUTION UNLIMITED.



**AIR FORCE RESEARCH LABORATORY
AIR FORCE MATERIEL COMMAND
EDWARDS AIR FORCE BASE CA 93524-7048**

UNCLASSIFIED

REPORT DOCUMENTATION PAGE			Form Approved OMB No. 0704-0188		
<p>Public reporting burden for this collection of information is estimated to average 1 hour per response, including the time for reviewing instructions, searching existing data sources, gathering and maintaining the data needed, and completing and reviewing this collection of information. Send comments regarding this burden estimate or any other aspect of this collection of information, including suggestions for reducing this burden to Department of Defense, Washington Headquarters Services, Directorate for Information Operations and Reports (0704-0188), 1215 Jefferson Davis Highway, Suite 1204, Arlington, VA 22202-4302. Respondents should be aware that notwithstanding any other provision of law, no person shall be subject to any penalty for failing to comply with a collection of information if it does not display a currently valid OMB control number. PLEASE DO NOT RETURN YOUR FORM TO THE ABOVE ADDRESS.</p>					
1. REPORT DATE (DD-MM-YYYY) 05-11-2007		2. REPORT TYPE Final Report		3. DATES COVERED (From - To) 30 Jan 2001 – 31 Mar 2008	
4. TITLE AND SUBTITLE Part 1 – The Lightcraft Technology Demonstration Program			5a. CONTRACT NUMBER		
			5b. GRANT NUMBER		
			5c. PROGRAM ELEMENT NUMBER 62500F		
6. AUTHOR(S) Franklin B. Mead, Jr.			5d. PROJECT NUMBER		
			5e. TASK NUMBER 48470159		
			5f. WORK UNIT NUMBER 549907		
7. PERFORMING ORGANIZATION NAME(S) AND ADDRESS(ES) AFRL/RZSP 10 E. Saturn Blvd. Edwards AFB CA 93524-7680			8. PERFORMING ORGANIZATION REPORT NO.		
9. SPONSORING / MONITORING AGENCY NAME(S) AND ADDRESS(ES) Air Force Research Laboratory (AFMC) AFRL/RZSP 10 E. Saturn Blvd. Edwards AFB CA 93524-7680			10. SPONSOR/MONITOR'S ACRONYM(S)		
			11. SPONSOR/MONITOR'S REPORT NUMBER(S) AFRL-RZ-ED-TR-2007-0078		
12. DISTRIBUTION / AVAILABILITY STATEMENT Approved for public release; distribution unlimited. Public Affairs No. 08014A.					
13. SUPPLEMENTARY NOTES					
14. ABSTRACT Part I – The Lightcraft Technology Demonstration Program (LTD) is a report on the development of laser propulsion at the Air Force Research Laboratory (AFRL) between 1996 and 1999. The LTD Program was originally planned in five phases. Phase I, Lightcraft Concept Demonstration, was to demonstrate the feasibility of the basic concept. This phase ended in December 1998. Phase II, Lightcraft Vertical Launches to Extreme Altitudes, was a five-year effort designed to extend Lightcraft flights in sounding rocket trajectories to 30 km with a 100 kW pulsed CO2 laser. Phase III, Lightcraft Dual Mode Vehicle, was planned as a two-year effort designed to launch the first laser-propelled vehicle, a functional Lightcraft, into space. Phase IV was to be a far-term effort, to be conducted over the next 10 to 15 years, to develop a launch capability for Lightcraft weighing 100 kg and costing less than \$1.5M to build and launch. The LTD concept was a nanosatellite in which the laser propulsion engine and satellite hardware were intimately shared. The forebody aeroshell acted as an external compression surface (i.e., the airbreathing engine inlet). The afterbody had a dual function as a primary receptive optic (parabolic mirror) for the laser beam and as an external expansion surface (plug nozzle) during the laser rocket mode which is used only in space. The primary thrust structure was the annular shroud. The shroud served as both air inlet and impulsive thrust surface during the airbreathing mode. In the rocket mode, the inlets are closed, and the afterbody and shroud combine to form the rocket thrust chamber and plug (“aerospike type”) nozzle.					
15. SUBJECT TERMS Lightcraft, laser propulsion, LTD, SSTO, nanosatellite					
16. SECURITY CLASSIFICATION OF:			17. LIMITATION OF ABSTRACT SAR	18. NUMBER OF PAGES 304	19a. NAME OF RESPONSIBLE PERSON Dr. Franklin B. Mead, Jr.
a. REPORT Unclassified	b. ABSTRACT Unclassified	c. THIS PAGE Unclassified			19b. TELEPHONE NO (include area code) N/A

STINFO COPY NOTICE AND SIGNATURE PAGE

Using Government drawings, specifications, or other data included in this document for any purpose other than Government procurement does not in any way obligate the U.S. Government. The fact that the Government formulated or supplied the drawings, specifications, or other data does not license the holder or any other person or corporation; or convey any rights or permission to manufacture, use, or sell any patented invention that may relate to them.

Qualified requestors may obtain copies of this report from the Defense Technical Information Center (DTIC) (<http://www.dtic.mil>).

AFRL-RZ-ED-TR-2007-0078 HAS BEEN REVIEWED AND IS APPROVED FOR PUBLICATION IN ACCORDANCE WITH ASSIGNED DISTRIBUTION STATEMENT.

FOR THE DIRECTOR:

//signed//
FRANKLIN B. MEAD, JR.
Project Manager

//signed//
STEVEN A. SVEJDA
Chief, Propellants Branch

//signed//
PHILIP A. KESSEL
Technical Advisor
Space & Missile Propulsion Division

This report is published in the interest of scientific and technical information exchange, and its publication does not constitute the Government's approval or disapproval of its ideas or findings.

This Page Intentionally Left Blank

TABLE OF CONTENTS

List of Figures	v
List of Tables	viii
Glossary	ix
Acknowledgements.....	xi
Preface.....	1
1.0. Introduction.....	1
1.1 Overview.....	1
1.2 Background.....	2
2.0. Phase I: The Lightcraft Technology Demonstrator Program.....	8
2.1 The Beginning – The Initial Contract to Develop a Flight Vehicle.....	8
2.2 The Initial Contract Work to be Accomplished.....	8
2.3 Test Series #1 (22-24 Jul 96)	11
2.4 Test Series #2 (12-14 Aug 96)	15
2.5 Test Series #3 (22-24 Oct 96)	20
2.6 Test Series #4 (9-11 Dec 96)	24
3.0. The Intergovernmental Personnel Act (IPA) Program	32
3.1 Introduction.....	32
3.2 Test Series #5 (24-26 Mar 97)	32
3.3 Test Series #6 (21-24 Apr 97).....	34
3.4 Test Series #7 (23-26 Jun 97)	38
3.5 Test Series #8 (25-28 Aug 97).....	43
3.6 Test Series #9 (29 Sep-2 Oct 97)	47
3.7 Test Series #10 (3-5 Nov 97)	55
3.8 Test Series #11 (2-5 Dec 97)	58
3.9 Test Series #12 (5-8 Feb 98).....	60
3.10 Test Series #13 (17-20 Mar 98)	62
3.11 Test Series #14 (16-18 Apr 98).....	67
3.12 Test Series #15 (28-31 May 98).....	72
3.13 Test Series #16 (24-26 Jul 98)	75
3.14 Test Series #17 (20-23 Aug 98).....	76
3.15 Test Series #18 (23-26 Sep 98).....	79
4.0. Low Speed Wind Tunnel Testing of a Laser Propelled Vehicle	82
5.0. Flights of a Laser-Powered Lightcraft During Laser Beam Hand-off Experiments	84
6.0. Review of Recent Progress during Laser-Powered Lightcraft Flights to Unlimited Altitudes.....	85
7.0. Laser-Powered, Vertical Flight Experiments at the High Energy Laser System Test Facility.....	87
7.1 Theoretical Studies.....	87
7.2 German Collaboration.....	88
7.3 Testing at White Sands Missile Range	89
7.4 Laser Beam Propagation Studies	91
7.5 Lateral and Attitude Control Propulsion.....	94

8.0. Computer Modeling.....	94
8.1 Performance Modeling of an Experimental Laser Propelled Lightcraft.....	94
8.2 Analysis of the Effect of Pulse Width on Laser Lightcraft Performance	95
8.3 Thermophysics characterization of Multiply Ionized Air Plasma Absorption of Laser Radiation.....	97
9.0. Summary	99
10.0. References.....	100
Appendix A. High Energy Laser Systems Test Facility	A-1
Appendix B. Acoustic Measurements of Lightcraft Horizontal Guided Wire Tests	B-1
Appendix C. Analysis of Flight Dynamics and Control of Laser Lightcraft Vehicles.....	C-1
Appendix D. Laser Propulsion Assessment.....	D-1
Appendix E. Conceptual Design of a 100 kW TEA CO ₂ Laser with Spark Preionization	E-1

List of Figures

Fig. 1 The Pulsed Laser Vulnerability Test System (PLVTS) Laser Facility, Test Cell 3, High Energy Laser Systems Test Facility (HELSTF), White Sands Missile Range (WSMR), NM.....	3
Fig. 2. First Laser Propulsion Concepts from Project Outgrowth Study	3
Fig. 3 . First Toroidal Laser Rocket Engine Concept	4
Fig. 4. Absorption Cavity Concept	4
Fig. 5. Pulsejet Concept	4
Fig. 6. Artist's Illustration of the Launch of a Laser Propelled Lightcraft	6
Fig. 7. Dr. Myrabo's Lightcraft Concept	6
Fig. 8. A Full-Scale Wooden Lightcraft Model.....	7
Fig. 9. Old Aerial View of the HELSTF, Looking Towards the West	9
Fig. 10. Basic Set-Up for Testing	12
Fig. 11. Examples of Linear Air Breakdown.....	12
Fig. 12. Picture from Rear of 8-inch Lightcraft Showing Plasma	13
Fig. 13. 8-Inch Model with Crumpled Aluminum Tape After Testing	13
Fig. 14. 8-Inch Model	13
Fig. 15. Still Photo Extracted From Video	13
Fig. 16. Energy Transmitted Through Laser Plasma	15
Fig. 17. Schematic Drawing of 8-Inch Lightcraft.....	15
Fig. 18. Pendulum System Set-up.....	16
Fig. 19. L/D Calibration Curve for 8-Inch Lightcraft.....	17
Fig. 20. Measured Coupling Coefficient of the 8-Inch Lightcraft as a Function of Nozzle Extension Length (a) and Laser Energy (b).....	18
Fig. 21. High Speed Camera Photographs (a) = Test #188 and (b) = Test #189	19
Fig. 22. Schematic Illustration of the Wire Test Configuration with the Nozzle Extension Connected	20
Fig. 23. Pendulum Set-Up Illustration Showing Calibration Technique	21
Fig. 24. Fiberglass Nozzle Extension Mounted on 8-Inch Lightcraft for	21
Testing on the Pendulum Impulse Test Stand.....	21
Fig. 25. Brass Reed Valve Plate Shown in Foreground.....	22
Fig. 26. Measured Coupling Coefficient of the 8-Inch Lightcraft as a Function of Nozzle Extension Length (a) and Laser Energy (b).	23
Fig. 27. Indoor Horizontal Wire-Guided Flight Tests	23
Fig. 28. 8-Inch Lightcraft Mounted on Horizontal Wire.	24
Fig. 29. 8-Inch Lightcraft Pendulum Tests.	25
Fig. 30. Direct Thrust Measurement Test Set-Up with the 8-Inch Lightcraft Using Piezoelectric Transducer (a) with Prof. Myrabo and (b) with Dr. Mead.....	26
Fig. 31. Direct Thrust Measurement with Conical Nozzle Lightcraft and	26
Piezoelectric Pressure Transducers Installed.....	26
Fig. 32. Picture of Experimental Set-Up with Diode Ladder for Measuring Velocity and Acceleration.....	27
Fig. 33. Picture of Lightcraft with Conical Shroud, Wiring from Photo Diode Ladder, and Photo Diode Mounting Details.	28

Fig. 34. Peak Forces for the First 23 Tests of the Load Cell, Full Scale 8-Inch Lightcraft Model.....	29
Fig. 35. Peak Force Normalized by Pulse Energy for Load Cell, Full Scale 8-Inch Lightcraft Model.	30
Fig. 36. Example of High Speed Photography Showing Plasma Breakdown on the Inside of the Shroud.	31
Fig. 37. Wire-Guided Laboratory Launch Set-Up.	33
Fig. 38. Lightcraft Models Tested Through March 1997.	34
Fig. 39. Thrust Stand Test Set-Up Illustrated with Various Vehicle Configurations.	35
Fig. 40. Calculated Coupling Coefficient (C_m) Versus Laser Energy per Pulse From Direct Impulse Measurements for a Number of Different Vehicle Configurations.....	36
Fig. 41. Pictures Illustrating Vertical Wire-Guided Flights with Diode Array Installed to Measure Acceleration.	37
Fig. 42. Horizontal Wire-Guided Flight Set-Up.	38
Fig. 43. Details of Wire-Guided Flight Set-Up Showing the Anchored Wire Attaching to the Standoff on the Optical Bench (a) and Looking Back From the Tower to the Open Window (b)	39
Fig. 44. View Looking Out the Window to the Tower with Lightcraft Mounted on Wire.	39
Fig. 45. Optical Configuration of the Pointing and Tracking System	40
Fig. 46. Tower Burn Pattern from Tower Illustrating Transition from Near to Far Field Structure	41
Fig. 47. Vertical Free Flight Launch Set-Up in Laboratory.	42
Fig. 48. New Truncated Cone Model with Smaller Bearings.....	43
Fig. 49. Details of Thrust Stand Load Cell Assembly.	43
Fig. 50. Experimental Set-Up for Vertical Free Flight Laboratory Tests.....	45
Fig. 51. Calorimeter Measurement (a) and a Laboratory View (b) Showing a Lightcraft Mounted on the Launch Rod and Beam Dump Attached to Ceiling	45
Fig. 52. Vertical Free Flight Test Pictures with Prof. Myrabo (a) and the First 5 Pulses of a Flight Shown in a Still Picture (b).....	46
Fig. 53. Still Camera Pictures of Vertical Free Flight Laboratory Tests	46
Fig. 54. Composite Picture Showing Parabolas #100 to #300 with Titanium Shroud on Far Left.	49
Fig. 55. Flat Top Flight Vehicle on Launch Rod (a) and Two Separate Flights of Flat Top Vehicles Shortly After Lift-Off (b) and (c)	50
Fig. 56. Series of Pictures Showing Vehicles #100 to #300, and Illustrating Plasma Formation in Vehicles #150 to #300	50
Fig. 57. Two Outstanding Flights That Reached the Ceiling	51
Fig. 58. Lightcraft Mounted on 400 ft Horizontal Wire Tied to Beam Stop	52
Fig. 59. Night Time Wire-Guided Test (a) and Details of Clipping Mechanism to Hold Lightcraft in Position Against Winds (b).....	53
Fig. 60. Group Photo: From L to R, Drs. Franklin Mead and Leik Myrabo (front), and Steve Squires, Mike Thurston, Chris Beirsto, and Dr. Don Messitt (back).	53
Fig. 61. Picture of Experimental Set-Up for Outdoor, Free Flight Tests.....	55

Fig. 62. Lightcraft Mounted on Launch Rod Prior to Flight	56
Fig. 63. Lightcraft Flights Inside 50 ft Canvas Channel	57
Fig. 64. PLVTS Performance Measurement	58
Fig. 65. Situation with Manlifter Extension (a) and a Night Flight Test with the Manlifter Extension in Place (b)	59
Fig. 66. Two Views of the Scaled Family of #200 6061 T6 Aluminum Lightcraft	60
Fig. 67. Flight Tests Using the Condor Crane	61
Fig. 68. Model #200 Lightcraft Scaling Relations	62
Fig. 69. Modified Thrust Stand	63
Fig. 70. Lightcraft Experimental Schlieren Apparatus	64
Fig. 71. Example of Schlieren (a) and Shadowgraph (b) Taken at +70 μ s From First Light Arrival at the Annular Focal Ring	65
Fig. 72. Black and White Shadowgraph Pictures of the Lightcraft Exhaust Flow Field to +140 μ s Illustrating Shock Wave Structure and the “Wrap Around” Phenomenon	66
Fig. 73. Exhaust Field Visualization Test Using Vapor Created by Pouring Liquid Nitrogen into a Bath of Water	67
Fig. 74. PLVTS Power Test	67
Fig. 75. Gold (Left) and Silver Plated Aluminum Coupon Tests, Before (a) and After (b)	68
Fig. 76. Lift-Off Tests (a) and High Altitude Flight Tests (b)	69
Fig. 77. Telescope Focus as a Function of Mirror Separation	70
Fig. 78. The FTT (a) and its Focus Length versus Mirror Separation (b)	71
Fig. 79. Condor Crane with Wind Sock and Wiffle Ball Measurement Line Attached	73
Fig. 80. Mr. James Shryne, in His Control Space, Under One of the Trailers	74
Fig. 81. Flight Test with Condor Crane	76
Fig. 82. Position of Cameras on Plywood Beam Dump	77
Fig. 83. 9’8 3/4” Inverse Mirror Spaced Beams at 120 ft and 0 ft.	79
Fig. 84. New Aluminum Pendulum Design	79
Fig. 85. New Pendulum and Piezoelectric Impulse Hammer Set-Up	80
Fig. 86. Line Focus Experiments Set-Up with Steel Plate Target	81
Fig. 87. Shadowgraph Set-Up for Simulated Lightcraft Focus	82
Fig. 88. Lightcraft Flight Experiment	86
Fig. 89. Thermodynamic Characteristics of Air	87
Fig. 90. Artist’s Cutaway Lightcraft Drawing	90
Fig. 91. COI Nicalon™ Shroud	91
Fig. 92. Comparison of Nicalon™ and Aluminum Shroud Performance	91
Fig. 93. Lightcraft Beaming Scenario Parameters	92
Fig. 94. Power Dependence of Irradiance	93
Fig. 95. Layout of Computational Grid (a) Computed Temperature Contours and Laser Ray Traces at 0.5 μ s, 10 μ s, and 20 μ s for (b) (c) and (d), Respectively	95
Fig. 96. A Comparison Between Theoretical and Measured Coupling Coefficients	95
Fig. 97. Computed Electron Temperature Contours for Laser Lightcraft Model #200-3/4 at 100 μ s Elapsed Time for 400 J of Laser Energy and 18 μ s Pulse Width	96

List of Tables

Table	Page
Table 1. Estimate for Propulsion Sciences Division, USAF Philips Laboratory MIRACL Cost Estimate.....	14
Table 2. Thrust Stand Test Results	35
Table 3. Measured Vertical Acceleration of Model C	37
Table 4. Mass Properties and Calculated Vertical Acceleration of ULS Models.....	44
Table 5. Results of Chemically Milling Lightcraft Parts	48
Table 6. Mass Inventory of Vertical Free flight Vehicles (grams)	51
Table 7. Results of First Outdoor Free-flight Tests	57
Table 8. Power vs. aperture measurements for the 8'-10½" Mirror Separation.....	59
Table 9. Vertical Free Flight Test Results	60
Table 10. 6061 T6 Aluminum Lightcraft #200 Style Model Mass (g) Characteristics.....	61
Table 11. Analysis of Good Flights from Video taken from 400-ft Scaffolding.....	62
Table 12. Weights and Sequence for Load Cell Calibration	63
Table 13. April Outdoor Free Flight Experiments.....	71
Table 14. Analysis of Highest Flights From Table 13	72
Table 15. PLVTS Tests, 29 & 31 May 1998, 28 Hz, 360 J, & 18 µs Pulse Widths...	73
Table 16. Lightcraft Component and Assembled Weights.....	74
Table 17. Flight Tests on 25 July 98, at 18 µs Pulse Widths, 360 J/Pulse and Calm Wind.....	75
Table 18. Mass Properties of Flight Vehicles.....	75
Table 19. Assembled Lightcraft Masses (g)	77
Table 20. Flight Test, 18 µs, 28 Hz, E _p =420 J	78

Glossary

AFRL – Air Force Research Laboratory
AFRPL – Air Force Rocket Propulsion Laboratory (now the Air Force Research Lab)
APS – American Physical society
 C_m & CC – Coupling Coefficient
CFD – Computational Fluid Dynamics
COI – Composite Optics, Inc.
CONUS – Continental United States
CW – Continuous Wave
DATTS – Directorate for Applied Technology, Test, and Simulation
DSP – Digital Signal Processor
 E_p – Laser Energy
ESLI – Energy Sciences Laboratories, Inc.
FTT – Field Test Telescope
GBL – Ground-Based Laser
GEO – Geosynchronous Earth Orbit
 GN_2 – Gaseous Nitrogen
HELLO – High Energy Laser Light Opportunity
HELSTF – High Energy Laser Systems Test Facility
IPA – Intergovernmental Personnel Act
ITAR – International Traffic in Arms Regulations
LC – Lightcraft
L/D – Length to Diameter Ratio
LEO – Low Earth Orbit
LLNL – Lawrence Livermore National Laboratory
LSC – Laser Sustained Combustion
LSD – Laser Sustained Detonation
LSWT – Low Speed Wind Tunnel
LTD – Lightcraft Technology Demonstration
MIRACL – Mid Infrared Advanced Chemical Laser
MIPR – Military Interdepartmental Purchase Request
MSFC – Marshall Space Flight Center
MSL – Mean Sea Level
NASA – National Aeronautical and Space Administration
NORAD – North American Aerospace Defense Command
NRL – Naval Research Laboratory
PAE – Power Amplifier Electronics
PL - Phillips Laboratory
PLVTS – Pulsed Laser Vulnerability Test system
PRF – Pulse Repetition Frequency
PSI – Physical Sciences, Inc.
RP – Repetitively Pulsed
RPI – Rensselaer Polytechnic Institute
SAR – Solid Ablative Rocket

SBIR – Small Business Innovation Research
SDIO – Strategic Defense Initiative Organization
SLBC – Sea Light Beam Director
STTR – Small Business Technology Transfer Program
TAV – Trans-Atmospheric Vehicle
UL – Ultra-Light
ULS – Ultra-Light Spinning
WSMR – White Sands Missile Range

Acknowledgements

A number of people were responsible for the success of this program detailed within this report. First, my sincere gratitude and thanks go to Prof. Leik Myrabo for his tireless efforts to make this unique research and development program so incredibly exciting and successful. Secondly, this program would never have been started without the initial financial support of the Astronautics Laboratory at Edwards AFB, then under the direction of Mr. Lee Meyer. It was Lee who provided the initial funding and managerial support to get the program started in FY 96. Thirdly, the financial support, in addition to that annually provided by the Air Force, from NASA's Marshall Space Flight Center (MSFC) through Mr. John Cole allowed the program to really "take off" during its second and third years. The momentum gained during these early years with this extra money carried the program through to its conclusion and allowed many experiments that never would have occurred without this financial support. And lastly, the crew of the PLVTS laser, Steve Squires, Chris Beairsto, and Mike Thurston, for their many hours of sacrifice and hard work which are ultimately responsible for the success of this program. Never have I worked with such a dedicated group of people in all my many years of civil service. These three people provided a continuous inspiration to all the people that worked on this program. Only once during the four years covered by this program did the experiments at HELSTF have to be cancelled due to the inoperability of the laser. This is a fantastic record for such a complex machine.

Franklin B. Mead, Jr.
Senior Project Engineer
25 October 2007

This Page Intentionally Left Blank

Preface

In 1995, Mr. Lee Meyer, then director of the Astronautics Laboratory at Edwards AFB requested that a study be done to define three advanced propulsion concepts that the laboratory could start working on. The three final concepts selected were the Maglifter, POGO, and Lightcraft concepts. NASA picked up the Maglifter concept, and additional studies of POGO defined a concept that was mainly airbreathing with very little rocket propulsion work. Thus, POGO was dropped from consideration. That left the Lightcraft concept which promised to reduce the cost of space launch by several orders of magnitude. Prof. Leik Myrabo was contacted and discussion ensued about how to develop the Lightcraft concept. This was the beginning of the program included in this report to demonstrate the Lightcraft physics and develop the concept for space transportation.

1.1 Overview

Part I – The Lightcraft Technology Demonstration (LTD) Program report covers the development of laser propulsion at the Air Force Research Laboratory (AFRL) between 1996 and 1999. Part 2 – Experimental 50-cm Laser Ramjet (X-50LR Program) covers work between 1999 and 2005 and is a limited distribution report, available only to DoD agencies. There is some overlap between Parts 1 and 2 where it was possible to include information already released to the public. Between 1999 and 2002, all Part 2 program information was considered public release following the usual laboratory approval cycle. However, after Nov 2002, when the U.S. Department of State declared laser propulsion development to be ITAR (export) controlled, information was selectively released through a careful review process.

The LTD Program was originally planned in five phases. Phase I, Lightcraft Concept Demonstration, was to demonstrate the feasibility of the basic concept. This phase ended in December 98. Phase II, Lightcraft Vertical Launches to Extreme Altitudes, was a five-year effort designed to extend Lightcraft flights in sounding rocket trajectories to 30 km with a 100 kW pulsed CO₂ laser. Phase III, Lightcraft Dual Mode Vehicle, was planned as a two-year effort designed to launch the first laser-propelled vehicle, a functional Lightcraft, into space. Phase IV was to be a far-term effort, to be conducted over the next 10 to 15 years, to develop a launch capability for Lightcraft weighing 100 kg and costing less than \$1.5M to build and launch.

Under Phase I, performance was measured with an impulse pendulum and piezoelectric thrust stand, shadowgraph and beam propagation (to 90 m) studies were accomplished, a pointing and tracking system was developed and demonstrated on horizontal wire-guided flights outdoors to 122 m, and outdoor vertical free-flights approaching 30 m were successfully conducted.⁽¹⁾ Low Mach number wind tunnel tests were also accomplished with a 23-cm diameter model, and later reported.⁽²⁾ The basic conclusion of all this work was that the feasibility and basic physics of the Lightcraft concept had been adequately demonstrated; but that a much larger, 100 kW class pulsed laser would be required to completely accomplish Phase II.

Phase II, initiated in January 1998, continued with the performance characterization of several #200 series models.⁽¹⁾ The #200 series consists of a number of different sized

vehicles all scaled to the same optical f-number. These models exhibit stability and self-centering in the near-field laser beam. This natural self-centering capability, termed as beam riding, turned out to be inherent in the conceptual design, and was not fully appreciated until after the completion of the LTD Program. Outdoor vertical free flights with the Model #200-3/4 Solid Ablative Rocket (SAR) impacted the plywood beam dump at about 40 m in Jul 99. The final vertical velocity at the end of these flights was so great that the nose (i.e., the forebody) was severely dented while the optic (afterbody) and shroud remained in good condition without visual damage.

These Lightcraft were called rockets because a solid ablative propellant ring made of Delrin® had been added at the internal extremity of the shroud. Delrin® is a solid form of formaldehyde that was selected because of its physical properties and performance under laser ablation tests performed in the 1980s.^(3,4) The addition of a propellant increased the coupling coefficient (CC) by a factor of 4 or 5 over that of plain air, and eliminated significant heat damage to the shroud and optic. Thus, addition of an ablative propellant demonstrated that overheating of the shroud and thermal stall could be postponed significantly beyond the 3 to 4 seconds previously noted,⁽¹⁾ while adding a significant increase in thrust performance.

With the extended lifetime and enhanced performance demonstrated by the addition of an ablative propellant, it was proposed to develop a laser "hand-off" technique using the Model #200-3/4 SAR vehicle with NASA contributing half the funding for the effort. The hand-off technique is the method by which the laser's light is transferred to consecutively larger telescopes during a Lightcraft launch. In other words, the laser light is initially directed through a small diameter telescope at the start of the launch and transferred to larger telescopes at pre-selected altitudes during the flight. The goal of these tests was to achieve altitudes on the order of 150 to 500 m.⁽²⁾

The objective of the "Lightcraft Technology Demonstrator (LTD) Program" was initially to conduct, before the end of calendar year 1998, a flight demonstration to a significant altitude. This was to be accomplished by launching a specially designed, ultralight Lightcraft (LC) to an altitude of between 0.6 km (0.38 mi) and 10 km (6.2 mi) using an existing laser at the High Energy Laser Systems Test Facility (HELSTF), White Sands Missile Range (WSMR), NM. This launch was to demonstrate the viability of laser propulsion for eventual low cost access to space.

As it turned out, all testing was performed at the HELSTF with the Pulsed Laser Vulnerability Test System (PLVTS) laser. This laser originally operated with pulse widths of 30 μ s and up to 10 Hz (pulses/s) and 1,000 J per pulse. Additional lasers for alignment and shadowgraph tests were used and are described in the respective text. The PLVTS was a 10.6 μ m CO₂ laser with a pulse width of 30 μ s located in a trailer (see Fig. 1). The PLVTS was built in 1989 by Textron under a \$3.5M contract for two lasers, and HELSTF took delivery in 1991. PLVTS, the second production laser, weighs 150,000 lbs, of which 20,000 lbs is capacitor weight. The first production laser was also obtained and placed in storage for the price of the contract.

1.2 Background

In a 1969 invention disclosure,⁽⁵⁾ Mr. Robert Geisler (AFRPL, Solid Rockets Branch) was the first to recognize that laser propelled rockets were possible with high powered

lasers. He envisioned laser energy transferred via a heat exchanger to a working fluid or used directly to heat fluidized particles dispersed in a working fluid. The working fluid, such as hydrogen or ammonia, was to be used to produce thrust in a conventional manner (see Fig. 2). An analysis of this concept was presented in the 1972 Air Force Project Outgrowth report.⁽⁶⁾



Fig. 1. The Pulsed Laser Vulnerability Test System (PLVTS) Laser Facility, Test Cell 3, High Energy Laser Systems Test Facility (HELSTF), White Sands Missile Range (WSMR), NM

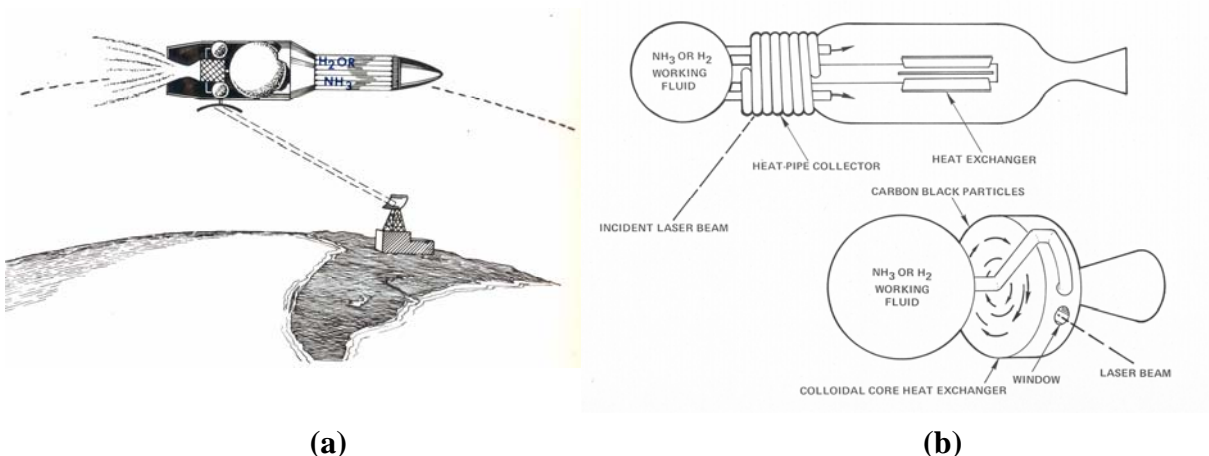


Fig. 2. First Laser Propulsion Concepts from Project Outgrowth Study

In May of 1972, an article by Dr. Arthur Kantrowitz,⁽⁷⁾ of AVCO Everett Research Laboratory, introduced the concept of launching payloads to orbit using high power ground-based lasers and initiated Government interest in laser propulsion. He envisioned an ablation process of a solid propellant using gigawatt-class lasers.

In a June 1973 proposal to the Air Force,⁽⁸⁾ AVCO was first to describe a toroidal shaped combustion chamber with a throat and expansion cone forming a plug or annular nozzle. As illustrated in Figure 3, this concept had many of the elements of a general

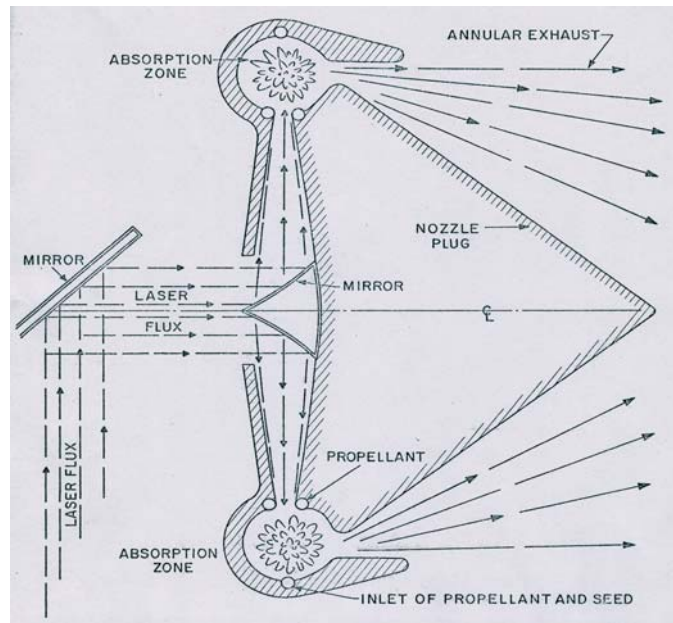


Fig. 3. First Toroidal Laser Rocket Engine Concept

class of vehicle concepts that have evolved into the concept called Lightcraft. This toroidal approach also illustrates a concept known as a "tractor" beam concept because the light enters from the front and pulls the vehicle forward.

For the last 39 years laser propulsion has been analytically and experimentally under continuous development. Between 1972 and the late 1980s, several concepts received considerable emphasis.⁽⁹⁾ Of those concepts, the laser Absorption Cavity concept (see Fig. 4) and the parabolic shaped Laser Pulsejet concept (see Fig. 5) were heavily funded.

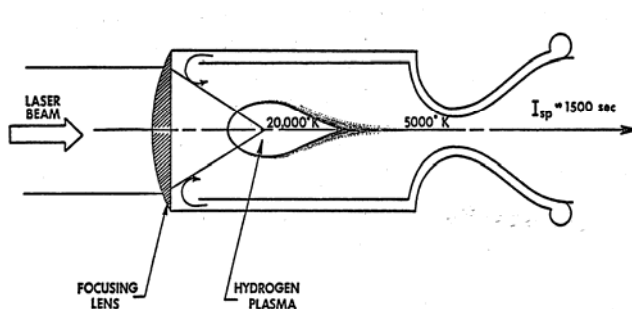


Fig. 4. Absorption Cavity Concept

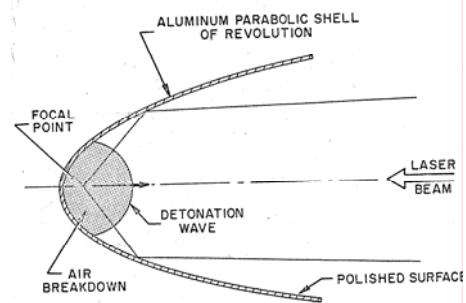


Fig. 5. Pulsejet Concept

The Absorption Cavity thruster was developed by Keefer.^(10,11,12) The Absorption Cavity concept is a continuously flowing gas concept and requires a Continuous Wave (CW) or non-pulsed laser. If it could operate in the ramjet/scramjet mode, it might be possible to use this device to carry payloads to an Earth orbit.

The Pulsejet concept was invented by AVCO, but most of the development work was done by Physical Sciences, Inc. (PSI).^(13,14,15) The Pulsejet operates by causing the formation of a very high temperature air plasma to occur at the focal point in a parabolic cone. Pulses allow a small amount of energy to be concentrated within very short time to amplify that energy many orders of magnitude; e.g., 108 J @ 18 μ s pulse width gives 6 MW, allowing plasma formation to occur. An advantage of this approach is that because the plasma formation does not occur on or at the wall surface, heating and thus materials are not as serious a problem. The disadvantage is that getting breakdown at a point removed from the walls is more difficult. A wall can reduce the breakdown laser intensity requirements by up to four orders of magnitude. To counter this problem, ways have been developed for extending an “ignition rod” to the focus to enhance breakdown. In addition, the shape illustrated in Figure 5 makes it difficult to refresh the air in the cavity between pulses. In fact, recent tests under a NASA Small Business Technology Transfer (STTR) contract have identified this problem specifically.⁽¹⁶⁾ This characteristic problem was shown to be reduced by making the parabola very flat, thus opening up the deep “well,” but tests indicated that there is considerable performance loss at the small f/numbers.⁽¹⁶⁾

During the late 1980s, the LTD concept, which was a laser propelled trans-atmospheric vehicle (TAV) concept, was analytically developed by Prof. Myrabo at Rensselaer Polytechnic Institute (RPI) for Lawrence Livermore National Laboratory (LLNL) and the Strategic Defense Initiative Organization (SDIO) Laser Propulsion Program.⁽¹⁷⁾ This laser launch concept (see Fig. 6) was envisioned to employ a 100 MW-class ground-based laser (GBL) to transmit power directly to the Lightcraft in flight. An advanced, combined-cycle engine would propel a 120 kg (265 lb) dry mass, 1.4 m (4.59 ft) diameter LTD, with a mass fraction of 0.5, to orbit. The LTD vehicle, once in orbit, would then become an autonomous sensor satellite capable of delivering precise, high quality information typical of today’s large orbital platforms.⁽¹⁷⁾ Here, the 1 m diameter afterbody optic (see Fig. 7) could serve as an optical telescope or as a receiving/transmitting antenna for low power laser or microwave communication systems.

forebody (nose) of the vehicle, and a 15 kg hydrogen (i.e., other propellants such as ammonia, methane, etc., could be used) propellant tank along with a helium pressurant tank are illustrated in the central and lower portions of the vehicle. A full scale wooden model was actually made to illustrate this LTD design.⁽¹⁷⁾

The LTD concept was a microsatellite in which the laser propulsion engine and satellite hardware were intimately shared. The forebody aeroshell acted as an external compression surface (i.e., the airbreathing engine inlet).⁽¹⁸⁾ The afterbody had a dual function as a primary receptive optic (parabolic mirror) for the laser beam and as an external expansion surface (plug nozzle) during the laser rocket mode which would only be used in space. The primary thrust structure was the annular shroud. The shroud serves as both air inlet and impulsive thrust surface during the airbreathing mode. In the rocket mode, the inlets are closed, and the afterbody and shroud combine to form the rocket thrust chamber and plug (“aerospike-type”) nozzle. These features were incorporated into the Lightcraft that was developed. A wooden model of the Myrabo Lightcraft is shown in Figure 8 with the forebody panels open to expose the solar cells on the inside.

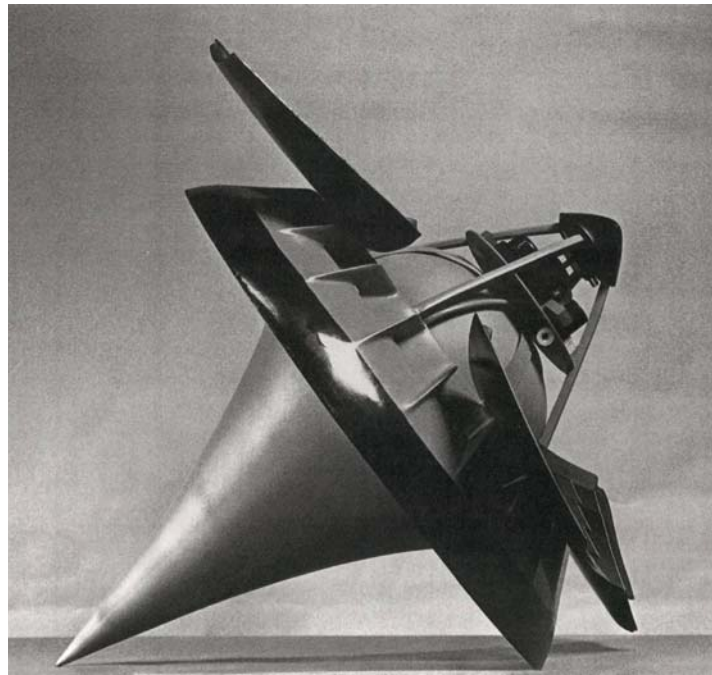


Fig. 8. A Full-Scale Wooden Lightcraft Model

The dominant motivation behind the LTD study was to provide an example of how laser propulsion could reduce, by an order-of-magnitude or more, the production and launch costs of sensor satellites. The 1989 study concluded that a vehicle production cost of \$1,000/kg was realizable, and that launch costs must be limited to less than \$100/kg for laser propulsion to play a significant role in the future of space transportation.

This outstanding study formed the basis for the AFRL’s subsequent program. The Lightcraft concept derives from the LTD concept developed at RPI for the SDIO Laser Propulsion program in the late 1980s.

2.0 PHASE I: THE LIGHTCRAFT TECHNOLOGY DEMONSTRATOR PROGRAM

2.1 The Beginning – The Initial Contract to Develop a Flight Vehicle

A proposal, #139-96-056E, was received from RPI, dated 9 November 1995, entitled **“Transatmospheric Laser Propulsion Experiments at HELSTF: Phase I,”** naming Dr. Leik N. Myrabo, Associate Professor, as the principle investigator. The proposed program cost was for \$49,996 for a one-year effort.

In response, following an evaluation of the proposal, the Phillips Laboratory (PL) initiated a \$50K program, via a Military Interdepartmental Purchase Request (MIPR) dated 26 Jan 1996, through the Army’s Benet Laboratory located at the Watervliet Arsenal, Watervliet, NY, with Dr. Charles A. Andrade as the program manager.

Phase I of this initial RPI contract was to demonstrate laser propulsion technology suitable for propelling an ultralight, 1 to 15 kg "drone" spacecraft up through the atmosphere with the CW megawatt-class Mid Infrared Advanced Chemical Laser (MIRACL) at HELSTF. For the most part, these engine experiments were to utilize existing mirrors and laser propulsion test apparatus that were previously constructed under the (then recently canceled) Laser Propulsion Program of the SDIO. However, several of the mirrors (and/or mirror faceplates) had to be coated for high reflectivity at the 3.8 μm wavelength of MIRACL. Laser propulsion engine performance data was to be gathered for two to four promising thruster designs. In addition, Phase I would demonstrate nutated beam delivery of a 10 inch diameter around the circular "race track" pattern of the drone's 2.2 m diameter receiver optics, an annular-ring, off-axis parabolic mirror. Pulsed engine tests were also to be carried out with HELSTF’s RP 10.6 μm carbon dioxide laser.

2.2 The Initial Contract Work to be Accomplished

The objective of this initial Phase I contractual effort was to conduct proof-of-concept laser propulsion experiments in support of a follow-on Phase II flight demonstration program. The objective of the Phase II Flight Demonstration program was: 1) Within a period of one year, to launch a 1 to 15 kg laser propelled, air breathing Lightcraft drone from the HELSTF to an altitude of 2 to 10 km using the then-current 75 second run time of the HELSTF MIRACL laser linked to the Sea Lite Beam Director; and, 2) To develop, within a one-and-a-half year period, a compatible laser-heated, liquid propellant rocket engine Lightcraft (LC) running on hydrogen, nitrogen, or air, designed for space transportation and operation in space. This would involve the development of a combined cycle engine that would lift the LC in the airbreathing mode up to perhaps Mach 5 at 30 km altitude and then transition to rocket mode for orbit insertion and operation in space.

Thrust generation tests were to be carried out for three different laser propulsion engine designs, to determine the engine most suitable for the flight demonstration. A variety of experimental apparatus were to be used in these tests including a dynamic impulse pendulum, a fully instrumented static impulse plate (equipped with numerous piezo-electric pressure transducers) to measure time-resolved pressures, several parabolic receiving mirrors and several 0.5 T permanent magnets.

Propulsion performance data was to be gathered from both of HELSTF's high power lasers: the pulsed 10.6 μm Pulsed Laser Vulnerability Test System (PLVTS) CO₂ laser, and the 3.8 μm Mid-Infrared Advanced Chemical Laser (MIRACL) D₂/F₂ laser. Next, this experimental data was to be compared with theoretical predictions for engine performance, and the engineering implications for the flight demonstration drone would be determined.

Task 1 consisted of a visit to the HELSTF and preparation of the experimental apparatus. Upon receiving the award for this project, the Principal Investigator was to immediately travel to the HELSTF facilities (see Fig. 9) to assess the requirements for carrying out a successful series of laser propulsion experiments. Extensive conversations with HELSTF staff were expected to reveal the optimum test plan for gathering engine performance data from at least two, week-long, testing series to be carried out during the first six months of 1996. The next High Energy Laser Light Opportunity (HELLO) (See **Appendix A**) opportunity was planned for February; others were scheduled for April and June 1996.



Fig. 9. Old Aerial View of the HELSTF, Looking Towards the West

Once the HELSTF requirements were known, the experimental apparatus was to be prepared for shipping to New Mexico. Most of the apparatus had already been fabricated under the previous SDIO support of the Laser Propulsion Program at RPI. However, other equipment needed to be purchased for the HELSTF tests, including new (expendable) mirror faceplates compatible with 3.8 μm lasers, 0.5 Tesla permanent magnets, pressure transducers, data acquisition system, etc.

Of particular interest in these Lightcraft tests was the simulation of the various schemes for enhancing “refresh” with unheated air into the laser-heating region by: a) forced convection (i.e., as delivered from the engine inlet); b) magneto-acoustic valving; c) vibrating reed valves (like used in the German V-I “Buzz bomb”); d) parallel propagating laser sustained detonation (LSD) wave geometry (i.e., LSD wave propagating parallel to the thruster surface); and perhaps, e) special contouring of the impulse plate surface.

Task 2 set theoretical performance goals for thruster experiments. Analytical and numerical predictions were to be derived for the impulse coupling and pressure time-history that an engine design would give to the thruster surface as anticipated for

HELSTF's two lasers, for the conditions of static and subsonic air "refresh" environments (Mach 0.1 to 1.0). The performance variations due to the thruster and LSD/plasma geometry, laser pulse shape, LSD wave velocity, and simulated flight Mach Number (and altitude, in future tests) would be assessed. (All Phase I tests were to be conducted under ambient conditions, which for White Sands Missile Range is slightly over 4000 ft. MSL.).

Two first-order computer models were currently available for predicting the time-integrated pressure delivered to the thrust surface. They were: a) a cylindrical, unpowered blast wave geometry that was triggered at the line focus (lying in the plane of the surface) by laser-induced air breakdown, and subsequent heating by an LSD wave that propagated nominal to the plate; and, b) a parabolic-shaped shock wave geometry that was generated by an LSD wave that propagated parallel to, and just above the thruster surface. These simple models neglected radiation losses and did not address performance enhancements due to magnetic nozzles.

Task 3 was to conduct impulse measurements with a dynamic pendulum. The impulse pendulum was 30 cm in diameter, rested on a coiled spring, and used magnetic induction (i.e., an electric coil and permanent magnet) to measure the delivered impulse. The pendulum surface was fabricated out of Plexiglas® and had recesses designed to accept either a block of steel, or a permanent ceramic magnet with either 0.5 or 1.0 T field, oriented perpendicular to the plate. The tests were to be performed at the local ambient pressure conditions; and it was realized that no artificial flow could be convected across the thruster plate without disturbing the impulse measurement.

This apparatus had already been utilized at the Naval Research Laboratory (NRL) in Washington, D.C. to measure the impulse delivered by 200-350 J pulses from the Pharos III neodymium glass laser (1.06 μm), so it was known to be fully functional and adequate for the HELSTF tests. At NRL, the pulsejet engine coupling coefficient increased from 100 N/MW to 180 N/MW when the magnet was inserted.

The data acquisition system was to record the impulse delivered to the pendulum from HELSTF's 3.8 μm MIRACL laser and the 10.6 μm RP laser—for a variety of thruster/beam geometries, with and without an applied magnetic field. A test plan matrix had been designed to enhance the timely identification of superior engine designs, so that effects of varying critical parameters on engine performance might be assessed.

If available at HELSTF, Schleiren photography and ultra-fast gated optical imaging cameras were to be employed to document the laser-induced breakdown, LSD wave transit, and evolving cylindrical shock wave patterns generated by the various engine designs tested. An important variable to be assessed was the effect of varying the energy deposition height above the thruster surface. By adjusting this energy line-source height, it was considered possible to maximize impulse coupling and minimize thermo-mechanical damage to the plate. Different results were anticipated for engine geometries with and without magnetic nozzles.

Task 4 was to measure time-resolved surface pressures with piezoelectric transducers. A special 30 cm by 30 cm pressure plate had been instrumented with numerous piezoelectric pressure transducers whose output is amplified before being recorded by the data acquisition system, for subsequent analysis. The apparatus was successfully applied in prior NRL laser-pulsejet experiments with the Pharos III laser, and was fully functional. Incidentally, this linear array of pressure transducers precluded the ability for

us to install permanent magnets needed for diagnosing the performance enhancing benefits of magnetic nozzles. However, since at least half of the impulse in prior "magnetic nozzle" experiments was communicated electromagnetically, the utility of measuring the surface pressures was considered secondary, at best.

The objective of the data gathered with these tests was to shed insight into the impulse generation process (i.e., pressure time-history) by comparing the integrated pressures with the total impulse obtained from the pendulum tests. The same engine test sequence used in Task 3 above would be applied here as well.

Task 5 was to compare experimental data with theoretical predictions. Theoretical predictions for thruster performance from above were to be compared and contrasted with experimental results derived for the combinations of beam orientations and engine geometries tested during these tests. Any substantial anomalies were to be noted, subjected to further analysis and, if possible, resolved. It was anticipated that magnetic nozzles might help engine performance to attain levels predicted by the simple analytical models, since they neglected plasma radiation losses as well as other inefficiencies of the thrust generation process.

Task 6 was to determine engineering implications for the drone flight demonstration. The results and lessons learned from a wide variety of airbreathing laser propulsion engine configurations were to be applied to a drone specifically designed for flight demonstrations in Phase II of the program. The integrated thermo-mechanical loads imposed upon the thruster surfaces were to be examined in light of existing advanced materials (hopefully uncooled) that could survive the planned 75 second flight. An attempt was to be made to assess the durability and suitability of innovative uncooled SiC and silicon optics (and their multi-layer high reflectivity coatings) to the extreme temperature exhaust gases evidenced by these laser propulsion experiments. The challenge in Task 6 was to identify the optimum solution for the engine/optics/airframe integration problem.

Task 7 was to prepare the final report. A final report comprehensively covering Tasks 1-6 was to be prepared as a separate document. Technical society presentations, archive journal papers, theses and dissertations might also be employed to document portions of the work.

2.3 Test Series #1 (22-24 Jul 96)

The initial series of laser propulsion experiments was carried out over a period of three days, 22-24 July 1996, at the HELSTF. A variety of experimental apparatus were used in these tests, including the dynamic impulse pendulum, the fully instrumented static impulse plate to measure time-resolved pressures, and several parabolic receiving mirrors. The specific facility utilized for these tests was the PLVTS located in Test Cell 3.

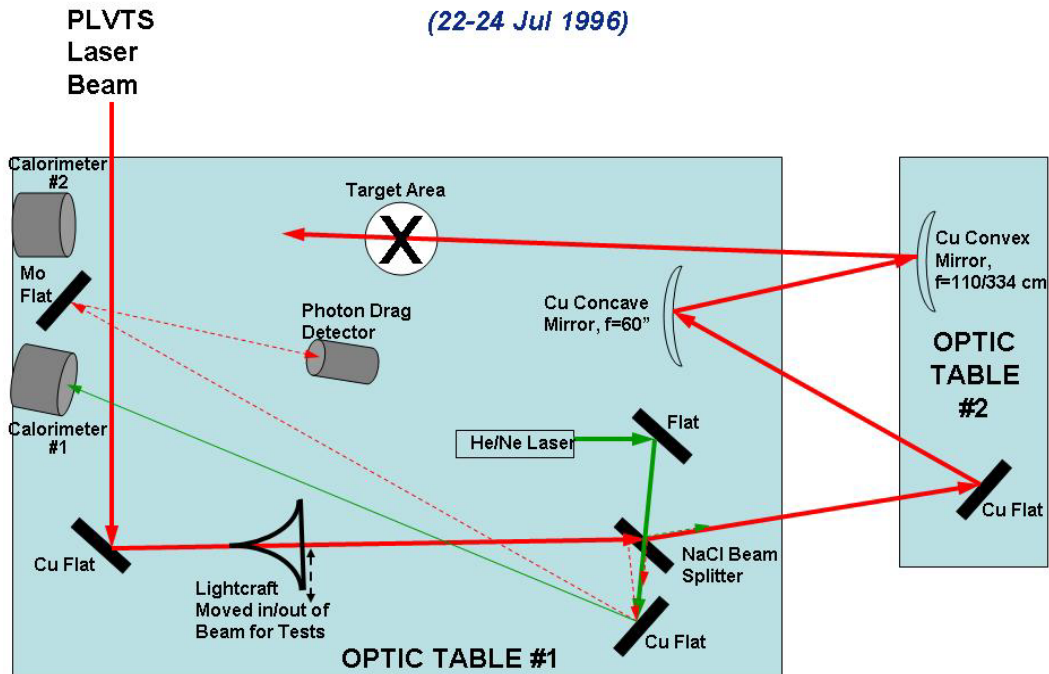


Fig. 10. Basic Set-Up for Testing

The basic experimental set-up on the optical bench is illustrated in Figure 10. The PLVTS laser beam enters the laboratory through a pipe that passes from the laser trailer through the laboratory wall. A He/Ne laser is typically used to assure alignment prior to final adjustments of the PLVTS beam using burn paper to assure that everything is adjusted properly.

The first two days were spent investigating the coupling of laser power (200 to 800 J/Pulse) to air-breakdown plasmas, and the transmitted impulse of these plasmas to various geometries with and without the presence of a magnetic field. Integrated color pictures of the linear air breakdown, using a Polaroid Camera firmly mounted on the optic table (Fig. 11), were taken of a number of test plasmas. These pictures illustrate at different magnifications the complexity and non-repeatability of these plasmas.

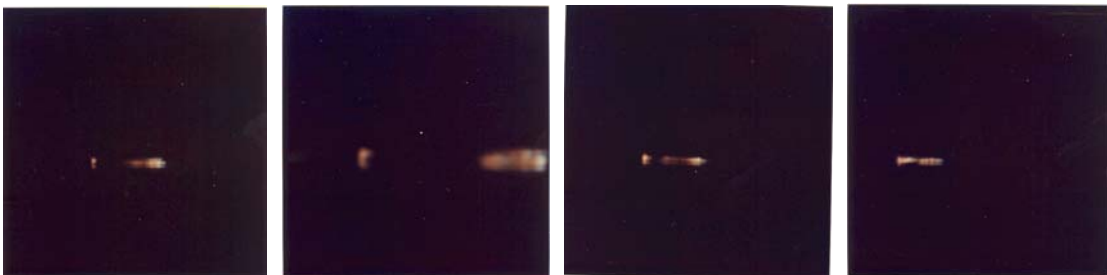


Fig. 11. Examples of Linear Air Breakdown

Initially, all that was available was the bare parabola afterbody of an 8-inch LC model. It was tried unsuccessfully to break down the air at the circular focal line with the

laser beam coming off the parabola (e.g., no shroud). To form an elementary shroud, aluminum tape was wrapped about the periphery of the parabola to form a crude cylindrical shroud. This geometry provided the first examples of breakdown in a shrouded afterbody. This is illustrated in a real time integrated photograph in Figure 12.

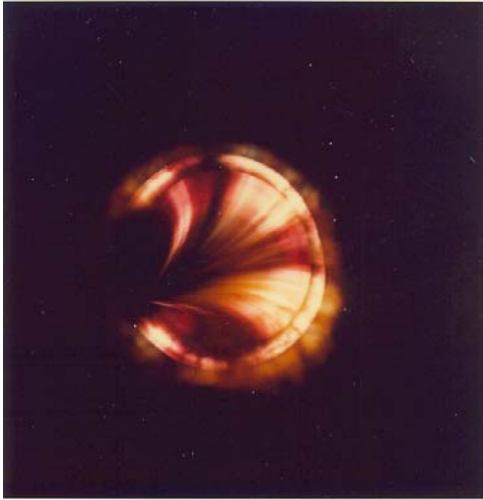


Fig. 12. Picture from Rear of 8-inch Lightcraft Showing Plasma



Fig. 13. 8-inch Model with Crumpled Aluminum Tape After Testing

Note that after several shots at high power, the aluminum tape became “crumpled” as illustrated in Figure 13. Note that the Lightcraft is firmly mounted, not on a pendulum as would be the case in many future test series.

The third day was almost totally dedicated to the first ever tests of a laboratory “Lightcraft” model (~8 inches in diameter). This model (See Fig 14) was tested with single laser pulses and several second, 10 Hz pulse trains up to power levels of 800



Fig. 14. 8-Inch Model



Fig. 15. Still Photo Extracted From Video

J/Pulse. The main goal of these tests was to demonstrate that adequate breakdown plasmas could be generated in a focused annular combustion chamber and to push the 2 kg Lightcraft along a wire. These tests were immensely successful. However, during the wire-guided tests, the laser failed entirely to move the Lightcraft on the wire. Attempts were made to reduce friction by spinning the Lightcraft on the wire before and during laser pulses. The Lightcraft had Teflon fittings in the front and rear for the wire to pass through. If one looks closely at Figure 15, the wire on which the Lightcraft is suspended is visible, illuminated by the laser produced plasma.

The original proposal included testing on MIRACL. However, scheduling and the cost estimate shown in Table 1, provided by Mr. Tony R. Marrujo who was in charge of MIRACL operation and testing, convinced Prof. Myrabo and Dr. Mead that they could not afford to use that laser with the budget constraints imposed on their program. The alternative PLVTS was able to provide hundreds of tests for a few thousand dollars per week. PLVTS thus could provide a lot of information very quickly at low cost, and as a result a lot of progress could be made during each test series.

**Table 1. Estimate for Propulsion Sciences Division, USAF Philips Laboratory
MIRACL Cost Estimate**

Item	Date	Fluids	Aerotherm	TRW	SLBD	Lockheed	NR	CSSD	MISC	Total
Piggyback (Low)	1997	15K	25K		50K	10K	20K	20K	5K	145K
Estimate assumes 5 sec piggyback onto Nautilus test at low power (40%)										
Dedicated (High)	1998	600K	50K	50K	50K	10K	100K	20K	5K	885K
Estimate assumes 60 sec dedicated test at high power (80%)										
Dedicated (Low)	1998	228K	50K	50K	50K	10K	100K	20K	5K	513K
Estimate assumes 60 sec dedicated test at low power										
Grand Total										1,543K

During the plasma breakdown tests, the amount of laser energy passing through the breakdown plasma to the second (#2) calorimeter was measured as a function of incident laser energy. This information is plotted in Figure 16. It can be seen that the laser energy passing through the plasma increases linearly with increasing incident laser energy.

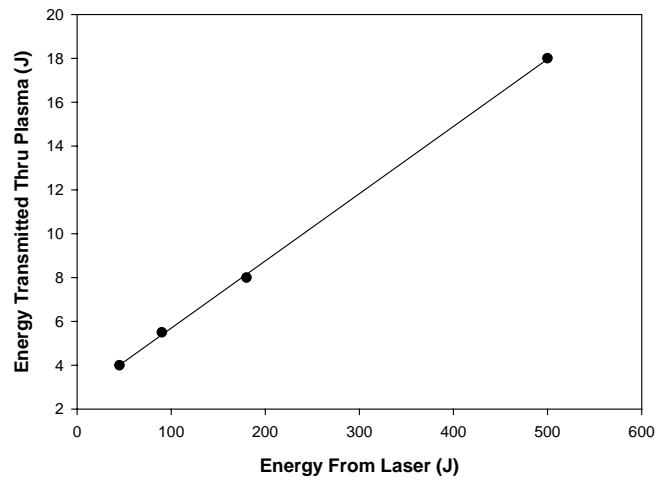


Fig. 16. Energy Transmitted Through Laser Plasma

2.4 Test Series #2 (12-14 Aug 96)

Tests were conducted to measure coupling coefficient (C_m) as a function of laser energy (J) and variable nozzle length using the 8-inch focal diameter aluminum Lightcraft mounted on a vertical pendulum (See Fig 17).

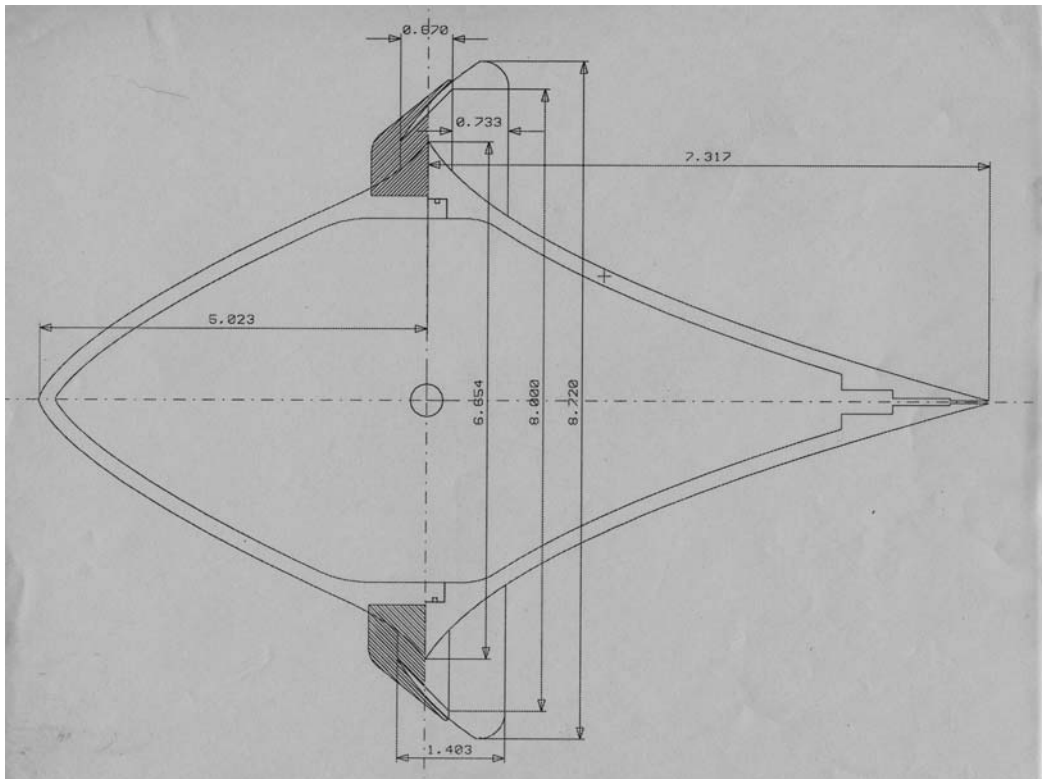


Fig 17. Schematic Drawing of 8-Inch Lightcraft

The pendulum length from the pivot to the Lightcraft center of gravity was 33.4 cm, so nozzles longer than this length were not considered a good idea, and aerodynamic drag was definitely a problem for these tests. The material used to construct the nozzle extensions was clear transparency film for copiers typically used for making slides for viewgraph presentations (Butyrate). Pieces of this material were taped together and cut to the desired length to form cylindrical tubes that extended the 8-inch focal diameter to values of 1, 2, and 3.

Calibration of the pendulum with full Lightcraft model and the various nozzle extensions was accomplished by swinging a known mass of clay on a string from a known height (h) to impact the pendulum system and measure the velocity imparted to the pendulum. The assumption here was that $mgh = \frac{1}{2}mv^2$, leading to the measured value of velocity, $v = (2gh)^{1/2}$ imparted to the pendulum system mass in terms of an impulse and measured displacement. This impulse was measured on an oscilloscope recording the voltage generated by the movement of an aluminum conductor through a magnet, as illustrated in Figure 18. The drop height selected was 37.8 cm, and therefore giving $\Delta v = 2.7227$ m/s. The delivered impulse would thus be $I = 2.7227m$ in units of Newton-seconds (N-s), where m is the mass of the clay calibration ball. Clay balls were assembled in masses of 25, 50, and 75 grams; and were weighed in the chemistry building on an electronic scale. A large number of calibration runs (≥ 8) were made for each of the clay balls, and an average voltage was calculated and divided into the theoretical impulse to give a calibration value in units of N-s/V. This procedure was repeated for each of three L/D extensions.

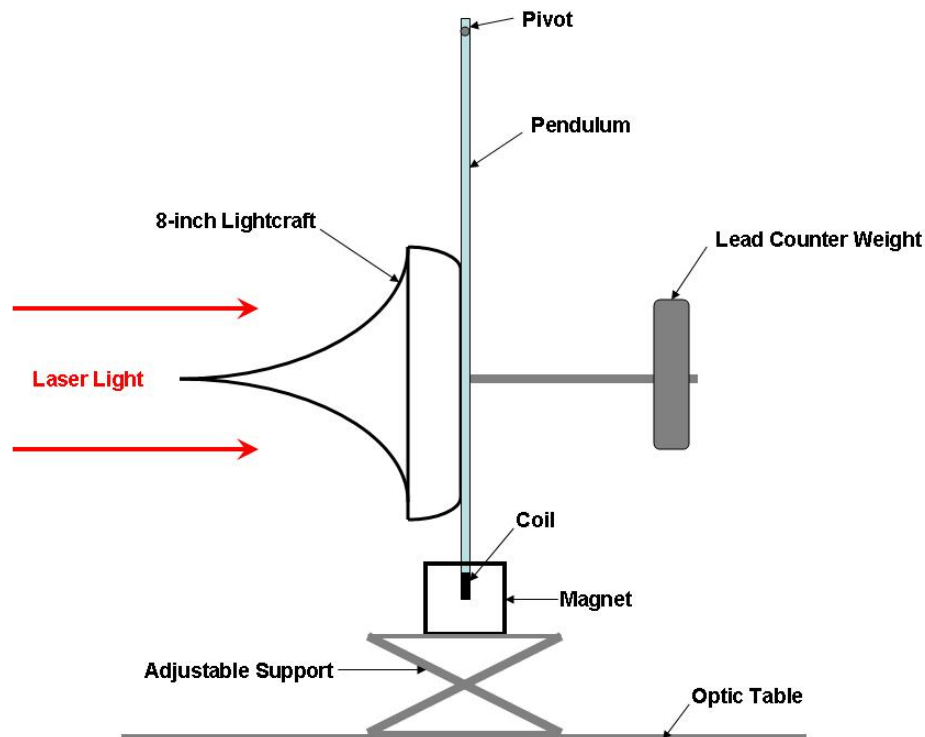


Fig. 18. Pendulum System Set-Up

The three points determined by this calibration procedure are illustrated in Figure 19. These points were fitted to a curve using a second order least squares curve fit which determined the equation of the fit. This equation was then used to calculate missing calibration values (i.e., $L/D = 0, 0.5, 1.5,$ and 2.5). Figure 19 shows the curve, gives the equation, and lists the calculated and experimental calibration values.

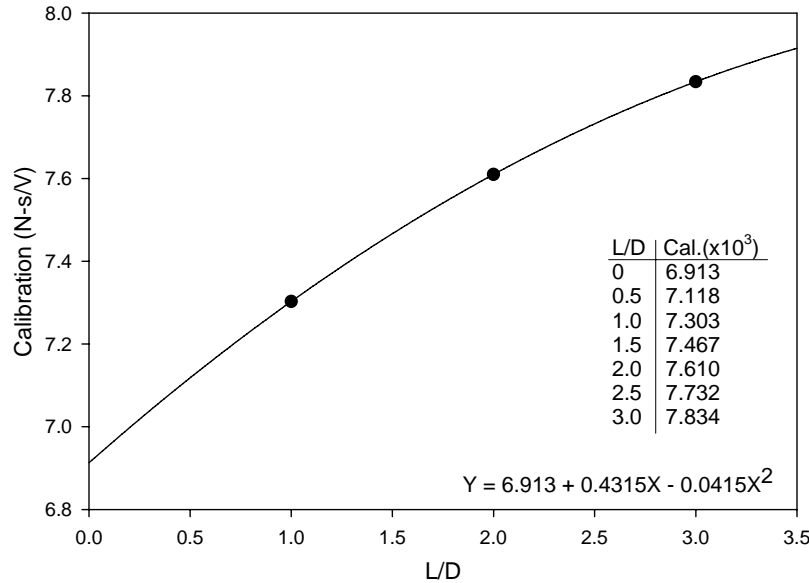


Fig. 19. L/D Calibration Curve for 8-Inch Lightcraft

The calibration values were then used to reduce all the voltage data. The results are illustrated in Figure 20, where the performance in terms of the coupling coefficient, C_m , is shown vertically, and L/D (a) and laser energy, b, are on the horizontal axis. Each point represents an average value of many runs at constant laser settings and geometries. As can be seen in Figure 20a, there is a large scatter in the data. This scatter seemed to be affected by slight changes in laser power over the duration of the tests, alignment problems, cleanliness of the optical mirrors in use for the experiments, and the measurement technique itself. With only 3 points for an L/D of 2 as illustrated in Figure 20b, the performance seems to peak at about 680 J, and can be improved by a factor of perhaps 3 or 4 by extending the nozzle to the values illustrated here.

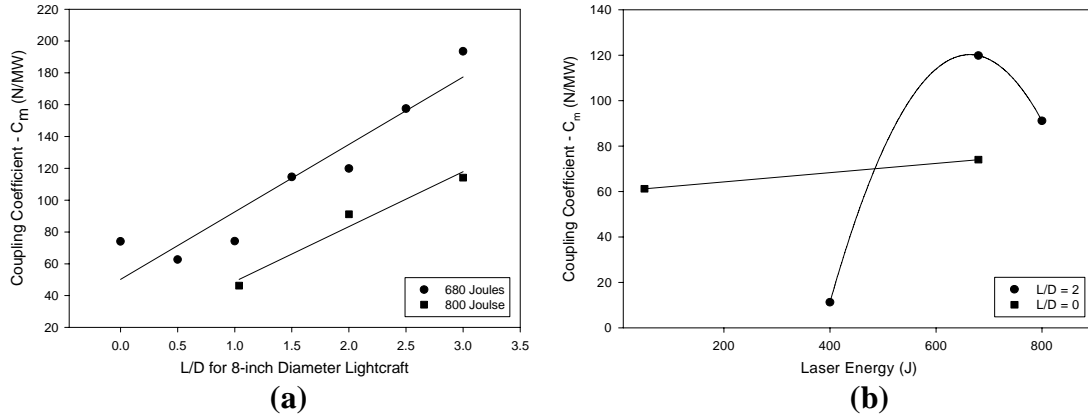


Fig. 20. Measured Coupling Coefficient of the 8-Inch Lightcraft as a Function of Nozzle Extension Length (a) and Laser Energy (b)

High Speed Photography: High speed photography was used in an attempt to gain an understanding of the plasma breakdown dynamics. The camera was a 4 Quik 05 from Stanford Computer Optics with an effective ASA rating of 50 to 500,000. The frame-grabber was Quick Capture by Data translation of 640 pixels x 768 pixels x 256 shades, using a Mac II fx PC. Timing was set by using a 12 V trigger from the laser ionizer to trigger an HP 8116A pulse generator. A -5 VDC, 30 μ s pulse from the 8116A triggered the camera shutter. Any required delay was subsequently generated by the camera, and the end of shutter triggered the frame-grabber. The camera was borrowed from Dr. Douglas Talley at the AFRL Aerophysics Branch, and the operator was Mr. Dave White from the Electric Propulsion group at the AFRL Lab. Each photograph was coordinated with an actual test number. This number, the shutter speed, trigger delay time, pulse energy, and f stop were recorded and later placed in the upper right hand corner of the photograph. There is also a G value, but its meaning has been lost in time. Two consecutive examples of the high speed photography are shown below in Figure 21. The shutter speed, $t = 50$ ns, the delay time, $d = 21.3$ μ s for a, and 21.2 μ s for b, and 800 J of laser energy at a camera setting of $f = 8.0$. From the actual trigger event, the laser light arrived at the thruster at about 19 μ s as best as could be figured, so the actual pictures are 2.3 and 2.2 μ s after laser energy arrival. Also if one consults the recorded data, tests 188 and 189 were conducted at 680 J (650 J on target = 10.18 J/cm), not 800 J.

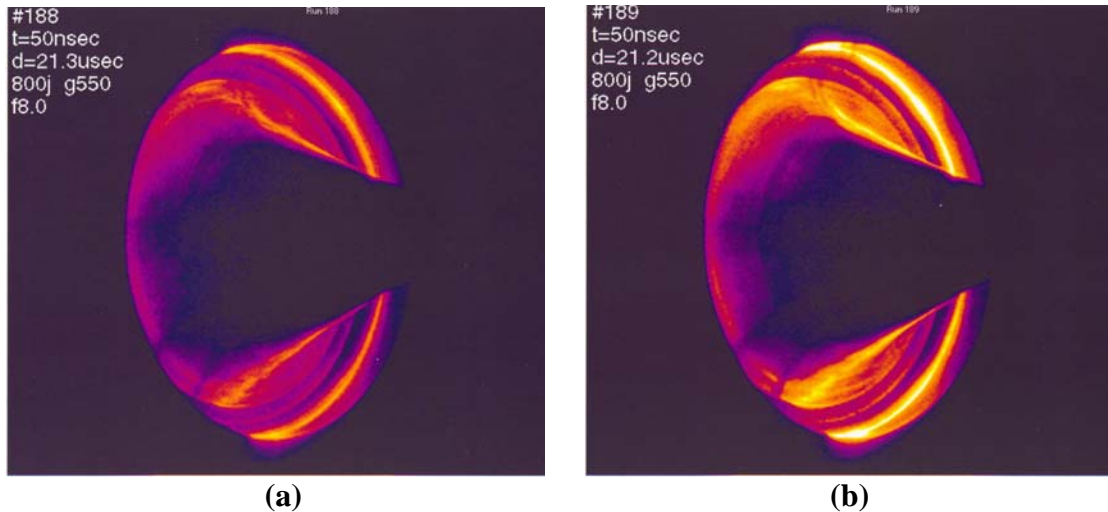


Fig. 21. High Speed Camera Photographs (a) = Test #188 and (b) = Test #189
(Taken with a 50 ns Shutter Speed and about 2 μ s after the Arrival
of the Laser Beam on the 8-Inch Lightcraft Shown in Figure 18)

Later tests with a 10 cm Lightcraft will show that the plasma breakdown occurs within a time range of about 50 to 120 ns, so the time in microseconds would at most be off by about 0.1 μ s. Thus the pictures were taken at about 2.2 and 2.1 μ s respectively after breakdown and plasma formation. In these pictures there is no nozzle extension ($L/D = 0.09$). It was really very difficult to get much information from these pictures. There was a lot of timing jitter in the laser energy, the camera focus was not very good, and internal reflections caused confusion on what was really being observed.

Music wire, 302 Stainless Steel Spring temper wire, was stretched tightly between two points. The Lightcraft was mounted on the wire with the nozzle extensions as illustrated in Figure 22. The wire used was 29 gauge, 0.075-in. diameter wire at approximately 68 ft/lb. The wire was run the length of the optic table and stretched sufficiently such that there was only a 1 cm sag in the center. The wire was coated with three coats of "Turtle Wax" to reduce drag. All attempts to get the Lightcraft to move using a variety of nozzle extension lengths and laser pulse repetition rates on the wire failed. However, later analysis by the HELSTF staff of the movies taken would determine, according to them, that the Lightcraft did move, if almost imperceptibly.

Specially designed three point bearings were inserted into the front and rear of the Lightcraft as illustrated in Figure 22. The nozzle extensions were constructed of 8½ x 11 inch sheets of plastic, Butyrate, which was not damaged by the ethyl alcohol that was used to clean it. It was not recorded, but it was believed that the vehicle weight was 2 kg. This was an extremely heavy vehicle to try to move on the wire.

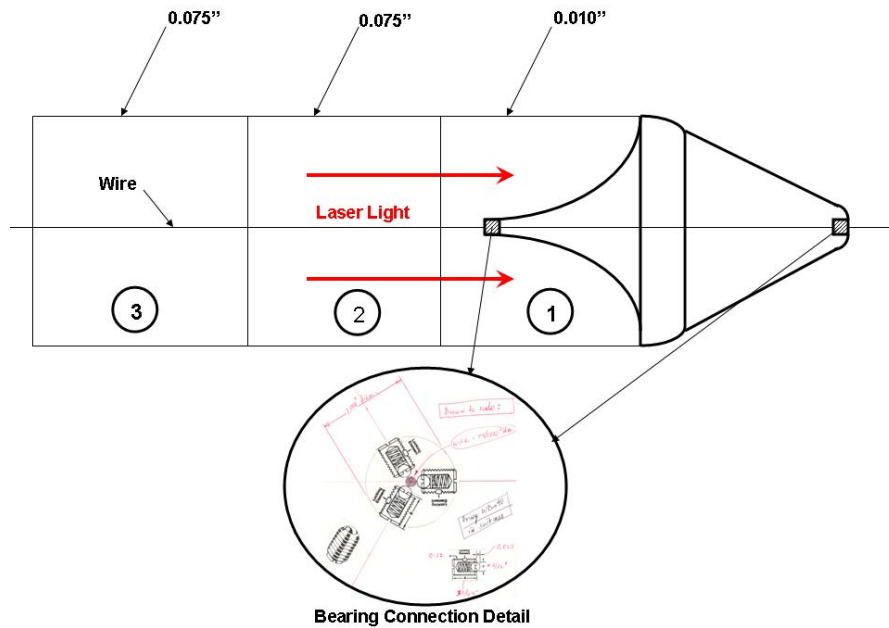


Fig. 22. Schematic Illustration of the Wire Test Configuration with the Nozzle Extension Connected

2.5 Test Series #3 (22-24 Oct 96)

The main objectives of this test series were to test the 8-inch diameter Lightcraft with a longer nozzle extension ($L/D = 6$), and to get the Lightcraft to move on the wire. With regards to the nozzle extension, the thought was that the $L/D = 3$ had been so successful that doubling the L/D value should produce even better performance. For the wire flight, the weight of the model had been cut in half to 1 kg, so it was fully expected that the vehicle would go zinging down the wire at great speed.

The set-up and calibration technique for the nozzle extension tests are illustrated in Figure 24. Again, calibration of the pendulum with full Lightcraft model and the L/D nozzle extension was accomplished by swinging a known mass of clay on a string from a known height (h) to impact the pendulum system and measure the velocity imparted to the pendulum. The assumption again being that $mgh = \frac{1}{2}mv^2$, leading to the measured value of velocity (e.g., $v = (2gh)^{1/2}$) imparted to the pendulum system mass in terms of an impulse and measured displacement. This impulse was measured on an oscilloscope recording the voltage generated by the movement of an aluminum conductor through a magnet slot, as illustrated in Figure 23. The drop height selected was 37.8 cm, and this height therefore gave a $\Delta v = 2.7227$ m/s. The delivered impulse would thus be $I = 2.7227m$ in units of Newton-seconds (N-s), where m is the mass of the clay calibration ball. Clay balls were assembled in masses of 25, 50, 75, 100, 125, and 150 grams; and were weighed in the chemistry building on an electronic scale. A large number of calibration runs (≥ 8) were made for each of the clay balls, and an average voltage was calculated and divided into the theoretical impulse to give a calibration value in units of N-s/V.

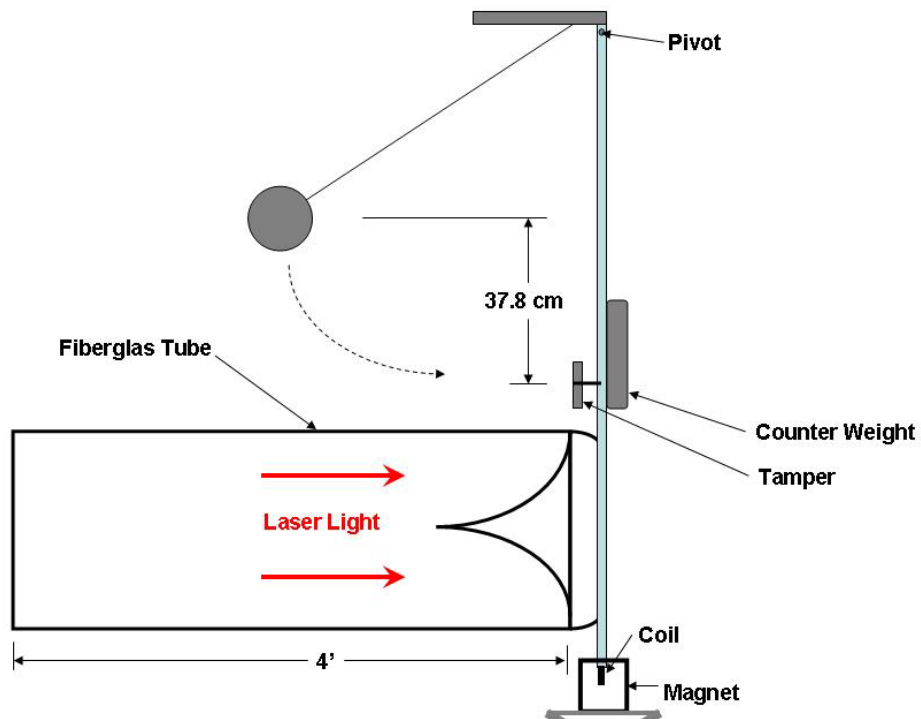


Fig. 23. Pendulum Set-Up Illustration Showing Calibration Technique

The nozzle extension tests were very disappointing. Not only was the performance poor, but the data didn't appear to be consistent with the previous tests. The nozzle extension was made of Fiberglass (see Fig. 24) and seemed to absorb plasma energy and

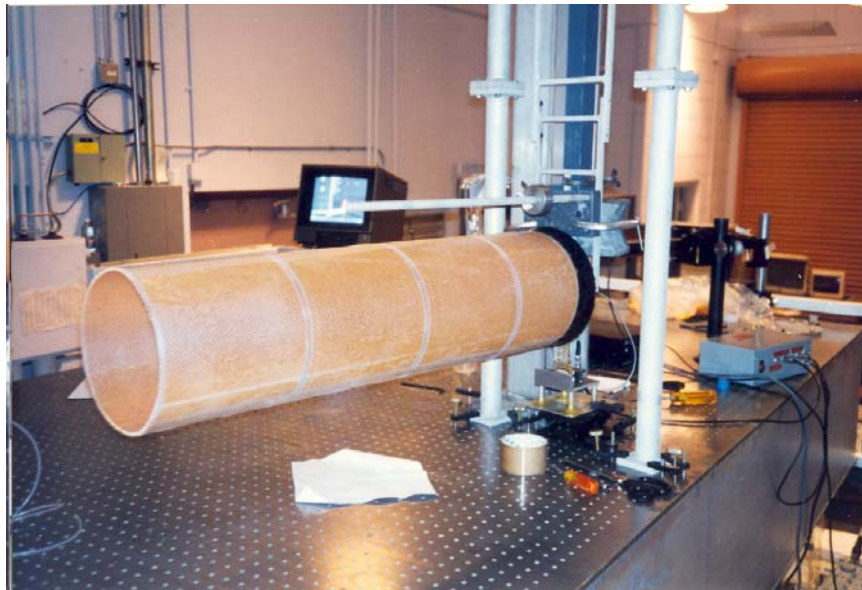


Fig. 24. Fiberglass Nozzle Extension Mounted on 8-Inch Lightcraft for Testing on the Pendulum Impulse Test Stand

emitted light. There was definitely an acoustic damping effect that was noticed. Note that the nozzle extension is made of four separate and equal length sections that have been connected together to form the entire length. The nozzle extension is held firmly in place on the Lightcraft shroud by heavy tape. The nozzle extension was fabricated at RPI prior to testing and then transported to the HELSTF for testing. There are video and pictures that were taken during these tests that thoroughly document the set-up and the actual tests. The video shows individual laser pulses and the resultant small, almost imperceptible movement of the pendulum. Very heavy counter weights had to be used to balance the pendulum so it was vertical. This added mass certainly contributed to the small displacements measured and reduced the accuracy of the tests.

For the pendulum tests, the heavy, 2 kg, Lightcraft model was used with the 4 ft fiberglass/Nomex nozzle extension pipe and 0.005, 0.004, and 0.003 inch brass flapper valves (reed valves) placed over the shroud side of the air inlets. Figure 25 shows a picture of one of the configurations.



Fig. 25. Brass Reed Valve Plate Shown in Foreground

Note that there are 24 reed valves machined into the outside perimeter of the flapper valve plate. On the inner circumference there are holes that match the screw positions for mounting the parabolic afterbody to the forebody. Thus the flapper valves were placed between the two pieces in order to cover the air inlets (See Fig 17). The thicker valves did not seem to have enough flexibility, and the 0.003 valves deformed and permanently bent toward the forebody.

Results of the impulse pendulum tests are shown in Figure 26. The bare (no nozzle extension) Lightcraft clearly performed much better than the Lightcraft with nozzle extensions. The drop-off in performance with the nozzle extension was very significant. In an attempt to get the extended nozzle performance to improve, a gaseous nitrogen purge was used between each test. However, no noticeable improvement was detected. Nozzle lengths included 48, 40, 32, and 24 inches. It would have been nice to have had shorter lengths to fill in the blanks at $L/D = 1$ and 2.

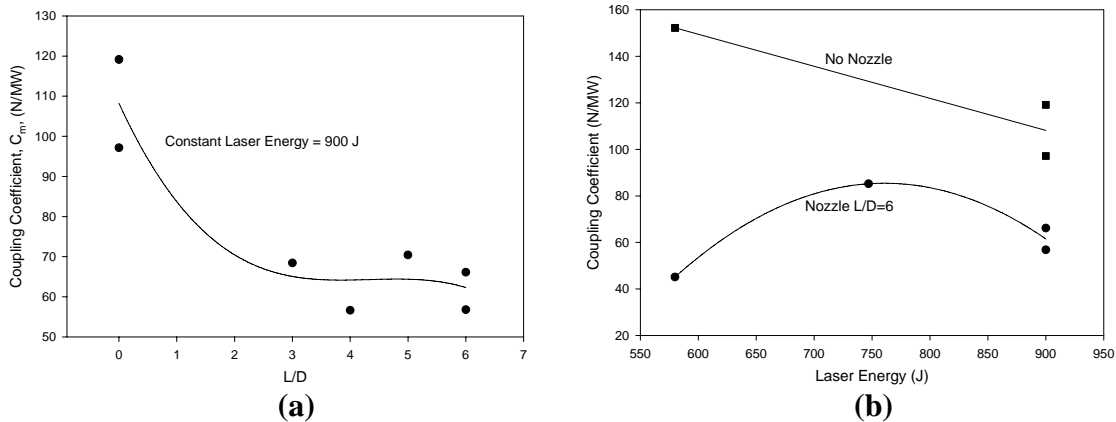


Fig. 26. Measured Coupling Coefficient of the 8-Inch Lightcraft as a Function of Nozzle Extension Length (a) and Laser Energy (b)

For the 8-inch Lightcraft coupling coefficient as a function of laser energy (Fig. 26b), it would have been nice to have taken more data at intermediate values of laser energy. The three point "nozzle $L/D = 6$ " curve is not well defined, and the "no nozzle" curve can only be a straight line without additional points. One would suspect that the "no nozzle" curve would be of similar shape to the "nozzle $L/D = 6$ " curve. Thus, one might suspect a maximum coupling coefficient occurring around 750 J at over 200 N/MW. This would be considerably higher performance than anything indicated in the first or second test series.

Horizontal, wire-guided flight tests were conducted on the third day of testing. Figure 27 illustrates the set-up. The piano wire was very tight, and the Lightcraft only displaced the wire by 4 mm when it was placed in the center of the 11 foot length. A rubber "bumper," shown in yellow, was fastened at the end of the wire in order to avoid damaging the Lightcraft by banging into the support rod at high speed.

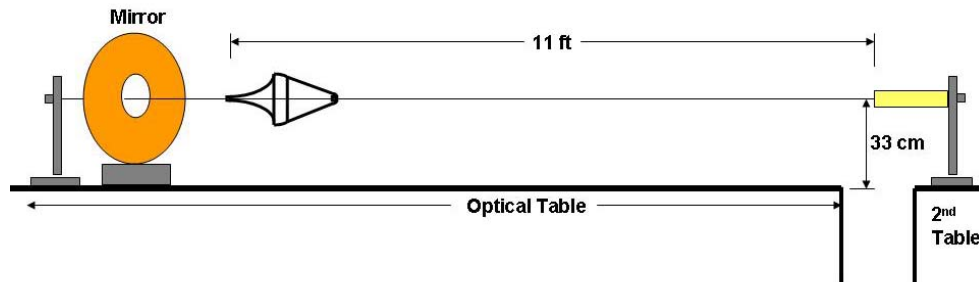


Fig. 27. Indoor Horizontal Wire-Guided Flight Tests

The Lightcraft did not have a nozzle extension; it was bare. The parabolic optic was polished and cleaned with alcohol before each run. This procedure caused an alcohol "boost" on the first pulse - the first pulse was larger than normal. The 0.004 in reed valves were used even though some were slightly bent. The model was "ultra" light (at that point in time) with tri-roller bearings. The larger bearing was on the front and the smaller bearing at the rear. The Lightcraft was initially positioned 1 ft from the turning mirror. Figure 28 is a photograph of the Lightcraft mounted on the wire. Laser light came into the laboratory from the laser trailer and was turned parallel to the Lightcraft, striking it from the left. A total of 36 tests were conducted and recorded on video tape which has now been converted to DVD format.

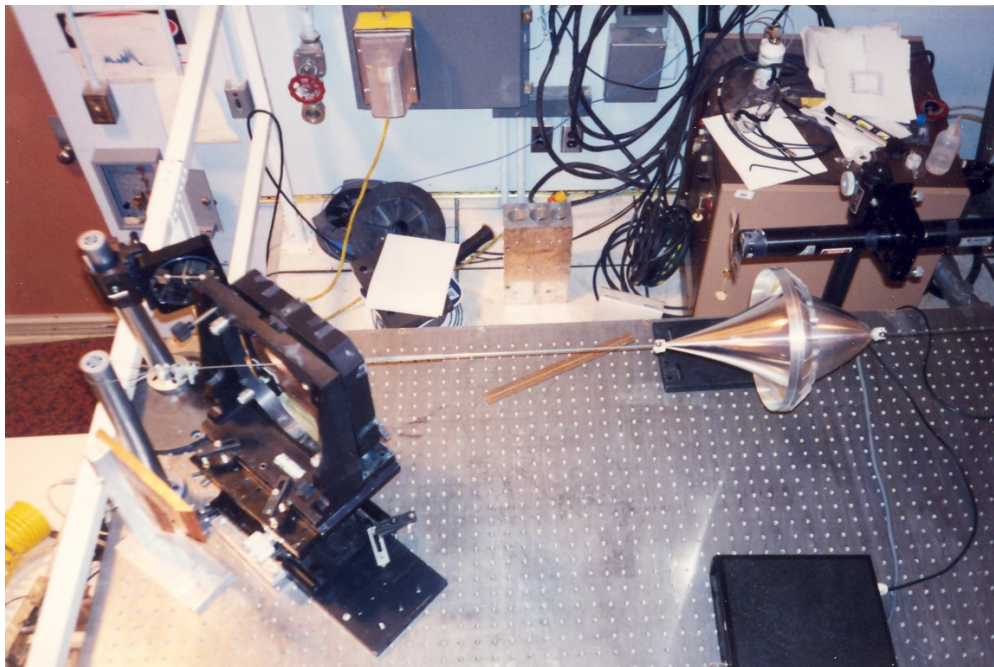


Fig. 28. 8-Inch Lightcraft Mounted on Horizontal Wire

There were 12 "panning" video shots taken by Mr. Squires from above, looking down on the table. These were the best and most dynamic video taken during these tests. Testing started with short bursts of the laser at 10 Hz, and increased in duration until the Lightcraft was able to reach the end of the wire by coasting. At that point it would bounce off the bumper and move rearward for a foot or more.

2.6 Test Series #4 (9-11 Dec 96)

Experiments conducted with the PLVTS pulsed CO₂ laser at HELSTF provided high quality force, pressure, and velocity data for a laser-powered engine. Fifty-seven tests were conducted during the first series, measuring the force history for an engine model with varying valve configurations and pulse repetition rates. Preliminary results indicated no difference in the force measurements for single pulse, 5 Hz, and 10 Hz. The valve

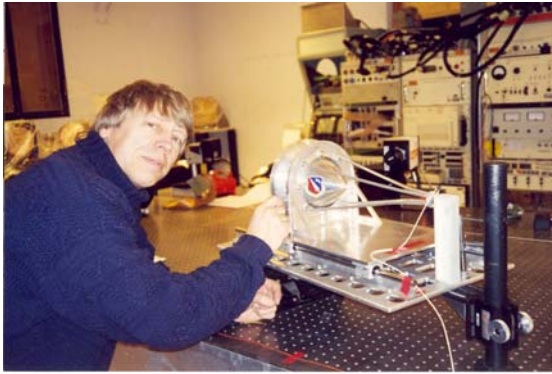
configuration appeared to have little influence on the peak force and coupling coefficient, with the preliminary data for all configurations within experimental scatter of each other. The normalized peak forces averaged between 30 and 45 lbs/kJ, with a maximum for the valveless configuration, at 16 lbs/MW, while the average peak value was 40 lbs/MW. The peak velocity of the wire-guided Lightcraft model was measured to be 7.3 fps, with an average acceleration of 0.16 g over 76 inches. Excellent pressure data was obtained, but the pressure gauges must be calibrated before the data can be interpreted.

Several experiments were conducted to gather information on the laser engine performance. Impulse measurements were made with the 8-inch model mounted as shown in Figure 29. A short summary of each experiment is provided below.

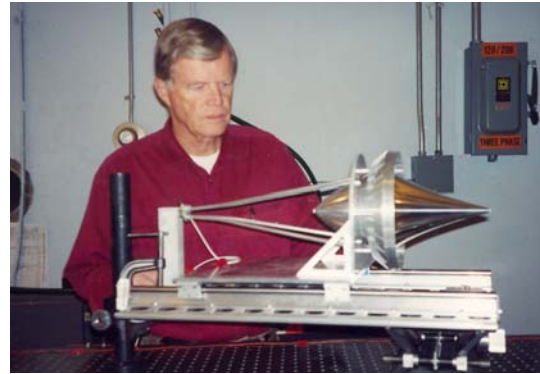


Fig. 29. 8-Inch Lightcraft Pendulum Tests

Load cell thrust measurements were made with the test stand illustrated in Figures 30 and 31. The first tests were performed on the full scale, 8-inch model which was instrumented only with a load cell to measure thrust. These experiments were given code names and saved in the Tektronix 2520 test files. Two test files were used because the disk space on the data acquisition unit was filled before completion of the test series. A photodiode was used to trigger the data acquisition unit, and an infrared detector was added midway through the test series to provide information about the laser pulse and coordination with optical diagnostics.



(a)



(b)

Fig. 30. Direct Thrust Measurement Test Set-Up with the 8-Inch Lightcraft Using Piezoelectric Transducer (a) with Prof. Myrabo and (b) with Dr. Mead

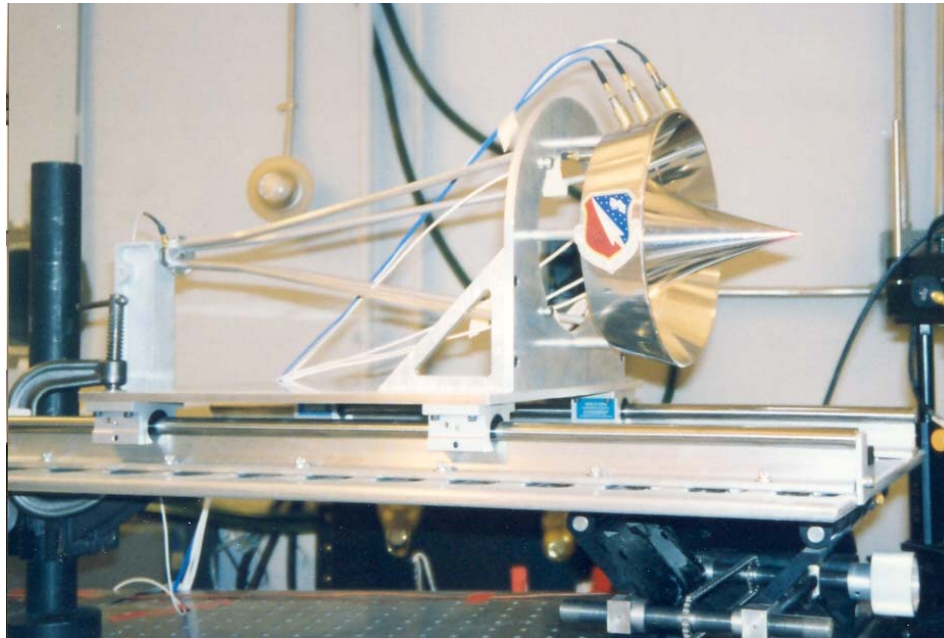


Fig. 31. Direct Thrust Measurement with Conical Nozzle Lightcraft and Piezoelectric Pressure Transducers Installed

The load cell was calibrated in situ by carefully setting various weights on a platform attached to the nose of the model. The charge amplifier was set to the long time constant option, which should have resulted in a time constant on the order of 10 s, long enough for an accurate static calibration. The data acquisition unit was set to record both the voltage change due to the weights and the time integrated voltage trace. The latter was used to record the data. The time integration provided an effective smoothing of the trace, removing any dependence on the procedure used to drop the weights. A preliminary calibration of 121 mV/lb was obtained. The calibration procedure was recorded on video tape.

The load cell calibrations were performed prior to and immediately following each test series. In all cases, the calibration coefficients did not change. This indicates that the calibration does not depend on the model configuration.

Force data was obtained for single and multiple laser pulses with various valve configurations. The load cell traces were recorded as voltage and time-integrated voltage traces. The latter were useful for quickly determining the impulse which was delivered to the model. A careful data reduction procedure is necessary for dealing with the integrated impulse measurements, since a slight drift which was present in the charge amplifier output resulted in a constant positive or negative bias on some traces. Although not a factor in the thrust measurement, the bias appears as an error in the impulse which is directly proportional to the time after trigger. A computer-based analysis of the results is required to remove this error.

A 65% scale model with conical shroud was instrumented with pressure transducers and installed on the thrust stand for simultaneous pressure and force measurements. This experimental set-up is shown in Figure 32. These experiments were given the code names and the data was saved on the Tektronix 2520 data acquisition unit.

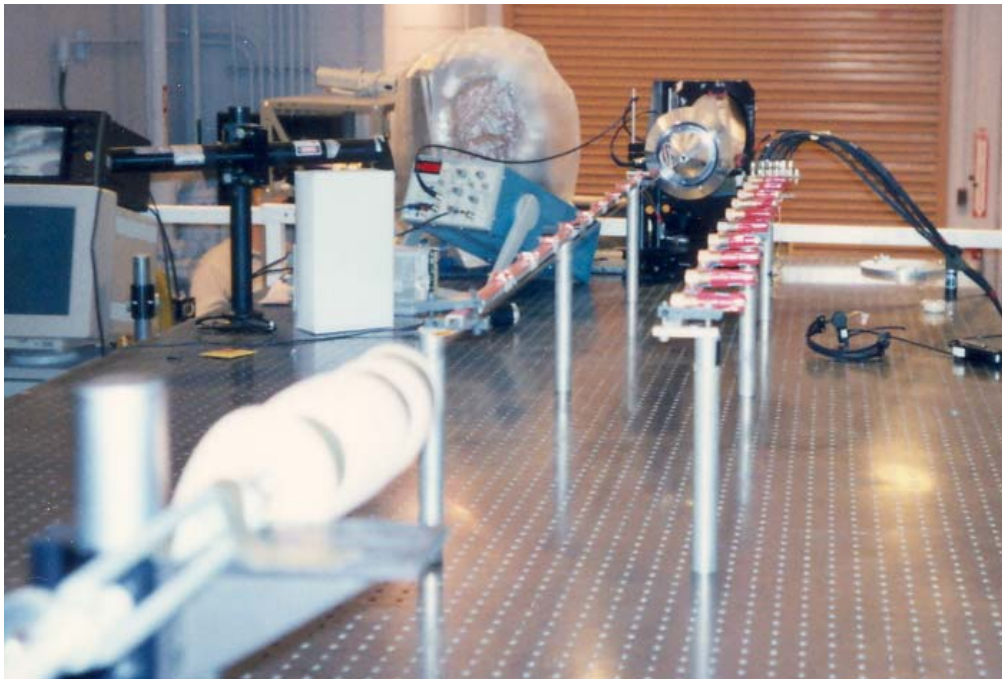


Fig. 32. Picture of Experimental Set-Up with Diode Ladder for Measuring Velocity and Acceleration

The sample rate of the data acquisition was not adequate to properly capture the pressure measurements. The clock time was limited to a minimum of 34 μ s because of the multiplexing nature of the cards used during these tests. A second set of experiments was conducted with two pressure transducers at a sample clock of 80 ns, which eliminated the aliasing caused by the slower clock. The 5 μ s sample clock of the

proposed 16 channel VXI data acquisition unit should be adequate for future experiments.

The first several tests produced limited results, as some of the amplifiers and other equipment were nonfunctional. Only one pressure measurement location could not be recovered by repair or swap-out of equipment. This pressure transducer was a Kissler quartz gauge located at the corner of the cowl and nozzle. Laser damage is the suspected reason for this malfunction. The area around the pressure transducer hole was blackened. Upon removal of the transducer, it was found that a small, circular score the diameter of the pressure tap hole was present on the transducer diaphragm.

This pressure data was never fully analyzed because the pressure transducers were not calibrated prior to the test series. The data files are available on CD.

Additional horizontal, wire-guided flight tests were conducted using the laboratory set-up illustrated in Figs. 32 and 33, and this time a photo diode array or "ladder" was added in an attempt to measure velocity and acceleration. Each photo diode had a detector opposite it placed in such a way that, as the vehicle moved down the wire, it would cut the light path for a certain period of time as it passed by. The signal of each sensor was sent to an oscilloscope where it was recorded during each test.

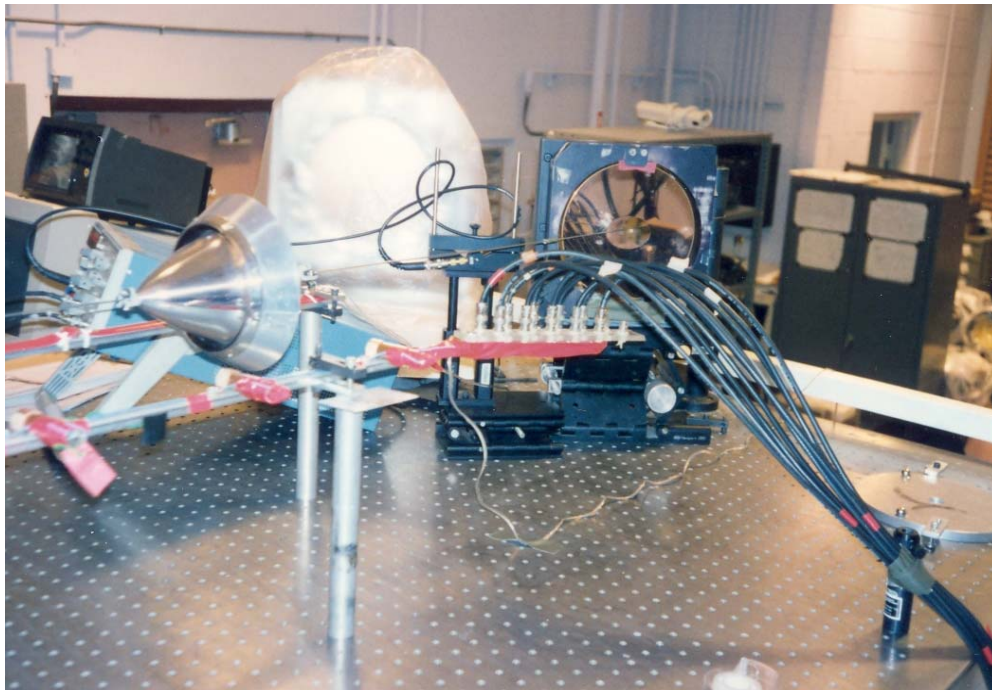


Fig. 33. Picture of Lightcraft with Conical Shroud, Wiring from Photo Diode Ladder, and Photo Diode Mounting Details

The photodiode array failed to operate properly. It was suggested that future designs should employ a resistor to provide limiting of direct current to the detector and emitter, instead of relying on the data acquisition unit as by Minucci⁽¹⁸⁾ and these wire guided tests.

The photodiode used for a trigger in the previous experiments was placed in the path of the Lightcraft model such that the annular cowl would interrupt the light falling on the detector. The apparent width of the cowl, together with the measured initial start time of the laser, was used to determine the velocity and average acceleration of the model.

However, by this time in the test series, the laser was not reliable. The pulse energy was suspect due to equipment failures, and it was noticeably sometimes skipping pulses.

The plot in Figure 34 contains an indication that the laser pulse energy changes significantly over the course of a test series. Here the data indicates an almost linear drop with time or test number. It is thus essential that laser power runs be conducted after every three to five experiments to provide more accurate data during future experiments.

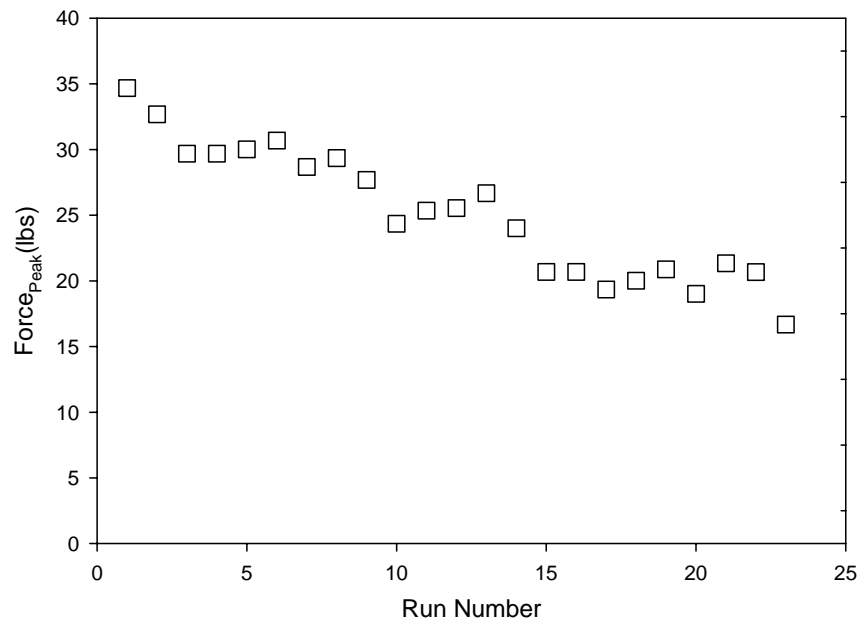


Fig. 34. Peak Forces for the First 23 Tests of the Load Cell, Full Scale 8-Inch Lightcraft Model

The data plotted in Figure 35 illustrates the variation in performance obtained with various Brass reed valve thicknesses and/or configurations. In this plot, the peak force has been normalized by dividing by the laser pulse energy in kilojoules.

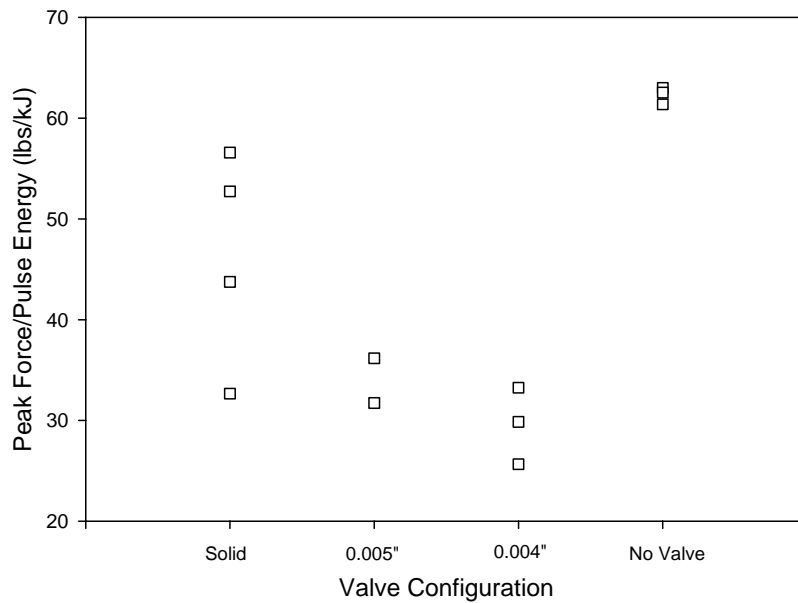


Fig. 35. Peak Force Normalized by Pulse Energy for Load Cell, Full Scale 8-Inch Lightcraft Model

High speed photographs were also taken during the thrust stand and pendulum tests of the 8-inch Lightcraft. Figure 36 illustrates an example of the breakdown characteristics observed at the ring focus on the inside of the aluminum shroud. This picture was taken from the side at a small angle off parallel in order to "look" inside the model from the rear. In the center of the picture can be seen the outline of the parabolic reflector. Multiple points of plasma initiation, most probably at the corners of the beam's square pattern, can be seen starting in the picture which was taken with a shutter speed of 100 ns.



Fig. 36. Example of High Speed Photography Showing Plasma Breakdown on the Inside of the Shroud
(Outline of Parabolic Reflector can be Seen in Center of Picture)

Thus ended the final series of tests under the initial contract awarded to Dr. Myrabo at RPI. The original RPI proposal had contained a number of suggested follow-on Phases which were never considered further. Hence, the ultimate goal of the entire program, which was to boost an ultralight spacecraft into low Earth Orbit in order to demonstrate a very low-cost alternative launch system for micro-satellites with payload masses equivalent to Sputnik or Explorer, was essentially abandoned at this point, and a more deliberate experimental and development course was pursued as described below. In other words, the development and launch of a fully functional satellite to Earth orbit using laser propulsion was much more difficult than previously perceived and would require much additional work.

3.0 THE INTERGOVERNMENTAL PERSONNEL ACT (IPA) LTD PROGRAM

3.1 Introduction

In January 1997, an IPA agreement was signed by Dr. Leik Myrabo that would effectively allow him to work full-time at the AFRL, Edwards AFB CA. Thus, the LTD program became an in-house program with testing conducted at HELSTF. Resources were provided annually by the Air Force, and over the first three years NASA Marshall provided substantial funding additionally to “jump start” the program. During the month of February 1997, Dr. Myrabo reported to the AFRL Laboratory as his primary work station. All test series between March 1997 and July 1999 were conducted through the IPA program. A separate support contract with the RPI machine shop was also established to support the program. Almost all the test hardware was fabricated in the RPI machine shop. Dr. Donald Messitt, then a Ph.D. candidate at RPI, and other graduate students were also incorporated into the program for support.

3.2 Test Series #5 (24-26 Mar 97)

Figure 37 illustrates the laboratory set-up for vertical flight tests. Laser light is reflected vertically by a large turning mirror with a hole in the center through which a launching rod projects from the optical table. Each vehicle (in this case the 65% vehicle is shown) designed for the vertical testing (see Fig. 38) had bearings installed at the front and rear. The launch rod slid through these bearings, and the vehicle was kept above the mirror by a piece of tubing placed on the launch rod below the vehicle. This piece of tubing can be seen projecting above the mirror's hole in Figure 37. Dual gaseous nitrogen (GN₂) nozzles were mounted on short fixed feed lines about the periphery of the shroud, as can be seen in Figure 37. The height of these nozzles was adjusted in order to provide the best spin-up of the test vehicle before launching with the laser beam.

For this series of tests, the laser was down all day Monday, 24 March 1977. The vertical flight (hover) tests were conducted all day Tuesday, 25 March. None of the flight vehicles lifted off the wire launcher. Horizontal wire guided "demos" were conducted all day Wednesday, 26 March, and for Discover TV in the afternoon. A copy of the Discover video taken during the afternoon demonstrations is included with the archived DVDs.

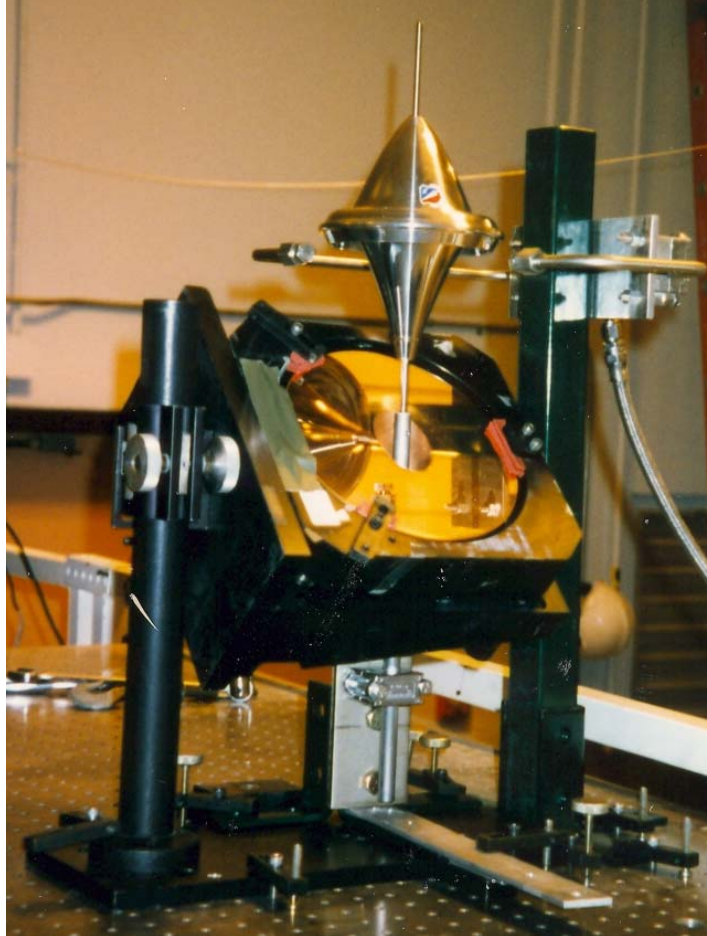


Fig. 37. Wire-Guided Laboratory Launch Set-Up

The data acquisition system was not functional during all three days of testing. As a result, no load cell or pressure data was taken.

Figure 38 illustrates the variation in models that had been developed to this date. The general trend was towards lighter and smaller models. The flat front end or half vehicles were an initial attempt to provide lighter vehicles. Even then, none of these flight vehicles were light enough to lift off the launch rod. So, it was a problem with weight and friction on the launch rod.

Of the horizontal wire-guided models, the work horse for these tests was the conical shroud model. The conical shrouds were good for about three flights before the laser light cut through the thin aluminum shroud material. Replacement shrouds had been fabricated in advance to cover this problem; and after each series of three test runs down the wire, the shrouds were quickly replaced. The video taken during these tests illustrates how the cutting occurred and the replacements were accomplished. Because the data acquisition system was not functional, acceleration and velocity measurements could not be taken during the horizontal wire-guided tests. However, the photodiodes could be turned on, and the lighting pattern of the photodiode ladder made for very impressive videos of the tests.

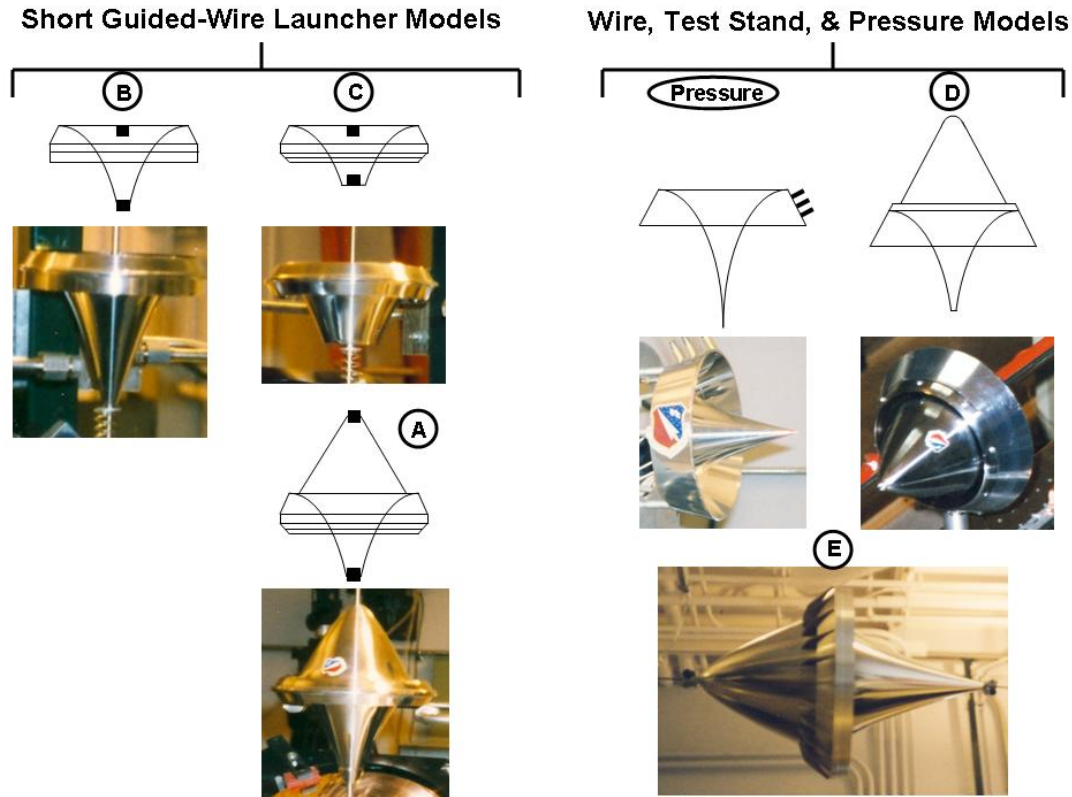


Fig. 38. Lightcraft Models Tested Through March 1997

There are certain characteristics of the wire-guided models that are illustrated in Figure 38 that will be carried through to the final selected configuration of the Lightcraft. Note that the shroud is now sloped inward below the focal ring, which now has a reinforcing thin band around it. These features were to be the strength of the flight vehicles developed in the future.

3.3 Test Series #6 (21-24 Apr 97)

A series of 38 thrust stand measurements were made (See set-up illustrated in Figure 39) during Monday and Tuesday, 21-22 April 1997. The results of these tests are detailed in Table 2 and shown graphically in Figure 40. Table 2 lists the run number in the first column, the number of total pulses and nomenclature for the first pulse following the comma in the second column, the laser energy level in the third column, the values for the coupling coefficient in terms of the average over the total number of pulses and the coupling coefficient for the first pulse following the comma in the fourth column, the vehicle model according to that indicated in Figure 38 in the fifth column, and some defining notes in the sixth or last column. In some cases, a value of total pulses and/or average coupling coefficient was not recorded. This is indicated in the table by a hyphen or dash (-).

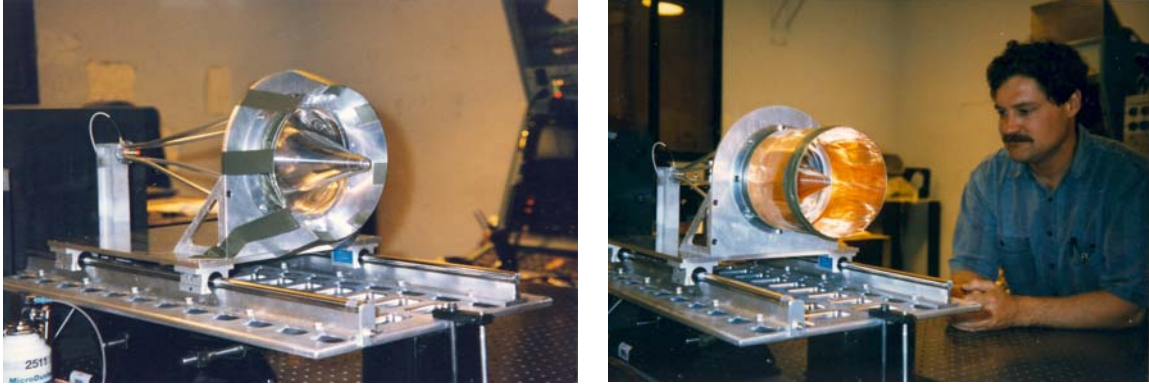


Fig. 39. Thrust Stand Test Set-Up Illustrated with Various Vehicle Configurations

Table 2. Thrust Stand Test Results

Run #	Pulses	J/Pulse	C _m	Model	Notes
1	15, 1 st	520	71.0, 69.1	E	Open Inlets
2	17, 1 st	564	75.1, 72.7	E	Same
3	11, 1 st	574	72.8, 87.1	A	Bare
11	28, 1 st	689	77.7, 89.2	E	Closed Inlets
12	31, 1 st	715	73.7, 80.5	E	Same
14	36, 1 st	741	85.5, 71.5	E	Same
15	28, 1 st	741	80.7, 70.2	E	Same
16	29, 1 st	733	46.9, 60.3	B	Bare
17	31, 1 st	757	50.5, 55.6	B	Same
18	35, 1 st	757	-, 57.1	B	Same
19	21, 1 st	666	88.7, 87.2	A	Bare
20	20, 1 st	666	-, 98.3	A	Same
21	29, 1 st	718	92.4, 94.1	A	Same
22	23, 1 st	686	-, 31.8	A	Nozzle (Converging/Diverging)
23	25, 1 st	757	-, 42.3	A	Same
24	38, 1 st	731	-, 41.0	A	Same
25	36, 1 st	731	93.3, 99.9	A	Bare
26	39, 1 st	705	76.1, 80.1	Pressure	No Transducers
27	42, 1 st	726	72.6, 78.1	Pressure	Same
28	46, 1 st	741	73.0, 75.7	Pressure	Same
29	37, 1 st	744	-, 26.8	B-5 ¹ / ₈ in.	w/Nozzle of L/D \approx 1.0
30	-, 1 st	731	-, 36.7	B-5 ¹ / ₈ in.	Same
31	-, 1 st	744	-, 52.2	B-5 ¹ / ₈ in.	
32	22, 1 st	684	-, 80.4	B-5 ¹ / ₈ in.	Same
33	-, 1 st	731	-, 80.7	B-5 ¹ / ₈ in.	Same
34	-, 1 st	705	-, 58.8	B-5 ¹ / ₈ in.	Same
35	-, 1 st	736	-, 46.1	B-5 ¹ / ₈ in.	Flared Exit
36	-, 1 st	705	-, 31.9	B-5 ¹ / ₈ in.	Same
37	-, 1 st	705	-, 58.0	B	Bare
38	-, 1 st	705	-, 51.7	B	Same

The data from Table 2 shown in Figure 40 is incremented in both symbol type and color to better illustrate the graphical results. As a reference to the configuration, refer to Figure 38. A second order curve fit was used for all the data except for the B-5¹/₈-in.

Flared which had only two points. Except for model "A Bare," the data was collected over such a small range of laser energies that it is difficult to make any significant comparisons. Some data goes up with increasing laser energy and some drops off. Model "A" appears to have provided the best coupling coefficient within the limits of the data, and the models having nozzles appear to have performed more poorly than the bare models, in general.

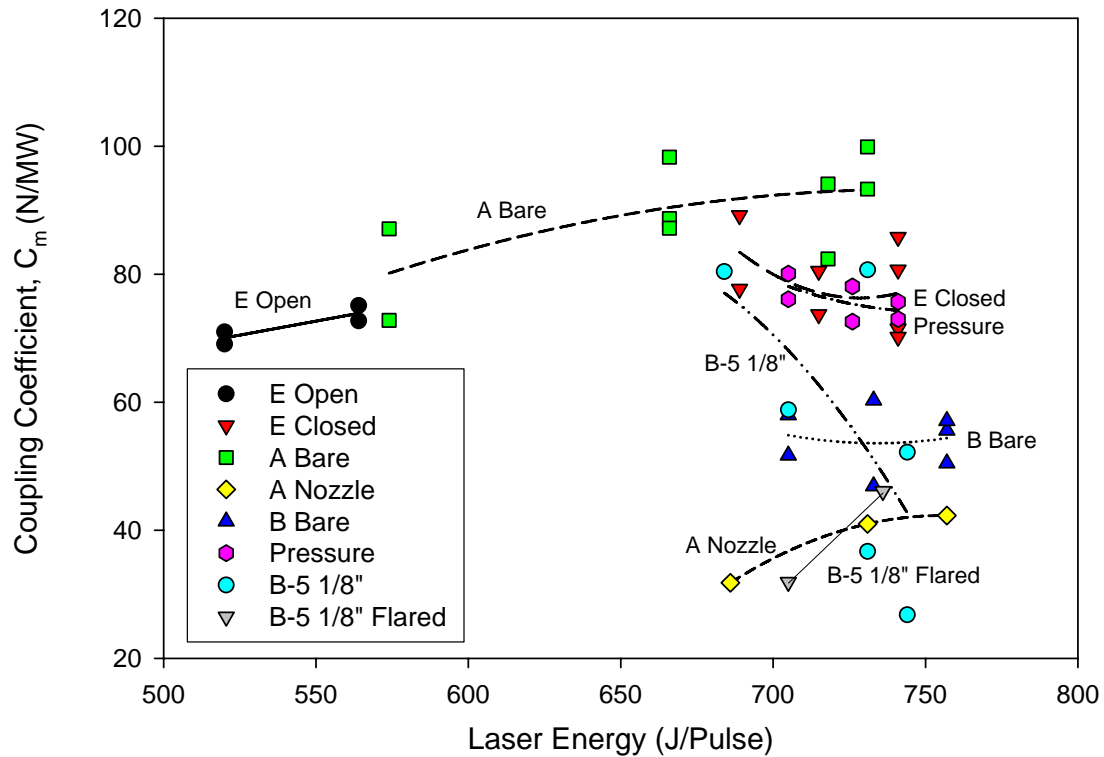


Fig. 40. Calculated Coupling Coefficient (C_m) Versus Laser Energy per Pulse From Direct Impulse Measurements for a Number of Different Vehicle Configurations

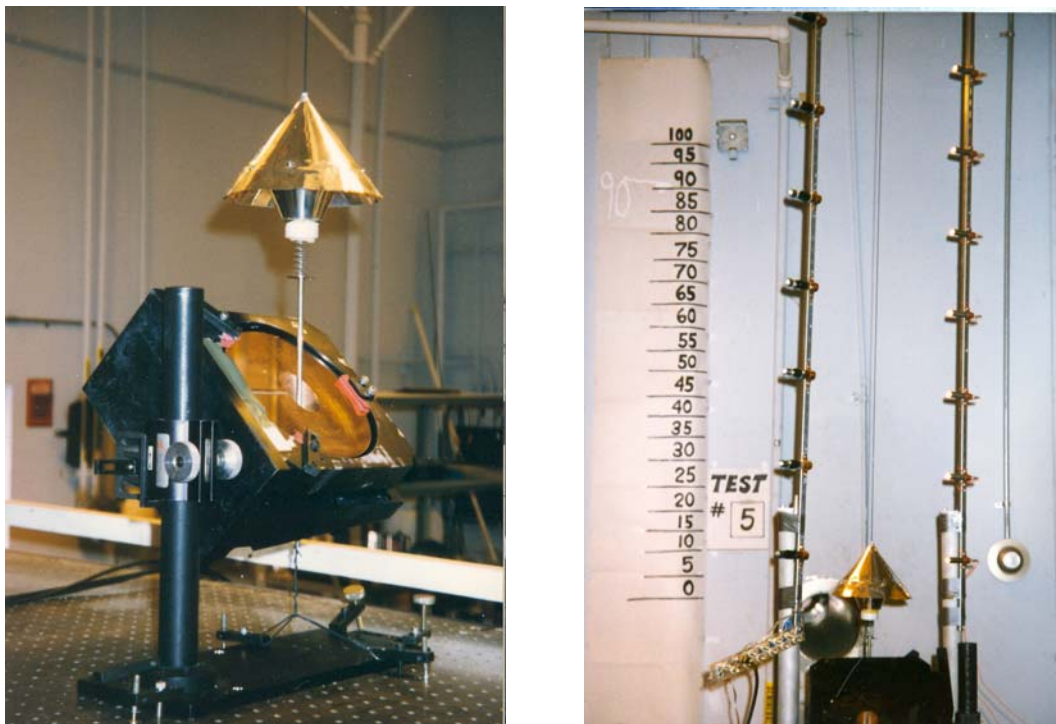


Fig. 41. Pictures Illustrating Vertical Wire-Guided Flights with Diode Array Installed to Measure Acceleration

Table 3. Measured Vertical Acceleration of Model C

Run #	Model	Acceleration (g's)
1	C	0.66
5	C	0.44
7	C	0.52

Vertical free-flight tests using a short 12-in. wire launcher (see Fig. 41) were set up to test the lightest 65% Lightcraft model (i.e., truncated cone w/0.005-in. conical forebody). Large grid graph paper was placed on the laboratory wall opposite the camcorders to register the flight position of the craft, and to perhaps record the vertical velocity and acceleration with the sensor array, if the flights were successful. The model was slowly spun up with compressed nitrogen prior to the vertical boost. Bubble-wrap was attached to the laboratory ceiling above the vertical wire launcher, and a large plastic recovery tarp was stretched across the lab – just above the 45° turning mirror on the optical bench. Flights were to be recorded with two or three shielded camcorders. If the conical nose cap was too heavy, it could be replaced by a 0.005-in. aluminum flat plate with a bearing at the center for the wire launcher. At the end of the day, a determination was made of the best experiments for "UltraScience" to videotape the following afternoon.

Wire-guided horizontal acceleration tests were set up using the newly light weighted 65% Lightcraft with the sheet metal aluminum shrouds. Six aluminum 0.012-in. thick shrouds were available for replacement, and a new 0.005-in. thick aluminum shroud with

replaceable 0.007-in. or 0.012-in. stainless steel igniter rings was available. Set-up incorporated the maximum run length by utilizing the same test set-up as for the March 97 tests. A coiled spring was mounted at the origin end of the wire to protect the turning mirror from a Lightcraft that might bounce back at high velocity. The photo diode light sources in the velocity sensor array were replaced to eliminate the 1600 Hz ripple from their signal, and incandescent grain-of-wheat bulbs with lenses were used instead. New lightweight tri-bearings were employed, and the drag force on these bearings was determined with unpowered sliding tests.

3.4 Test Series #7 (23-26 Jun 97)

The final design of the flight-worthy 50-60 g Lightcraft engine/vehicle was now complete, and the limited production of this model was underway. Hence, the focus of this and future tests at HELSTF was to be on the development and evaluation of PLVTS tracking and beam control concepts – ones that can take Lightcraft flights from the laboratory to the outdoor propagation range.

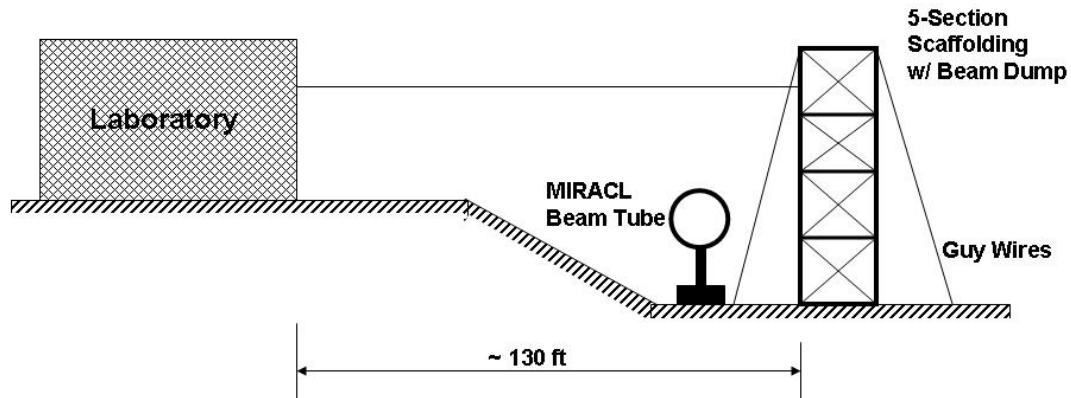


Fig. 42. Horizontal Wire-Guided Flight Set-Up

A wire-guided flight experiment was set. A ~144 ft piece of 0.051-in., 23 gage wire was firmly anchored in the lab to a standoff assembly on the optics table (see Fig. 43a) and run out the window (see Fig. 43b) to a scaffolding tower as illustrated in Figure 42. In the lab, the wire was connected by wrapping to avoid cutting when placing vehicles on the wire.



(a)



(b)

Fig. 43. Details of Wire-Guided Flight Set-Up Showing the Anchored Wire Attaching to the Standoff on the Optical Bench (a) and Looking Back From the Tower to the Open Window (b)

The wire was firmly anchored to the scaffolding tower through the center of a 4 x 8 foot piece of black-painted plywood which was placed on the tower as a beam dump, as shown in Figure 44. Thus when testing, the laser beam was directed out the window and into the desert test range.

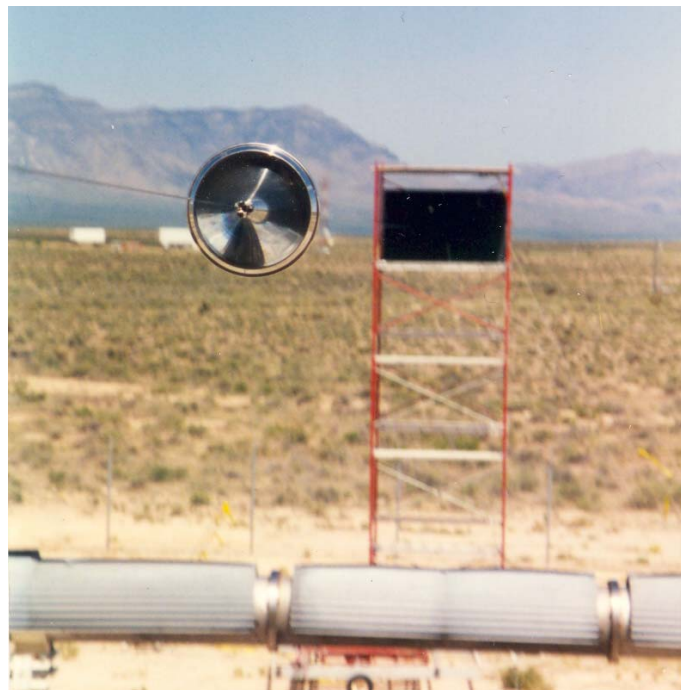


Fig. 44. View Looking Out the Window to the Tower with Lightcraft Mounted on Wire

The laser was aligned, and a tracking system was set up. It was decided that sunlight tracking was the best option, so the Lightcraft wire-guided flights were to be started outside. The first dynamic test was a propulsion demonstration down a 122-meter horizontal wire guided path (see Fig. 44). The design and implementation of an optical tracking and beam control system was required to maintain beam alignment during this wire guided study as well as for beam control during follow-on vertical free flight tests.⁽²⁵⁾

In order to minimize cost on the control system, several components were identified which were available to the program and which would satisfy the necessary beam control requirements. These components included a Ford Aerospace beam steering mirror, a DBA optical tracker and a Panasonic visible gated camera system. The Ford Aerospace mirror was originally used with the Field Test Telescope to provide active control of a high power continuous wave carbon dioxide laser during the initial shoot-down of a target drone in the late 1970s. The mirror utilized a speaker coil actuated light weighted (uncooled) elliptical molybdenum mirror and a Kaman proximity sensor for mirror position feedback. As such, it was well suited for use with the PLVTS laser device. The control system, being of the 1970s vintage, was not utilized during this effort. Instead, an Innovative Integration SBC31 Digital Signal Processor (DSP) based on a Texas Instruments TMS320C31 DSP/laptop computer was programmed to accept centroid offsets from the DBA optical tracker and to generate analog drive signals which would be sent to the Power Amplifier Electronics (PAE) voltage to current driver amplifier. The SBC31 DSP was programmed to provide steering mirror spring cancellation, servo control loop compensation, and gain for the various cage (position) and track modes. A gyroscopic track mode was also incorporated to evaluate the ability to counteract the Lightcraft angular momentum during illumination. Prior to programming the SBC31 DSP, the steering mirror and control loops were modeled using the Matlab/Simulink software. Figure 45 provides the optical scheme used during the pointing and tracking test series.

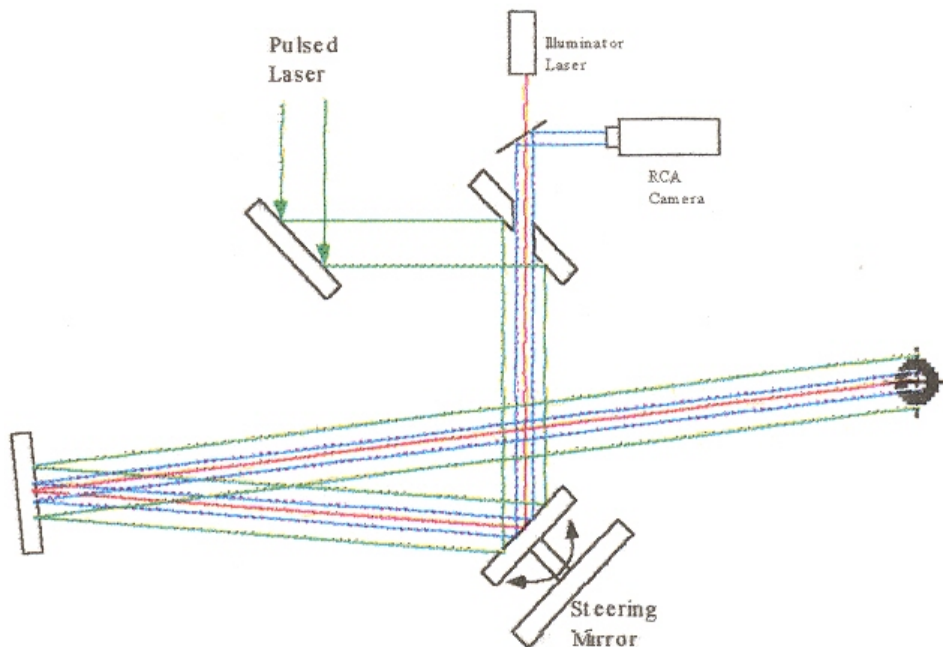


Fig. 45. Optical Configuration of the Pointing and Tracking System

A block diagram of the azimuth and elevation closed loop tracking algorithm was developed and can be seen in the referenced document.⁽²⁵⁾ Several illumination and optical imaging schemes were evaluated during the pointing and tracking effort. The evaluated techniques included a passive "floodlight" illumination using a gated visible tracking camera, active illumination using a 50 mW He/Ne laser (boresighted with the gated tracking camera) and a plasma tracking technique. Also evaluated were the Lightcraft dynamics and the requirement to provide angle control (beam steering mirror) versus translation control (stepper motor mirror) of the laser beam. The plasma-tracking concept was inherently unstable due to self-tracking of the laser beam. The low power laser illuminated tracking technique, although promising, required the installation of a corner cube which was vulnerable to the PLVTS laser pulse. The passive "flood light" illumination worked quite well and was subsequently used for the follow-on wire guided and laboratory free flight experiments. In this technique, the camera's electronic shutter was gated and synchronized to the pulsed laser such that the camera would not image the plasma flash. The tracking system employs several operating modes including cage, track, auto track, and spring cancellation during an acquisition and track routine. As we move further from the launch pad, the visible camera may be replaced by an infrared camera to take advantage of the thermally dark sky background during vertical free flight testing.

We compared the effect of different gas loading mixtures by measuring the delivered power at the window and beam dump. The 8/1/1 mixture of He/N₂/CO₂ propagates best and was compared to the 3/2/1 mixture that had been used to the present. Supposedly the 8/1/1 mixture will deliver less power, but it propagates better down range. This turned out to be a trivial fact. We found that the power was only reduced by 10% at the tower compared to the power at the window, and that the beam pattern at the tower was somewhere between the near field hollow square and the far field Maltese cross. The beam burn pattern at the tower is shown in Figure 46.



Fig. 46. Tower Burn Pattern Illustrating Transition From Near to Far Field Structure

Nine tests were conducted on the horizontal wire with the 3/2/1 mixture with total pulses varying from a maximum of 92 pulses to a minimum of ~20 pulses. At 92 pulses, the vehicle was extremely hot, and there was concern for the structural integrity of the shroud.

The 8/1/1 laser gas mixture seemed to deliver too low a power to be useful. Models moved too slowly and only advanced ~20 ft in 50 pulses. A higher gas pressure was tried, but didn't seem to help much. A total of three tests were conducted with the 8/1/1 gas mixture ratio before returning to the 3/2/1 laser gas mixture ratio still at an elevated pressure.

There was instant success. The very first test saw the Lightcraft cover the entire 130 ft length of wire in ~92 pulses.

The second test went only halfway down the wire, but a tail wind came up and blew it all the way to the blackboard. The laser had fired intermittently and the blackboard was seared in the lower left hand quadrant of the centerline. The maximum number of pulses was somewhere between 100 and 110.

The last guided wire flight test failed when the rear bearing separated from the model at about 20 ft into the flight, causing severe friction and bringing the model to an abrupt stop. During all these wire flights we were super cooling the models with carbon dioxide ice sprayed on each model until it was slightly frosted on the shroud. It was not a good idea to put frost on the optics.

At this point the focus switched to the vertical free flight set-up in the laboratory. The experimental set-up is illustrated in Figure 47.

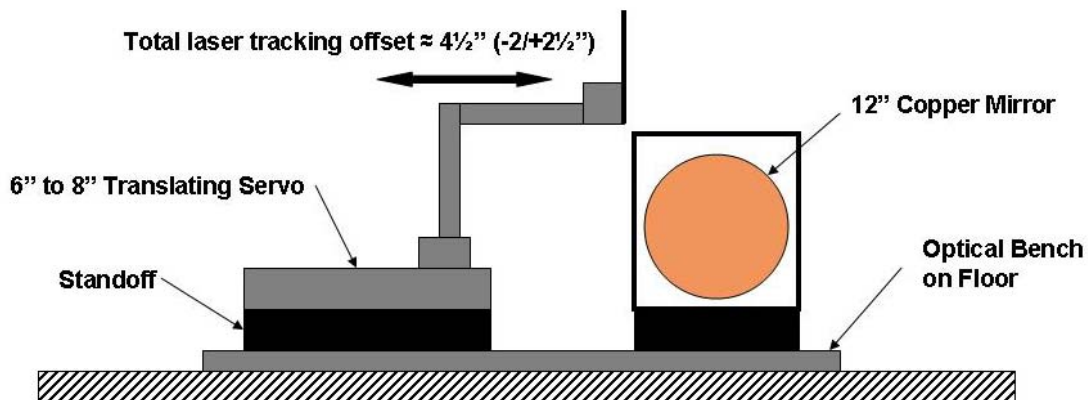


Fig. 47. Vertical Free Flight Launch Set-Up in Laboratory

A large sheet of plastic and fish netting was strung to catch the vehicles as they fell from the air. Thin wires were woven above the 12-in. turning mirror to protect it. A large trout net on a long pole was also available to catch the vehicle before it could hit the ground or some optical component. The first model tested was a new 53 g truncated cone model with smaller spin bearings (see Fig. 48). As a back-up, there was a 0.012-in. aluminum shroud that could be used to replace the 0.005-in. shroud should it become damaged. This would avoid delaying progress with too much time lost making repairs. The initial test tried to propel a rapidly spinning, slow spinning, and non-spinning model, but there was no lift-off. To help the situation, the wires protecting the 12-in. turning mirror were removed. The initial attempted flights had used a laser power of between 529 J and 538 J. A 66 g version of model A (see Fig. 38) also failed to lift off the launch rod. The power was raised to 770 J, and the final flight attempt was a success. The vehicle went all the way, and the laser set the rubber bumper at the blackboard on fire. Unfortunately, there was no video confirmation of this flight.

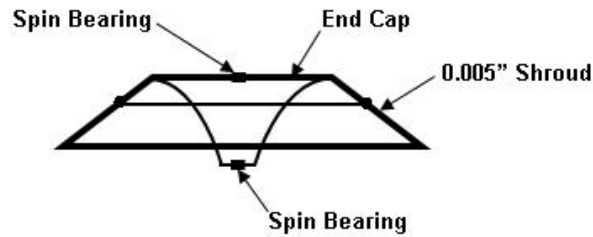


Fig. 48. New Truncated Cone Model with Smaller Bearings

3.5 Test Series #8 (25-28 Aug 97)

Thrust stand testing was initiated on five new spinning and non-spinning, flightweight Lightcraft with flat plate forebodies. All but the 300% were spin balanced. The tests were designed to obtain the coupling coefficient for all five of the new models in order to decide the best configuration for larger models (30 to 60 cm focal diameter).

Calibration of the thrust stand was accomplished by dropping known masses from a set height. The clay masses were: 298 g, 667 g, 1249.5 g, 2276 g, 4509.3 g, and 5758.8 g (4509.3 + 1249.5 g). The resulting calibration value of 0.598 mV/g was very close (within 2.5%) to the April value obtained. For these tests, a washer was placed between the smaller active load cell face and the end plate as a spacer so that the end plate could be tightened, and a locking nut was necessary on the brass screw because the threads were now nearly stripped on the strut end plate (see Fig. 49).

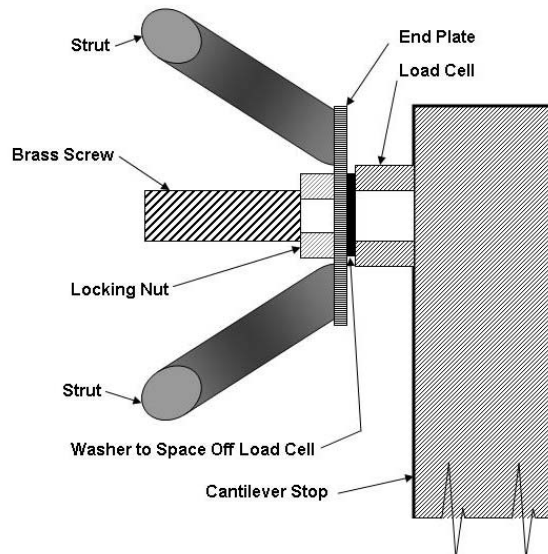


Fig. 49. Details of Thrust Stand Load Cell Assembly

Thrust stand tests were conducted at 3 Hz with 20 to 60 pulses. Alignment of the laser for thrust stand testing was accomplished with a He/Ne laser on the old Model "A" (see Fig. 38) engine and by centering the He/Ne laser on the end of the brass rod prior to

mounting the Lightcraft test articles. Testing began with an ultra-light spinable version of model A with 30 pulses at 3 Hz.

These tests were recorded with one flat-lighting high intensity lamp at 1,000 frames/s with 400 ASA VXD Kodak film, and 5 different "f" stops for a period of 1 s on each test. The camera takes 2 s to get up to speed, and then a substantial period of time to wind down - a total of 36 s. The rear bearings were broken on the 200%, 250%, and 300% ULS models because they contacted the surface of the washer. Thus, a larger washer had to be placed between the rear bearings and the load cell to avoid loading the bearings altogether with a limited number of 6 pulses. The results indicated that the C_m of all 5 models was about the same (~ 125 N/MW at 644 J/pulse), and that the C_m value increased as the energy per pulse (E_p) increased. Table 4 gives the mass properties and calculated vertical acceleration of each of the models based upon the thrust stand measurements.

Table 4. Mass Properties and Calculated Vertical Acceleration of ULS Models

Model -ULS (Ultra-light Spinning)	Cone ⁽¹⁾ (g)	Shroud ⁽¹⁾ (g)	Total ⁽²⁾ (g)	Vert. Accel. @ 533 J (g's)	Vert. Accel. @ 640 J (g's)	Vert. Accel. @ 770 J (g's)	Vert. Accel. @ 824 J (g's)
100% (A)			52.85	1.294	1.554	1.870	2.000
150%	16.5	30.0	52.5				
200%	14.5	35.0	54.0	1.258	1.511	1.818	1.944
250%	12.5	41.5	57.0				
300%	15.5	41.0	61.0	1.114	1.338	1.61	1.722
Horizontal UL			66.0	1.029	1.236	1.487	1.591

⁽¹⁾ Without Bearings and Screws

⁽²⁾ With Bearings and Screws

Vertical free flight tests in the laboratory were conducted using the set-up illustrated in Figure 50. All of these tests were conducted without active tracking (i.e., the beam was fixed for each test). The previous free flight tests in the laboratory had been conducted with active tracking, and the vehicles had not stayed in the beam (e.g., the tracking system had not been able to control the vehicles).

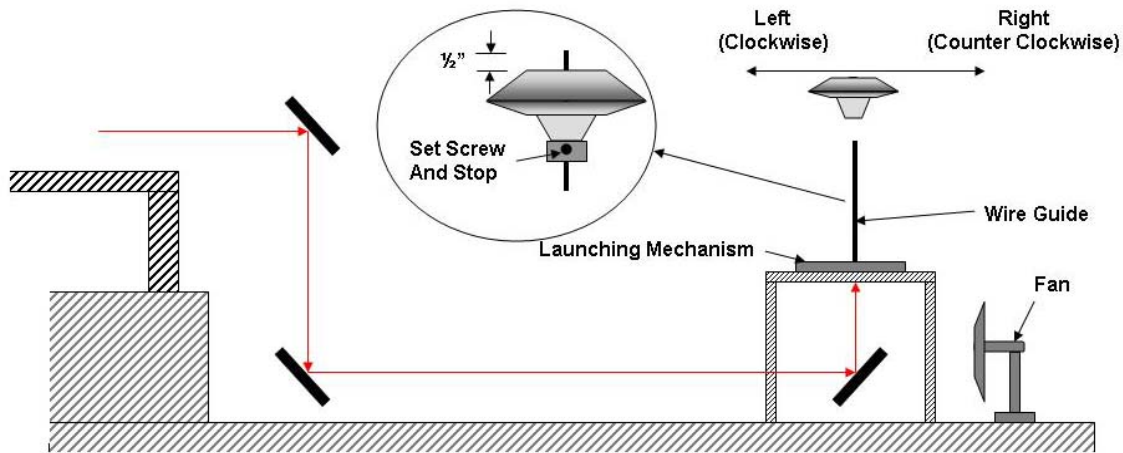


Fig. 50. Experimental Set-Up for Vertical Free Flight Laboratory Tests

There were five mirrors in the optical train which substantially reduced the power available at the launch point. The launcher device was the same as used previously with the 6-in. to 8-in. translating servo that moved the launch rod out of the beam after launch. The fan was an attempt to blow any exhaust gases or particles away from the turning mirror's surface. It was always felt to be important to protect the surface of the turning mirror.

The laser energy at the launch point was measured with the large "ball" calorimeter (71 kJ/ohm), known as the 8-ball, which was approximately 2 ft in diameter. The 8-ball calorimeter is shown mounted at the vertical free flight location in Figure 51a.



(a)



(b)

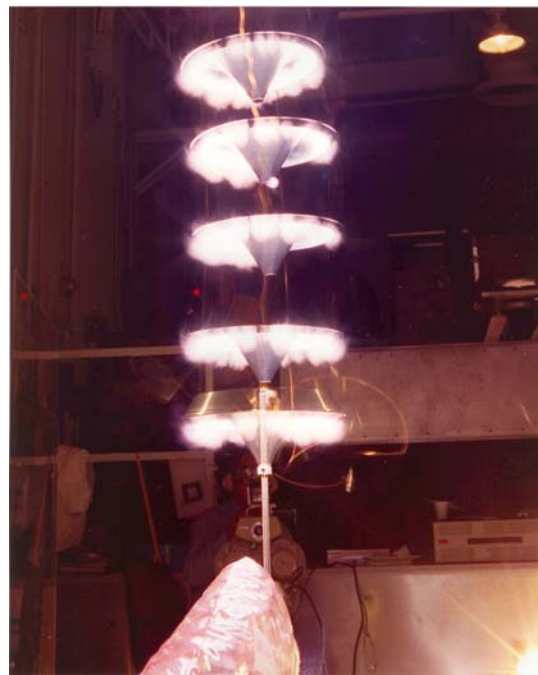
Fig. 51. Calorimeter Measurement (a) and a Laboratory View (b) Showing a Lightcraft Mounted on the Launch Rod and Beam Dump Attached to Ceiling

This figure shows the 8-ball mounted over the final turning mirror before the servo-launcher was placed on the table at the left. The power measurement was accomplished in 25 s. Figure 51b shows the servo-launcher mounted on the table, and gives a broader view of the laboratory. In this figure, the 4 x 8 ft plywood, black painted, beam stop can also be seen attached to the ceiling. The distance from the launch platform to the beam stop was about 17 ft.

Figures 52 and 53 show pictures taken of the vertical free flight tests. A number of problems occurred during these tests. First, the models had trouble lifting off the launch rod. Initially, the vehicles were placed at a position all the way down on the rod. Later, to try to alleviate the "hang-up" problem, a stop with a set screw was placed on the rod such that the rod only protruded 1/2 in. above the top of the vehicle, as illustrated in Figure 50. It was hoped that this arrangement would allow the vehicle to hop off the launch rod on the first laser pulse.



(a)



(b)

Fig. 52. Vertical Free Flight Test Pictures with Prof. Myrabo (a), and the First 5 Pulses of a Flight Shown in a Still Picture (b)

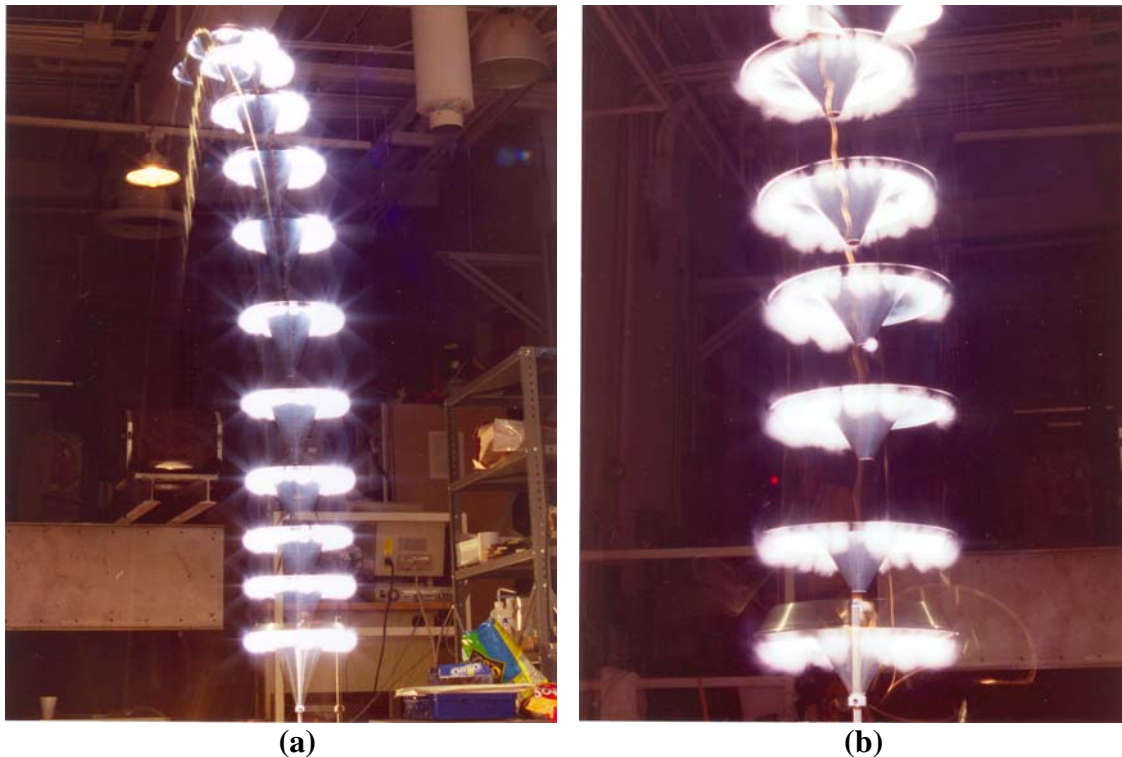


Fig. 53. Still Camera Pictures of Vertical Free Flight Laboratory Tests

The vertical free flight tests were started by spinning the vehicles clockwise, and they characteristically drifted out of the beam to the left. When spun counterclockwise, they drifted off the beam to the right (see Fig. 50).

During these flight tests, the bearing kept falling out of the vehicles, especially number #300. To try to retain them better, super glue was applied. This helped slightly.

3.6 Test Series #9 (29 Sep - 2 Oct 97)

Tests conducted during the last week in September and into October 1997 included additional vertical free-flight tests with 14-cm to 15-cm models weighing less than 50 g. These models were chemically milled to reduce their weight. They were able to reach the maximum available altitude inside the laboratory, which was about 5 m.⁽¹⁹⁾ These flights were very spectacular. Again, the models were spin stabilized, but the laser beam was fixed for these flights (i.e., there was no active tracking). In a typical flight, the Lightcraft accelerated quickly to an altitude where it seemed to move slightly out of the beam. Sometimes, it re-centered itself, but most of the time it drifted out of the beam and fell back down, where it was captured in a long handled fishing net. By catching the Lightcraft, damage was avoided to the model, which would occur if it hit the cement floor, or to the all-important beam turning mirror located beneath the launch stand.⁽¹⁹⁾

Chemical milling is used extensively by the aircraft industry to provide tremendous weight savings in wrought, cast, or forged materials. By this point in time, weight of the vehicles had become a critical parameter for flight vehicles. Caspian, Inc. (formerly Chemical Energy of California) in San Diego CA, was contacted and asked to chemically mill 10 representative CNC-lathed, 6061 T6 aluminum parts from 0.015-in. to 0.007-in.

wall thickness. Appropriate un-masked areas were to be indicated with a felt pen for milling. The chemically milled parts were to be delivered to the laboratory at Edwards AFB by 26 Sep 97, for testing at WSMR the following week. Caspian accepted the task, but noted that 99% of aerospace and missile components parts that are chemically milled

Table 5. Results of Chemically Milling Lightcraft Parts

Part No.	Comments
100a1 - Nose 100a2 - Nose	Chem mill to 0.005-in. wall thickness Current mass = 18.35 g New mass = <u>8.35 g</u> Removed 10.00 g * Do not etch center hole inner surface.
100b - Optic	Current mass = 21.09 g New mass = <u>16.50 g</u> Remover 4.50 g * Part thickness should fall by 0.003 in. to about 0.010 in. or 0.012 in. * Do not etch center hole inner surface
150b - Optic	Current mass = 16.5 g New mass = <u>14.0 g</u> Removed 2.5 g * Do not etch center hole inner surface
200b - Optic	Current mass = 14.5 g New mass = <u>12.5 g</u> Removed 2.0 g * Do not etch center hole inner surface
300b	Current mass = 15.54 g New mass = <u>12.00 g</u> Removed 3.54 g * Do not etch center hole inner surface
200a - Shroud	Current mass = 35.0 g New mass = <u>27.0 g</u> Removed 7.0 g * Acid etch <u>top surface</u> starting from 0.015 in. down to 0.006 in. * Acid etch <u>side surface</u> (conical) from 0.015 in. to 0.010 in. (only remove ~0.005 in.) * Do not etch center hole inner surface
150a - Shroud	Current mass = 30.0 g New mass = <u>25.0 g</u> Removed 5.0 g * Center disc must not fall below 0.006 in. thickness * Do not remove material from inside bearing surface of center hole.
250a - Shroud	Current mass = 41.5 g New mass = <u>30.0 g</u> Removed 11.5 g * Acid etch <u>top surface</u> from 0.015 in. to 0.005 in. thickness * Acid etch <u>side surface</u> (conical) from 0.015-in. to 0.010-in. thickness. * Do not etch inside of center hole bearing surface
300a - Shroud	Current mass = 41.3 g New mass = <u>30.5 g</u> Removed 10.8 g * Acid etch <u>top surface</u> from 0.015-in. to 0.005-in. thickness * Acid etch <u>side surface</u> (conical) from 0.015-in. to 0.010-in. thickness. * Do not etch inside of center hole bearing surface

are thicker than 0.025 in., and that it would take a small project to develop the technology required to make the parts at 0.007 in. \pm 0.001 thickness. The cost of the start-up project for the ten representative parts was \$5,000. The Table 5 indicates the initial and final conditions of the ten parts that were chemically milled by Caspian.

On site at HELSTF/WSMR, Test Cell 3, the model parts were laid out on a table prior to assembly. The optics, shrouds, and a titanium shroud are shown as a composite of two photographs in Figure 54 for the flat top models. The #100 series is the tallest, and the shortest is the #300 series. The Top Flight Precision Magnetic Balance was used to statically balance all the vehicles before flight so that they could be spun up to very high rpm's prior to launch. Thus, all the models were spin-stabilized during flight.



**Fig. 54. Composite Picture Showing Parabolas #100 to #300
with Titanium Shroud on Far Left**

A flat top vehicle is shown in Figure 55 mounted on the launch rod. To launch, this vehicle would be spun up to $> 3,000$ rpm with a high pressure nitrogen gas jet issuing from a hose connected to a 2,000 psi nitrogen bottle. Several seconds before the laser's first pulse, the person blowing the gN_2 on the vehicle would set the hose down and retreat to a safe location away from the launch.

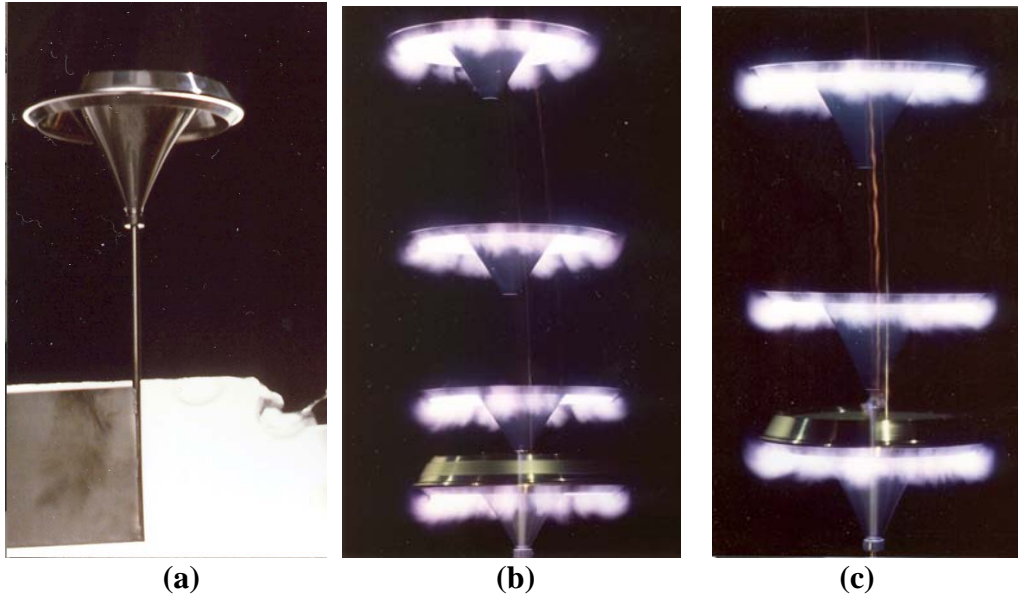


Fig. 55. Flat Top Flight Vehicle on Launch Rod (a), and Two Separate Flights of Flat Top Vehicles Shortly After Lift-Off (b), and (c)

The #100 series to #300 series models are shown as individual photographs in Figure 56. Models #150 to #300 are shown with time integrated plasma pictures. Note the subtle differences in the plasma structure as a function of the model number. The model #200 was eventually picked as the vehicle to pursue in the future.

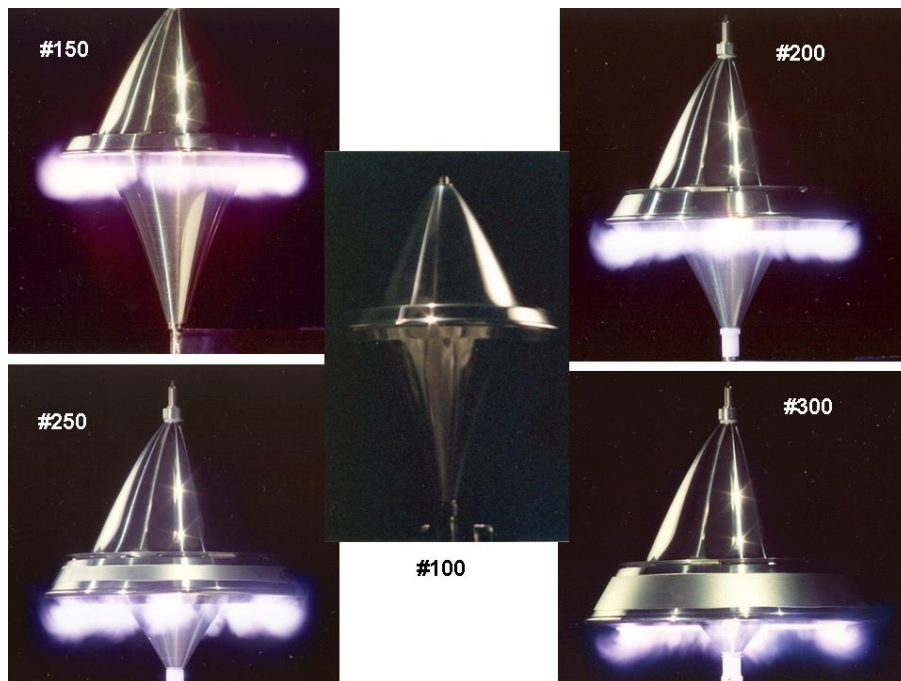


Fig. 56. Series of Pictures Showing Vehicles #100 to #300, and Illustrating Plasma Formation in Vehicles #150 to #300

The mass inventory of the flight test articles is tabulated below in Table 6, along with the results of the flat top flight tests.

Table 6. Mass Inventory of Vertical Free Flight Vehicles (grams)

	Nose	Optic	Shroud	Assembly	Comments
#100b	13.2 ^c	16.29 ^c	13.87	43.33	New
#100a	Flat	22.00	26.00 ^b	51.71	Flew good ~5'
#150	Flat	12.72 ^c	27.17 ^c	39.89	Flew many high flights, pegged ceiling
#200	Flat	10.25 ^c	32.17 ^c	42.42	Damaged optic - warped first flight
#250	Flat	12.75	35.33 ^c	48.08	
#300	Flat	12.49 ^c	37.40 ^c	49.89	

b = included bearing weight

c = chemical milled

Two different flight test photos are shown in Figure 57. These are classic photos that have been shown in print and video countless times. Note the beam dump connected to the ceiling at 17 ft from the launch platform. Mr. Mike Thurston is shown in both these pictures as the net man. These vehicles came down tail first or optic first, and if allowed to hit the cement floor would damage the tip of the parabola. They were still spinning at high speed when they came down, so a combination of spin and falling velocity would not only damage the parabola but could launch the vehicle in random directions from the point of contact.

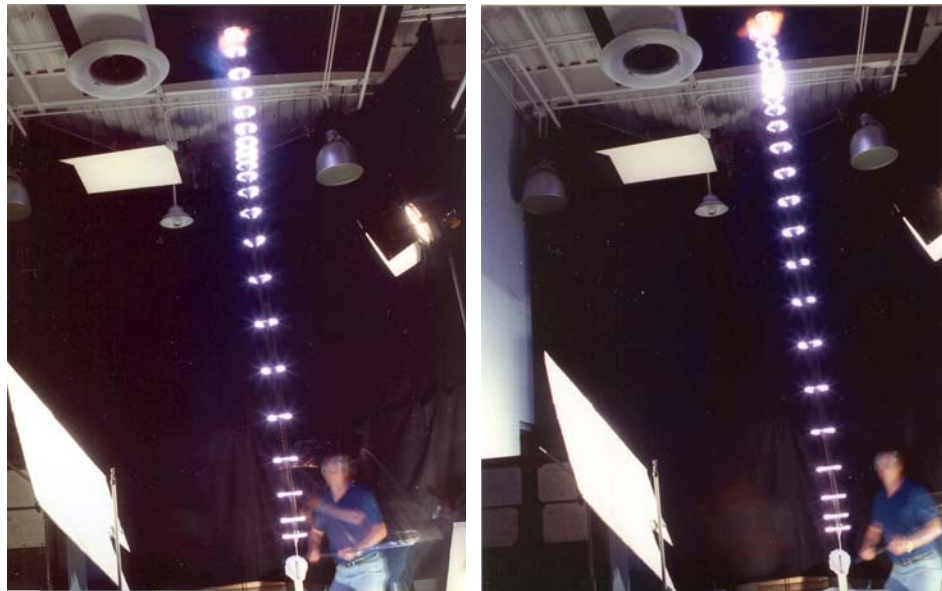


Fig. 57. Two Outstanding Flights That Reached the Ceiling

Horizontal guided-wire tests outside over a length of 400 ft were again used to demonstrate the laser pointing and tracking system to even greater distances. Both night and day flights along the wire showed that the tracking system would follow the Lightcraft to this ultimate distance successfully.

The scaffolding tower was moved outside the fence to a new position that was 400 ft from the window. This is shown photographically in Figure 58. Here the heavier model "a" is shown mounted on the wire which stretched from inside the laboratory on the optical table to the tower. The height of the tower and the beam stop was such that the wire was very close to horizontal.



Fig. 58. Lightcraft Mounted on 400 ft Horizontal Wire Tied to Beam Stop

These tests required an active tracking system that was set up in the lab. The wire sagged in the middle, and as the vehicle moved along the wire it bounced up and down. So, these flights were a good test of our ability to track the vehicle over the complete 400 ft distance. Tests conducted at night (see Fig. 59a) required that the vehicle be illuminated by high power spot lights and automotive lights from our cars, trucks, or vans. Occasionally, a flying insect would cross into these lights as the laser was firing and divert the tracking system from the vehicle, thus ending a test. The tracking system was unable to re-acquire the target once it lost it.

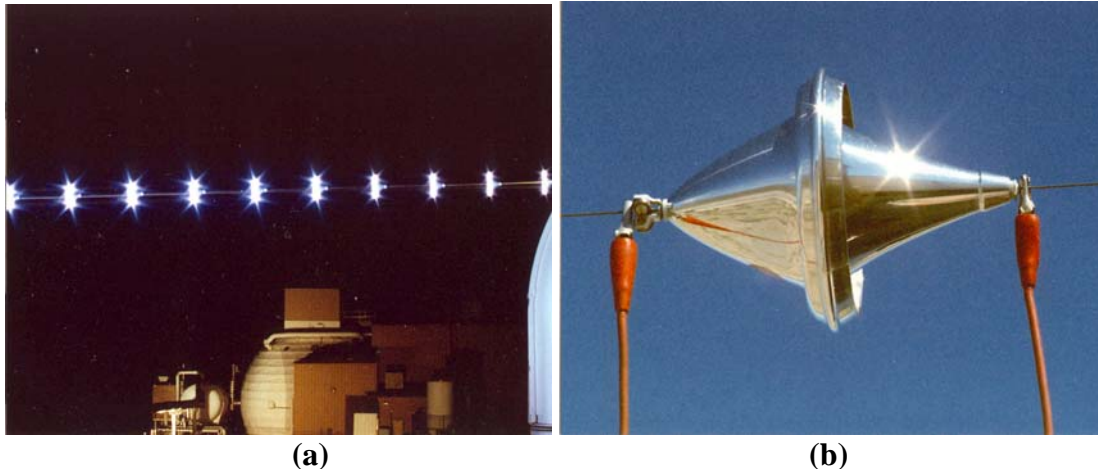


Fig. 59. Night Time Wire-Guided Test (a), and Details of Clipping Mechanism to Hold Lightcraft in Position Against Winds (b)

Since the wire sloped towards the center of length from each end, the slightest breeze or breath of moving air would cause the vehicle on the wire to move forward. A wind blowing from the other direction could also easily push the vehicle backwards. Thus, clips were placed on the wire, both front and back, to maintain the vehicle in starting position until ready for laser firing and subsequent test. This holding method is illustrated in Figure 59b.

A now-famous group photograph was taken during this test period. This photograph printed in Fig. 60 was used for numerous videos seen on television and presented at several professional meetings.



Fig. 60. Group photo: From L to R, Drs. Franklin Mead and Leik Myrabo (Front), and Steve Squires, Mike Thurston, Chris Beairsto, and Dr. Don Messitt (Back)

It is a credit to the group that the picture turned out so well because it was taken at about 1 am after about 17 hours of work. The PLVTS crew consisted of Mr. Steve Squires, Mr. Chris Beairsto, and Mr. Mike Thurston. The Lightcraft crew consisted of Dr. Franklin Mead, Dr. Leik Myrabo, and at that time a graduate student Mr. Don Messitt (now Dr. Messitt).

Acoustic measurements of Lightcraft horizontal guided wire tests (**Appendix B**) were made by Dr. Messitt. Preliminary acoustic data was acquired as a secondary objective during laser propulsion flight tests in October, 1997. In these experiments, the vehicle was flown horizontally and guided by a thin wire. Two inexpensive microphones were located downrange of the launch point, and were connected to a digital audio tape recorder. The signals were recorded and analyzed to determine if a more costly, dedicated experiment was warranted.

The noise from a Lightcraft liftoff was simulated. Sound pressure levels in excess of 140 dB were predicted for an observer 20 m away from a 5,555 kg vehicle. The model used to generate these noise predictions could not be validated using the October tests due to the use of relatively low quality equipment, which was not calibrated to record sound pressure level.

Acoustic data from microphone recordings was analyzed to determine the trajectory of the Lightcraft. The trajectory was successfully extracted with a method using the time delay between two microphones, and with a Doppler-based technique. Trajectory data may be obtained for future Lightcraft tests by a combination of the two techniques. The microphones should be positioned near to the launch point to take advantage of the sensitivity of the two-microphone method, with the Doppler analysis used for longer ranges. The effect of echoes may cause substantial interference, and must be evaluated at pulse repetition frequencies higher than 10 Hz.

Laser mirror coupon tests were accomplished for Energy Science Laboratories, Inc. (ESLI). A pulsed laser damage threshold examination of the Laser Mirror Test Panel provided by ESLI was conducted on 28 Oct 97 by the Directorate for Applied Technology, Test and Simulation (DATTS) at the HELSTF, WSMR NM. The purpose of the testing was to examine the material performance of the coupons when exposed to 10.6 μ pulsed laser radiation. The material has application potential in the construction of the U.S. Air Force Research Laboratory Advanced Concepts Branch Lightcraft vehicle. The test series was conducted using both a sub-aperture near field “flattop” profile and a far field near Gaussian beam profile. The far field beam provides the uniform profile necessary for the quantitative damage threshold measurements. The near field laser beam provides the complex mode structures present in the beam during the actual Lightcraft propulsion experiments.

The results of the tests showed that the coupon with the best visual appearance (which had been labeled Coupon #3) provided a significantly higher damage threshold than the other samples in both the near field and far field tests. The bare substrate damage threshold significantly surpassed that of all the coupons. The results of the test series were tabulated in the report.

3.7 Test Series #10 (3-5 Nov 97)

For the first time, outdoor, free flight tests were conducted. A very large, single piece of canvas was raised 50 ft into the air using an onsite crane, as shown in Figure 61. At the top of the crane's extended arm was a platform bucket, and attached to this bucket was a 4 ft x 8 ft piece of black painted plywood like the one used in the laboratory as a beam dump. The "tarp" was wrapped around this plywood and allowed to hang down, forming a 3-sided channel through which the vehicles could fly. This set-up was required for safety reasons because it was thought that "glints" of laser light off the vehicles might cause eye damage to people working in the general area of the flight tests. The open side of the tarp channel, as shown, faces towards the open laser range where laser light does not represent a challenge. The beam dump is required to avoid sending laser light into space where it might accidentally contact a satellite flying over the test area. The tarp also provided protection from the wind, but any significant wind would severely disturb the hanging configuration and send ripples through it.



Fig. 61. Picture of Experimental Set-Up for Outdoor, Free Flight Tests

The same basic launch technique and mechanical system that was described for the indoor flight tests was now moved outside and set up at the base of the tarp channel (see Fig. 62) such that the Lightcraft would rise straight up and fly inside the channel. However, for this set of flight tests the launch pin was not retracted after the vehicles

cleared the end. The vehicles were spun to very high rpm prior to flight for gyroscopic stabilization. The nose of the model was 3 ft off the ground.

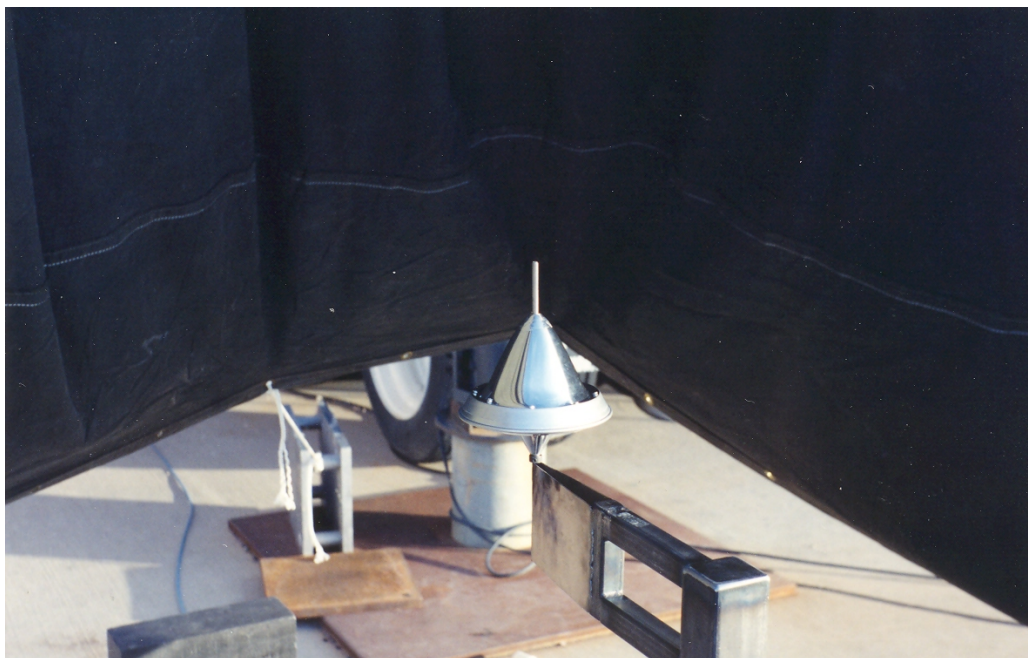


Fig. 62. Lightcraft Mounted on Launch Rod Prior to Flight

The models used for flight tests included those listed below. The masses were measured on a digital scale in the WSMR chemistry lab.

1. Flat top model #100
2. Model #150 with chem-milled nose and shroud (47.785 g)
3. Model #200 with chem-milled nose and shroud (48.601 g)
4. Model #250 with chem-milled nose and shroud (54.206 g)
5. Model #300 with chem-milled nose and shroud (52.809 g)
6. Model #150- $\frac{3}{4}$ scale (new tiny model)
7. Model #150- $\frac{2}{3}$ scale (new tiny model)

During these flight tests the weather was good and the winds, if any, were very light for the first two days. On day 3, winds were strong with large gusts. Initially, we tried flight testing after dark, but the net catchers were blinded by the plasma pulses. We had trouble with the shrouds getting extremely hot, and in some cases actually melting. The results in terms of altitude of our first outdoor flight tests are indicated in Table 7. The model #200 was the best, and models #150 and #300 were about the same.

Table 7. Results of First Outdoor Free-flight Tests

Model	Day 1 Altitude	Day 2 Altitude
#150	17 ft & 12 ft	20 ft
#200	36 to 37 ft	36 ft
#250	25 ft	25 ft
#300	Not tested	18 to 20 ft

Many Lightcraft ejected their rear bearings (0.814 g) upon the launch rod, so the flight weight was actually less than that specified above.

The small #150-1/2 and 2/3 models did not fly well, and were limited to altitudes under 12 ft. They were so small and lightweight that the GN₂ jet from the nozzle used for spin-up could easily levitate these models prior to launch.

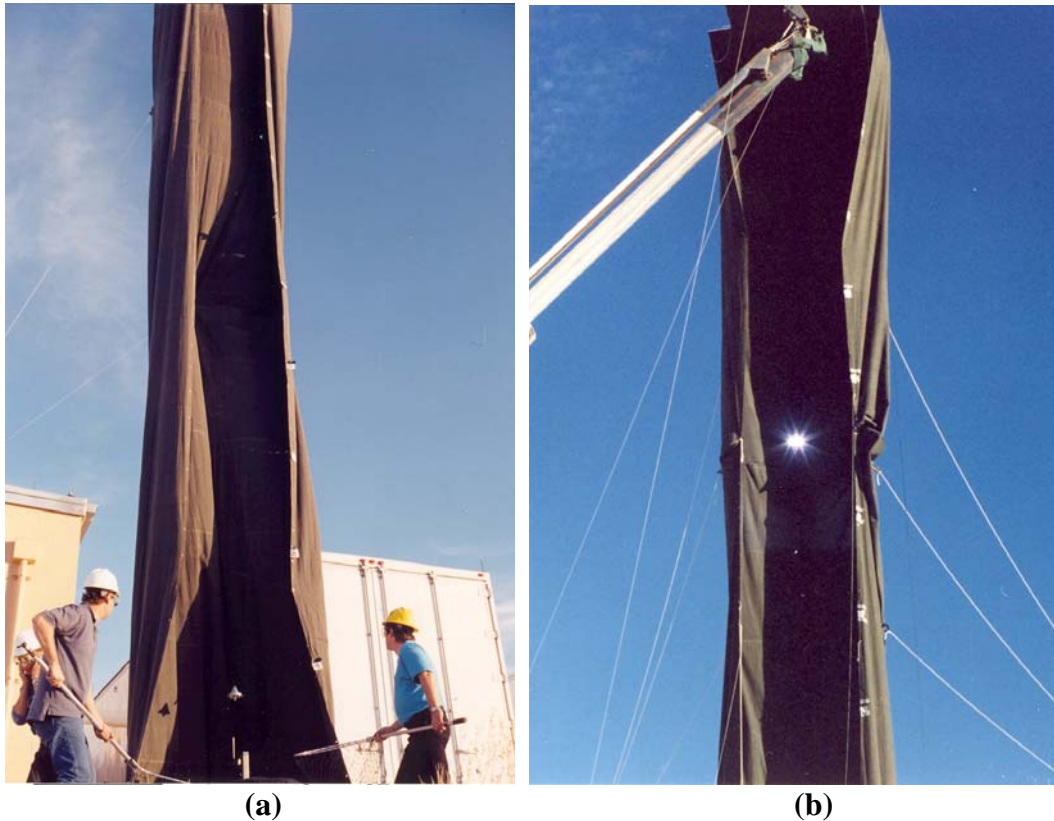


Fig. 63. Lightcraft Flights Inside 50-ft Canvas Channel

Shown in Figure 63 is the launch of a Lightcraft vehicle within the tarp channel. Figure 63a shows the Lightcraft vehicle shortly after launch and between pulses which were at 10 Hz, and Figure 63b shows the flight as it nears the top of the channel at a point in time when the plasma is very bright. The people seen with the nets in Figure 63a are Chris Beairsto on the left and Mike Thurston on the right. Prof. Myrabo can barely be seen in the background behind Chris.

3.8 Test Series #11 (2-5 Dec 97)

The performance of the PLVTS laser is shown in Figure 64. This information was taken from the PLVTS record book. It illustrates the fact that power increases as the pulse repetition frequency (PRF) increases. The value in Joules may be determined for each point by dividing by the PRF. It will be seen that the Joules per pulse drop as the frequency increases.

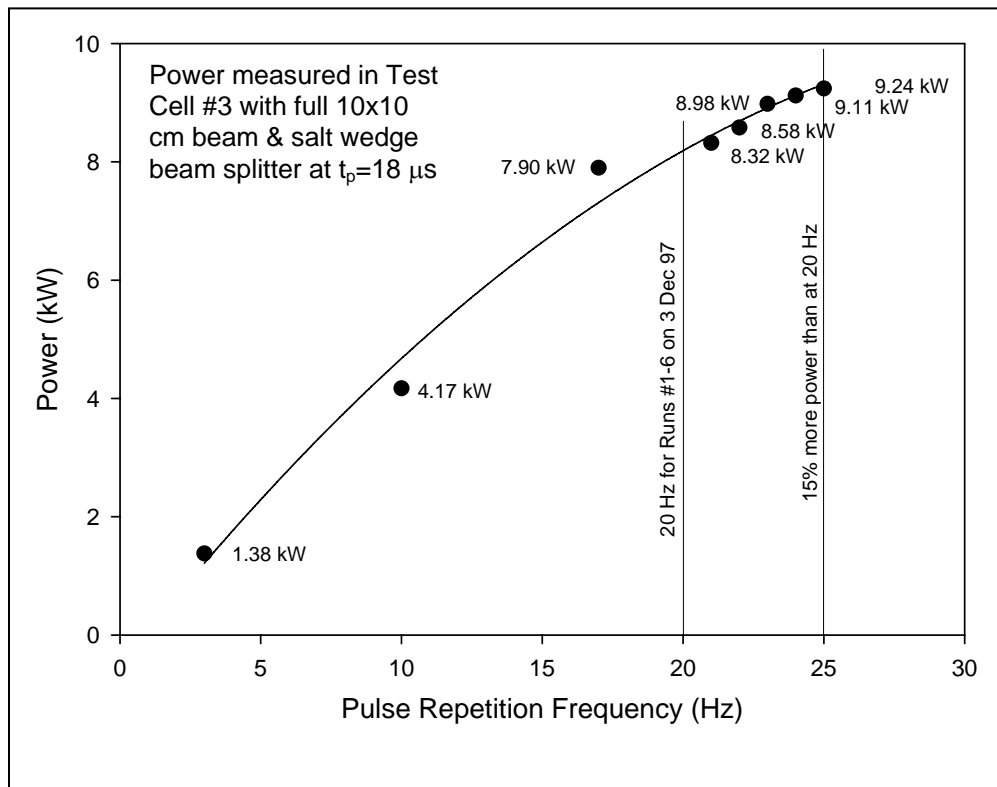


Fig. 64. PLVTS Performance Measurement

We discussed using the Hughes 50 cm FTT (Field Test Telescope) which had 11 mirrors in the optical train. The 10x10 cm beam must be clipped to 11.62 cm diameter to fit thru the FTT, resulting in a power loss of 8 to 10%. It was questionable whether or not we could ever get Lightcraft models light enough to fly on the FTT. An alternate approach was to use a reducing telescope to produce the 6.67x6.67 cm beam (9.427 cm diagonal), which adds only two mirrors to the optical path. Burn patterns for the new reducing telescope arrangement of 8'10½" and 9'2" spacing were made at distances of 0, 30, 60, 75, and 90 ft. Burn patterns for the 400 ft range, and power versus aperture measurements were conducted for the 8'10½" spacing with the results indicated in Table 8. All data was taken at a PRF of 2 Hz and a pulse width (τ_p) of 18 μ s. For these tests, the power out of the laser (E_p) was 460 J.

Table 8. Power vs. Aperture Measurements for the 8'10½" Mirror Separation

Aperture (in)	Captured Energy (J)	Comments
8 (20.32 cm)	217 to 219	Full effective aperture of calorimeter
6 (15.24 cm)	181	125% or 5/4
4.8 (12.2 cm)	133 to 139	Standard optic diameter
4.323 (10.98 cm)	111 to 114	9/10 scale
4.0 (10.16 cm)	114 to 121	5/6 scale
1.5 (3.81 cm)	28 to 36	Center spot of burn pattern

After their first free vertical flights, the rear bearings were removed from models #200-9/10 and #150-¾ giving new masses of 41.419 g and 24.637 g, respectively. However, these two models shook badly when spun up to high rpm. It was thought at this point that the bearings could be eliminated altogether with no penalty. All that was needed was to grease the launch rod slightly. The loss of bearings was greatly slowing down the launch rate.

We arrived early to catch an hour of testing before the HELSTF opened and we were not required to have the tarp in place during this period. The model #150-¾ seemed to fly well with the lightest nose, and the model #200-9/10 easily flew up to the 65'3-in. plywood.

White tag markers were initially placed on the tarp at 4 ft intervals. These were later changed to 10 ft intervals, and some of these markers can be seen in Figure 65 on the right-hand side facing outward. These markers were used to get an estimate of flight altitude.

A Manlifter extension was used to raise the plywood beam stop to 78'2-in. above the launcher height (see Fig. 65). However, the 20 ft extension became too unstable (e.g., too weak) in early morning winds, and the height had to be reduced back down to the original height.

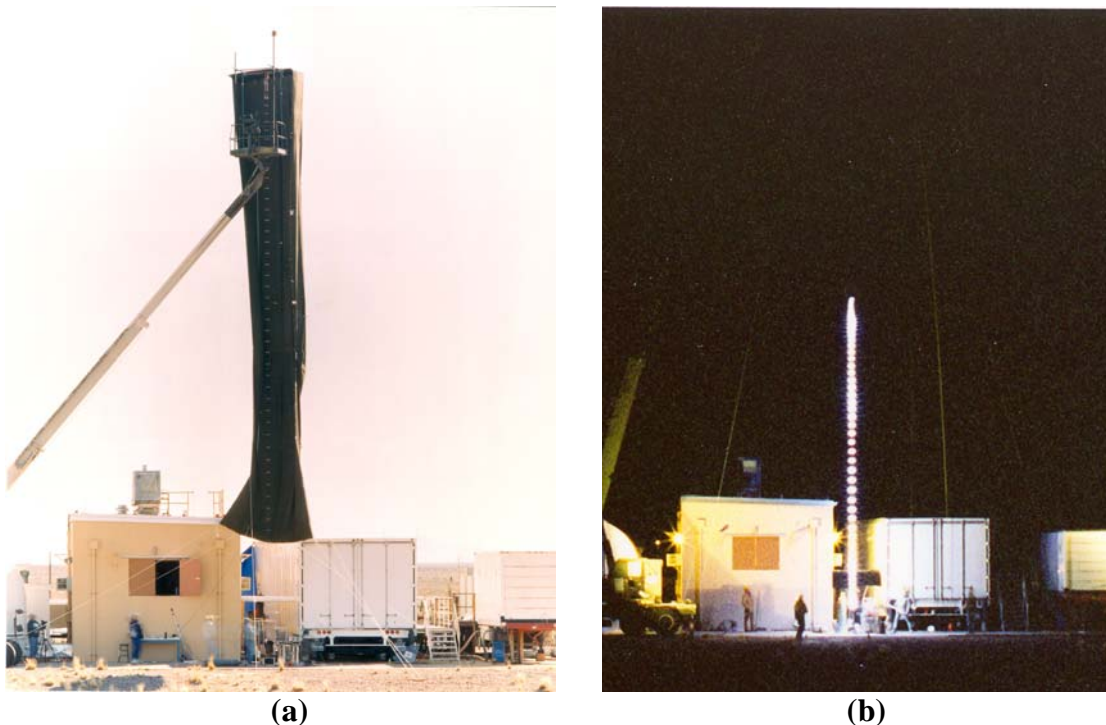


Fig. 65. Situation with Manlifter Extension (a) and a Night Flight Test with the Manlifter Extension in Place (b)

We were able to get a crane with a 90 ft boom height; but with a 4 ft loss because of the hook we were only really getting 86 ft, which was roughly equal to the Manlifter with the extension. So, not much was gained.

In summary, the following results were obtained from the flight tests conducted with a 6.67x6.67 cm beam; 8'10-in. reducing telescope mirror separation, and 20 Hz PRF. These results are illustrated in Table 9 below. It can be seen that the model #200s achieved the highest flights.

Table 9. Vertical Free Flight Test Results

Models	Assembled Mass (g)	Flights	# of Laser Pulses	Est. Height (ft)	Comments
150	47.966	2	74*, 170 (burned)	12, 50	Used, chem milled shroud
200	46.112	2	101*, 179 (burned)	25, 72.5	New, chem milled shroud
250	52.00	2	53, 158 (burned)	25, 50	New, chem milled shroud
200-9/10	41.857	3	78,56,140 (burned)	65', 68, 70	New, polished shroud
150- $\frac{3}{4}$	25.074	5	51,33,50,49,65 (burned)	25,30,30,8, 20	New, polished shroud
150- $\frac{2}{3}$	20.412	2	36,22	8,8	Wouldn't stay in beam
200-5/6	35.36	3	66,67,112 (burned)	50,35,60	New, nose not chem milled

* Note that shrouds take up to 75 to 100 pulses without melting (90' to 120' at best climb rate).

3.9 Test Series #12 (5-8 Feb 98)

A series of 48 flight tests, of which 22 were considered successful, were conducted with a variety of Lightcraft vehicles. The test vehicles included the 5/6, 9/10, 10/10, and 11/10 scales of the #200 Lightcraft with small bearings and a loose small wire vertical launcher. Each of these models had three chemical milled shrouds available, except for the 10/10 model, which had 2. The 5/6 and 9/10 shrouds and optics were too small and light to necessitate chem.-milling – only the noses were chem.-milled.



Fig. 66. Two Views of the Scaled Family of #200 6061 T6 Aluminum Lightcraft⁽²¹⁾

For the 10/10 and 11/10 models, both noses and optics were milled. Also available for testing, were the old #150-2/3 (20.41 g), the #150-3/4 (25.07 g), and #200-10/10 (46 g) vehicles. Pictures of the #200 series are shown in Figure 66, and the weight characteristics are illustrated in Table 10.

Table 10. 6061 T6 Aluminum Lightcraft #200 Style Model Mass (g) Characteristics

Model Size	Nose	Optic	Shroud #1	Shroud #2	Shroud #3	1st Assembled Mass*
5/6	6.06	9.50	14.00	15.00	14.50	31.92
9/11	11.00	6.64	17.00	18.00	18.00	37.00
10/10	10.37	14.05	16.76	17.95	21.00	43.54
11/10	10.80	13.68	27.50	28.50	29.50	54.35

* Includes mass of 8 screws and nuts, no lock washers, plus 2 bearings (2.36 g)

The PLVTS laser, except for a short series of 6 tests at 19 Hz, was operated at 20 Hz and 18 μ s pulse widths. The mirror separation was set at 9 ft - 7 in to give a beam size of 6.67 x 6.67 cm. The beam stop was elevated by the "Condor" crane to a height of 120 ft (117 ft from top of launcher) as illustrated in Figure 67. These pictures were taken by Mr. James Shryne using a Hasselblad camera with 10 mm film. Note the rope with white tags, spaced at 5 ft intervals used to estimate the height of Lightcraft flights. The last visible tag is 4 ft from the platform. Also visible are the Lightcraft launches defined by a vertical series of light pulses. A 16 mm video camera running at 100 fps was used in "look-down" mode from the platform, and an additional 16 mm camera with a long lens was mounted next to the launcher in a "look-up" mode.



Fig 67. Flight Tests Using the Condor Crane

During this series of tests, we were given a tour of the Driver and Emerald lasers which, for the most part, are in storage at HELSTF. This was in anticipation of a future requirement for a higher power laser.

The results of the tests are documented in Table 11.

Table 11. Analysis of Good Flights from Video Taken from 400-ft Scaffolding

Model Number	Estimated Height (ft)
200-5/6	57, 61, 51, 60, 56, 36, 41, 39, 46
200-9/10	43, 44, 38, 35, 35, 46, 34, 33, 35, 46
200-10/10	21, 22, 31

As a result of all the tests and the measured masses of the #200 Lightcraft vehicles, the scaling properties were determined for this vehicle without screws, fasteners, and bearings. These properties are illustrated in Figure 68 for the 6061-T6 aluminum Lightcraft assembled parts.

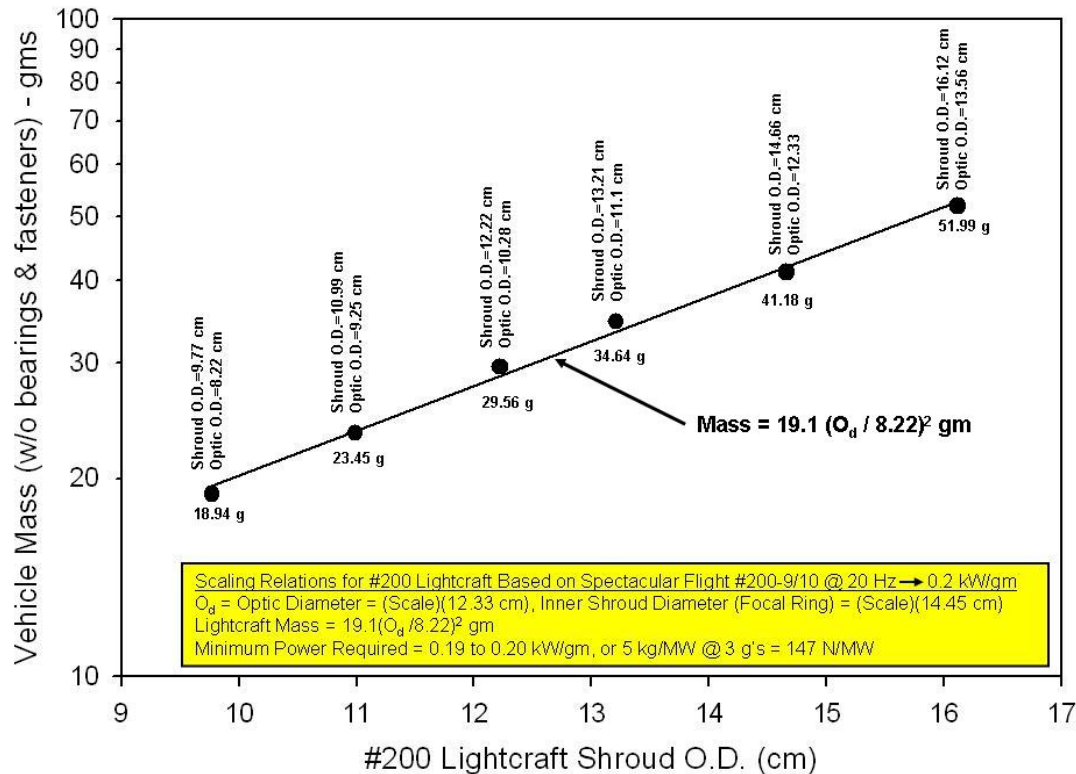


Fig. 68. Model #200 Lightcraft Scaling Relations

3.10 Test Series #13 (17-20 Mar 98)

The March tests were to emphasize in-door, static experiments on six different vehicle sizes of Model #200 Lightcraft, with receiver optics ranging from 8.22 to 13.56 cm in diameter. Schlieren photos were taken of the thrusters using the DATTS 3-ns pulsed glass laser (@ 0.532 μ m) to capture the shock wave position vs time. Engine plume visualization studies were performed using the DATTS water-mist system (alternatives included cigarette smoke, oil-mist, and thermofax paper ablation), with both the AFRL high speed (100 frames/sec) 16 mm camera and the camcorder. Thrust stand tests with a piezoelectric load cell were to measure: a) impulse coupling coefficients (CC)

vs. beam off-set and angular misalignment (both axial and lateral or side forces); b) CC vs. thruster size; c) CC vs. laser pulse duration; d) CC for two different near-field beam geometries (10x10 cm, and 6.67x6.67 cm), and far-field beam, to determine thruster beam-riding characteristics (i.e., inherent thrust-vectoring abilities) as a function of range.

There were some upgrades to PLVTS for this series of tests. A second set of fans was installed in the gas flow loop. The pulse period τ_p was still set at 18 μ s, but the PRF could now go up to 30 Hz. Calibration of the load cell consisted of using the following weights in the listed order of succession:

Table 12. Weights and Sequence for Load Cell Calibration

Sequence	a	b	c	d	e	f	g	h	i	j	k
Weights	163	425	886	2233	4516	9516	588	425	366	203	163
Combinations							222+203+163	222+203	203+163		

Model #200-10/10 Lightcraft engine was mounted on the newly modified thrust stand (see Fig. 69). The decision was made to start off with the 10 cm x 10 cm beam, and later get data with the 6.67 cm x 6.67 cm beam and telescope mirror separation of 8' – 10.5-in. which was previously used on the December 97 tests for vertical flight experiments.

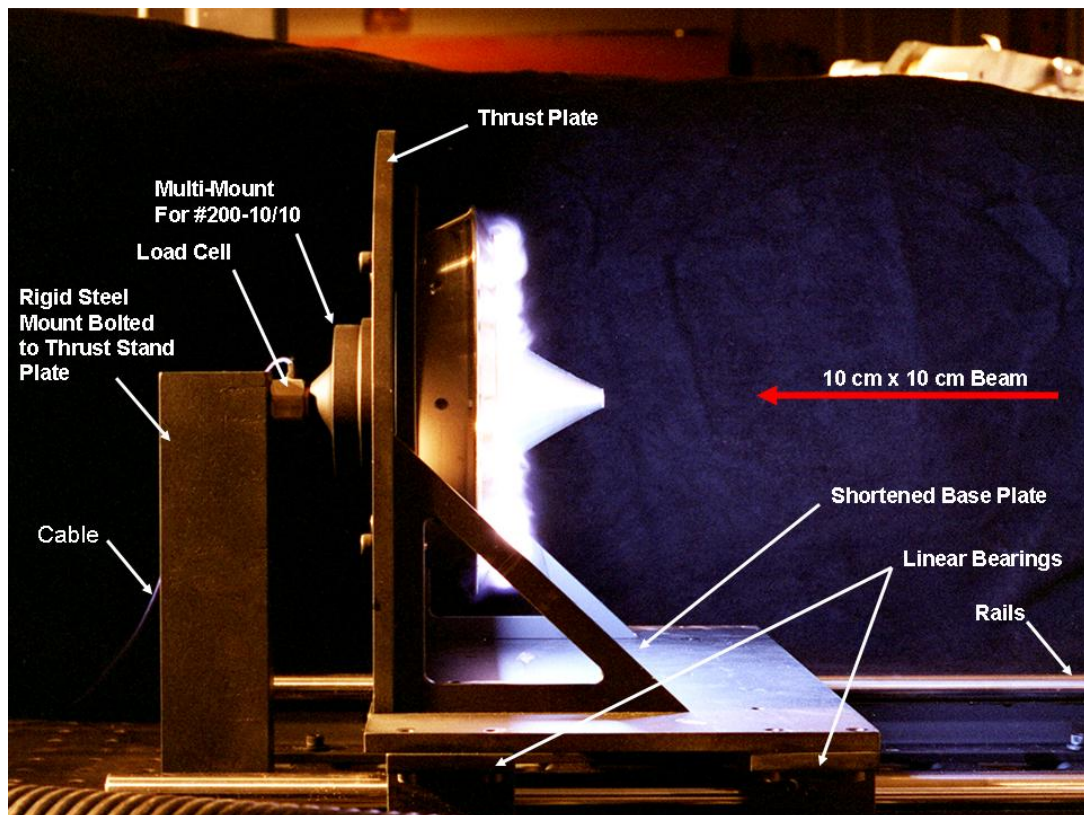


Fig. 69. Modified Thrust Stand

A frequency-doubled ($0.532\text{ }\mu\text{m}$) YAG laser was used for Schlieren and shadowgraph studies of the Lightcraft exhaust flow field during the pulsed detonation wave expansion. The configuration used for the Schlieren tests is illustrated in Figure 70.

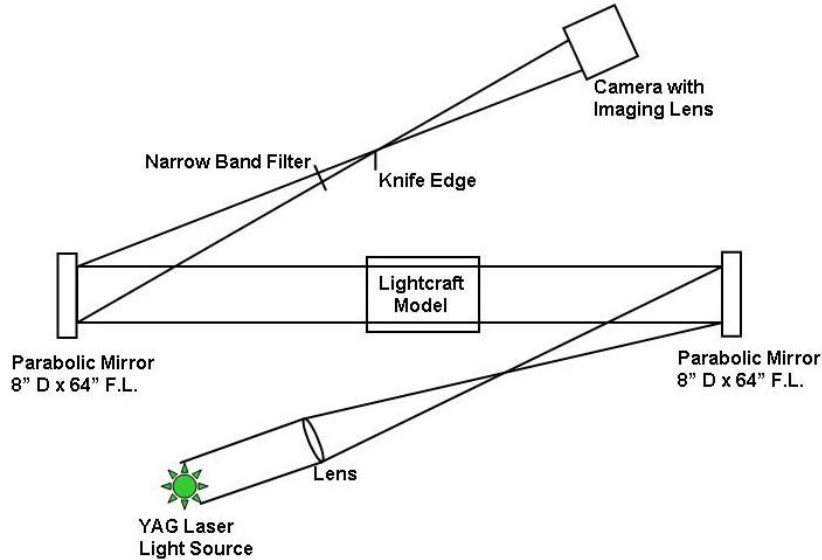
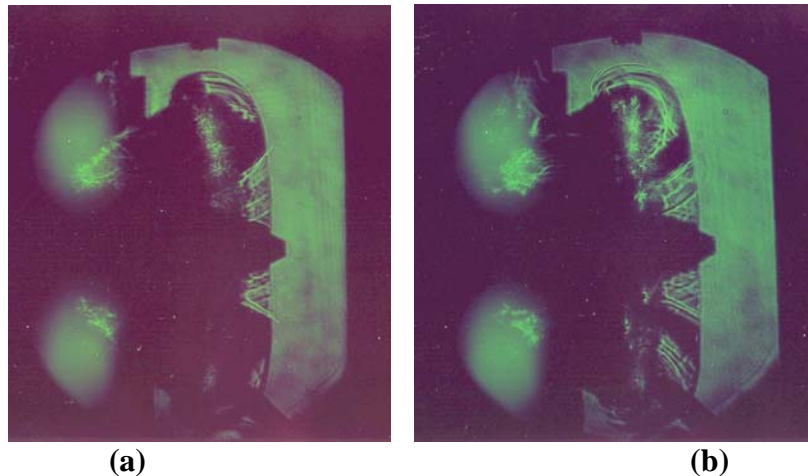


Fig. 70. Lightcraft Experimental Schlieren Apparatus⁽¹⁹⁾

For the shadowgraph pictures, the lens and knife edge on the camera side of the experiment were removed. A narrow band filter was used to remove broadband radiation from the plasma. The laser had to be severely attenuated from the 200 mJ/pulse to avoid over-exposing the film in the Polaroid camera. The YAG laser had a pulse duration of 3 ns, with timing jitter in the sub nanosecond range, and was triggered by the PLVTS firing circuit with a built-in controllable delay. The delay in the circuit allowed pictures to be taken at discrete time increments up to 6,000 μs following the time of first light arrival at the annular focal point of the engine.⁽²²⁾

We used color Polaroid 4-in. x 5-in. film, number 55 – 80 ASA, without negatives, and shot 48 Schlieren followed by 17 shadowgraph pictures (total 65 pictures) of the #200-10/10 thruster mounted to the modified thrust stand with the 10 cm x 10 cm beam at 18 μs pulse widths. Examples of these pictures taken at +70 μs are illustrated in Figure 71.



**Fig. 71. Example of Schlieren (a) and Shadowgraph (b),
Taken at +70 μ s From First Light Arrival at the Annular Focal Ring**

As can be seen, there are slight differences in the pictures. Schlieren photography gives information about density gradients, while shadowgraph photography gives information about how density varies throughout the flow field.

Subsequently, 120 shadowgraph pictures were taken with Polaroid type 51 HC – B&W-negative (high contrast) film at 5 μ s intervals. An example of these photographs is shown in Figure 72, starting at 25 μ s when the shock wave can easily be seen emerging (it actually took 19 μ s to emerge) from the Lightcraft and continuing out to 140 μ s. Actual photography of the flow field was taken as long as 1,680 μ s from arrival of laser light at the annular focal ring.

This sequence of pictures illustrates the exhaust flow field over the initial critical portion of the shock wave expansion. The progression of the shock wave out of the engine's annular plug nozzle is clearly evident in this sequence, and the shock wave is seen to eventually “wrap around” the outer perimeter of the engine's shroud. This wrap around phenomenon is clearly undesirable because it reduces the impulse derived from the laser pulse, and ultimately degrades the coupling coefficient.

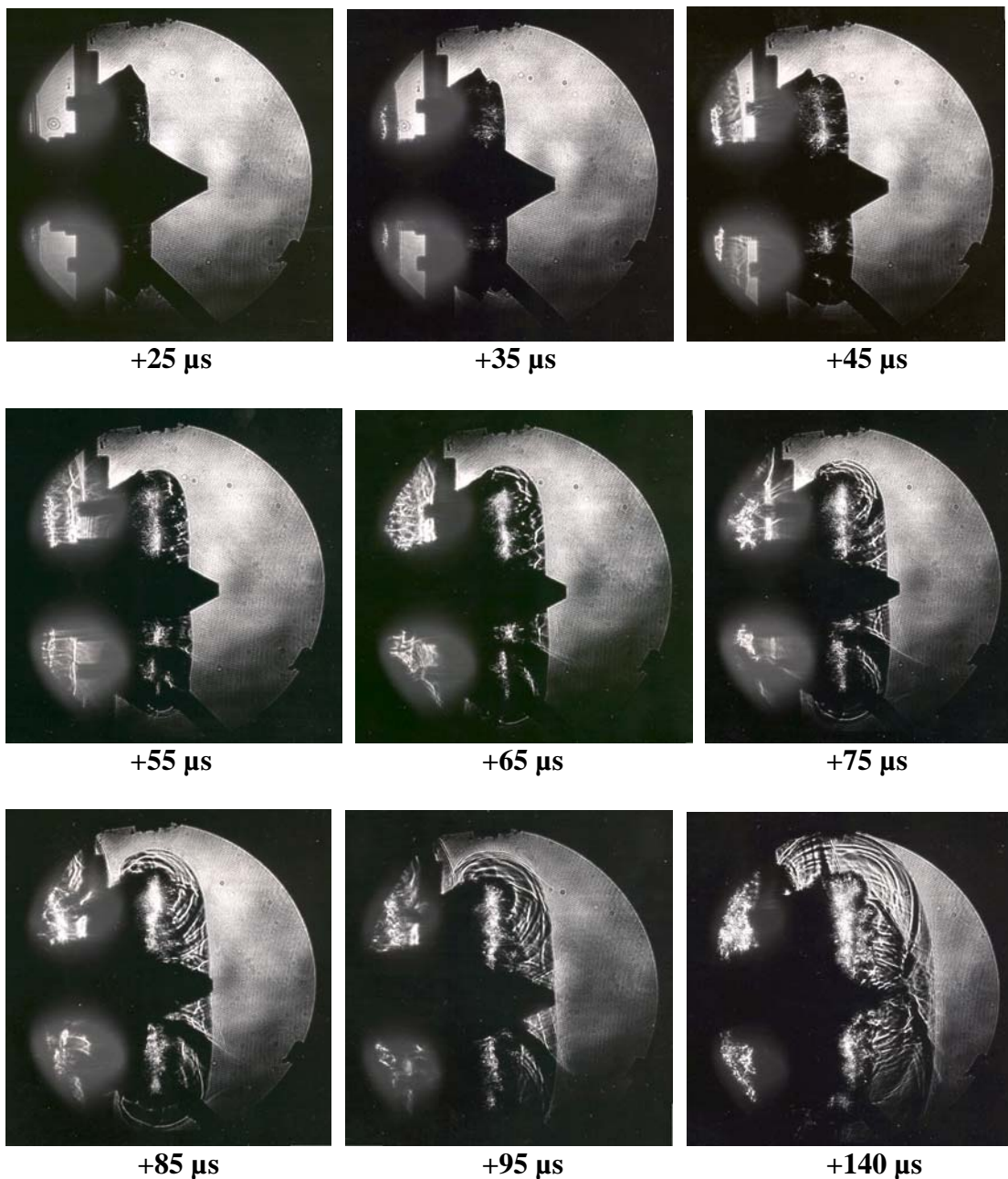


Fig. 72. Black and White Shadowgraph Pictures of the Lightcraft Exhaust Flow Field to +140 μ s Illustrating Shock Wave Structure and the “Wrap Around” Phenomenon

For these shadowgraph pictures, the Lightcraft #200-10/10 was again used and, as before, firmly mounted on the modified thrust stand.

A series of single pulse tests were conducted with the Lightcraft #200-10/10 mounted on the thrust stand to visualize the flow field using a mist created by pouring liquid nitrogen into a pan of water and letting the resultant vapor expand into the thruster's flow field. Once the vapor was in the area of the flow field, the laser sent a pulse to the thruster, and

the resulting hot gas emission from the thruster visibly moved the vapor much as a strong wind would have done. Figure 73 shows a still picture taken of these tests. Movie pictures taken of the tests gave a much more detailed view of the exhaust flow. The movies are very dynamic and graphic. Both single pulse and multiple pulses at 1 Hz were used to visualize the exhaust flow field.

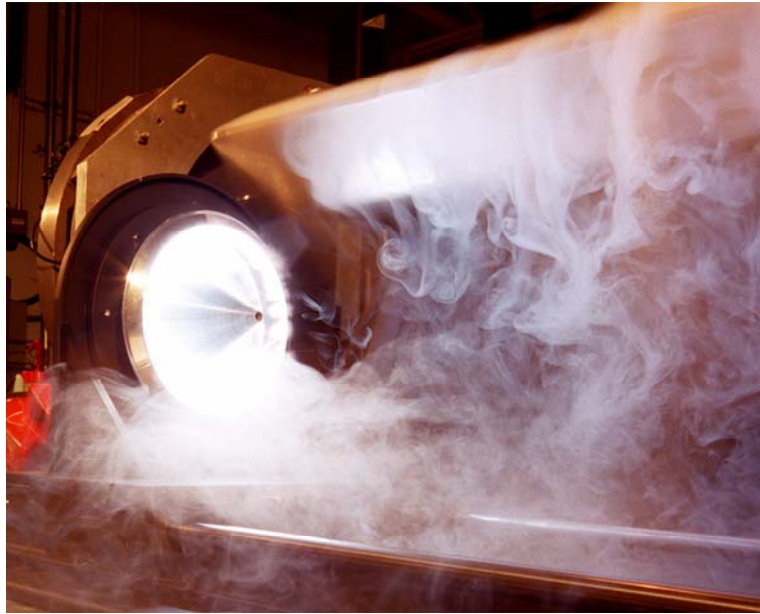


Fig. 73. Exhaust Field Visualization Test Using Vapor Created by Pouring Liquid Nitrogen Into a Bath of Water
(The Water Bath is Above and to the Right)

3.11 Test Series #14 (16-18 Apr 98)

Initially, some power tests were run at various frequencies and 18 μ s pulse widths. The following results that were obtained are shown in Figure 74. The first two measurements at 4,300 and 8,020 W were made with the smaller “SciTech” calorimeter and the last two measurements at 8,740 and 11,880 W were made with the “Big Ball” calorimeter. Three of the data points align very nicely with a second order least squares curve fit. The one point at 401 J and 20 Hz does not fit with the rest of the data. It appears that something was wrong in

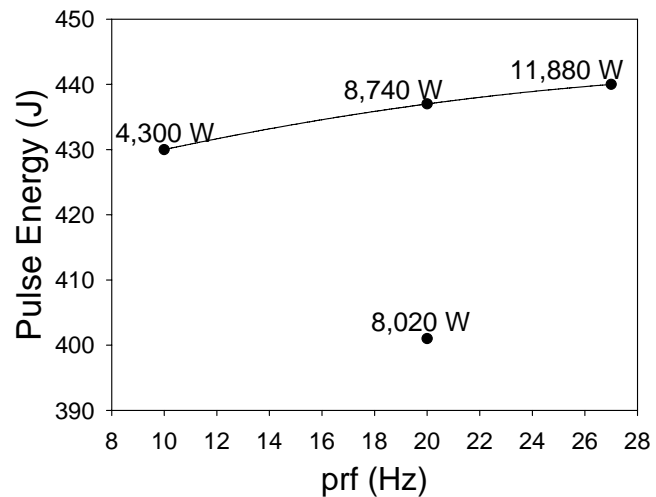
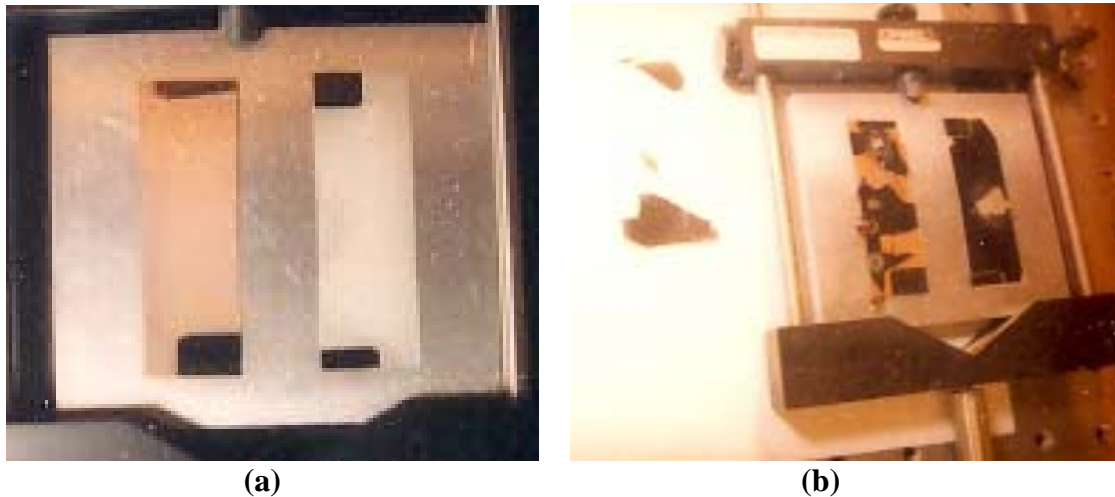


Fig. 74. PLVTS Power Test

the measurement of this data point. From these data it appears that one can expect 440 W at 27 Hz from the PLVTS. This is more than the rated output of 10 kW. For these tests, the PLVTS had all four fans (2 sets) installed. The measured flow velocity was 10.5 m/s (Clearing factor = 1.3:1).



(a) (b)
Fig. 75. Gold (left) and Silver Plated Aluminum Coupon Tests, Before (a) and After (b)

Coupon tests were conducted with two samples provided by ESLI. Pictures of the coupons mounted in a supporting frame are shown in Figure 75 before and after the tests. The coupons consisted of gold and silver plating on an aluminum base plate. The coupons were irradiated with 250 mJ/cm^2 at 27 Hz and $18 \mu\text{s}$ pulses for 3 seconds. This energy was sufficient to “peel off” large pieces of the gold and silver plating. From the pictures, it appears that the gold plating suffered the most damage.

Outside free flight tests were conducted and filmed. A movie crew from Windfall Films was present to film the flight tests. The resulting movie entitled **Science Frontiers: Super Laser**, aired on The Learning Channel on 5 October 98, at 10 pm ET. The program had previously been broadcast in the United Kingdom and received very positive feedback. A VHS copy or the finished film was sent to the AFRL to document this event.

A Condor crane was used to hold the beam dump at 115 ft (launcher at 3.5 ft high) above ground level. A Robo Cam was placed on the plywood beam dump in a “look-down” position. It was remotely controlled from the ground. A remotely controlled 16 mm camera was placed under the launch stand in a “look-up” position, and a Beta Cam was placed on the 400 ft scaffolding tower to give a side view from almost exactly the launch point height. Estimated flight altitudes were obtained from the Beta Cam position. A rope with “Wiffle” balls spaced every 10 ft was also hung from the beam dump platform. This rope and the Wiffle balls were highly visible in the Beta Cam video and provided an excellent estimation of flight altitude. Still pictures, like those shown in Figure 76, were also taken during the flight tests. Clearly seen in Figure 76b is the Wiffle ball rope and the integrated plasma flashes of the flight. The flight illustrated in Figure

76b is one of the better flights. Figure 76a, taken at night, illustrates “lift-off” from the launch stand. As always, the vehicles were spun to very high rpm with a nitrogen jet for stabilization during flight.

For these flight tests, models #200-10/10, 9/10, and 5/6 with new rear optic bearing retainer clips were available for testing. Each model had three shrouds available, labeled a, b, and c. The model #200-10/10 had a new nose and 2 new shrouds (the rear shroud lip was cut to 0.10-in. from 0.20-in.) recently chem. milled by Caspian.

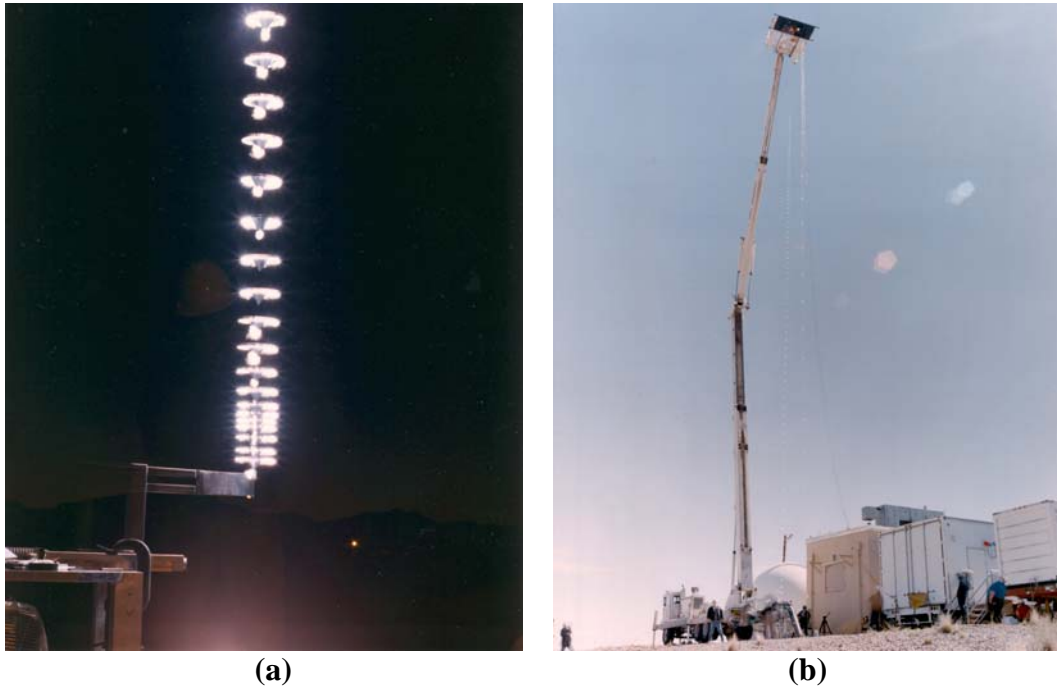


Fig. 76. Lift-Off Tests (a) and High Altitude Flight Tests (b)

For testing inside or outside, three different telescope settings were investigated to control the size of the square laser image in the near field. The 8'10½-in. beam was a fairly large beam, the 9'8¾-in. beam was a good mid-sized, reduced beam, and the 10'-7 in. was the smallest beam which tended to burn out the optic's point. The telescope mirror separation versus telescope focal distance for these three positions is illustrated in Figure 77.

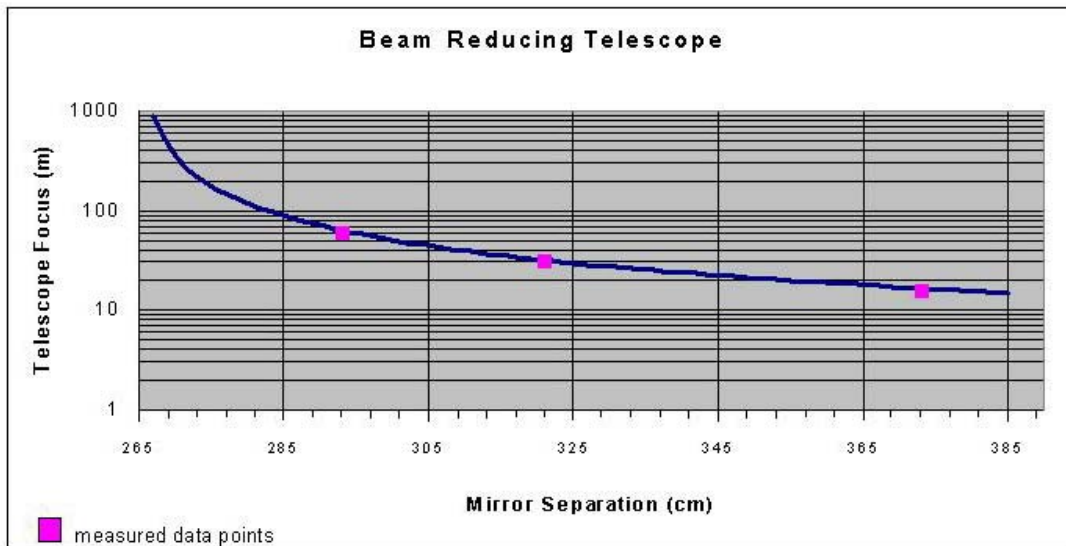
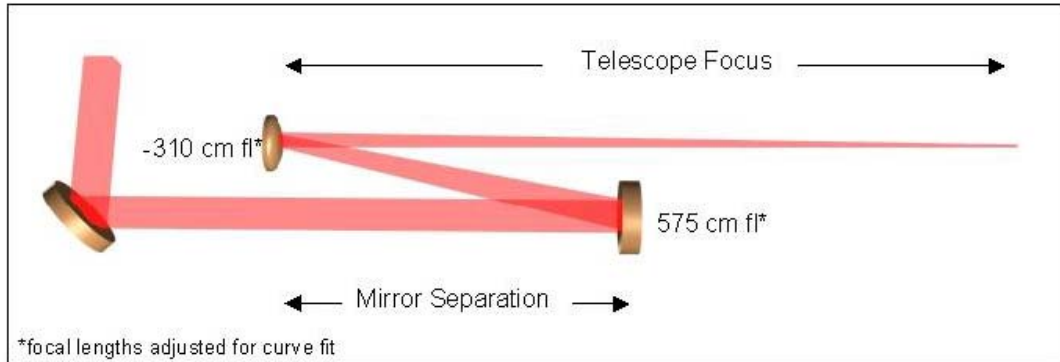


Fig. 77. Telescope Focus as a Function of Mirror Separation

The Field Test Telescope (FTT), shown in Figure 78, was used for testing at extreme distances. Its focus as a function of mirror separation is illustrated in Figure 78b.

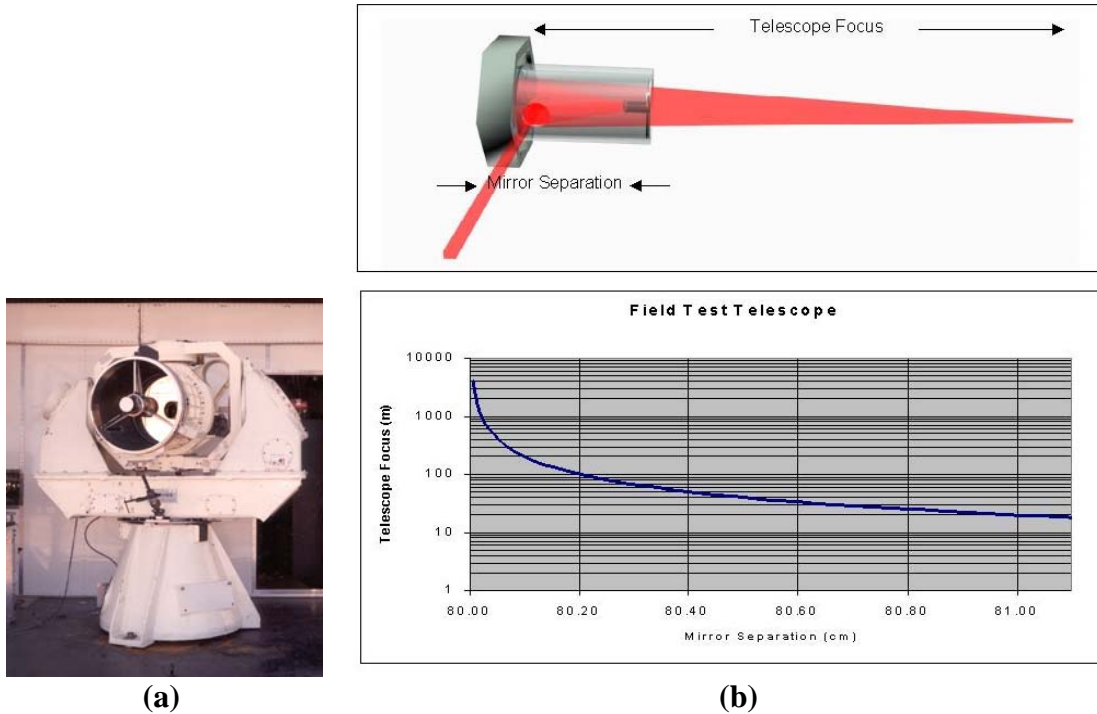


Fig. 78. The FTT (a) and its Focus Length versus Mirror Separation (b)

Table 13 lists the 32 flights and the particular test conditions, including mirror separation. Also given are the estimated flight altitudes with comments detailing the condition of the various vehicles after each flight.

Table 13. April Outdoor Free Flight Experiments

Run	Model	Scale	PRF	Pulses	Height (ft)	Telescope Separation	Comments
1	150	2/3	25	19	10-12	8 ft10 ½ in.	6.67x6.67 cm beam
2	200	9/10	"	100	~60	"	Shroud OK
3	"	"	"	123	~55	"	Burned shroud, broke lower bearing
4	"	10/10	"	177	~60	"	Burned shroud
5	"	5/6	"	81	~60	"	Model OK
6	"	"	"	59	40	"	"
7	"	"	"	108	?	"	"
8	"	"	"	118	~70*	"	"
9	"	"	"	55	~40	"	"
10	"	"	"	108	~50	"	"
11	"	"	25	140	~80*	"	Shroud burned
12	"	5/6	30	62	~53	"	Shroud OK
13	"	¾	30	74	27	"	"
14	"	5/6	26	49	37	"	"
15	"	5/6	27	161	57	8 ft10 ½ in.	Burned shroud
16	"	11/10	"	101	36	9 ft2 in.	Inverse telescope
17	"	11/10	"	92	27	None	10x10 cm beam, no telescope
18	"	¾	"	121	91*	10 ft 7 in.	Burned shroud, inverse telescope

Table 13, Cont'd (April Outdoor Free Flight Experiments)

Run	Model	Scale	PRF	Pulses	Height (ft)	Telescope Separation	Comments
19	200	2/3	“	?	21	“	
20	150	¾	“	25	26	“	
21	200	2/3	“	44	Low	“	
22	“	10/10	27	92	27	“	
23	200	10/10	30	198	65*	“	Burned out optic & shroud
24	150	¾	“	48	25	“	
25	200	2/3	“	64	46	“	
26	200	2/3	“	106	75*	“	Burned shroud
27	150	2/3	“	?	Dud	“	
28	200	5/6	“	98	55	“	Cracked shroud
29	“	5/6	“	102	50	“	“
30	“	5/6	30	?	?	“	“
31	“	9/10	28	134	35-40	“	Shroud OK
32	200	9/10	30	195	36	10 ft 7 in.	Burned out optic, shroud OK

If the highest flight altitudes are analyzed for time of flight, average velocity, constant acceleration, and thrust, the results can be seen in Table 14. There is no real trend here, but in general the highest flights had lower thrust; and the highest flying vehicle was the #200-3/4. The assumption of average velocity is probably pretty good, because open shutter photographs show that the acceleration occurs early in the flight, and constant velocity occurs for the remainder of the flight. Therefore, constant acceleration occurs early in the flight and goes to a value near zero for the remainder of the flight. If it is assumed that the initial acceleration occurs during the first 10 ft or so, as the photographs

Table 14. Analysis of Highest Flights from Table 13

Height-See Table 13	Mass (g)	Flight Time (s)	Const. Velocity† (ft/s) / (mph) / (m/s)	Const. Acceleration* (ft/s ²) / (m/s ²)	Max. Thrust‡ (lbf) / (N)
65'	48.40	6.60	9.85 / 6.72 / 3.00	4.85 / 1.48	0.124 / 0.55
70'	32.56	4.72	14.83 / 10.11 / 4.52	11.00 / 3.35	0.097 / 0.43
75'	21.50	3.5	21.43 / 14.61 / 6.53	22.96 / 7.00	0.081 / 0.36
80'	32.56	5.60	15.71 / 10.71 / 4.79	12.34 / 3.76	0.099 / 0.44
91'	27.50	4.48	20.31 / 13.84 / 6.19	20.62 / 6.28	0.079 / 0.44

† Assumes constant velocity over entire flight

* Assumes all acceleration occurs over the first 10 ft of flight

‡ Assumes maximum thrust occurs over the first 10 ft of flight under constant acceleration

show, then much higher values of acceleration occur. If the distance over which acceleration occurs is 3 ft or 5 ft, then acceleration values triple or double. This would lead to considerably higher thrust values. Thus the accelerations shown in Table XIV are probably more accurate than if the acceleration were considered constant over the entire flight. Near the end of the flight there is typically a negative acceleration which has also been neglected here. The weights were determined from measured values of the nose, shroud, and optic; and include an additional mass of 2.5 g for the screws, lock washers, and nuts. Even though there is a wide variation in mass, time, velocity, and acceleration, the thrust is relatively uniform between 0.36 and 0.55 N, with thrust values essentially the same for three of the five flights.

3.12 Test Series #15 (28-31 May 98)

The goal for this test series was to break 90 ft height of Goddard's 2nd flight. To do this we planned to start with the 10 ft 7-in. spacing on the inverse telescope mirrors and move closer if necessary. The Peter Jennings ABC News crew was to arrive on 29 May for filming, and the BBC news group was scheduled to arrive on 31 May for filming. It was during this test series that we planned to try our first titanium shroud in vertical free flight with #200-5/6 at 16.5 gm – mostly 8 to 9 mils thick; and, try the lithium-aluminum shrouds (2195 Li-Al) with the #200-5/6, 3/4, & 2/3 vehicles.

Beam propagation burns for an 8 ft 10 ½-in. inverse telescope were performed on 27 May 1998 out to a distance of 201 ft at 3 ft increments. Power measurements for various size apertures at ~2 cm intervals. Chris Beirsto wanted to continue beam propagation measurements out to 400 ft during this test period when and if the winds were too high to test. A Condor crane (see Fig. 79) was used for these tests with a Robo-cam placed in a look-down position. For the first time, the program had its own wind sock, which measured a top wind speed up to 15 mph when fully extended. The height measurement to the back stop plywood from the launch point using the radar gun was 119 ft (launch point is 3.5 ft from ground).



Fig. 79. Condor Crane with Wind Sock and Wiffle Ball Measurement Line Attached

Table 15. PLVTS Tests, 29 & 31 May 1998, 28 Hz, 360 J, & 18 μ s Pulse Widths

Run #	Model	Pulses	Est. Height (ft)	Mirror Separation	Comments	Wind (m/s)
1	150-3/4	122	15	10 ft 7 in.	10 kW, max power on target	Calm
2	200-3/4	102	65	10 ft 7 in.	Burned out optic, Li-Al Shroud	“
3	200-5/6	98	55	8 ft 10½ in.	Burned off Li-Al shroud-rear edge	“
4	200-2/3	97	49	8 ft 10½ in.	Burned off Li-Al shroud-rear edge	“
5	200-5/6	106	45	8 ft 10½ in.	Burned off Li-Al shroud-rear edge	“
6	150-3/4	52	30	9 ft 8¾ in.	—	
7	150-3/4	72	30	“	—	2 m/s
8	200-2/3	63	40	“	Li-Al Shroud	—
9	200-5/6	Dud	0	“	Li-Al Shroud	—
10	200-5/6	94	53	“	Li-Al Shroud	—
11	200-5/6	100	61	“	Ti shroud destruction flight	—
12	200-2/3	42	35	“	—	—
13	200-2/3	89	55	10 ft 7 in.	—	2 m/s
14	200-2/3	76	49	10 ft 7 in.	—	
15	200-11/10	106	32	-	Full 10x10 cm beam	5 m/s
16	200-11/10	144	35	-	Full 10x10 cm beam, burned shroud	3 m/s

Figure 80 shows the set-up used to control multiple cameras, both still and motion. Thus, one person was able to coordinate each camera. At this time, we had look-up, look-down motion cameras, and two still cameras. Plus there was the remote (~ 400 ft) motion camera manned by Dr. Mead on the scaffolding.



Fig. 80. Mr. James Shryne, in His Control Space Under One of the Trailers
(From this position, he was able to control the operation of a number of motion and still cameras.)

Table 16. Lightcraft Component and Assembled Weights

Model	Assembled (g)	Shroud (g)	Assembled 6061-T6 Al (g)
200-5/6 Ti	37.8	16.5	32.5
200-5/6 Li-Al	33.3	12.0	32.5
200-2/3 Li-Al	21.0	6.5	21.5
200-3/4 Li-Al	26.5	9.0	27.5
200-9/10	37.64	—	37.64
200-10/10	48.4	—	48.4
200-11/10	54.5	—	54.5

3.13 Test Series #16 (24-26 July 1998)

For this series of flight tests the Condor crane (See Fig 81) height was measured to be 117 ft above launch point. A crew from Extreme Machines filmed some of the machines. A new launcher had been built in the RPI machine shop and was shipped directly to the test site for use during this test series. Silver and copper sputter coated titanium shrouds from ESLI were also flown in. The test flight results are listed in Table 17, and the mass properties of the test vehicles are listed in Table 18.

Table 17. Flight Tests, 25 July 98, at 18 μ s Pulse Widths, 360 J/Pulse, Calm Wind

Run #	Model	PRF (Hz)	Pulses	Height (ft)	Mirror Separation	Comments
1	150-3/4	28	28	58	9 ft 8 3/4 in.	
2	200-5/6	28	78	47	9 ft 8 3/4 in.	Silver coated titanium shroud
3	200-2/3	28	84	66	9 ft 8 3/4 in.	Silver coated titanium shroud
4	200-2/3	28	98	81	9 ft 8 3/4 in.	Al shroud (LN ₂ Config.)
5	200-2/3	28	104	73	9 ft 8 3/4 in.	Al shroud (LN ₂ Config.)
6	200-2/3	28	58	52	9 ft 8 3/4 in.	Al shroud (LN ₂ Config.), optic very beat up
7	200-9/10	27	108	69	8 ft 10 1/2 in.	Al shroud, thrust stand optic
8	200-9/10	27	132	57	8 ft 10 1/2 in.	Same model landed on roof of building
9	200-9/10	27	130	12	8 ft 10 1/2 in.	Same model wouldn't release
10	200-5/6	27	89	8	8 ft 10 1/2 in.	Ti shroud, damaged before

Table 18. Mass Properties Of Flight Vehicles

Model	Shroud	Optic	Flight Mass (g)
200-5/6	Coated Ti	Al	36.9
200-2/3	Al	Silver coated Ti	23.1
200-2/3	Al	AL	21.7
200-2/3 (LN ₂ Config.)	AL	AL	21.65
200-9/10	Al	Al	38.5



Fig 81. Flight Test with Condor Crane

3.14 Test Series #17 (20-23 Aug 1998)

The new LN₂ Lightcraft launcher was ready for testing. It did not have inserts for upper and lower bearings yet. The cable end that attached to the upper Lightcraft bell crank retract arm needed something to limit its movement because it still slipped.

Two film crews were here during this test period: 1) CNN Interactive on Friday, 21 Aug 98 (Andy Walton); and, 2) British film crew on Saturday and Sunday, 22-23 Aug 98 (Gala Carr – Union Skyline, Ch 4 TV, London; and, producer John Purdee).

This was the first and only time that a fish-eye lens was used to get good close-ups of launches with the 10/10 and 9/10 models with time-lapse 35 mm and 16 mm high speed cameras.

A major goal for this test series was hitting the 120-foot beam dump with the LN₂ models - 2/3 model with cylindrical tank, a 3/4 model with foil diaphragm splitter tank, and a 5/6 model with foil diaphragm splitter tank.

The measured height of the crane beam dump plywood with measuring tape and laser radar range finder was 121'9" to ground.

Telescope spacing for these tests are 8'10½" (big beam, same as 3 Dec 1997 tests), 10 ft 7 in. (smallest beam, burned out the optics point of 3/4 on 29 May 98 and 9/10 and 10/10 on 17 April 1998 tests), and 9'8¾" (good mid-sized, reduced beam, best for small Lightcraft). The assembled Lightcraft masses are listed in Table 19.

Table 19. Assembled Lightcraft Masses (g)

Model	Assembled (g)	Comments
150-3/4	25.10	Warm-up vehicle
150-2/3	19.85	Warm-up vehicle
200-3/4	26.93	Brand new optic with bearing & hole
200-5/6	28.80	LN ₂ type shroud, optic polished up
200-9/10	39.21	Used slightly, bulged shroud, optic point damage
200-10/10	48.90	Older shroud, minor rock damage near optic point

For the Lightcraft #200-2/3, which was designed to carry a small tank of LN₂ for cooling of the shroud, the component masses were:

- Tank mass = 5.32 g measured on-site
- Shroud mass = 5.5 g measured by RPI Machine Shop
- Optic mass = 5.5 g measured by RPI Machine Shop
- Nose mass = 6.5 g measured by RPI Machine Shop
- Assembled mass = 24.93 g measured on-site

The look-down camera positions mounted on the plywood beam dump for these tests are illustrated in Figure 82.

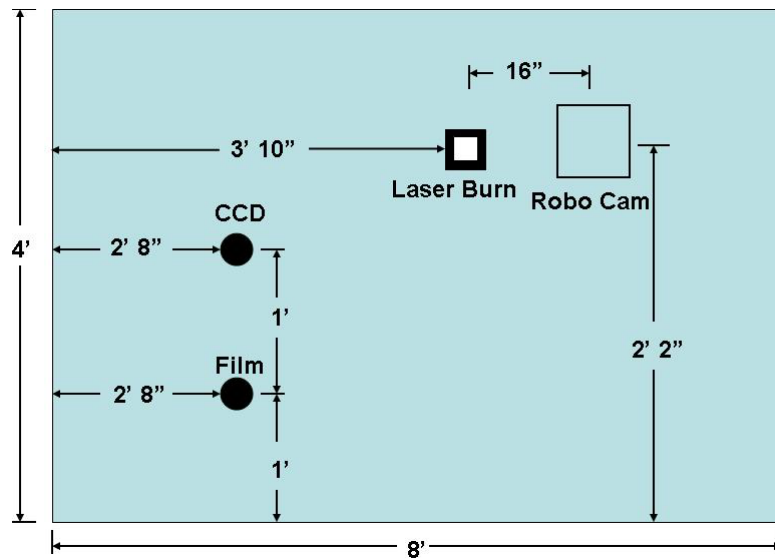


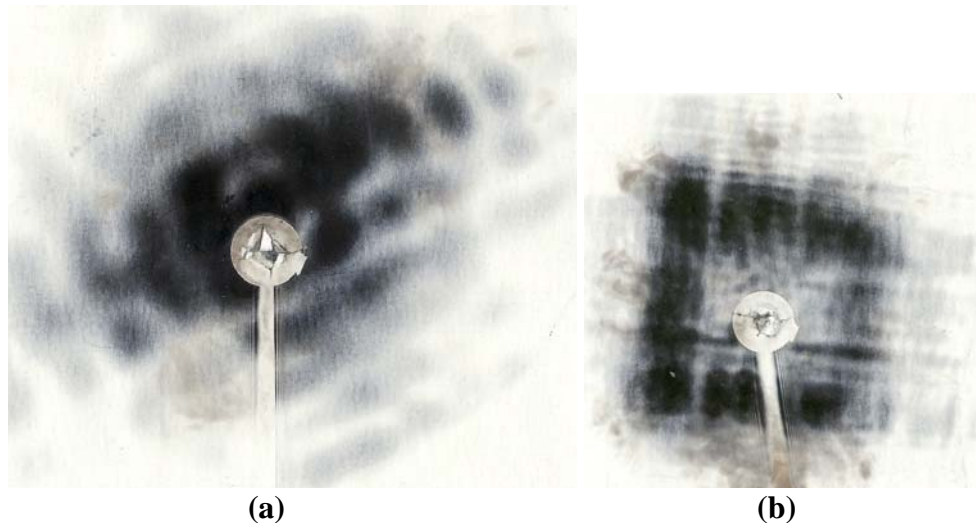
Fig. 82. Position of Cameras on Plywood Beam Dump

The experimental results of the flight tests are listed in Table 20. Note that the #200-5/6 and #200-3/4 flew the highest, and had no difficulty releasing from the wire launcher. The #200-3/4 consistently flew the highest, ever since the ~91 ft flight on 18 Apr 98.

Table 20. Flight Test, 18 μ s, 28 Hz, $E_p=420$ J

Run #	Model	Shroud	# of Pulses	Alt. (ft)	Mirror Sep.	Wind (m/s)	Comments
1	150- $\frac{3}{4}$	—	41	~10	8 ft 10 $\frac{1}{2}$ in.	3.43 - 4	Blowing towards Frank
2	150- $\frac{3}{4}$	—	84	12-15	“	—	—
3	200-10/10	Al	113	20	“	—	Stuck on launcher, burned shroud
4	200-9/10	Al	98	51	“	4 - 4.4	Stuck on launcher, burned shroud
5	200-5/6	Al-LN ₂	86	80	“	—	Ht. from video, burned shroud
6	200- $\frac{3}{4}$	Al/Li	68	43	“	—	Lost bearing, left beam, beam too big
7	200- $\frac{3}{4}$	Al/Li	49	20-25	9 ft 8 $\frac{3}{4}$ in.	2.6 - 4.0	—
8	200-5/6	Al-LN ₂	—	—	—	3.5 - 4.5	Scrubbed flight, too windy
9	200- $\frac{2}{3}$	Al-LN ₂	—	—	9 ft 8 $\frac{3}{4}$ in.	Nil	Dented rim, skipped out
10	200- $\frac{2}{3}$	Al-LN ₂	—	—	“	—	Added funnel in lower bearing
11	200- $\frac{2}{3}$	Al-LN ₂	—	—	“	Nil	Added funnel in lower bearing
12	200- $\frac{2}{3}$	Al-LN ₂	—	—	10 ft 7 in.	“	Wobbling at take-off
13	200- $\frac{2}{3}$	Al-LN ₂	—	—	“	“	Very high spin rate, damaged optic
14	200-5/6	Al-LN ₂	108	80	9 ft 8 $\frac{3}{4}$ in.	“	Retainer bearing optic, failed shroud
15	200- $\frac{3}{4}$	Al/Li	100	~15	“	“	Kicked out of beam, shroud OK
16	200-5/6	Al-LN ₂	103	77	“	“	Shroud bulged but held
17	200-9/10	Al	111	80	“	“	Old optic, shroud failed
18	200- $\frac{3}{4}$	Al/Li	42	48	“	“	Liftoff at 80' range, blew shroud
19	200-5/6	Al-LN ₂	78	48	“	“	Liftoff at 80' range, dented nose
20	200- $\frac{3}{4}$	Al/Li	83	~20	“	“	Liftoff at 120', stuck on wire, blew shroud
21	200- $\frac{2}{3}$	Al-LN ₂	63	~10	“	3.0 - 4.0	Liftoff at 120', new optic
22	200- $\frac{2}{3}$	Al-LN ₂	65	<10	“	—	Liftoff at 120', jumps out of beam
23	200- $\frac{3}{4}$	Al-LN ₂	102	~20	“	2 ~ 2.5	Liftoff at 120', shroud failed early
24	200- $\frac{3}{4}$	Al-LN ₂	78	~15	“	1.8 - 2.4	Liftoff at 120', stuck on launcher
25	200- $\frac{3}{4}$	Al-LN ₂	52	~15	“	0.7 - 1.4	Liftoff at 120', sticks on launcher
26	200- $\frac{3}{4}$	Al-LN ₂	94	100	“	2.5	Liftoff at 0', moved to top of launcher

Note that the beam was propagated 80 to 120 ft before turning vertical at the base of the launcher, and even the #200-3/4 stuck on the launcher stand due most likely to the decreased laser power. The #200-2/3 took off without delay, but didn't capture enough beam power to keep flying, while being auto-centered in the beam. The laser beam was too large in diameter (see Fig. 83) for self centering at 120 ft.



(a) (b)
Fig. 83. 9'8 3/4" Inverse Mirror Spaced Beams at 120 ft and 0 ft.
 (Size Approximately to Scale)

3.15 Test Series #18 (23-26 Sep 1998)

Day 1 was pendulum experiments (See Fig 84). The Plan was to measure impulse versus range, pulse duration, and angular beam offset. The pendulum experiments were looking very nice. The impulse hammer gave a very good calibration, and an accelerometer was used instead of the fragile coil which had been used previously. For these tests an old optic and shroud had to be used because the RPI machine shop didn't get the new one done in time.

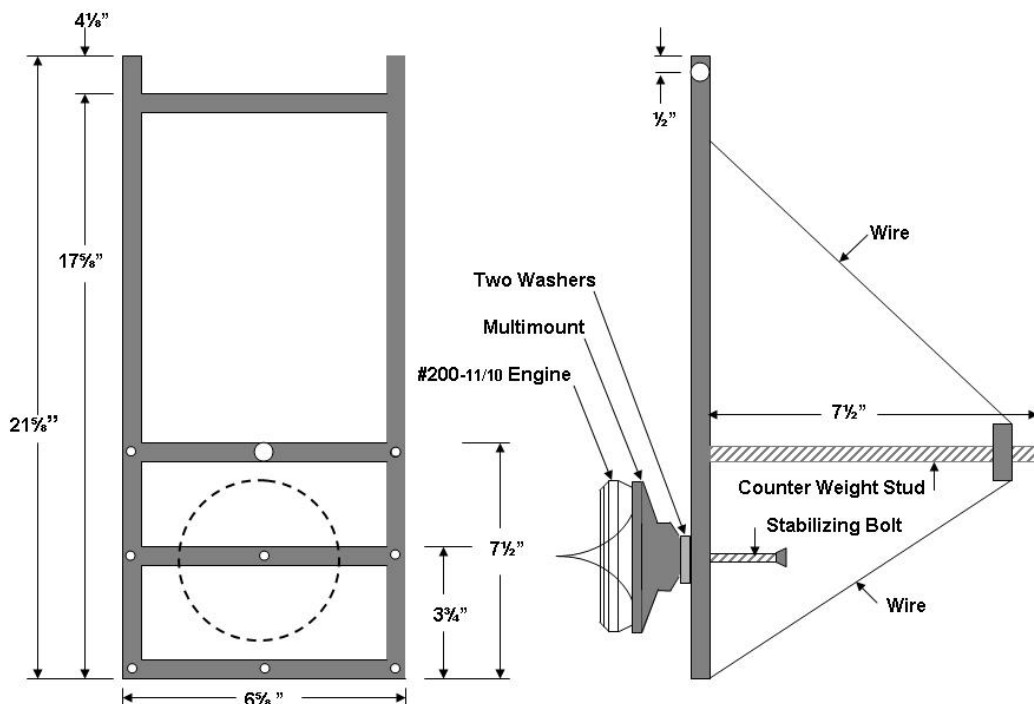


Fig. 84. New Aluminum Pendulum Design

Day 2 started off with shadowgraph photographs using the thrust stand mount, Day 3 was dedicated to thrust stand measurements, and Day 4 was composed of two experiments. The first experiment used the pendulum to determine the variation in coupling with the height of the breakdown. The laser was focused into a line at different heights from a flat plate, using a mirror provided by Prof. Myrabo. After this experiment was completed, the flat plate was replaced with two plates at an angle, with the focus in the corner, intended to be a 2D simulation of the vehicle's shroud. Heat transfer gauges were installed on the plates to determine the blast wave position with time. Heat flux data was also obtained, but the gauges were not calibrated for lack of time.

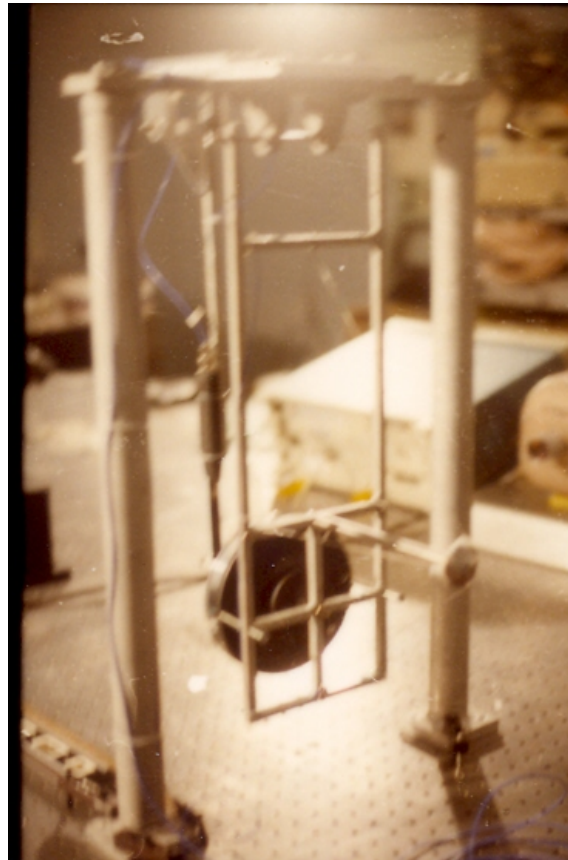


Fig. 85. New Pendulum and Piezoelectric Impulse Hammer Set-Up

This was the first use of the impulse hammer for calibration of the pendulum assembly. The hammer was a Modally Tuned Impact Hammer Kit, Series 291, purchased from The Model shop, Inc., Cincinnati OH. The hammer functions to transfer force into an electrical signal which is convenient for display and analysis. A variety of “tips” were supplied to allow tailoring the hammer’s response to impact such that the best trace was obtained. Figure 85 shows the #200-11/10 Lightcraft mounted on the pendulum and the hammer hanging parallel to the pendulum such that the tip just barely touches the point of the optic but does not displace the pendulum perceptibly. An accelerometer, attached to

the lower end of the pendulum was used to read the laser-generated impulse. However, we were unable to get the accelerometer, which used an unshielded cable, to work for the impulse measurement. The very high peak initial impulse was always clipped. It was decided to abandon this approach and use the standard coil/magnet sensor next time. The coil/magnet typically gave 8-10 volts output while the accelerometer typically gave millivolts.

Shadowgraphs of flat plate with thin film platinum heat transfer gages ($1\text{ }\mu\text{s}$ response time) were made using the surplus SDIO mirror with the line focus right at the flat plate surface (See Figs. 86 and 87). There were a total of 12 gages, 6 on each side of the focal line. The $\sim 1.25\text{ mm}$ radius focal line is 10 cm out and 4.6 cm up from the outer edge of the SDIO aluminum mirror. On inspecting the mirror surface, many tooling lines were clearly in evidence, leading one to believe that the mirror would scatter a lot of laser power. The laser was set for $18\text{ }\mu\text{s}$ pulse width for the attempt at taking shadowgraph photos. The beam was chopped to $2.5\text{ cm} \times 10\text{ cm}$ and brought to a focus at the target centerline, which was at the midpoint of the 12 heat gage strip. Direct physical inspection of the burn mark on the steel impulse plate revealed that most of the beam energy was within a 9.8 cm line length ($\sim 10\text{ cm}$).

Laser induced cylindrical plasmas and blast waves generated over a flat plate (see Fig. 86) were photographed using the shadowgraph technique. The position of the blast wave edge was recorded as a function of time. The measurements indicated that the energy deposition from the laser was becoming uncoupled from the blast wave toward the end of the $18\text{ }\mu\text{s}$, CO_2 laser pulse. The blast wave edge position history was useful for validating CFD models of the laser-air interaction.⁽²⁴⁾

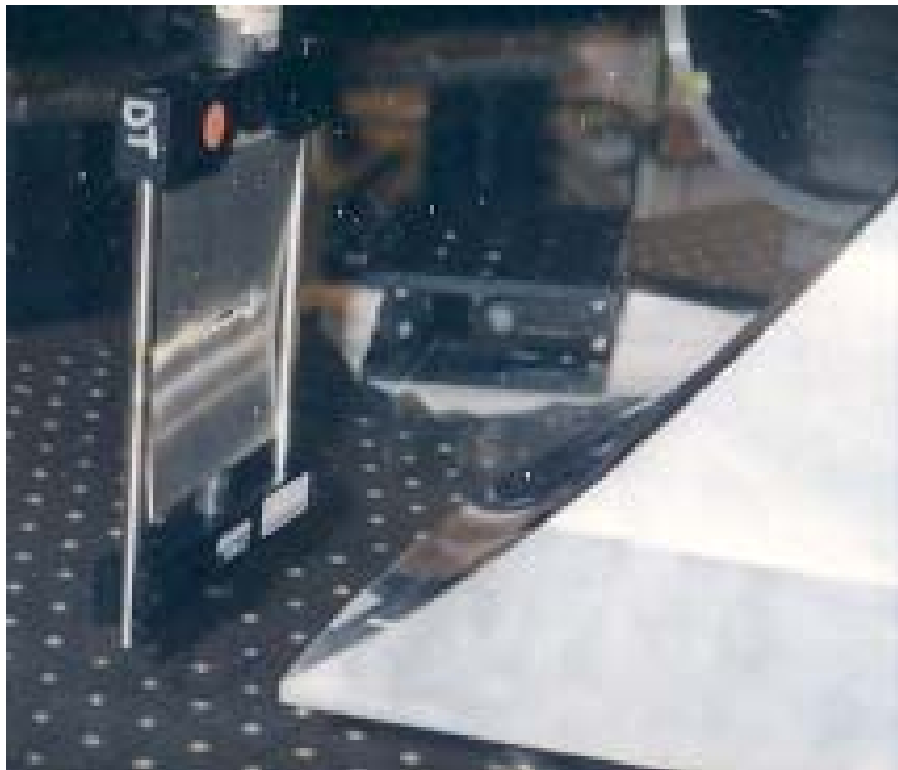


Fig. 86. Line Focus Experiments Set-Up with Steel Plate Target

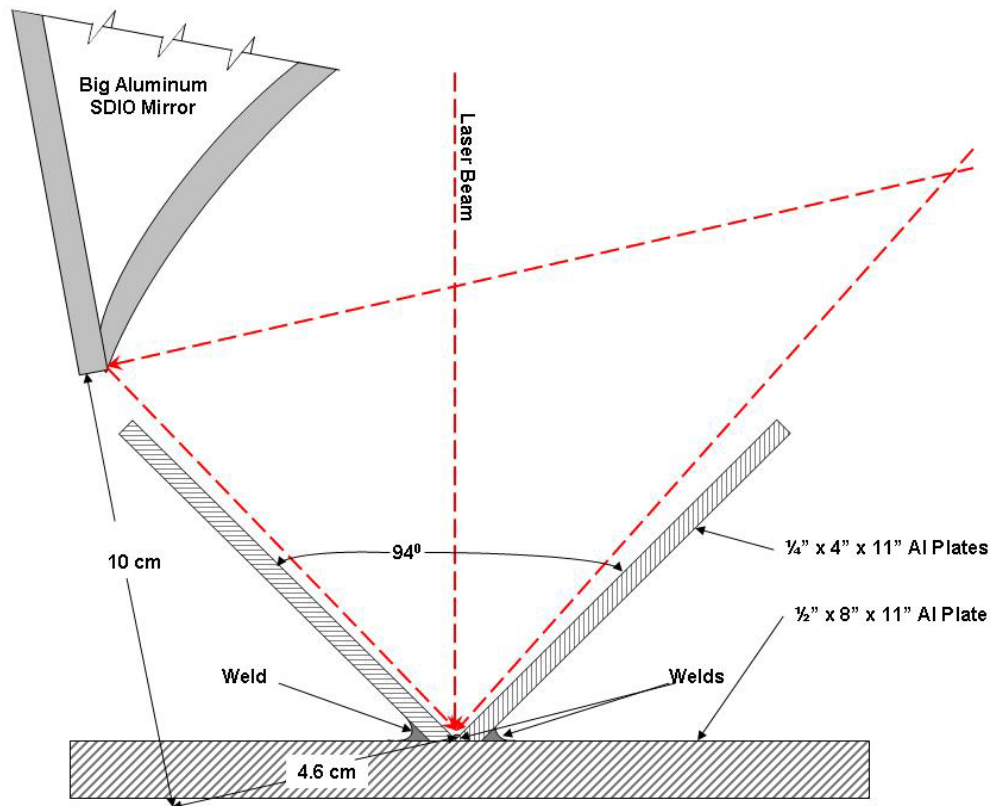


Fig. 87. Shadowgraph Set-Up for Simulated Lightcraft Focus

4.0 LOW SPEED WIND TUNNEL TESTING OF A LASER PROPELLED VEHICLE⁽²⁾

An investigation was conducted to determine the low speed aerodynamic characteristics of a 9-in. diameter laser Lightcraft. The vehicle rotational velocity and deflection angle were varied to determine the effects on the Lightcraft's aerodynamic performance. For the case of zero deflection angles, it was observed that the rotational velocity had no effect on the aerodynamic coefficients, with the drag coefficient remaining constant at 0.51. However, the aerodynamic center appeared to move aft when the model was rotated at higher velocities. For a yaw angle of 25° the lift and drag coefficients remained constant at 0.0 and 0.60, respectively, while the effects of rotation manifested themselves in the side force coefficient.

The present study was undertaken to determine the aerodynamic qualities of the LTD as a function of the free stream velocity, rotational velocity, and deflection angle. More specifically, the lift, drag, and side force coefficients in addition to the aerodynamic center, were examined. Results from this investigation can serve a variety of purposes. Measured forces can be compared to numerical solutions to validate possible computa-

tional codes. The coefficients are useful for determining which aspects of the Lightcraft require improvement, while the derivatives of the coefficients are necessary to perform flight dynamic stability and control calculations of the LTD.

The study was conducted in the RPI 4-ft. x 6-ft. Low Speed Wind Tunnel {LSWT} with a 9-in. focal diameter version of the LTD geometry. Aerodynamic forces on the Lightcraft were measured using the yoke balance system, which was fitted with six load cells. A thermocouple, pressure sensor, and Hall Effect sensor provided free stream temperature, pressure, and rpm data, respectively.

An axisymmetric, rotating model of a laser propelled vehicle was tested in the RPI 4-ft x 6-ft LSWT. In these experiments, the free stream velocity, rotational velocity, and yaw angle were varied. Aerodynamic characteristics of the 9-in. diameter Lightcraft were studied as a function of these three variables. Initial findings indicated that at a deflection angle of 0° , lift, drag and side force are unaffected by the rotational velocity. The calculation of the aerodynamic center indicated a location aft of the center of gravity, approximately 9 in. from the nose. This would correspond to a point very near the rearmost edge of the craft, which has a length-to-diameter (L/D) ratio of nearly 1.0. Hence, the result was questionable, and further study is warranted to resolve this issue.

For the 25° displacement case, the lift and drag were found to be independent of rotational velocity. Although a slight dependence was expected, its magnitude, if any, would not be measurable due to the sensitivity of the system. Plots of the side force coefficient indicate some dependency on the rotational velocity, increasing by 30 percent for the 2,200 rpm case. This effect is commonly referred to as the Magnus Effect.

The study provided the required low speed aerodynamic data for the Lightcraft. It also exposed some areas which need to be investigated further. The results indicated that the model had not been completely isolated from the support system. In low speed wind tunnel testing, this is a difficult and frequently encountered problem. Note that RPI's LSWT balance system was equipped with a yoke both above and below the test section, which would allow the model to be mounted both upright and inverted. After averaging the two results, the effect of the support should be greatly reduced. Future experiments would not only verify the results of this study, but also provide data for the large range of deflection angles in between the two conditions studied (i.e., 0 and 25°). This would determine what type of impact the Magnus effect has with respect to angle of yaw. A pressure survey of the model would reveal further information pertaining to the separation regions and their relative sizes, as well as an estimate of possible wall effects in the test section. This data could also be used to validate computational methods. The computational solutions, once validated, can provide a more detailed description of the flow structure for several different cases. A simple smoke generator could provide flow visualization, and additional 3-D data for validating computational fluid dynamics (CFD) code predictions.

The results of this investigation served as input coefficients for a flight simulation code to predict the flight dynamics and control, and stability characteristics of the Lightcraft. For a complete study it is necessary to test the model at yaw angles of 0 to 180° , since on the return to earth, the vehicle is basically flying backwards. To accomplish this expanded study of Lightcraft aerodynamics, a new model and support system is required.

Finally, it was strongly recommended that the fore and aft aeroshells of future models be more robust than the current, which are 0.015- and 0.010-inches thick. Just the opposite is true for the cowl section; since this was the first rotating model tested in the RPI tunnel, it was initially advised that this section be rather sturdy. For future studies, somewhat thinner cowl sections should be acceptable.

5.0 FLIGHTS OF A LASER-POWERED LIGHTCRAFT DURING LASER BEAM HAND-OFF EXPERIMENTS⁽²⁵⁾

The objective of the laser beam "hand-off" technique was to extend laser Lightcraft flights to significantly higher altitudes in the range of 150 to 300 m. The hand-off technique is the method by which the laser light beam is transferred to consecutively larger telescopes during a Lightcraft launch. In other words, the laser light is initially directed through a small diameter telescope at the start of the launch. Then, as the Lightcraft speeds to higher and higher altitudes, the laser light is suddenly shifted, at a prearranged altitude, to a larger diameter telescope. This larger telescope allows the beam to be appropriately focused at the higher altitudes. This is a tricky maneuver and requires practice and development.

During the current single hand-off experiments, it was expected that the Lightcraft would achieve altitudes on the order 305 m using the 10 kW PLVTS laser. These tests, if successful, would then provide enhanced promise of achieving the 30 km altitude with a larger 100 kW class laser at some point in the future. Testing to these extreme altitudes also requires NORAD clearance and coordination with WSMR flight and safety groups.

A step-by-step plan to accomplish the laser hand-off tests was conceived. First, it was necessary to develop several new pieces of equipment (i.e., a new laser launch stand and an improved pendulum impulse test stand). Ceramic composite shrouds also had to be purchased for the flights, which were expected to last for 30 s or more, because even with the Delrin® propellant insert,^(3,4) it was expected that that aluminum shrouds would fail prematurely. Then, the laser beam characteristics were to be measured as a function of distance (lab bench, 100, 250, 500, 1,000, and 1,500 ft) using a van with an optical bench to measure field energy distribution as a function of pulse width, PRF, resonator magnification, and telescope magnification. At these distances while the laser was being characterized, single pulse tests to measure coupling coefficient (CC) using the aluminum Model #200-3/4 SAR Lightcraft were to be accomplished. Once the beam and Lightcraft performance had been characterized, then short-duration free flight tests would be conducted to validate range and telescope apertures required for the extended altitude free flight demonstration. These tests would also be used to perfect the laser hand-off technique. Finally, with clearance from NORAD and support from the proper WSMR range and safety groups, free vertical flight tests and laser hand-off experiments would be conducted to extreme altitudes using the most promising Lightcraft configurations and range conditions.

The laser single pulse energy was varied from about 50 to 450 J/pulse in desired increments within the laboratory. Typically, the energy is initially set and measured at each desired energy level using a salt window to deflect a small portion of the beam into

a calibrated calorimeter prior to firing on the Lightcraft. At each energy level, five data points are typically taken. Additional data points may be taken if inconsistencies are noted!

Tests of performance with the FTT were made at distances of 475 ft, 998 ft, 1,506 ft, and 1,750 ft. Preliminary analyses of these data indicated that flights through the range of 145 m to 300 m would be difficult because the focused beam was very small and the Lightcraft does not perform well under this condition. Improved performance in the FTT far field beam could only be achieved by defocusing the beam. This was considered to be necessary in order to conduct flights to altitudes of 1,000 ft.

Short duration flight tests were deemed necessary to find out if the Lightcraft would still be self-centering (i.e., a beam rider) in the far field. Because of the change of the beam shape in the far field, it was not known *a priori* whether the Lightcraft would remain a beam rider. Thus, it was imperative to conduct short duration vertical tests in the far field to check for this condition and to practice the laser hand-off technique under controlled conditions. These tests were conducted in the 500-Meter Building on the HELSTF laser test range at a distance of 533 m. This building faces the PLVTS laser facility and has large sliding doors which, when open, provide sufficient space for the laser beam to enter, hit a turning mirror and then the Lightcraft and its launcher, which were mounted on a table with a square hole in the center. Four vertical free flights were conducted of not more than 1 s duration to avoid hitting the ceiling and damaging the Lightcraft. Severe problems with beam jitter caused by time varying thermal variations in the air through which the beam traveled were evident during alignment and testing. Also, the beam wanted to slide off target during multiple pulses, which was probably caused by a loose mirror somewhere in the FTT mirror train. All four launch tests were successful to some degree. The best flight showed the Lightcraft climbing to a little under a meter above the launch stand. All flights exhibited beam rider capability, and none were ejected from the beam. In fact, the Lightcraft actually seemed to try to follow the beam as it moved during the flights.

6.0 REVIEW OF RECENT PROGRESS DURING LASER-POWERED LIGHTCRAFT FLIGHTS TO UNLIMITED ALTITUDES⁽²⁶⁾

Measurements of the CC for the laser Lightcraft in both the near and far fields of the PLVTS laser with a small telescope and the 50 cm FTT were completed incrementally over a horizontal distance of 533 m (1,750 ft). Preliminary analysis of the data indicated that the Lightcraft should be able to fly vertically to this altitude, although questions still existed about how it would fare through the 145 m to 300 m altitudes. The process of establishing the procedures to conduct vertical flights to unlimited altitudes with NORAD and WSMR clearances were in place and the first unrestricted vertical free flights were conducted in October 2000, to a maximum altitude of 41 m. Within the next several months, it was expected that vertical flights might set new altitude records of greater than 500 m. Although there were many issues left to address before proceeding beyond the current 30 Hz/10 kW limitation of the PLVTS, the tuning of the laser parameters would continue to provide the wider envelope performance required to understand the full

potential of the laser propulsion vehicle performance. In the near term, it was expected that improving the laser gas flow would allow higher average power operation at the shorter pulse widths. Beyond that, we hoped to examine increasing the power supply throughput in order to increase the average power capability of the laser. The program was entering into a test phase in which measurements would establish an optimal telescope aperture transition range. This phase of the Lightcraft Flight Experiment testing (see Fig. 88) will require a fusion of vehicle operating parameters with laser propagation characteristics. As the vehicle is propelled skyward, the launching telescope aperture must be increased to maintain the proper sized far field profile on the vehicle. As this program tends to be quite dynamic in nature, we have not yet seen a limit to the coupling of the laser propelled vehicle and the PLVTS laser device.



Fig. 88. Lightcraft Flight Experiment

7.0 LASER-POWERED, VERTICAL FLIGHT EXPERIMENTS AT THE HLSTF⁽²⁷⁾

7.1 Theoretical Studies

NASA's Marshall Space Flight Center has developed a CFD model of the Lightcraft using air as a propellant. This model has been used to predict performance over a wide range of conditions, including altitude. At the AFRL, theoretical analysis of the overall energy conversion of a Lightcraft propelled by laser-heated air has been accomplished and presented, based upon the Lightcraft geometry that incorporates an inverted parabolic reflector that focuses laser energy into a torus-shaped volume where it is absorbed by a unit of propellant mass that is subsequently expanded in the geometry of a aerospike-type plug nozzle. Figure 89 shows a transformation of the

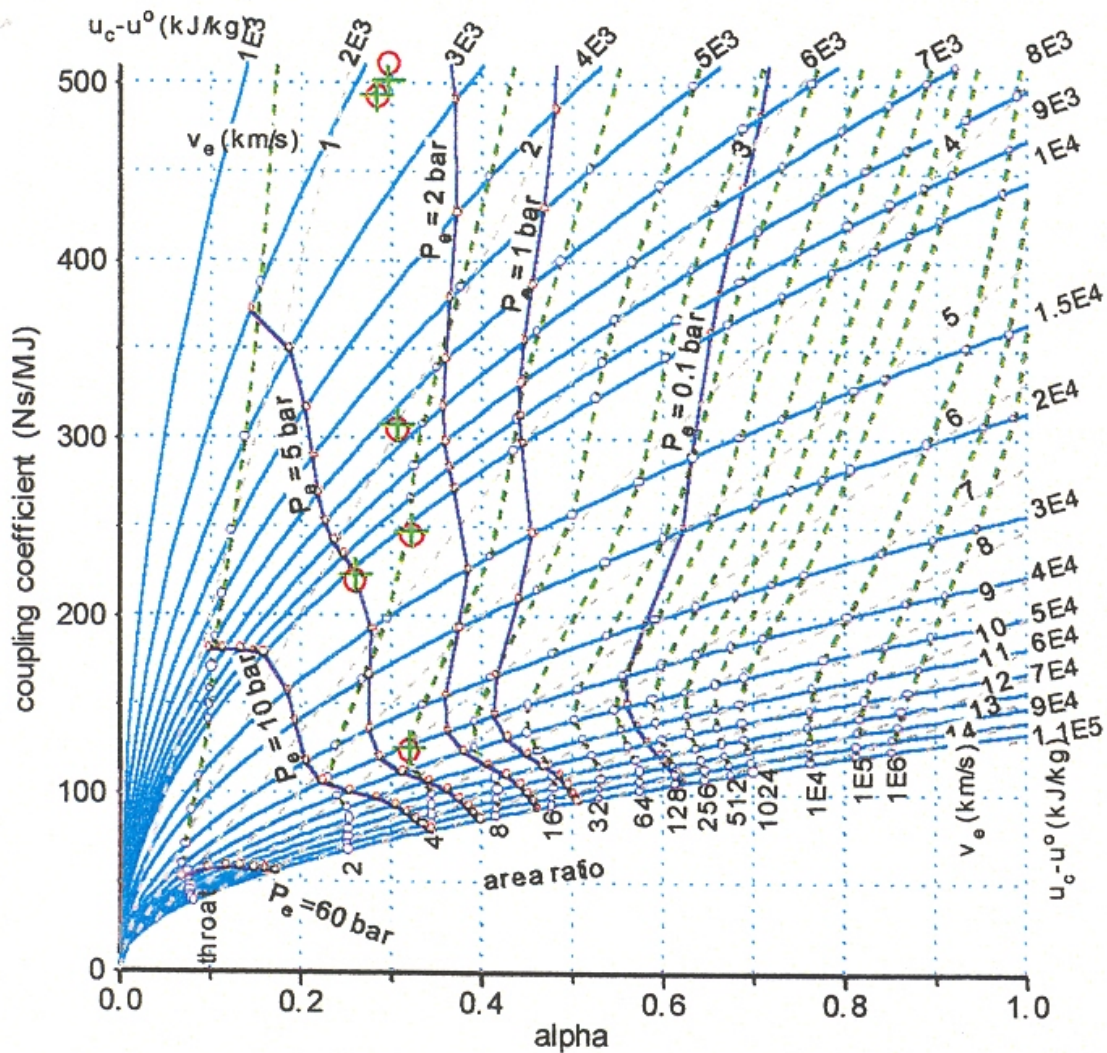


Fig. 89. Thermodynamic Characteristics of Air

chemical equilibrium Mollier diagram for air up to 24,000 K. Figure 89 is based on the database maintained at NASA's Glenn Research Center, which is certified accurate up to 20,000 K and is based upon extended 9-parameter fits to enthalpy, heat capacity, and entropy of neutral species and singly charged ions. Above 20,000 K, doubly charged ions begin to contribute, but these are not included in the database.

Figure 89 also shows a series of vertical lines which are representations of equilibrium isentropic expansions that originate from initial states located along the constant density line, $\rho = 1.18 \text{ kg/m}^3$, and specific internal energies ranging from 1 to 100 MJ/kg. Since the entropy of the initial and final states is equal, the thermodynamic state of the propellant in the exit surface is uniquely defined when only one additional property in the exit surface is specified, such as the exit pressure or the expansion ratio, δ , which is the ratio of the area of the exit surface to the area of the sonic surface or nozzle throat.

The analysis of experimental results showed that the 10-cm Lightcraft converted $\sim 25\%$ of the incident laser energy to propellant kinetic energy: $\alpha \approx 0.25$. The upper limit to α was obtained from thermodynamic analysis of the conversion of propellant internal energy to propellant kinetic energy when air at a specified internal energy and density undergoes optimum blow-down expansion to 1 bar ambient pressure. The equation of state of the partially ionized propellant under conditions of chemical equilibrium is captured in the analysis. For laser-heated air at STP density (1.18 kg/m^3), the upper limit α varies from 0.33 to 0.30 as the internal energy decreases from 100 to 1 MJ/kg ($\sim 24,000$ to $\sim 2,000$ K) when chemical equilibrium is maintained during blow-down expansion. For frozen composition expansion using the initial composition, the upper limit of α ranges from 0.25 to 0.27 as the internal energy varies from 100 to 1 MJ/kg. For laser heated air at the Mach 5 stagnation density (5.90 kg/m^3) these values increase by $\sim 15\%$.

7.2 German Collaboration^(28,29,30)

At the end of 1998, the Institute of Technical Physics of the German Aerospace Center began some basic investigations of a simple lightcraft configuration, and wire-guided flights and pendulum measurements of the impulse coupling coefficients were conducted in the laboratory.⁽³³⁾ The lightcraft was made of a thin Aluminum sheet drawn over a paraboloid, and had a diameter of 10 cm and a height of 62.5 cm. The focal distance from the apex is 1 cm. The inner surface was polished for better reflectance. The mass of the shell without any modification was 17 g and was increased by 5g when a thin tube was added for sliding on a wire. Tests of the lightcraft utilized the DLR multi-spectral laser, operating with CO_2 gas at a wavelength of 10.6 microns. Performance results of the lightcraft were presented at the SPIE's International Symposium on High-Power Laser Ablation in Santa Fe, NM in 2000.⁽²⁸⁾ In Sep 2000, the AFRL initiated an experimental program through the European Office of Aerospace Research and Development (EOARD) with the Institute of Technical Physics, Stuttgart, Germany.⁽²⁹⁾

Due to the differences in the experimental setup and the reported coupling coefficients, it was in our common interest to directly compare the performance. Arrangements were made to demonstrate the AFRL experimental procedures and pendulum impulse test stand with the Lightcraft for the Germans at HELSTF. This was done in Oct 2000. The same experimental equipment (including the Lightcraft) that had

been used for the demonstration was then packaged and sent to Stuttgart with the data so that the Germans could duplicate the HELSTF tests and note any differences that might be attributable to their laser. To accomplish this, coupling coefficient measurements were performed in air and with Delrin® ablative propellant using both stable and unstable laser modes. With the beam from the stable resonator, achievable pulse energies were limited to about 310 J due to physical size limits. The unstable resonator allowed pulse energies up to 410 J. All tests were conducted in ambient air.

The results showed that the two pendulums did not give the same results. This could be accounted for through dynamic and structural analysis. It is believed that the geometrical factors with respect to the prevailing, mass dependent physical pendulum length are the source for an error in the measurement with the AFRL pendulum. The variation in performance of the AFRL Lightcraft varied less than 6%, independent of resonator type and operation with or without Delrin®. In contrast, the variations of the German lightcraft performance were in excess of 10%. The data obtained with the stable resonator in the tight focus mode most closely agrees with the published Lightcraft performance. Improved performance was obtained with the unstable resonator.

Several other striking differences were noted. The AFRL Lightcraft with its toroidal shape showed different and stronger dependencies on the pulse energy compared to the German lightcraft with its parabolic shape. The performance of the AFRL Lightcraft with air as the propellant was poor when compared to the German lightcraft. With Delrin® in the AFRL Lightcraft, the two concepts performed comparably at moderate pulse energies; but at sufficiently high pulse energies the AFRL Lightcraft clearly outperformed the German lightcraft.

7.3 Testing at White Sands Missile Range

The objective of the current Phase II vertical flight test program was to extend Lightcraft vertical free flights to significantly higher altitudes. Using the available 10 kW, PLVTS, CO₂ electric discharge laser at the HELSTF, WSMR, NM, the vertical flight test program was attempting vertical free-flights to altitudes in the range of 150 to 500 m with the 1/10th-scale model (200-3/4th SAR) Lightcraft. Figure 90 illustrates with an artist's conception the model that was used for testing with the fuel shown inside the shroud.

This figure shows the laser light from the lower left impinging on the parabolic surface and being focused in a circular ring on the inside of the shroud where the intensity is sufficient to form a high temperature, high pressure plasma which expands out the back to provide thrust for each pulse of the laser. As illustrated, the inside of the vehicle is hollow. The total weight is about 30 g.

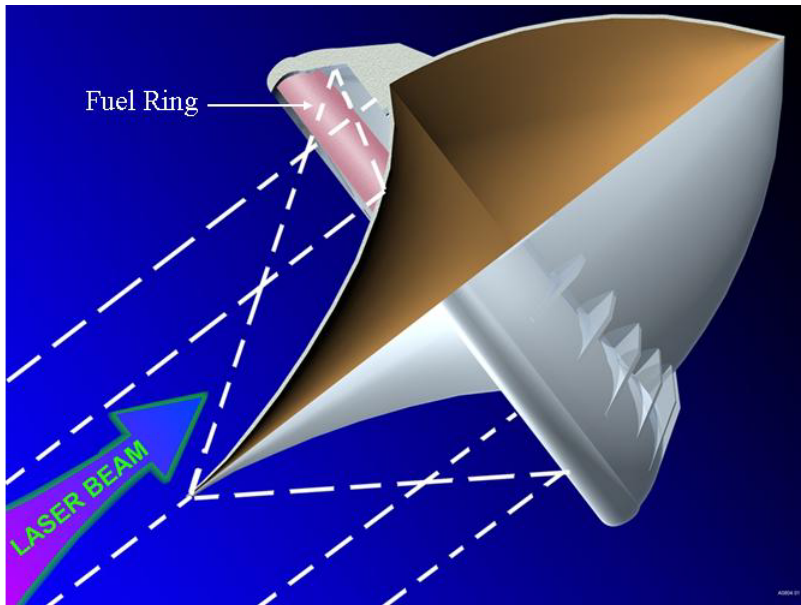


Fig. 90. Artist's Cutaway Lightcraft Drawing

For these flights, the laser is usually operated at 25 pulses per second with 18 μ s pulse widths. Three different telescopes are used for these flights. The first telescope, the "launch telescope" used for lift-off, is the same telescope that's been used for flight-testing during past flight experiments. The second telescope is a "transition telescope" used to bridge the distance between the effective operational altitudes (distances) of the launch telescope and the 50-cm Field Test Telescope (FTT). In other words, there is an intermediate distance in which neither the launch telescope nor the FTT works well with the Lightcraft. Flight test durations much over three seconds have in the past resulted in the destruction of the Aluminum shroud. One of the beneficial effects of the Delrin® propellant has been to extend the flight time, and thus altitude, because of the cooling effects of the ablation process. But this has always been considered as only an interim approach until high temperature materials can be incorporated into the vehicle construction. The first 1/10th-scale model composite, ceramic shroud was fabricated (see Fig. 91) and tested in the laboratory on the pendulum impulse test stand. This new shroud is comprised of an amorphous SiNC matrix reinforced with a Nicalon™ fiber. It was fabricated by Composite Optics Inc. (COI), San Diego, CA.

Figure 92 illustrates a comparison of performance obtained on the pendulum impulse test stand. The well-established performance of the Aluminum shroud is illustrated by the bottom curve in Figure 92. The upper curve illustrates the performance of the Nicalon™ shroud, which was tested starting at the lowest energy per pulse level, and proceeding, step wise, to the higher energy per pulse levels. This was done because we wanted to establish the upper limit at which this new shroud would survive. As can be seen in Figure 92, the shroud survived to over 400 J. At that point, some separation of the fiber "butt" joint was seen, and the experiments were stopped. The performance at the lower energy levels appears to be high because of initial outgassing. At the higher energy levels, the Aluminum and Nicalon™ performance appears to be essentially the same. We

suspect that if an additional set of tests were conducted after outgassing had been eliminated, the lower energy levels would essentially match the Aluminum curve.

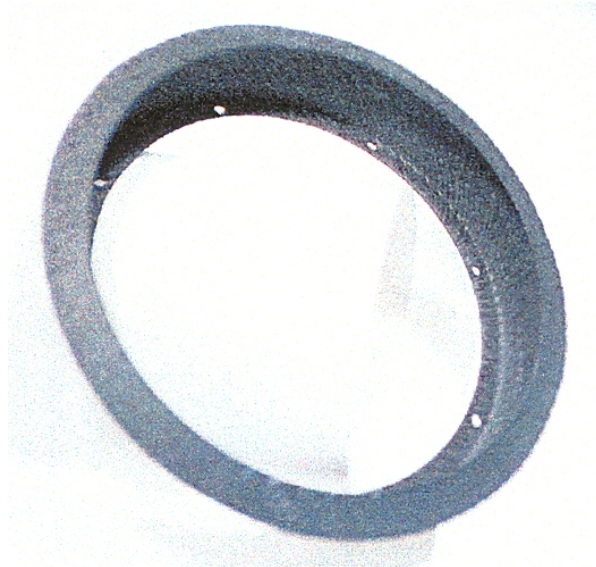


Fig. 91. COI Nicalon™ Shroud

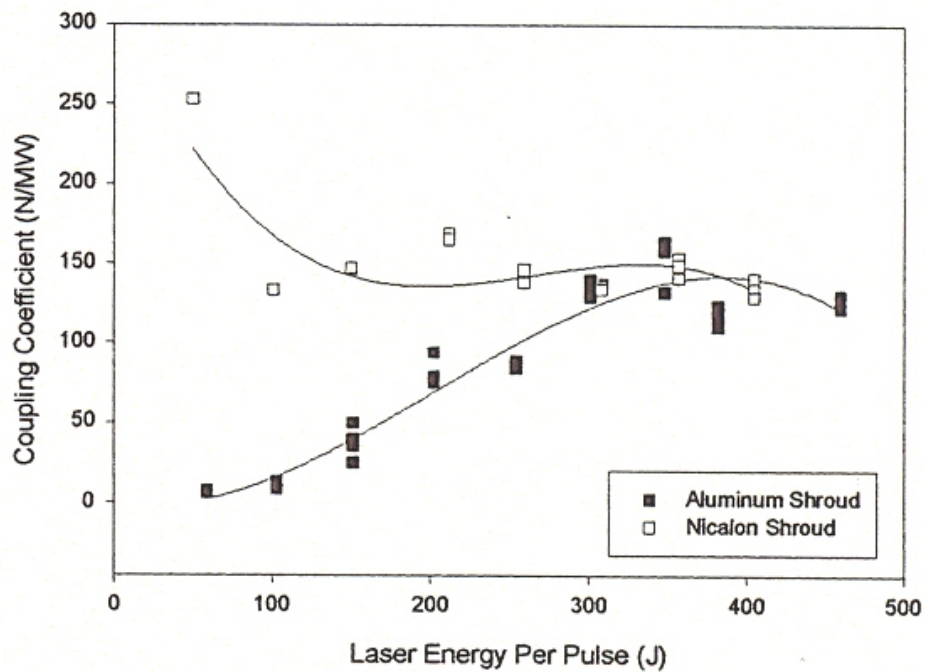


Fig. 92. Comparison of Nicalon™ and Aluminum Shroud Performance

7.4 Laser Beam Propagation Studies

The Air Force Research Laboratory's Propulsion Directorate examined the use of high power CO₂ lasers focused at long ranges through the atmosphere for purposes of high specific impulse propulsion of small payloads into the upper atmosphere and into space. Defense Strategies & Systems Inc, of Great Falls, VA, performed an analysis of propagation of such lasers under varying atmospheric conditions using scenarios of interest for this application.

They examined the performance that could be achieved by pointing and focusing a high power CO₂ laser, operating at an isotopic line near 11.2 microns, into small spot sizes under the range of conditions likely to control achievable intensities. Figure 93 illustrates the parameter selection for this study. Off-zenith angles down to 19° above the horizon were examined for three different variations of atmosphere.

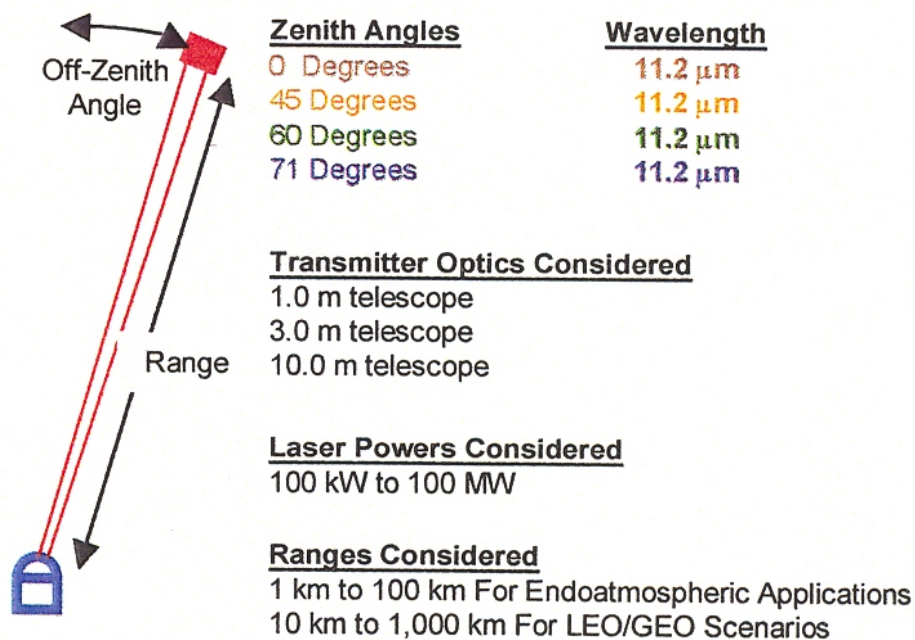


Fig. 93. Lightcraft Beaming Scenario Parameters

Typical weather conditions at WSMR were considered as representative of possible launch conditions. In the study, Condition 1 denotes the best conditions to be experienced routinely; Condition 2 denotes average conditions; and, Condition 3 is for degraded conditions that may be experienced 10% of the time.⁽²⁷⁾ These atmospheric variations differed mainly in the amounts of aerosols present at high altitudes. This analysis included the combined effects of thermal blooming, turbulence, and linear extinction. Thermal blooming is much less of a problem than it would be for the more common version of CO₂ lasers at 10.6 microns. The study also included the effects of laser beam quality, transmitter optics quality, and pointing jitter of the transmitted beam. Figure 94 illustrates the propagation of isotopic CO₂ through the atmosphere under Condition 3. As a reference, the 10-cm Lightcraft reaches an irradiance of 107 W/cm² at a pulse energy of about 608 J.

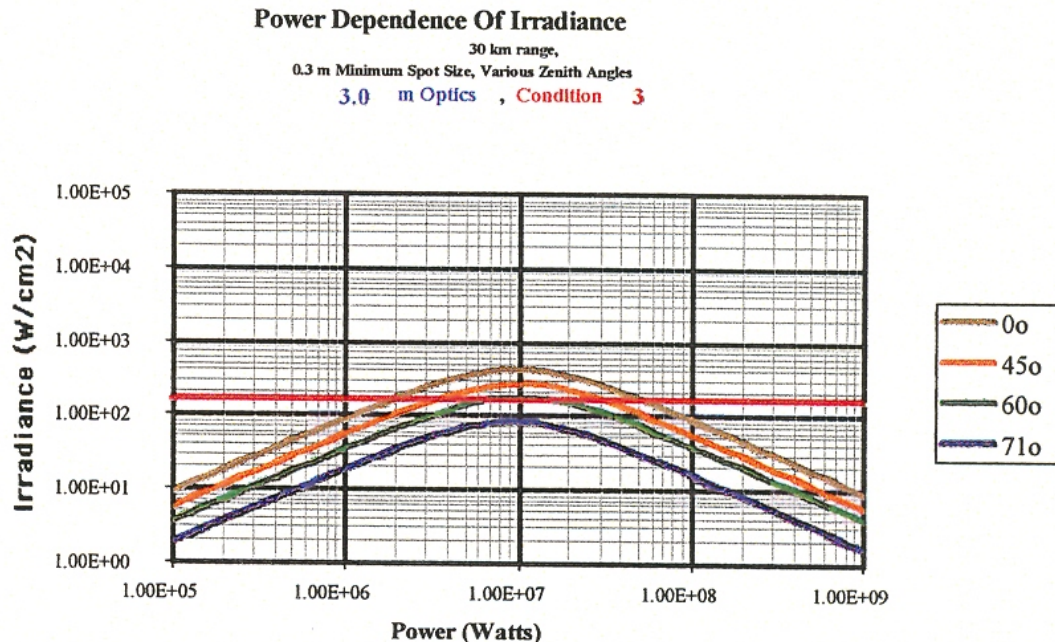


Fig. 94. Power Dependence of Irradiance

The study determined that, under most meteorological conditions, a 3 MW isotopic CO₂ laser coupled with a 3-meter diameter, ground-based beam director can propagate a beam with more than 140 W/cm² to a distance greater than 30 km into the atmosphere without the need for an adaptive optics system. That flux density was taken as the minimum for effective Lightcraft propulsion. They assumed meteorological conditions likely to bracket those that will be experienced at the White Sands Missile Range (WSMR), NM. Detailed data describing those expected conditions were collected.

Using those values and a detailed propagation model they had developed,⁽²⁷⁾ Defense Strategies & System, Inc., calculated the expected irradiance and far field beam diameters as a function of transmitted power, range, beam director diameter and zenith angle, with and without adaptive optics. The zero degree zenith angle has the highest irradiance for a given laser power. At larger zenith angles measured from the vertical, the beam spends more time in the lower atmosphere, suffers more due to thermal blooming and turbulence, and reaches a peak irradiance at lower transmitted laser powers.

The best conditions for Lightcraft propagation will most likely occur during the winter months and during early morning or early evening, when the adiabatic lapse rate changes sign and the turbulence reaches a minimum. The least favorable conditions will most likely occur during the summer months in the middle of the day. But, like weather, both extremes will occur at many other times and seasons.

The study indicates that, even under degraded meteorological conditions, half the transmitted laser energy can be maintained within a 1-meter Lightcraft receiving aperture beyond 30 km for a zenith angle of 0° and beyond 28 km for a zenith angle of 45°. Beam diameters could be controlled to less than 1 m out to 80 km, although that would probably not be justified for this endoatmospheric application.

Low altitude turbulence is the dominant beam spreading mechanism for which the adaptive optics would be required. For long-range propagation out to ranges well beyond

100 km, larger optics, higher power levels, and adaptive optics compensation would be desired. In the case of a high-altitude Lightcraft, the beam diameter would be desired to be not much larger than a meter out to ranges of several hundred kilometers. If a turning mirror or relay mirror were to be used, that mirror would be at 500 km or greater to prevent drag from the upper atmosphere. For this scenario, a beam of less than 10 m would be desired at ranges out to 1,000 km.

7.5 Lateral and Attitude Control Propulsion

In May 2000, the AFRL initiated a Phase I Small Business Innovation Research (SBIR) contract with SY Technology, Inc., in Huntsville, AL, to start the development of a lateral and attitude control system for the Lightcraft. Lateral control is required to keep the vehicle properly positioned in the laser beam throughout its launch into orbit. Attitude control is required to keep the vehicle oriented properly with respect to the beam (i.e., pointed at the GBL). The Phase I goal was to determine the requirements of the control system and then to design the control technologies which meet these requirements. The Phase I control concept was based upon the dimensions of a quarter-scale (25 cm) Lightcraft design.

8.0 COMPUTER MODELING

8.1 Performance Modeling of an Experimental Laser Propelled Lightcraft^(32, 33,34)

A computational plasma aerodynamics model has been developed by NASA to study the performance of laser propelled Lightcraft. The computational methodology was based on a time-accurate, three-dimensional, finite-difference, chemically reacting, unstructured grid, and pressure-based formulation. The underlying physics were added and tested systematically using a building-block approach. The physics included in the model were non-equilibrium thermodynamics, non-equilibrium air-plasma finite-rate kinetics, specular ray tracing, laser beam energy absorption and refraction by the plasma, non-equilibrium plasma radiation, and plasma resonance. The simulated physics are discussed and compared with those of *tests* and literature.

A series of transient computations were performed for average laser pulse energies of 75, 100, 150, 200, 300, and 400 J for Model #200-3/4, and 400, 600, and 800 J for Model A. Maximum computed temperatures ranging from 51,000 to 60,000 K fall within the computed post-shock temperatures of 20,000 to 60,000 K. LSD occurs in all cases with maximum Mach number reaching 2.8. Laser sustained combustion (LSC) then ensues as the plasma front expands, and the Mach number decreases to subsonic value. The predicted coupling coefficients for the Lightcraft compared reasonably well with those of tests conducted on a pendulum apparatus.

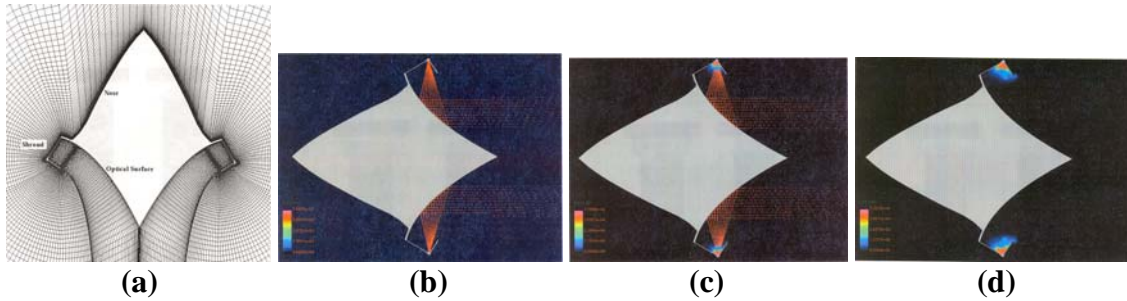


Fig. 95. Layout of Computational Grid (a), Computed Temperature Contours and Laser Ray Traces at 0.5 μ s, 10 μ s, and 20 μ s for (b), (c), and (d), Respectively

Figure 95a shows the layout of a computational grid. Only half of the grid shown in Figure 95a is actually solved due to the axisymmetric formulation. Figure 95b shows the computed temperature contours and laser beam traces at an elapsed time of 0.5 μ s and an average laser pulse energy of 400 J. Figure 95c shows the temperature contours at an elapsed time of 10 μ s where the optical breakdown is being fed by the laser energy and the plasma front grows. Figure 95d shows the temperature contours at an elapsed time of 20 μ s, and the laser beam is turned off since the pulse width is fixed at 18 μ s. Thus, the shock wave is not being maintained by the laser.

Figure 96 shows a comparison of model predicted and experimental measured coupling coefficients.

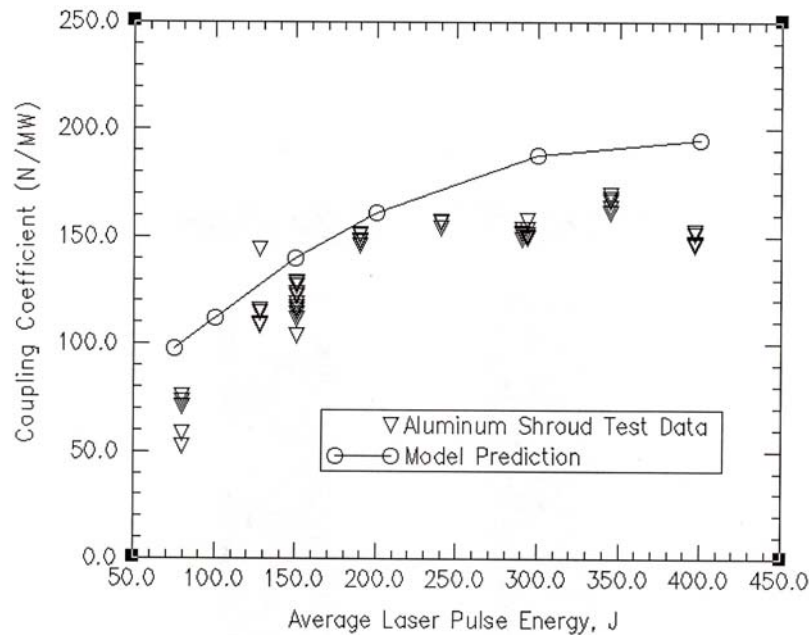


Fig. 96. A Comparison Between Theoretical and Measured Coupling Coefficients

8.2 Analysis of the Effect of Pulse Width on Laser Lightcraft Performance⁽³⁵⁾

A transient computational plasma aerodynamics analysis was performed to compare the coupling coefficients of a laser Lightcraft generated at several laser pulse widths. The computational methodology was based on a time-accurate, multi-dimensional, finite-difference, chemically reacting, unstructured grid, pressure-based formulation. The underlying physics model includes high-temperature thermodynamics, non-equilibrium air-plasma finite-rate kinetics, specular ray tracing, laser beam energy absorption and refraction by plasma, and plasma resonance. The optical breakdown of air at the focal point of the laser Lightcraft Model #200-3/4 by a 10 kW CO₂ laser during the impulse experiment was simulated. The results indicated that pulse width is an important parameter in determining the performance.

A series of computations were performed for average laser pulse energies of 75, 100, 150, 200, 300 and 400 J at pulse widths of 50, 30, 18, 10 and 1 μ s for Model #200-3/4. Electron temperature contours were computed at an elapsed time of 100 μ s for 400 J of laser pulse energy and 18 μ s pulse width (See Fig 97).

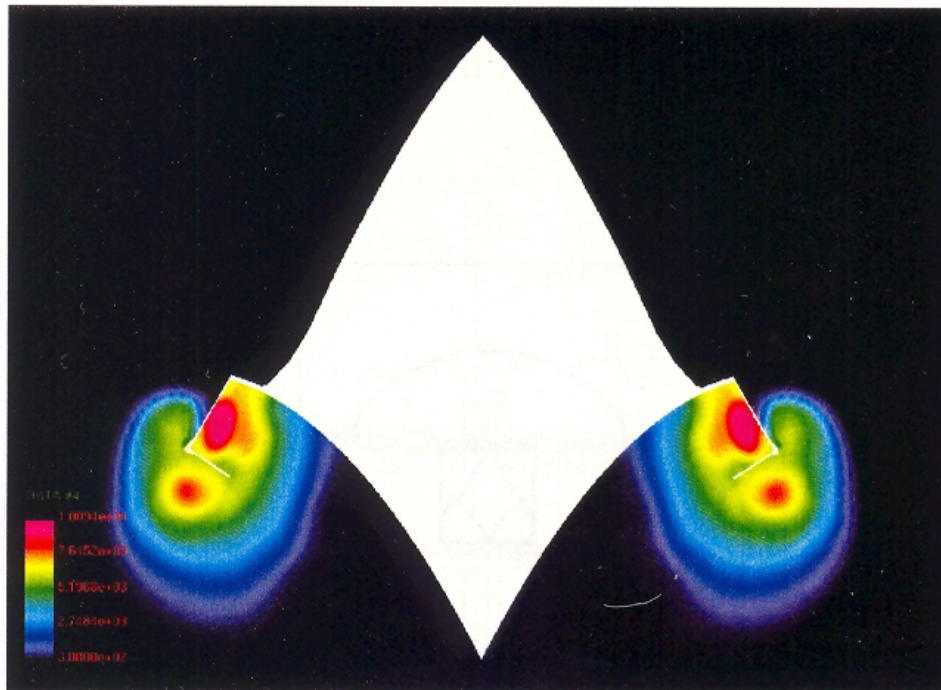


Fig. 97. Computed Electron Temperature Contours for Laser Lightcraft Model #200-3/4 at 100 μ s Elapsed Time for 400 J of Laser Energy and 18 μ s Pulse Width

By this time, the pressure wave has just passed the tip of the aerospike and finished propelling the Lightcraft. The temperature contours represent the decoupled plasma wrapping around the shroud to finish the motion caused by a single optical detonation.

Maximum Mach numbers, maximum electron number densities, maximum electron temperatures, and maximum pressures were also computed versus elapsed time for a laser

pulse energy of 200 J. These time-varying maximum scalar profiles provide an efficient way of detecting the underlying laser pulse width associated physics, and are obtained by performing scalar searches throughout the entire computational domain, at the end of each computational step. The calculations also indicated that shorter pulse width cases pack more energy in a shorter time, thereby generating higher electron number densities and peaking at shorter times. Calculations showed that as the pressure wave leaves the Lightcraft, the air in the thrusting surface area evacuates and the local pressure drops. Once the pressure wave completely leaves the area and its evacuating effect diminishes, the depleted air mass is replenished from the surrounding air and the pressure returns to that of the ambient. The difference between the lowest integrated mass during the air evacuation and the starting mass is the mass displacement caused by the laser heating and may be used as an indicator of the efficiency of laser heating.

It can be seen that the shorter the pulse width, the stronger the shock strength, thereby the larger the air displacement. Through a comparison of the coupling coefficients at various pulse widths, it was seen that in general the coupling coefficients are gradually higher for shortening pulse widths from 50, 30, to 18 μs . However, the 50 μs case did not ignite until 200 J and the 30 μs case did not ignite until 150 J. The 10 μs case gives slightly higher coupling coefficients than those of the 18 μs case. For non-ignition cases in 50 and 30 μs pulse widths, the incident laser energy intensity is probably insufficient to cause ignition. At 10 μs pulse width, plasma resonance probably prevented some electrons in the plasma front to fully absorb the laser energy. At 1 μs pulse width, the plasma was not ignited until at 150 J of laser pulse energy. Even at 150 J, the coupling coefficient was lower than those of 30, 18, and 10 μs pulse widths. This is probably caused by a combination of plasma resonance and a very short time of laser heating. The result indicated that the notion of packing the laser energy into shorter pulses does increase the performance but is complicated by the pulse width physics of plasma resonance and heating time. The pulse width is therefore an important parameter in determining optimal Laser Lightcraft design and operating conditions.

8.3 Thermophysics Characterization of Multiply Ionized Air Plasma Absorption of Laser Radiation^(36,37)

Thermodynamic functions (and curve fits) generated in this study for multiply ionized ions, atoms, and molecules were used as a database for a series of constant pressure (one atmosphere) and temperature, thermal equilibrium computations, in order to obtain the necessary compositions of electrons, ions, atoms and molecules for laser absorption coefficient calculations. In the pressure and temperature ranges of interest, chemical equilibrium was assumed to be a reasonable assumption after the initial breakdown. Minimization of free energy of a thermochemical system was used as the algorithm for achieving the equilibrium state. Starting with the air plasma single ionization species, the temperature was allowed to increase, such that the molecules disappear quickly and atoms emerge. And then atoms disappear, while electrons and ions (N^+ and O^+) rise; eventually, the species concentrations of electrons and ions level off at about 32,000 K. The final electron mole fraction of 0.5 is the result of single ionization. In the plasma, the concentrations of NO^+ , N_2^+ , and O_2^+ were found to be negligible.

The impact of multiple ionization of air plasma on the inverse Bremsstrahlung absorption of laser radiation was investigated for air breathing laser propulsion. Thermochemical properties of multiply ionized air plasma species are computed for temperatures up to 200,000 K, using the hydrogenic approximation of the electronic partition function; and those for neutral air molecules are also updated for temperatures up to 50,000 K, using available literature data. Three formulas for absorption were calculated, and a general formula was recommended for the multiple ionization absorption calculation. The plasma composition required for absorption calculation is obtained by increasing the degree of ionization sequentially, up to quadruple ionization, with a series of thermal equilibrium computations. The calculated second ionization absorption coefficient agrees reasonably well with that of available data. The importance of multiple ionization modeling is demonstrated with the finding that area under the quadruple ionization curve of absorption is found to be twice that of single ionization. The effort of this work is beneficial to the computational plasma aerodynamics modeling of laser Lightcraft performance.

At low temperatures, the calculated absorption coefficient was extremely low and rose sharply with increasing temperature starting around 8,000 to about 20,000 K. where the absorption coefficient passed through a maximum. The calculated absorption then dropped monotonically from the maximum as the system reached full single ionization, eventually nearing zero value around 80,000 K. However the main interest is at lower temperatures where the electron-atom, and electron-molecular inverse Bremsstrahlung absorptions should show some contribution, but none was observed; indicating the free-free inverse Bremsstrahlung absorption is indeed the main absorption process.

Although only reported to 27,000 K, the importance of second ionization was evident because the single ionization formulas under-predicted the absorption coefficient at high temperatures where double ionization occurs. This has strong implications for laser Lightcraft performance computations using computational plasma aerodynamics. The implication of double ionization also implies the potential importance of triple ionization, and finally it was found that the plasma composition required for the absorption coefficient calculation was best obtained by increasing the degree of ionization sequentially, up to quadruple ionization.

In summary, a thermophysics characterization of inverse Bremsstrahlung absorption of laser radiation was performed. Thermo-chemical properties of multiple ionized air plasma species were generated, using a hydrogenic approximation of the electronic partition function; and those for neutral air molecules were also generated using updated literature data. Three formulas for absorption were calculated, and a general formula was recommended for multiple ionization absorption calculations. A series of thermal equilibrium computations were performed to show the effect of multiple ionization on the free electron concentration and on the inverse Bremsstrahlung absorption coefficient. The calculated second ionization absorption coefficient agreed reasonably well with available literature data. In addition, it was found that the area under the quadruple ionization curve of absorption was about twice that of the single ionization. The result of this study can be applied to the computational plasma aerodynamics modeling of laser propulsion physics.

9.0 SUMMARY

The Lightcraft Technology Demonstration Program (LTD) report covers the development of laser propulsion at the Air Force Research Laboratory (AFRL) between 1996 and 1999. The LTD Program was originally planned in five phases. Phase I, Lightcraft Concept Demonstration, was to demonstrate the feasibility of the basic concept. This phase ended in December 98. Phase II, Lightcraft Vertical Launches to Extreme Altitudes, was a five-year effort designed to extend Lightcraft flights in sounding rocket trajectories to 30 km with a 100 kW pulsed CO₂ laser. Phase III, Lightcraft Dual Mode Vehicle, was planned as a two-year effort designed to launch the first laser-propelled vehicle, a functional Lightcraft, into space. Phase IV was to be a far-term effort, to be conducted over the next 10 to 15 years, to develop a launch capability for Lightcraft weighing 100 kg and costing less than \$1.5M to build and launch.

Under Phase I, performance was measured with an impulse pendulum and piezoelectric thrust stand, shadowgraph and beam propagation (to 90 m) studies were accomplished; a pointing and tracking system was developed and demonstrated on horizontal wire-guided flights outdoors to 122 m, and outdoor vertical free-flights approaching 30 m were successfully conducted.⁽¹⁾ Low Mach number wind tunnel tests were also accomplished with a 23-cm diameter model, and later reported.⁽²⁾ The basic conclusion of all this work was that the feasibility and basic physics of the Lightcraft concept had been adequately demonstrated, but that a much larger, 100 kW class pulsed laser would be required to completely accomplish Phase II.

Phase II, initiated in January 1998, continued with the performance characterization of several #200 series models.⁽¹⁾ The #200 series consists of a number of different sized vehicles all scaled to the same optical f-number. These models exhibit stability and self-centering in the near-field laser beam. This natural self-centering capability, termed as beam riding, turned out to be inherent in the conceptual design, and was not fully appreciated until after the completion of the LTD Program. Outdoor vertical free flights with the Model #200-3/4 Solid Ablative Rocket (SAR) impacted the plywood beam dump at about 40 m in Jul 99. The final vertical velocity at the end of these flights was so great that the nose (i.e., the forebody) was severely dented while the optic (afterbody) and shroud remained in good condition without visual damage.

These Lightcraft were called rockets because a solid ablative propellant ring made of Delrin® had been added at the internal extremity of the shroud. Delrin® is a solid form of formaldehyde that was selected because of its physical properties and performance under laser ablation tests performed in the 1980s.^(3,4) The addition of a propellant increased the coupling coefficient (CC) by a factor of 4 or 5 over that of plain air, and eliminated significant heat damage to the shroud and optic. Thus, addition of an ablative propellant demonstrated that overheating of the shroud and thermal stall could be postponed significantly beyond the 3 to 4 seconds previously noted,⁽¹⁾ while adding a significant increase in thrust performance.

With the extended lifetime and enhanced performance demonstrated by the addition of an ablative propellant, it was proposed to develop a laser "hand-off" technique using the Model #200-3/4 SAR vehicle with NASA contributing half the funding for the effort. The hand-off technique is the method by which the laser's light is transferred to consecutively larger telescopes during a Lightcraft launch. In other words, the laser light

is initially directed through a small diameter telescope at the start of the launch and transferred to larger telescopes at pre-selected altitudes during the flight. The goal of these tests was to achieve altitudes on the order of 150 to 500 m.⁽²⁾

The objective of the “Lightcraft Technology Demonstrator (LTD) Program” was initially to conduct, before the end of calendar year 1998, a flight demonstration to a significant altitude. This was to be accomplished by launching a specially designed, ultralight Lightcraft (LC) to an altitude of between 0.6 km (0.38 mi) and 10 km (6.2 mi) using an existing laser at the HELSTF, WSMR, NM. This launch was to demonstrate the viability of laser propulsion for eventual low cost access to space.

All testing was performed at the HELSTF with the PLVTS laser. This laser originally operated with pulse widths of 30 μ s and up to 10 Hz (pulses/s) and 1,000 J per pulse. Additional lasers for alignment and shadowgraph tests were used and are described in the respective text.

For additional information, three unpublished reports are included as **Appendices C, D and E**. These reports summarize the work done on flight dynamics and control of the Lightcraft, scaling of costs for high power lasers, and a conceptual study of a 100 kW CO₂ laser.

10.0 REFERENCES

1. Mead, F.B., Jr., Myrabo, L.N., and Messitt, D.G., “Flight and Ground Tests of a Laser-Boosted Vehicle,” AIAA 98-3735, 34th AIAA/ASME/SAE/ASEE Joint Propulsion Conference & Exhibit, Cleveland OH, 13-15 Jul 1998.
2. Panetta, A.D., et al., “Low Speed Wind Tunnel Testing of a Laser Propelled Vehicle,” #1999-01-5577, SAE International and AIAA 1999 World Aviation Conference, San Francisco CA, 19-21 Oct 1999.
3. Reilly, D.A., “Advanced Propellants for Laser Propulsion,” in *Proc. 1987 SDIO Workshop on Laser Propulsion*, J.T. Kare, ed., LLNL CONF-8710452, LLNL 1990, PP. 145-156.
4. Kare, J.T., “Laser Launch – The Second Wave,” First International Symposium on Beamed Energy Propulsion, , Huntsville AL, 5-7 November 2002, AIP Conference Proceedings, V. 664, Andrew V. Pakhomov – Editor, pp. 22-33.
5. Geisler, Robert L., “Laser Augmented Rocket Propulsion and Auxiliary Power,” Air Force Invention No. 6157, Invention Disclosure, May 69.
6. “Advanced Propulsion Concepts - Project Outgrowth,” AFRPL-TR-72-31, F.B. Mead, Jr., Editor, Air Force Rocket Propulsion Laboratory, Edwards AFB CA, Jun 72, pp. II-53-II-63.
7. Kantrowitz, Arthur, “Propulsion to Orbit by Ground-Based Lasers,” *Astronautics & Aeronautics*, V. 10, No. 5, May 72, pp. 74-76.
8. “Laser Propulsion for Launch to Earth Orbit and Other Applications,” A Proposal for Space and Missile Systems Organization, AERLP 263, AVCO Everett Research Laboratory, Inc., June 1973.

9. Mead, F.B., Jr., "Beamed Energy (Laser) Propulsion – A Perspective," Professional Development Program, Future Flight Propulsion: Advanced Concepts in Rocket Propulsion, Nuclear Systems, Advanced Physics, and High-Energy Density Propellants, AIAA/ASME/SAE/ASEE Joint Propulsion Conf. & Exhibit, Huntsville AL, 20-21 July 00.
10. Keefer, D. et al., "Laser thermal Propulsion," Reprint from *Orbit-Raising and Maneuvering Propulsion: Research Status and Needs*, 84, pp. 129-148.
11. Keefer, D.R., Hendriksen, B.B. and Braerman, W.F., "Experiment Study of a Laser Sustained Air Plasma," BRL MR 2416, USA Ballistic Research Lab., Aberdeen Proving Ground MD, Oct 74.
12. Keefer, D., Jeng, S-M, and Welle, R., "Laser Thermal Propulsion Using Laser Sustained Plasmas," IAF-86-17S, 37th Congress of the International Astronautical Federation, Innsbruck, Austria, 4-11 Oct 86.
13. Rosen, D., et al., "Experimental and theoretical Studies of a Repetitively-Pulsed Laser Powered Thruster," PSI TR-371, AFOSR, Bolling AFB, Washington DC, Mar 84.
14. Rosen, D.I., Kemp, N.H., and Miller, M., "Studies of a Repetitively-Pulsed Laser Powered Thruster," PSI TR-358, Physical Sciences Inc., Woburn MA, Jan 83.
15. Knowles, T.R., "Composite Thruster for Laser-Assisted Propulsion," Interim Presentation for NASA contract NAS3 00136 (STTR Phase 2), Energy Science Laboratories, Inc., 24 Oct 00.
16. "Pulsed Laser Propulsion – A Program Status Presentation to DARPA," Physical Sciences Inc., 1 Aug 80.
17. Myrabo, L.N., "Transatmospheric Laser Propulsion," Final Technical Report, Rensselaer Polytechnic Institute, Prepared under Contract No. 2073803 for Lawrence Livermore National Laboratory and the SDIO Laser Propulsion Program, 30 June 1989.
18. Minucci, M.A.S., "An Experimental Investigation of a 2-D Scramjet Inlet at Flow Mach Numbers of 8 to 25 and Stagnation Temperatures of 800 to 4,100 K," Ph.D. Dissertation, Rensselaer Polytechnic Institute, 1991, pp. 73-74.
19. Mead, F.B., Jr., Myrabo, L.N., and Messitt, D.G., "Flight Experiments and Evolutionary Development of a Laser Propelled, Trans-Atmospheric Vehicle," Space Technology and Applications International Forum (STAIF), Albuquerque NM, 25-29 Jan 1998.
21. Myrabo, L.N., U.S. Patent # 6,488,233, Assignee: The United States of America as represented by the Secretary of the Air Force, 3 Dec 2002.
22. Myrabo, L.N., Messitt, D.G., and Mead, F.B., Jr., "Ground and Flight Tests of a Laser Propelled Vehicle," AIAA 98-1001, 36th Aerospace Sciences Meeting & Exhibit, Reno NV, 12-15 Jan 1998.
23. Mead, F.B., Jr., Myrabo, L.N., Messitt, D.G., "Flight Experiments and Evolutionary Development of a laser-propelled Transatmospheric Vehicle," Proceedings of the SPIE – The International Society for Optical Engineering, v. 3343, pt. 1-2, p. 560-563, Sep. 1998, SPIE High Power Ablation Conference, Santa Fe, NM, 27-30 Apr 1998.
24. Messitt, D.G., Myrabo L.N., & Mead, F.B., Jr., "Laser Initiated Blast Wave for Launch Vehicle Propulsion," AIAA 2000-3848, AIAA/ASME/SAE/ASEE 36th Joint Propulsion Conference, Huntsville AL, 17-19 Jul 2000.

25. Mead, F.B., Jr., Squires, S., Beairsto, C., and Thurston, M., "Flights of a Laser-Powered Lightcraft During Laser Beam Hand-off Experiments," AIAA 2000-3484, 36th AIAA/ASME/SAE/ASEE/ Joint Propulsion Conference and Exhibit, Huntsville AL, 16-19 Jul 2000.
26. Mead, F.B., Jr., and Larson, C.W., "Review of Recent Progress During Laser-Powered Lightcraft Flights to Unlimited Altitudes," International Conference on Lasers 2000, Albuquerque NM, 4-8 Dec 2000.
27. Mead, F.B., Jr., and Larson, C.W., "Laser-Powered, Vertical Flight Experiments at the High energy Laser System Test Facility," AIAA 2001-3661, 37th AIAA/ASME/SAE/ASEE Joint Propulsion Conference and Exhibit, Salt Lake City UT, 8-11 Jul 2001.
28. Schall, W.O. et al., "Lightcraft Experiments in Germany," Deutsches Zentrum für Luftund Raumfahrt e.V. (Germany), Paper # 4065-57, SPIE's International Symposium on High-Power Laser Ablation 2000, Santa Fe NM, 23-28 Apr 2000.
29. Schall, W.O., Eckel, H.-A., and Walther, S., "Lightcraft Impulse Measurements under Vacuum," AFRL-PR-ED-TR-2002-0044, AFRL/AFMC, Edwards AFB CA 93524-7048, Aug 2003.
30. Schall, W.O., et al., "Properties of Laser Ablation Products of Delrin® with CO₂ Laser," Final Report, EOARD Grant No. FA8655-03-1-3061, DLR – German Aerospace Center, Institute of Technical Physics, Pfaffenwaldring 38-40, D-70569 Stuttgart, Germany, May 2004.
32. Wang, T.-S., et al., "Performance Modeling of an Experimental Laser Propelled Lightcraft," AIAA 2000-2347, 31st AIAA Plasmadynamics and Lasers Conference, Denver CO, 19-22 Jun 2000.
33. Wang, T.-S., et al., "Advanced Performance Modeling of Experimental Laser Lightcrafts, AIAA 2001-0648, 39th AIAA Aerospace Sciences Meeting & Exhibit, Reno NV, 8-11 Jan 2001
34. Wang, T.-S., et al., "Advanced Performance Modeling of Experimental Laser Lightcraft," *J. Propulsion And Power*, V. 18, No. 6, Nov-Dec 2002, pp. 1129-1138.
35. Wang, T.-S., Mead, F.B., Jr., and Larson, C.W., "Analysis of the Effect of Pulse Width on Laser Lightcraft Performance," AIAA 2001-3664, 37th AIAA/ASME/SAE/ASEE Joint Propulsion Conference and Exhibit, Salt Lake City UT, 8-11 Jul 2001.
36. Wang, T.-S., and Rhodes, R., "Thermophysics Characterization of Multiply Ionized Air Plasma Absorption of Laser Radiation," AIAA 2002-2203, 33rd AIAA Plasmadynamics and Lasers Conference, Maui HI, 20-23 May 2002.
37. Wang, T.-S., and Rhodes, R., "Thermophysics of Characterization of Multiply Ionized Air Plasma Absorption of Laser Radiation," *J. Thermophysics and Heat Transfer*, V. 17, No. 2, Apr-Jun 2003, pp. 217-224.

Appendix A

High Energy Laser Systems Test Facility



HELSTF Welcome Page

About HELSTF

The High Energy Laser Systems Test Facility (HELSTF) is located at White Sands Missile Range, New Mexico. HELSTF has been managed by the U.S. Army Space and Missile Defense Command (USASMDC) since October 1990. HELSTF is designated as the Department of Defense (DoD) National Test Facility for high energy laser test and evaluation. HELSTF is the home of the Mid Infrared Advanced Chemical Laser (MIRACL), the United States' most powerful laser, which is a CW, megawatt class deuterium-fluoride laser operating in a band from 3.6 to 4.2 microns. In the more than ten years since operations began, HELSTF has supported a broad range of both laser and non-laser related test activities. High energy laser tests have included damage and vulnerability testing for all three uniformed services as well as materials and chemical research for industry and academia.

Non-lasing tests at HELSTF have (among other things) provided NASA a test-bed in the Large Vacuum Chamber (LVC) to test orbital and suborbital devices to verify proper operation prior to launch. Several organizations, including the Ballistic Missile Defense Organization, have used the high energy laser's beam pointing device to collect high quality infrared and visual spectra imagery of missiles in flight.

The wide array of laser systems, instrumentation, and test facilities make HELSTF a unique national asset. This document briefly describes the systems and facilities available to your test program. The lasers and associated systems were built to be configurable to the needs of the experimenter. The staff has over ten years of test experience and can tailor a test program to meet your most exacting requirements.

Site Location and Characteristics

HELSTF is located on the White Sands Missile Range (WSMR) in south-central New Mexico. WSMR is situated in the Tularosa Basin between the San Andreas and Sacramento mountain ranges and occupies an area sixty miles east-to-west by one hundred and twenty miles north-to-south. White Sands is at an approximate elevation of 3960 feet above mean sea level. White Sands Missile Range main post is located 25 miles east of Las Cruces, NM, 50 miles southwest of Alamogordo, NM, and 50 miles north of El Paso, TX. HELSTF is located 23 miles northeast of White Sands Missile Range main post on U.S.

Appendix A

The mean temperature in the basin is 65 degrees Fahrenheit, with a mean relative humidity of 38%. The area is known for its exceptionally clear weather, averaging 300 days per year with little or no cloud cover. Because of low humidity and negligible atmospheric pollution, visibility averages 36 miles and often exceeds 100 miles. HELSTF's location at the southern end of the Missile Range, midway between the east and west missile range boundaries, with full access to WSMR land and air space, ideally situates the site for outdoor testing.

Some of our facilities

- ☐ Mid-Infrared Advanced Chemical Laser (MJRACU)
- ☐ SEALITE Beam Director (SLBD)
- ☐ Laser Demonstration Device CLDD)
- ☐ Pulsed Laser Vulnerability Test System (PL VTS)
- ☐ Vacuum Test System (VTS)
- ☐ Effects Test Area (ETA)
- ☐ Hazardous Test Area (HTA)

High Energy Laser Light Opportunity (HELLO)

The HELLO test program is a local HELSTF initiative designed to make HELSTF's high energy lasers and facilities available to U.S. based industry, academic institutions, and research laboratories. We have upgraded our facilities to operate in an assembly line manner with a standardized user interface. This enables us to make very high laser power levels available at very low costs. The availability of megawatts of laser light at affordable prices will open large new areas of commercial research in chemical and materials processing.



Appendix A

Mid-Infrared Advanced Chemical Laser (MIRACL)



Capabilities

- ☐ Megawatt-class variable power, with good beam quality
- ☐ Continuous-wave mid-infrared (3.8 microns)
- ☐ Reliable operation demonstrated in more than 150 lasing tests and over 3000 seconds of lase time during the last decade.
- ☐ 70 seconds maximum lase duration.

The Mid-Infrared Advanced Chemical Laser (MIRACL) was the first megawatt-class, continuous wave, chemical laser built in the free world. It is a deuterium fluoride (DF) chemical laser with energy spectra distributed among about 10 lasing lines between 3.6 and 4.2 microns wavelength. Since it first lased in 1980, it has accumulated well over 3000 seconds of total lasing time. It remains the highest average power laser in the US.

MIRACL operation is similar to a rocket engine in which a fuel (ethylene, C_2H_4) is burned with an oxidizer (nitrogen trifluoride, NF_3). Free, excited fluorine atoms are one of the combustion products. Just downstream from the combustor, deuterium and helium are injected into the exhaust. Deuterium combines with the excited fluorine to give excited deuterium fluoride (DF) molecules, while the helium stabilizes the reaction and controls the temperature. The laser's resonator mirrors are wrapped around the excited exhaust gas and optical energy is extracted. The cavity is actively cooled and can be run until the fuel supply is exhausted. The laser's output power can be varied over a wide range by altering the fuel flow rates and mixture.

The laser beam in the resonator is approximately 21 cm high and 3 cm wide. Beam shaping optics are used to produce a 14 cm square beam shape which is propagated through the rest of the beam train. Diagnostics for evaluating the beam shape, absolute power and intensity profile are used on each firing of the laser. The beam can be directed to a number of different test areas or to the SLBD.

Programs Supported

- ☐ Static Target Vulnerability Tests
 - ☐ Materials and Coatings
 - ☐ Aircraft and Missile Components
 - ☐ Effectiveness of Laser Hardening Techniques
- ☐ Flying Target Vulnerability Tests
 - ☐ Subsonic and Supersonic Missile Engagements
- ☐ Propagation Phenomenology
 - ☐ Effects of turbulence and thermal blooming on HEL beam propagation
 - ☐ Tracking in Presence of High-Power Beam

Appendix A

- ☐ Effect of Obscurants
- ☐ Laser Technology R&D
 - ☐ High-Power Adaptive Optics o Material Windows
 - ☐ Gratings and Coatings
- ☐ HELLO Commercialization Tests
 - ☐ Advanced Coatings
 - ☐ Cloud Boring
 - ☐ Chemical Processing

Appendix A

SEALITE Beam Director (SLBD)



Capabilities

- ☐ High line-of-site rates and accelerations
- ☐ Primary mirror diameter: 1.8m
- ☐ Focus range: 400m to infinity
- ☐ Primary track sensor: 8 to 12 micron FLIR
- ☐ FLIR track sensor field of view: 4 X 5 micro radians
- ☐ Shared aperture visible track sensor field of view: 0.3 X 0.3 micro radians

The SEALITE Beam Director (SLBD) is mounted on top of Test Cell 1. It consists of a large aperture (1.8 meter) gimbaled telescope and optics to point the MIRACL or other laser beam onto a target. The high power clear aperture is 1.5 meters. The remaining 0.3 meters is normally reserved for a tracker using the outer annulus of the primary mirror. The system is extremely agile and capable of high rotation and acceleration rates. The SLBD weighs 28,000 pounds, of which 18,000 are on the movable portion. The SLBD can also be used as a sensor platform.

The telescope is capable of focusing from a minimum range of 400 meters to infinity. A suite of infrared and visible sensors on the top of the gimbal (off axis from the HEL aperture) is used to acquire and track the target. These sensors look through a 40 cm telescope that can focus over the same range as the SLBD telescope and also correct for parallax between the two lines of sight. Boresight between the SLBD telescope and the sensor is maintained by an automatic laser alignment system. In addition, an aperture sharing element in the high power beam path makes it possible to track a target through the full 1.5 meter telescope aperture even when the high power beam is propagating.

These elements have been combined into an integrated system that can acquire and track targets at extended ranges, accept a very high energy beam, focus and aim the beam on a moving target, and keep this beam at the same position as long as necessary to destroy or disable the target. The SLBD has successfully engaged five BQM-34 drones as well as a supersonic Vandal missile, all at tactically significant ranges.

In addition to directing the high energy laser beam, the HELSTF SLBD has been used very successfully to passively track and image missiles in flight. The inherently precise pointing of the device and its ability to track very high speed targets make it an ideal platform for capturing in-flight imagery. The SLBD has been used as a sensor platform for tracking and imaging a number of Theater Missile Defense (TMD) launches and intercepts, including LANCE, ERINT, and LEAP. A 1000 frame-per-second, digital, infrared camera has been used to collect two-dimensional intercept measurements from targets and interceptors at over Mach 6 closure rates. Calibrated infrared sensors placed in the SLBD's optical train have been used to collect IR imagery for plume and hardbody thermal characterization.

Appendix A

SLBD Passive Imaging Sensor Characteristics

SENSOR	WAVE-BAND	FRAME RATE	FIELD OF VIEW	ARRAY SIZE	APERTURE
LWIR	8-12 m	up to 1000 fps	700 rad	128 x 128	1.5m
MWIR	3-5 m	up to 1000 fps	700 rad	128 x 128	1.5m
FLIR	8-12 m	60 Hz/264 lines	4 x 5 mrad	scanned	40 cm
NFOV TV	visible	60 Hz/264 lines	5 x 6.5 mrad	510 x 492	40 cm
Wide FOV	visible	30 Hz	6.6 x 8.8 mrad	510 x 492	90 mm
Wide FOV AMBER	3-5 m	up to 109 Hz	12 mrad	128 x 128	50 mm
MIT High Frame Rate	visible	2000 Hz	100 rad to 1 mrad	64 x 64	1.5m

Tests Supported

- ☐ High-power dynamic with flying drone (BQM 34)
- ☐ Conventional defense initiative with flying drone
- ☐ High velocity target test with VANDAL missile
- ☐ High altitude target tests with flying drone
- ☐ Missile and plume tests using the 1.5m aperture
 - ☐ Radiometrically calibrated images
 - ☐ Spectral radiometry

Appendix A

Pulsed Laser Vulnerability Test System



Capabilities

- ☐ Moderate to high energy pulsed CO₂ laser system
- ☐ Fully portable, self contained laser system
- ☐ Proven design with low operational costs
- ☐ Full-beam diagnostic instrumentation suite
- ☐ 50 cm static beam pointing telescope
- ☐ State-of-the-art data acquisition system
- ☐ Capable of interfacing with precision pointer tracker
- ☐ Full access to all HELSTF capabilities

The Pulsed Laser Vulnerability Test System provides the capability of conducting susceptibility and vulnerability testing of U.S. weapon systems to possible threat directed-energy weapons. The PLVTS is a CO₂ electric discharge laser of moderate to high energy per pulse.

The PLVTS, consists of several subsystems mounted in portable vans/trailers. These subsystems include:

- ☐ High energy CO₂ Pulsed Laser device.
- ☐ PLVTS Beam Director Assembly (BDA).
- ☐ Beam transfer, diagnostic and alignment system.
- ☐ Control equipment.
- ☐ Electrical power generation equipment.
- ☐ Data acquisition and processing equipment.

The high energy CO₂ pulsed laser device is an AVCO-built HPPL-300 laser. The device uses an electron beam to excite the CO₂ gas and create the lasing action. Functional characteristics of this device are as follows:

PLVTS Characteristics

Type laser	Pulsed wave, closed cycle CO ₂
Pulse Repetition rate	1 to 10 pps (selectable)
Pulse width	30 microseconds

Appendix A

The PLVTS beam can be extracted from the system by one of two methods. The primary method is through a static Beam Pointing Telescope (BPT). The BPT is a 50-cm Cassegrainian telescope which allows manual pointing and focusing of the HEL beam to downrange targets. The second method is through simple turning flats which redirect the 10-cm beam to an external facility for effects testing.

Although designed to operate as a stand-alone system, the PL VTS is homesteaded at Test Cell 3 at the HELSTF. When operated at HELSTF, the PLVTS can be integrated with the existing HELSTF control, diagnostics, and data acquisition systems. In the stand-alone mode, the PLVTS uses integral control and data acquisition systems based on internal computer(s).

Programs Supported

- ☐ Laboratory and tactical range test environments
- ☐ Atmospheric propagation experiments
- ☐ Visible and IR sensor susceptibility testing
- ☐ Material damage assessments
- ☐ Commercial applications

Appendix B

Dr. Don Messitt's Acoustic Measurements of Lightcraft Horizontal Guided Wire Tests

Introduction

Preliminary acoustic data was acquired as a secondary objective during laser propulsion flight tests in October, 1997. In these experiments, the vehicle was flown horizontally, and guided by a thin wire. Two inexpensive microphones were located downrange of the launch point, and were connected to a digital audio tape recorder. The signals were recorded and analyzed to determine if a more costly, dedicated experiment was warranted.

The noise from a Lightcraft liftoff was simulated in Ref. 1. Sound pressure levels in excess of 140 dB were predicted for an observer 20 m away from a 5555 kg vehicle. The model used to generate these noise predictions could not be validated using the October tests due to the use of relatively low quality equipment, which was not calibrated to record sound pressure level.

Calibration for Determination of Lightcraft Trajectory

Initially, the Lightcraft was held in place at known locations, and the PLVTS laser was used to place a single pulse into the engine. The noise generated by this pulse was intended to be used as a calibration signal to determine the Lightcraft trajectory. The difference in time that the signal was recorded by the two microphones varied with downrange distance as shown in Fig. 1. Unfortunately, calibration data was obtained only on the nearly linear portion of the curve, corresponding to downrange distances close to the launch point. The calibration data could not be used to accurately determine all coefficients of the calibration curve, and the data was only used at distances very close to the initial position.

Appendix B

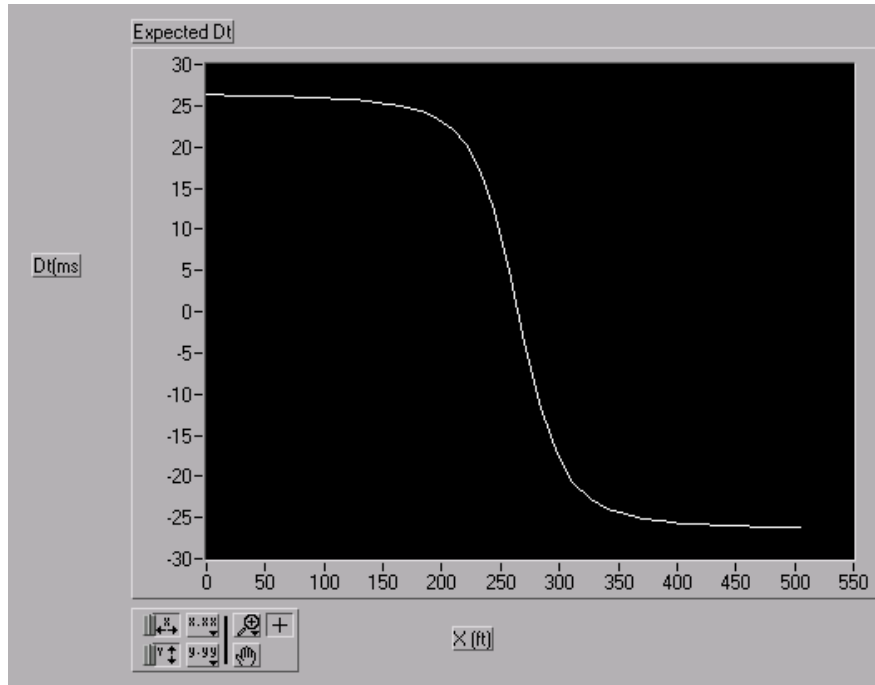


Fig. 1. Expected variation of time difference with range

Two LabView programs were constructed to evaluate the data. One used the original concept of plotting the trajectory as a function of the time delay between arrival of the laser induced blast wave sound pulses at two separate locations. The other used the Doppler Effect, and required only one microphone to generate a trajectory.

The LabView Virtual Instrument (VI) *Record Wave File* was used to transfer the signal from the DAT to a Microsoft Windows wave file. A typical result for one pulse is plotted in Fig. 2, showing the voltage amplitude of the recorded sound as a function of time. The signal could not be converted into pressure levels due to the low quality of the microphones and lack of calibration equipment.

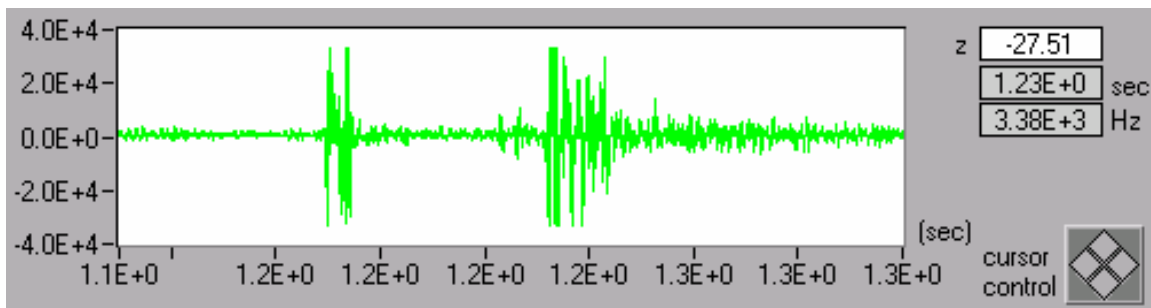


Fig. 2. Single pulse and its echo

The noise measurements were corrupted by extensive echoes. An echo signal is evident on Fig. 2. These echoes did not effect the trajectory measurements, but significantly interfered with spectral analysis.

The ambient speed of sound, distance between the microphones, and distance from the wire to the microphones were taken from measurements recorded in the experiment

Appendix B

notebook, and used by a second VI to determine the trajectory from the wave file. The laser pulse repetition frequency was 10 Hz. The zero reference time was chosen as the time that the first microphone recorded the first pulse. The VI was constructed to ignore the echoes, by eliminating pulses which were out of phase with the main signal. The vehicle downrange position was computed using the equations listed below and illustrated in Fig. 3.

$$x^2 + a^2 = c^2$$

$$(x + b)^2 + a^2 = (c + \Delta c)^2$$

$$\left\{ \sqrt{x^2 + a^2} + \Delta c \right\}^2 - \left\{ (x + b)^2 + a^2 \right\} = 0$$

The resulting trajectory was fitted with a least squares polynomial curve. The first and

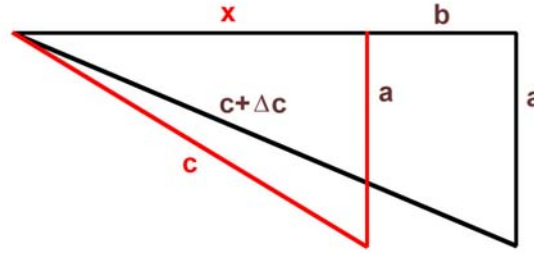


Fig. 3. Calibration schematic

second derivatives of this curve were used to calculate the velocity and acceleration, respectively, with respect to time.

The second trajectory analysis method used only a single signal source and the Doppler effect. A separate VI was written for the Doppler analysis. The peaks were recorded in the same manner as the previous VI, and the following equation was applied to the results:

$$u = 1140(1 - 10\delta s)$$

where u was the velocity, in ft/sec, 1140 was the average speed of sound for 10/01/97, 10 was the pulse repetition rate of the laser, in Hz, and δs was the time between peaks, in seconds. The curve was then fitted with a least squares polynomial. The curve was integrated to obtain downrange distance, and differentiated to calculate acceleration. The VI was evaluated by comparison with the time-of-arrival method, and by comparison between both microphones for the same test. The result was satisfactory for the initial portion of the test. The error increased as the vehicle approached the microphone, as would be expected as the sound source became near to the observer.

Appendix B

Spectral Analysis

A limited spectral analysis was conducted to determine if additional information could be extracted from the acoustic data. The data files from selected channels and tests were analyzed using a time-dependent spectrogram, cf. Fig. 4. There were some interesting observations, such as the peaks in the instantaneous frequency content of one of the echoes, Fig. 4. However, there were no major results and a more detailed investigation was deemed out of scope of the current effort.

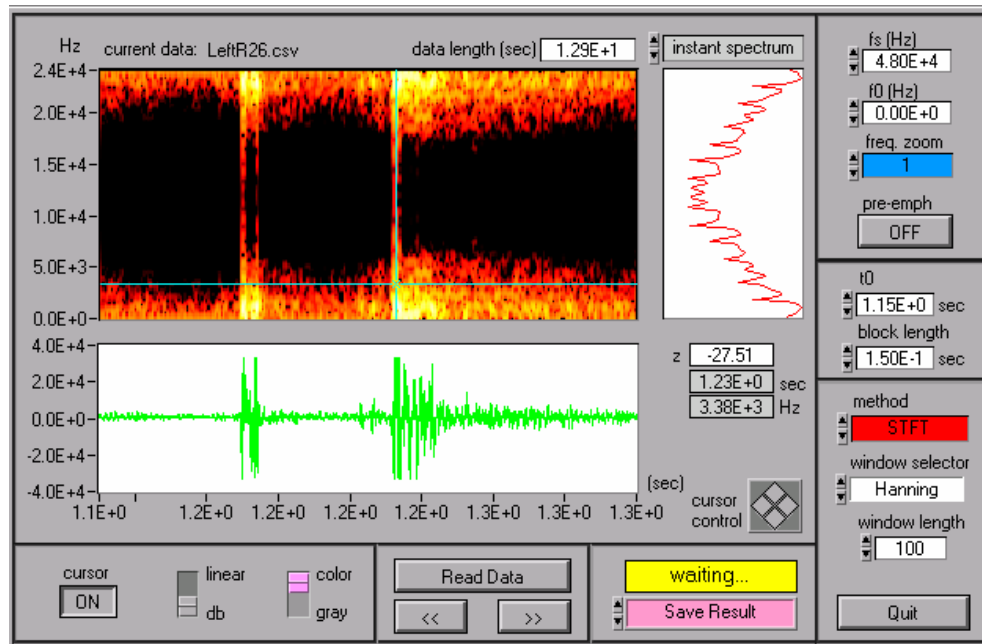


Fig. 4. Time dependent and instantaneous spectrum

Results and Discussion

The maximum velocity of roughly 20 ft/sec was achieved after the vehicle traveled approximately 50 ft. The maximum acceleration occurred at the start of the test, but did not exceed 0.4 g. The values were much lower, however, for the last group of tests conducted in the afternoon. The signal was much noisier, making it more difficult to determine the start of the pulse and its distinction from an echo.

All the runs were not fully evaluated. Run 25 lasted only a few pulses. During run 28, the laser arced several times and skipped pulses. The skipped pulses made it difficult to distinguish echoes from the actual signal. During run 32, there was substantial wind, resulting in a noisy signal that was difficult to decipher. It was also the last test where both channels were recorded.

Appendix B

Conclusions

Acoustic data from microphone recordings was analyzed to determine the trajectory of the Lightcraft. The trajectory was successfully extracted with a method using the time delay between two microphones, and with a Doppler based technique. Trajectory data may be obtained for future Lightcraft tests by a combination of the two techniques. The microphones should be positioned near to the launch point to take advantage of the sensitivity of the two microphone method, with the Doppler analysis used for longer ranges. The effect of echoes may cause substantial interference, and must be evaluated at pulse repetition frequencies higher than 10 Hz.

This Page Intentionally Left Blank

Appendix C

RLBA Engineering Report 00-02 (Rev. A)

R. L. BIELAWA ASSOCIATES, INC.
Corporation for Engineering Consulting
2217 Rockefeller Lane #C
Redondo Beach, CA 90278

RLBA Engineering Report no. 00-02
(Revision A)

Analysis of Flight Dynamics and Control of Laser Lightcraft Vehicles (Contract no. F0470099M4062)

Submitted to:

AFRL/PRSP
Edwards AFB CA, 93524-6351

October 15, 2000
(Revised December 17, 2000)

ABSTRACT

This research program was directed to the development of an advanced flight dynamic simulation of the laser Lightcraft flight vehicle. The two objectives of the analysis were: 1) to provide a comprehensive analytic simulation, that could be used both to simulate existing model test results, and as a capability for advanced design of Lightcraft configurations, and 2) to implement the analysis in the form of a FORTRAN computer code. Both these objectives have been successfully met. The advanced features provided by this research program include a modeling of a dual-spin configuration, as well as a generic multi-variant PID control system. Also, a constrained minimization resource was incorporated to enable the identification of optimized control laws for attitude control.

Prepared by:

Richard L. Bielawa, Pres.,
R. L. Bielawa Associates, Inc.

Appendix C

RLBA Engineering Report 00-02 (Rev. A)

ACKNOWLEDGEMENTS

This research project was performed under U. S. Air force Contract no. F0470099M4062; Dr. Franklin B. Mead Jr. Technical Contract Monitor. The author wishes to express his gratitude to Dr. Leik Myrabo and Mr. Andrew Panetta for their contributions to the effort and especially to Dr. Mead for his encouragement and patience.

Appendix C

RLBA Engineering Report 00-02 (Rev. A)

CONTENTS

Acknowledgements	ii
List of Figures	vi
Abstract	vii
1.0 Introduction	1
2.0 Equations of Motion for Basic Dynamic System	5
2.1 Basic Assumptions	5
2.2 Degrees of Freedom	7
2.2.1 Coordinate System	7
2.2.2 State Vectors	7
2.3 Basic Form of Equations of Motion	8
2.3.1 Force Equilibrium Equations	8
2.3.2 Geocentric and Geodetic Coordinates	8
2.3.3 Moment Equilibrium Equations	9
2.3.4 Auxiliary Equations	10
2.3.5 Augmented State Vector	12
2.4 External Aerodynamics	13
2.4.1 Body Fixed System to Wind Axis System Transformation	13
2.4.2 Definition of External Aerodynamic Loadings	15
2.4.3 Interpolation of Tabulated Aerodynamic Data	15
2.4.4 Application of Coordinate Transformations to Aerodynamic Forces and Moments	16
2.4.5 Perturbational Airloads	16
2.5 Propulsion Characteristics	19
2.5.1 Laser Beam Transmission Characteristics	19
2.5.2 Gross Coupling Coefficient and Thrust Characteristics	20
2.5.3 Side Force and Moment Coupling	22
2.5.4 Laser Pointer System	23
2.5.4.1 Coordinate System Transformations	24
2.5.4.2 Range Distance	25
2.5.4.3 Laser Beam Offsets	26
2.5.4.4 Body Force and Moment Components	28
2.5.5 Perturbational Propulsive Forces and Moments	30
2.6 Gravity Forces	37
2.6.1 Gravitational Acceleration	37
2.6.2 Total Gravity Loads	38
2.6.3 Perturbational Gravity Loads	39

Appendix C

RLBA Engineering Report 00-02 (Rev. A)

3.0 Eigenvalue Solution	41
3.1 Linearization of the Mechanical Terms	41
3.1.1 Assumptions	41
3.1.2 Basic Linearized Equations of Motion	42
3.2 Inclusion of Perturbational External Aerodynamics, Propulsion Offset Characteristics and Gravity Loads	42
3.2.1 Perturbational Airloads	42
3.2.2 Perturbational Propulsive Loads and Moments	43
3.2.3 Perturbational Gravity Forces	44
3.3 Canonical Form of Equations Required for Typical Solution	44
4.0 Dual-spin Configuration	47
4.1 Supplementary Assumptions	47
4.1.1 General	47
4.1.2 Mechanical Systems	48
4.1.3 Action of Thrust and Drag	49
4.2 Supplemental Equations of Motion	50
4.2.1 Revised Augmented State Vector and Supplementary Equations	50
4.2.2 Kinetic Energy	51
4.2.3 Potential Energy and Generalized Forces	51
4.2.4 Final Form of Dynamic Equations	53
4.2.5 Eigenvalue Solution Considerations	55
5.0 Attitude Control Characteristics	59
5.1 Modeling Considerations	59
5.1.1 Physical Considerations	59
5.1.2 Basic Control Law Strategies	60
5.2 Implementations of Moment Control Mechanisms	61
5.2.1 Feed Back Moment Description	61
5.2.2 Details of the Error Vector	63
5.3 Incorporating the Control System Simulation into the Nonlinear Equation Set	65
5.4 Supplement to Eigenvalue Solution	66
5.4.1 Expansion of Perturbational State Vector	69
5.4.2 Effect of the Moment Limiters	69
5.4.3 Final Form of Eigenvalue Problem	70
6.0 Summary of Results and Recommendations	71
6.1 Summary	71
6.2 Recommendations	71
7.0 References	73
Nomenclature	75

Appendix C

RLBA Engineering Report 00-02 (Rev. A)

Appendix A – The LITE_DYN Computer Code	81
A.1 General Operation of LITE_DYN	81
A.2 Inputs	81
A.2.1 File Operations	81
A.2.2 Structure of the Input File	82
A.2.3 Case Termination	83
A.2.4 Description of Data Items within Each Data Block	83
A.2.5 Supplemental Keyboard Data Input	95
A.3 Program Termination	95
A.4 Notes for Efficient Program Usage	95
A.4.1 The Eigenvalue Solution	95
A.4.2 The Time-history Solution	96
 Appendix B – Earth Geodetic vs Geocentric Coordinate Conversions	 97
B.1 Geocentric Cartesian Coordinates	98
B.2 Geodetic to Geocentric Conversion	98
B.3 Geocentric to Geodetic Conversion	99
 Appendix C – Default External Aerodynamic Loads Description	 101
 Appendix D – Implementation of the CONMIN Optimization Feature	 105
D.1 The CONMIN Program for Constrained Function Minimization	105
D.2 Extent of Coding Incorporated in the LITE_DYN Code	105
D.3 FORTRAN coding of CONMIN-related User-Defined Subroutines	107
 Appendix E – Descriptions of Standard Outputs	 111
E.1 Eigenvalue Results	111
E.2 Time-history Results	111
E.3 Termination State Vector	113
E.4 CONMIN Results	113

Appendix C

RLBA Engineering Report 00-02 (Rev. A)

List of Figures

1	Basic vehicle coordinate system	7
2	Geometry defining airloads coordinate system transformation	14
3	Gross coupling coefficient vs Mach no. and altitude	20
4	Coupling coefficient attenuation factor due to linear offset	21
5	Coupling coefficient attenuation factor due to angular offset	21
6	Sign conventions for lateral force and transverse moment due to linear and angular offsets	22
7	Side force coupling coefficient factor due to linear offset	23
8	Vehicle and launch point local Earth-fixed coordinate systems	24
9	Geometry defining decomposition of propulsive side forces and moments due to lateral and angular offsets	29
10	Basic kinematics of dual-spin configuration	46
11	Interaction of thrust and drag on bearing structure compressive load	48
12	Schematic of Generic Lightcraft Control System	61
B.1	Geocentric vs Geodetic Coordinates	97
C.1	lift coefficient variation with Reynold's no. and spin rate, $\alpha = 26.32$ deg.	102
C.2	drag coefficient variation with Reynold's no. and spin rate, $\alpha = 0$	102
C.3	drag coefficient variation with Reynold's no. and spin rate, $\alpha = 26.32$ deg.	103
C.4	Y-force coefficient variation with Reynold's no. and spin rate, $\alpha = 26.32$ deg .	103
C.5	pitching moment coefficient variation with Reynold's no. and spin rate, $\alpha = 26.32$ deg.	104
C.6	yawing moment coefficient variation with Reynold's no. and spin rate, $\alpha = 26.32$ deg.	104

Appendix C

RLBA Engineering Report 00-02 (Rev. A)

ABSTRACT

This research program was directed to the development of an advanced flight dynamic simulation of the laser Lightcraft flight vehicle. The two objectives of the analysis were: 1) to provide a comprehensive analytic simulation, that could be used both to simulate existing model test results, and as a capability for advanced design of ightcraft configurations, and 2) to implement the analysis in the form of a FORTRAN computer code. Both these objectives have been successfully met. The advanced features provided by this research program include a modeling of a dual-spin configuration, as well as a generic multi-variant PID control system. Also, a constrained minimization resource was incorporated to enable the identification of optimized control laws for attitude control.

Appendix C

RLBA Engineering Report 00-02 (Rev. A)

Analysis of Flight Dynamics and Control of Laser Lightcraft Vehicles

1.0 Introduction

Two milestones in the development of the Laser Lightcraft flight concept are first, the publishing of Reference 1, which presents in-depth conceptual developments of most of the critical system design issues, and second, the successful test flights of several Lightcraft models, powered entirely by the Lightcraft propulsion principle. The purpose of the study presented herein is to advance the technology base of this concept. Specifically, the present analysis provides a comprehensive simulation of the flight dynamics of the Lightcraft in realistic arbitrary flight scenarios. This simulation gives time-history solutions of the dynamics of the Lightcraft's flight trajectories which are governed by realistic external aerodynamics and detailed characteristics of the laser propulsion system. In addition to the analysis formulations outlined in the present document, a FORTRAN computer code (LITE_DYN) has been written to implement all the features discussed herein.

This analysis and the supplemental LITE_DYN computer code provide timely and seminal contributions to the two aforementioned milestones. With regard to the model tests, the analysis provides a tool for confirming and thereby understanding the physics of the flight behavior of the test models. With regard to the conceptual development, the analysis provides a new technology resource not covered by Reference 1: the development of a tool for the design of practical flight stability and control systems. These two issues have, to a large degree, defined the features of the resulting analysis:

In Support of Model Tests:

1. The dynamic modeling of a three-dimensional solid in flight with attendant aerodynamic, gravity and propulsive forces. In particular, the analysis accounts not only for both the gyroscopic characteristics of the Laser Lightcraft, but the corrections needed to account for Earth rotation.
2. Arbitrary launch conditions. The simulation accounts for Earth oblateness, giving geodetic to geocentric (and reverse) conversions. Also, the analysis accounts for both standard and non-standard atmospheric conditions at the launch point with regard to pressure and temperature measurements as are typically available.
3. Variable atmospheric conditions. The analysis provides for a lateral wind shear variable with altitude in both direction and wind speed. In addition, the atmospheric properties, density, sonic speed and kinematic viscosity, are variable with altitude and matched to the actual conditions at the launch point.

In Support of Advanced Development:

4. Dual-spin Configurations. For any practical Laser Lightcraft flight vehicle, some part of the vehicle should not be subject to the high-g environment caused by the spin-up of the

Appendix C

RLBA Engineering Report 00-02 (Rev. A)

engine portion of the spacecraft. A non-spin portion of the spacecraft would necessarily be required for standard on-board instrumentation, computers, payload, etc, in the case of unmanned vehicles, and certainly for eventual manned flight. The present analysis provides a modeling of the dual spin characteristics, with the added consideration of a flexible bearing mount between the two portions of the spacecraft. A principal requirement for implementing the dual-spin configuration is to provide a realistic mechanical basis for the attitude control system.

5. A generic, multi-variant attitude control system. Together with the dual-spin configuration, the analysis provides for flight condition sensing aboard the non-spin portion of the Lightcraft as well as the application of the attitude control moments on that portion as well. Because much is unknown about the key issues of controlling the Lightcraft, the control system selected is completely multi-variant with a completely arbitrary set of coupled feedback gains available for the control system designer. Because of the high angular momentum resulting from the spin of the propulsive system, significant gyroscopic effects will be present which will impose unique control requirements involving significant cross-coupling. While some of the feedback sensing is relatively straightforward (angular rates and attitude angles), provision is made for feedback sensing of one set of quantities not yet technically practical: the angular offsets of the Lightcraft with the laser beam.

The approach was to keep to generally conventional technology and the system is configured basically as a PID system with moment amplitude limiters. Additionally, direct open-loop control moments can be applied either separately or concert with the feedback control moments.

6. A resident constrained minimization resource. Since the selection of a suitable control law is yet to be made, the analysis provides for the use of a more or less standard piece of technology, the CONMIN minimization algorithm. Since some of the control law selection is subject to user preference, provision has been made for practical modification of the LITE_DYN code to allow for the selection of the requisite cost function (a scalar to be minimized). Provision has been made, however, for using either the time-history solution in combination (or not) with the results of the eigenvalue solution.

Mathematical Considerations:

The rigorous modeling of the flight dynamics of the Laser Lightcraft necessarily involves a set of nonlinear equations whose terms are usually not available in analytic form. As a consequence, a standard numerical solution technique for solving differential equations, the Runge-Kutta technique was selected as being a robust and accurate method for time-history solutions. Additionally, provision was made for giving eigenvalue solutions, to be performed at regular intervals through out the time-history solution, as a basis for verification and understanding of the involved physics. Both types of solution are made available to the selection of the CONMIN cost function.

Appendix C

RLBA Engineering Report 00-02 (Rev. A)

Organization of the Report:

The formulations presented in this report follow a path of increasing complexity and comprehension. Chapter 2 presents the major formulations for the basic Lightcraft configuration. Definitions of all the principal forces impacting on the Lightcraft are developed and the final set of nonlinear equations are developed therein. Chapter 3 deals with the eigenvalue solution of the material in Chapter 3. Methods are presented for suitably linearizing the solutions about any arbitrary point in time of the time-history solution. Chapter 4 presents the developments necessary for modeling the dual-spin configuration. "First-cut" attention is paid to the elasto-mechanical characteristics of the bearing and structural support characteristics. Simple lateral bending of the structure around the bearing is accounted for in the form of an isotropic spring stiffness restraining the non-spin and spin portions of the Lightcraft to each other. Finally in Chapter 5 formulations are presented for incorporating the selected multi-variant attitude control system dynamics. In both Chapters 4 and 5, the approach has been to present the additional completely nonlinear dynamics, as a set of modifications to the previous results, and then to present the modifications required for the eigenvalue solution.

Additional technical development is presented in the appendices. Appendix A is the principal appendix, which presents information on the operation of the LITE_DYN computer code. Although this computer code is not WINDOWS-based, and run instead in a DOS environment, it has significant flexibility in operation and in the recording of the output response data. Appendix B presents the development necessary for converting from geodetic to geocentric and in reverse. Appendix C presents details on the low-air-speed default external aerodynamic data used. Appendix D presents information on implementing the imbedded CONMIN algorithm and how to modify the LITE_DYN FORTRAN coding to achieve any specific optimization objective that a user might want to implement. Appendix E presents a description of the numerical structuring of the output files generated by the LITE_DYN computer code.

Finally, Chapter 6 presents a summary of the development of this research program and, more importantly, a list of recommendations for continuing and building upon the results of the present analysis. While no direct specific numerical results were generated by this project, significant resources are now available from it for a wide variety of studies.

Appendix C

RLBA Engineering Report 00-02 (Rev. A)

2.0 Equations of Motion for Basic Dynamic System

2.1 Basic Assumptions

Assumptions that lead to the general derivation of the governing equations of motion are as follows:

- a) The equations of motion are derived using the conventional “body-fixed” aircraft coordinate system (see Ref. 2). The x -axis is forward along the axis of symmetry; the y -axis is to starboard, and generally parallel to the local horizon, and the z -axis is directed “downward” using the standard right-hand convention. The appropriate Euler angles are defined (relative to the local horizontal and vertical directions), in order, by: first, the azimuthal (heading) angular deflection, Θ , about the local vertical to the Earth, and second, the pitch angle, θ_y , about the y -axis. Additionally, for the dual-spin configuration, wherein the forward part of the vehicle does not spin, the third Euler angle is taken to be the roll angle of that forward portion, ϕ , about the x -axis.
- b) The Earth is an oblate ellipsoid with equatorial radius of 6378.1363 km polar radius of 6356.7517 km. It furthermore rotates with a rotational rate of $7.292115856 \times 10^{-5}$ rad/sec. The scalar value of acceleration due to gravity, g , varies in accordance with the standard spherical harmonic expansion of the Earth’s gravitational field. This gravitational field is, furthermore, independent of longitude. Vectorially, the gravitational acceleration acts normal to the tangent of the oblate ellipsoid, i.e., along the line defining the geodetic latitude.
- c) The rotation of the vehicle relative to inertial space is taken to consist of the components of the Earth’s rotation plus the rotation of the vehicle relative to the Earth. In both cases, only the y -axis and z -axis components are considered. In the former case, the y - and z -axis components of the Earth’s rotation velocity are Q_{ie} and R_{ie} , respectively. The similarly defined components of the vehicle angular velocity relative to the Earth are, q and r , respectively. Moreover, these components are then used to define the “non-spin” angular momentum.
- d) The “spin” angular momentum of the laser Lightcraft vehicle is defined using the initial spin rotational speed, Ω , about the x -axis. This component of angular momentum is significantly greater than the “non-spin” angular moment, as defined from the components of inertial angular velocity of the vehicle as a whole. This assumption results in the linearization of the mechanical portions of the equations. Additionally, it is assumed that the spin angular momentum is constant (no frictional and/or aerodynamic retardation effects).
- e) In actuality, the vehicle operates in two cyclic modes of flight: 1) the “powered” portions of the flight wherein the pressure pulses (due to laser impingement) are acting to thrust the vehicle, and 2) the coast portions, wherein the Lightcraft is free of the lifting pressure pulse, and is reestablishing fresh air in the pressure annulus. The analysis herein assumes that the vehicle is only operating in a single mode of flight: the “average” of these two modes of flight, wherein the propulsion is assumed to be variable, but continuous and time-averaged over each propulsion cycle.

Appendix C

RLBA Engineering Report 00-02 (Rev. A)

f) Two separate fluid dynamic loadings impact on the vehicle. On one hand, are the external aerodynamics, that operate in all flight regimes. On the other hand, are the overpressures caused by the hot gasses in the pressure annulus that operate only during the laser pulses. Each of these fluid dynamic loadings are unaffected by the other.

g) Each of the fluid dynamic loadings generate forces and moments on the Lightcraft vehicle that are generally nonlinear functions of the applied control and response variables. The external loadings are defined by the freestream dynamic pressure, q_0 , the angle of attack and side-slip angle, α and β , respectively, the spin rate (about the longitudinal axis) Ω_x , and the location of the aerodynamic center, x_{AC} . The internal loadings are defined by the effective laser power impinging on the Lightcraft vehicle, the lateral translation of the laser beam from the center line of the vehicle, and the angular orientation of the beam with the centerline of the vehicle.

h) In each case, the loadings can be represented quasi-statically (omitting response rate dependency) with the use of tabulated functions of the appropriate variables. The interpolations of the tabulated functions are accomplished using “spline-fit” techniques. (see Ref. 3).

Additional assumptions relate to the two types of dynamic response descriptions considered: a) time history responses and b) eigenvalue results.

i) In the time-history solution, all responses are deterministic without any consideration of random inputs. The applied loadings to the vehicle in the time-history solution consist of lateral windage effects and the variability of laser power impacting on vehicle due to range and off-zenith orientation of the laser source. The small angle assumption is not invoked for any of the time-history response angles.

j) In the eigenvalue solution, all angular response variables are “small”, and perturbations are taken of all the loadings impacting on the vehicle.

Appendix C

RLBA Engineering Report 00-02 (Rev. A)

2.2 Degrees of Freedom

2.2.1 Coordinate System

The usual “airplane” body-fixed coordinate system is utilized (Ref. 2) with the x -axis defined along the (spin) axis of symmetry and taken to be positive in the forward direction. By convention we may select the y -axis direction arbitrarily, with the proviso that it will generally be taken parallel to the instantaneous horizon and positive to the right (or starboard direction). The z -axis is taken to form a right-hand orthogonal tri-axial system. These axes are shown in the Figure. 1:

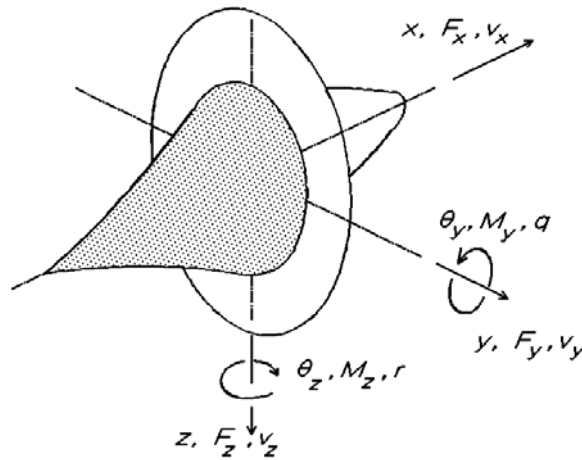


Fig. 1 Basic vehicle coordinate system

2.2.2 State Vectors

The state vector of basic system degrees of freedom, $\{Y(t)\}$, is given by the following expression:

$$\{Y\} = \begin{Bmatrix} v_x \\ v_y \\ v_z \\ q \\ r \end{Bmatrix}$$

(1)

Additional elements of the state vector are defined in subsequent sections wherein additional dynamic elements are considered.

Appendix C

RLBA Engineering Report 00-02 (Rev. A)

2.3 Basic Form of Equations of Motion

2.3.1 Force Equilibrium Equations

In their most general form the body-fixed coordinate system equations of motion (Euler's equations) entail the use of the three components of inertial angular velocity, P , Q , and R . For present purposes, however, the rotation about the x -axis, P , is taken to be zero. The resulting equation set is then given by:

$$\begin{aligned} m(\dot{v}_x + Qv_z - Rv_y) &= \sum_i F_{x_i} = F_x^{(a)} + F_x^{(p)} + F_x^{(g)} \\ m(\dot{v}_y + Rv_x) &= \sum_i F_{y_i} = F_y^{(a)} + F_y^{(p)} \\ m(\dot{v}_z - Qv_x) &= \sum_i F_{z_i} = F_z^{(a)} + F_z^{(p)} + F_z^{(g)} \end{aligned} \quad (2a,b,c)$$

where the summation over i relates to the various sources of applied forces [external aerodynamics $(..)^{(a)}$, propulsive forces $(..)^{(p)}$ and gravity $(..)^{(g)}$]. The specific definitions of these forces are covered in subsequent sections. Also, the components of inertial angular velocity, Q and R are given by:

$$\begin{aligned} Q &= Q_{ie} + q \\ R &= R_{ie} + r \end{aligned} \quad (3)$$

The components of the Earth's inertial angular velocity, Q_{ie} and R_{ie} are expressible in terms of the magnitude of the Earth's rotation speed, $\mathbf{6}_{ie}$ ($= 7.292115856 \times 10^{-5}$ rad/s), the Earth latitude angle, $\mathbf{2}$, the heading angle, $\mathbf{5}$, and the vehicle pitch angle relative to the local horizon, θ_y :

$$\begin{aligned} Q_{ie} &= -\omega_{ie} \cos \lambda \sin \psi \\ R_{ie} &= \omega_{ie} (\cos \lambda \sin \theta_y \cos \psi - \sin \lambda \cos \theta_y) \end{aligned} \quad (4a,b)$$

2.3.2 Geocentric and Geodetic Coordinates

In order to include correctly the effects of the Earth's inertial angular velocity and gravitation in the dynamic description, the use of the *geocentric* frame of reference must be used. However, both the vehicle's and the laser's positions are defined using altitude, bearing angle and elevation (or pitch) angle, all of which are defined in the *geodetic* frame of reference. Accordingly, conversions are required for interchanging between these two coordinate systems. These conversions are developed in Appendix B. In the actual FORTRAN program that implements the equations developed herein, the conversions are provided as a subsidiary computational subroutine. Where a distinction must be made, any variable being defined in the

Appendix C

RLBA Engineering Report 00-02 (Rev. A)

geodetic system will be denoted with a (\neq). Thus, the terms in above Eqs 4a&b are defined in the geocentric coordinate system.

2.3.3 Moment Equilibrium Equations

The formulation of the moment equations of motion is based on the simplified gyro equations developed by Wrigley & Hollister (Ref. 4). This development distinguishes between “spin” angular momentum and “non-spin” angular momentum. The “spin” angular velocity has the magnitude of \odot and gives rise to the following expression for “spin” angular momentum:

$$\vec{H}_{spin} = J\Omega\vec{i} \quad (5)$$

and the following expression for “non-spin” angular momentum:

$$\vec{H}_{non-spin} = I_d \left[(q + Q_{ie})\vec{j} + (r + R_{ie})\vec{k} \right] \quad (6)$$

where the diametral moment of inertia, I_d , is the same as I_{yy} (or) I_{zz} and J is the same as I_{xx} . and the corresponding expression for “non-spin” angular velocity:

$$\vec{\omega}_{non-spin} = (q + Q_{ie})\vec{j} + (r + R_{ie})\vec{k} \quad (7)$$

The simplified gyro equation gives the following form for the vector equations of motion in pitch and yaw:

$$\dot{\vec{H}}_{non-spin} + \vec{\omega}_{non-spin} \times \vec{H}_{spin} = \vec{M} = \sum_i M_{y_i} \vec{j} + \sum_i M_{z_i} \vec{k} \quad (8)$$

where, again, the summations on the right-hand sides of the equation represent the summations of all the externally applied moments. This vector equation can be written in explicit form as:

$$\begin{aligned} I_d (\dot{q} + \dot{Q}_{ie}) + J\Omega(r + R_{ie}) &= \sum_i M_{y_i} = M_y^{(a)} + M_y^{(p)} + M_y^{(c)} \\ I_d (\dot{r} + \dot{R}_{ie}) - J\Omega(q + Q_{ie}) &= \sum_i M_{z_i} = M_z^{(a)} + M_z^{(p)} + M_z^{(c)} \end{aligned} \quad (9a,b)$$

where the derivatives with respect to time of Q_{ie} & R_{ie} are easily calculable from Eqs. 4a&b:

Appendix C

RLBA Engineering Report 00-02 (Rev. A)

$$\begin{aligned}\dot{Q}_{ie} &= -\omega_{ie} \left(-\dot{\lambda} \sin \psi \sin \lambda + \dot{\psi} \cos \psi \cos \lambda \right) \\ \dot{R}_{ie} &= \omega_{ie} \left[-\dot{\lambda} \left(\sin \lambda \sin \theta_y \cos \psi + \cos \lambda \cos \theta_y \right) \right.\end{aligned}$$

(10a&b)

and where the $(..)^{(a)}$, $(..)^{(p)}$, and $(..)^{(c)}$ superscripts refer, respectively, to moment components due to aerodynamic, propulsive, and control sources.

All of the basic equations can then be written in the final most useful form:

$$\begin{aligned}\dot{v}_x &= \frac{1}{m} \sum F_x - (Q_{ie} + q)v_z + (R_{ie} + r)v_y \\ \dot{v}_y &= \frac{1}{m} \sum F_y - (R_{ie} + r)v_x \\ \dot{v}_z &= \frac{1}{m} \sum F_z + (Q_{ie} + q)v_x \\ \dot{q} &= \frac{1}{I_d} \left[\sum M_y - J\Omega(R_{ie} + r) \right] - \dot{Q}_{ie} \\ \dot{r} &= \frac{1}{I_d} \left[\sum M_z + J\Omega(Q_{ie} + q) \right] - \dot{R}_{ie}\end{aligned}$$

(11a,b,c,d,e)

2.3.4 Auxiliary Equations

In addition to the basic set of equations given in the previous section, the following equations define the differential equations for the for auxiliary variables that vary in response to the basic response variables:

Total velocity:

$$V = \sqrt{v_x^2 + v_y^2 + v_z^2}$$

(12)

Appendix C

RLBA Engineering Report 00-02 (Rev. A)

Local flight-path elevation and bearing angles:

$$\Phi = \tan^{-1} \frac{v_x \sin \theta_y - v_z \cos \theta_y}{\sqrt{v_y^2 + (v_x \cos \theta_y + v_z \sin \theta_y)^2}}$$

$$\chi = \tan^{-1} \frac{v_x \cos \theta_y \sin \psi + v_y \cos \psi + v_z \sin \theta_y \sin \psi}{v_x \cos \theta_y \cos \psi - v_y \sin \psi + v_z \sin \theta_y \cos \psi}$$

(13a,b)

Horizontal (tangential) and vertical velocities:

$$V_t = V \cos \Phi = \sqrt{v_y^2 + (v_x \cos \theta_y + v_z \sin \theta_y)^2}$$

$$V_z = V \sin \Phi = v_x \sin \theta_y - v_z \cos \theta_y$$

(14a,b)

(Geocentric) latitude rate:

$$\dot{\lambda} = \frac{V \cos \Phi \cos \chi}{R_{gc}}$$

(15)

Longitude rate:

$$\dot{L} = \frac{-V \cos \Phi \sin \chi}{R_{gc}}$$

(16)

Incremental geocentric radius:

$$\Delta \dot{R}_{gc} = V \sin \Phi = V_z$$

(17)

Local pitch attitude angle:

$$\dot{\theta}_y = q + \frac{V_t}{R_{gc}}$$

(18)

Heading angle:

$$\dot{\psi} = r \cos \theta_y - \dot{L} \sin \lambda$$

(19)

Mass rate:

$$\dot{m} = \dot{m}_0$$

(20)

Appendix C

RLBA Engineering Report 00-02 (Rev. A)

[Note that the mass rate is essentially a constant, defined by the appropriate input value. It generally has a non-zero value only for the rocket flight mode outside the atmosphere.]

Components of Lightcraft range vector (details given in Section 2.5.4.2):

$$\dot{\vec{S}}_{LC}^{(1)} = \begin{bmatrix} \dot{S}_{x_{LC}}^{(1)} & \dot{S}_{y_{LC}}^{(1)} & \dot{S}_{z_{LC}}^{(1)} \end{bmatrix} \begin{Bmatrix} \vec{i}_1 \\ \vec{j}_1 \\ \vec{k}_1 \end{Bmatrix} \quad (21)$$

2.3.5 Augmented State Vector

The development of Section 2.3.3 can then be combined with the definition of the basic state vector to form an augmented state vector:

$$\{Y\}_{augmented} = \begin{Bmatrix} v_x \\ v_y \\ v_z \\ q \\ r \\ m \\ \Delta R_{gc} \\ \lambda \\ L \\ \psi \\ \theta_y \\ S_{x_{LC}}^{(1)} \\ S_{y_{LC}}^{(1)} \\ S_{z_{LC}}^{(1)} \end{Bmatrix} \quad (22a)$$

And the equations of motion can then be written as:

$$\{\dot{Y}\}_{augmented} = \left\{ F\left(t, \vec{Y}_{augmented}\right) \right\} \quad (22b)$$

Appendix C

RLBA Engineering Report 00-02 (Rev. A)

Equation 22b is then in the required form for obtaining a time-history solution. The equation set constitutes a set of nonlinear equations that must be solved numerically. The method selected for solving the equation set is a fourth-order variant of the Runge-Kutta method with Gill coefficients (Ref. 5). Note also that those variables defined in the geodetic system are calculated “after the fact” using the corresponding variables in the geocentric system together with the conversions offered in Appendix B. These variables thus do not need separate differential equations for their solution.

2.4 External Aerodynamics

2.4.1 Body Fixed System to Wind Axis System Transformation

There exists only a limited amount of existing external airloads applicable to the laser Lightcraft. Presently, the only set of test data available to the author is the subsonic data described in Ref. 6. In general, one would want to locate the aerodynamic coefficients at some well-defined point on the Lightcraft similar to the “aerodynamic center”, for conventional wings. Without incurring any loss of generality, we will dispense with attempting to define such a longitudinally positioned point and instead define the aerodynamic coefficients *at the nose of the vehicle*.

As is the usual method for presenting aerodynamic data, however, wind axes are used to define the airloads. Hence, a transformation is required to apply the airloads to the vehicle, whose equations are, however, written in body-fixed coordinates. To this end, three rotational transformations are required. Before these transformations can be defined, however, the total (effective) angle of attack must be defined. Since the Lightcraft is symmetric about the x -axis, the effective aerodynamic angle-of-attack, α_{equiv} , is actually the vector sum of the actual flight path angle-of-attack, α , and the side-slip angle, β :

$$\alpha_{equiv} = \sqrt{\alpha^2 + \beta^2} \quad (23)$$

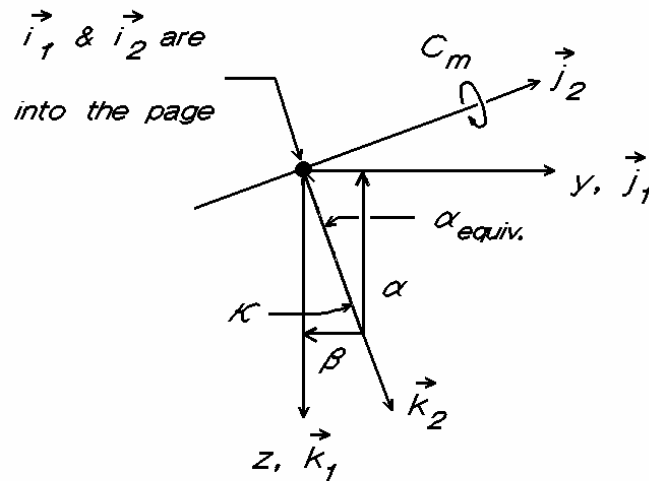
where the actual angle-of-attack and side-slip angles are given by:

$$\alpha = \tan^{-1} \frac{v_z}{v_x} \quad \beta = \tan^{-1} \frac{v_y}{v_x} \quad (24a\&b)$$

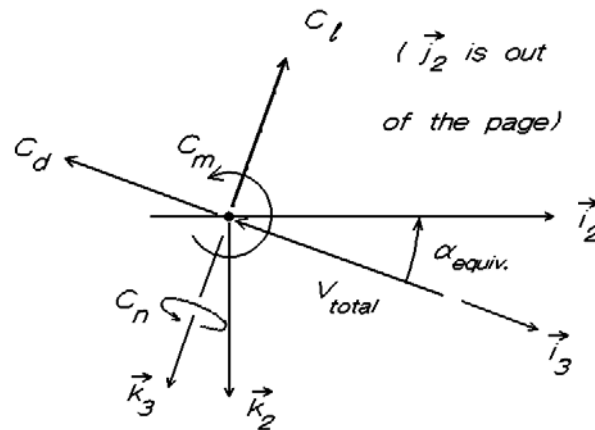
As shown in the Figure 2(a), the $()_1$ coordinate system is taken to be the body-fixed system affixed to the vehicle. The angle, κ , represents the orientation of the equivalent angle-of-attack relative to the body-fixed system:

$$\kappa = \tan^{-1} \frac{\alpha}{\beta} \quad (25)$$

The rotation about the x_1 -axis defines the $()_2$ coordinate system. Then, taking a rotation about the y_2 -axis, by the angle, α_{equiv} , defines the $()_3$ coordinate system, which is in fact the wind-axis system (see Figure.2(b)).



(a) rear view along the x -axis of the vehicle



(b) view along the y_2 -axis

Fig. 2 Geometry defining airloads coordinate system tranformation

The resulting coordinate system transformation relating the body-fixed system, $()_3$, to the wind axis system, $()_{wa}$, is then given by:

$$\left\{ \begin{matrix} \vec{i} \\ \vec{j} \\ \vec{k} \end{matrix} \right\}_3 = \begin{bmatrix} \cos \alpha_{equiv.} & 0 & -\sin \alpha_{equiv.} \\ \sin \kappa \sin \alpha_{equiv.} & \cos \kappa & \sin \kappa \cos \alpha_{equiv.} \\ \cos \kappa \sin \alpha_{equiv.} & -\sin \kappa & \cos \kappa \cos \alpha_{equiv.} \end{bmatrix} \left\{ \begin{matrix} \vec{i} \\ \vec{j} \\ \vec{k} \end{matrix} \right\}_{WA} = \left[T_{WA \rightarrow 3}^{(a)} \right] \left\{ \begin{matrix} \vec{i} \\ \vec{j} \\ \vec{k} \end{matrix} \right\}_{WA}$$

(26)

Appendix C

RLBA Engineering Report 00-02 (Rev. A)

2.4.2 Definition of External Aerodynamic Loadings

The experimental aerodynamic loadings presented in Ref. 6 have been successfully cast in an appropriate nondimensional form. This form defines the airloads as functions of the equivalent angle of attack, α_{equiv} , the Reynold's no., Rn , and a similarly defined nondimensional spin rate. Furthermore, for these data the aerodynamic coefficients are defined at the *nose point of the vehicle* and hence, the aerodynamic reference center, $FS_{arc} = 0$. Using the maximum radius to be the characteristic length, these parameters are then respectively defined

$$\bar{\Omega} = \frac{\Omega R^2}{v}$$

as:

$$Rn = \frac{VR}{v} \quad (27a,b)$$

Using these parameters the experimental aerodynamic coefficients of Ref. 6 were fit to the following functional forms:

$$\begin{aligned} C_X &= C_{X_0} \left(1 + \eta_{X_1}^{(0)} Rn + \eta_{X_2}^{(0)} Rn^2 + \eta_{X_3}^{(0)} Rn^3 \right) + \\ &\quad C_{X_\alpha} \alpha \left(1 + \eta_{X_1}^{(1)} Rn + \eta_{X_2}^{(1)} Rn^2 + \eta_{X_3}^{(1)} Rn^3 \right) \\ C_D &= C_{D_0} \left(1 + \eta_{D_1}^{(0)} Rn + \eta_{D_2}^{(0)} Rn^2 + \eta_{D_3}^{(0)} Rn^3 \right) + \\ &\quad C_{D_2} \alpha^2 \left(1 + \eta_{D_1}^{(2)} Rn + \eta_{D_2}^{(2)} Rn^2 + \eta_{D_3}^{(2)} Rn^3 \right) \end{aligned} \quad (28a,b)$$

where C_X refers alternatively to C_L , C_Y , C_m , or C_n (i.e., the lift, y-force, pitching and yawing moments) and C_D refers to the drag coefficient. Note that while all of the former coefficients are taken to be linear with angle-of-attack, the drag coefficient is taken to have a quadratic functionality. Furthermore, all of the η_{Xi} and η_{Di} terms on the right-hand side are functions of

the nondimensional spin rate, $\bar{\Omega}$. The data from Ref. 6, fitted with the indicated functionality, serve as default aerodynamic data. These data, as fitted with the above-described functionality, are presented in graphical form in Appendix C.

Appendix C

RLBA Engineering Report 00-02 (Rev. A)

2.4.3 Interpolation of Tabulated Aerodynamic Data

Within the context of efficient usage of the input of the required external aerodynamic coefficients to the **LITE_DYN** computer code, a suitable means must be provided for determining q_∞ values for arbitrary values of nondimensional spin rate. Spline-fit interpolation was selected for providing this interpolation chore. The algorithms used to implement this spline-fit interpolation were taken from Ref. 3.

2.4.4 Application of Coordinate Transformations to Aerodynamic Forces and Moments

The actual forces and moments on the vehicle are then dimensionalized in the usual manner and resolved into the body fixed coordinate system using the transformation matrix defined in Eq 6:

Forces:

$$\left\{ F^{(a)} \right\} = \left\{ \begin{matrix} F_x^{(a)} \\ F_y^{(a)} \\ F_z^{(a)} \end{matrix} \right\}_{BF} = q_\infty S_{ref} \left[T_{WA \rightarrow 3}^{(a)} \right] \left\{ \begin{matrix} -C_D \\ C_Y \\ -C_L \end{matrix} \right\}_{WA} = q_\infty S_{ref} \left[T_{WA \rightarrow 3}^{(a)} \right] \{ C_F \}_{WA} \quad (29)$$

Moments at the aerodynamic reference center:

$$\left\{ M^{(a)} \right\}_{arc} = \left\{ \begin{matrix} M_x^{(a)} \\ M_y^{(a)} \\ M_z^{(a)} \end{matrix} \right\}_{BF} = q_\infty S_{ref} \left[T_{WA \rightarrow 3}^{(a)} \right] l_{ref} \left\{ \begin{matrix} 0 \\ C_m \\ C_n \end{matrix} \right\}_{WA} = q_\infty S_{ref} l_{ref} \left[T_{WA \rightarrow 3}^{(a)} \right] \{ C_M \}_{WA} \quad (30a)$$

Moments at the vehicle center of gravity:

$$\left\{ M^{(a)} \right\}_0 = \left\{ M^{(a)} \right\}_{arc} + \left(FS_{arc} - FS_{cg} \right) \left\{ \begin{matrix} 0 \\ F_Z^{(a)} \\ -F_Y^{(a)} \end{matrix} \right\}_{BF} \quad (30b)$$

where FS_{cg} & FS_{arc} are the vehicle fuselage stations, respectively, of the vehicle center of gravity and aerodynamic reference center. Note that the aerodynamic reference center is nominally taken to be zero. The dynamic pressure is defined in the usual manner:

$$q_\infty = \frac{1}{2} \rho_\infty \left(v_x^2 + v_y^2 + v_z^2 \right) \quad (31)$$

Appendix C

RLBA Engineering Report 00-02 (Rev. A)

2.4.5 Perturbational Airloads

As is required for the eigenvalue solution (as is described in detail in a subsequent section), the perturbational forms of the airloads are required. The starting point is the general form of any of the body-fixed airloads:

$$\left\{ F^{(a)} \right\}_{BF} = S_{ref} \frac{1}{2} \rho_{\infty} \left(v_x^2 + v_y^2 + v_z^2 \right) \left[T_{WA \rightarrow 3}^{(a)} \right] \left\{ C_F \right\}_{WA} \quad (32)$$

Since the angle-of attack and side-slip angle are defined only in terms of the three velocity components, the perturbational airloads will be defined only in terms of derivatives with respect to each of these velocity components. Thus, the general expression for the derivatives of perturbational body-fixed (*force*) airloads with respect to the k 'th component of velocity (i.e., $v_k = v_x, v_y$ or v_z) can be expressed as:

$$\left\{ \frac{\partial F^{(a)}}{\partial v_k} \right\}_{BF} = \rho_{\infty} S_{ref} \left\langle v_k \left[T_{WA \rightarrow 3}^{(a)} \right] \left\{ C_F \right\}_{WA} + \left[\frac{\partial T_{WA \rightarrow 3}^{(a)}}{\partial v_k} \right] \left\{ C_F \right\}_{WA} + \left[T_{WA \rightarrow 3}^{(a)} \right] \left\{ \frac{\partial C_F}{\partial v_k} \right\}_{WA} \right\rangle$$

where v_k refers to either v_x, v_y or v_z and where (33)

$$\begin{aligned} \left[\frac{\partial T_{WA \rightarrow 3}^{(a)}}{\partial v_k} \right] &= \left[\frac{\partial T_{WA \rightarrow 3}^{(a)}}{\partial \kappa} \right] \left(\frac{\partial \kappa}{\partial \alpha} \frac{\partial \alpha}{\partial v_k} + \frac{\partial \kappa}{\partial \beta} \frac{\partial \beta}{\partial v_k} \right) + \\ &\quad \left[\frac{\partial T_{WA \rightarrow 3}^{(a)}}{\partial \alpha_{equiv.}} \right] \left(\frac{\partial \alpha_{equiv.}}{\partial \alpha} \frac{\partial \alpha}{\partial v_k} + \frac{\partial \alpha_{equiv.}}{\partial \beta} \frac{\partial \beta}{\partial v_k} \right) \end{aligned} \quad (34)$$

and:

$$\left[\frac{\partial T_{WA \rightarrow 3}^{(a)}}{\partial \kappa} \right] = \begin{bmatrix} 0 & 0 & 0 \\ \cos \kappa \sin \alpha_{equiv} & -\sin \kappa & \cos \kappa \cos \alpha_{equiv} \\ -\sin \kappa \sin \alpha_{equiv} & -\cos \kappa & -\sin \kappa \cos \alpha_{equiv} \end{bmatrix} \quad (35)$$

$$\left[\frac{\partial T_{WA \rightarrow 3}^{(a)}}{\partial \alpha_{equiv}} \right] = \begin{bmatrix} -\sin \alpha_{equiv} & 0 & -\cos \alpha_{equiv} \\ \sin \kappa \cos \alpha_{equiv} & 0 & -\sin \kappa \sin \alpha_{equiv} \\ \cos \kappa \cos \alpha_{equiv} & 0 & -\cos \kappa \sin \alpha_{equiv} \end{bmatrix} \quad (36)$$

$$\left\{ \frac{\partial C_F}{\partial v_k} \right\}_{WA} = \left\{ \frac{\partial C_F}{\partial \alpha_{equiv}} \right\} \left(\frac{\partial \alpha_{equiv}}{\partial \alpha} \frac{\partial \alpha}{\partial v_k} + \frac{\partial \alpha_{equiv}}{\partial \beta} \frac{\partial \beta}{\partial v_k} \right) \quad (37)$$

Appendix C

RLBA Engineering Report 00-02 (Rev. A)

$$\frac{\partial \xi}{\partial \alpha} = -\frac{\beta}{\alpha_{equiv}^2}; \quad \frac{\partial \xi}{\partial \beta} = \frac{\alpha}{\alpha_{equiv}^2}; \quad \frac{\partial \alpha_{equiv}}{\partial \alpha} = \frac{\alpha}{\alpha_{equiv}^2}; \quad \frac{\partial \alpha_{equiv}}{\partial \beta} = \frac{\beta}{\alpha_{equiv}^2}$$

(38a,b,c,d)

and:

$$\frac{\partial \alpha}{\partial v_x} = -\frac{v_z}{v_x^2 + v_z^2}; \quad \frac{\partial \alpha}{\partial v_y} = 0; \quad \frac{\partial \alpha}{\partial v_z} = \frac{v_x}{v_x^2 + v_z^2}$$

(39a,b,c)

$$\frac{\partial \beta}{\partial v_x} = -\frac{v_y}{v_x^2 + v_z^2}; \quad \frac{\partial \beta}{\partial v_y} = \frac{v_x}{v_x^2 + v_z^2}; \quad \frac{\partial \beta}{\partial v_z} = 0$$

(40a,b,c)

In a similar manner, the derivatives of the perturbational components of body-fixed (*moment*) airloads with respect to the components of velocity are expressible as:

$$\left\{ \frac{\partial \mathcal{M}^{(a)}}{\partial v_k} \right\}_{BF} = q_{\infty} S_{ref} l_{ref} \left\langle v_k \left[T_{WA \rightarrow 3}^{(a)} \right] \{C_M\}_{WA} + \left[\frac{\partial T_{WA \rightarrow 3}^{(a)}}{\partial v_k} \right] \{C_M\}_{WA} + \left[T_{WA \rightarrow 3}^{(a)} \right] \left\{ \frac{\partial \mathcal{C}_M}{\partial v_k} \right\}_{WA} \right\rangle$$

(41)

Similar to Eq.35, the derivative of the wind-axis coefficients is expressible as:

$$\left\{ \frac{\partial \mathcal{C}_M}{\partial v_k} \right\} = \left\{ \frac{\partial \mathcal{C}_M}{\partial \alpha_{equiv}} \right\} \left(\frac{\partial \alpha_{equiv}}{\partial \alpha} \frac{\partial \alpha}{\partial v_k} + \frac{\partial \alpha_{equiv}}{\partial \beta} \frac{\partial \beta}{\partial v_k} \right)$$

(42)

All other terms in Eq. 41 have been previously defined. The partial derivative vectors, Eqs. 33 & 41 are then used to define the linearized equations, as described in a subsequent section. Note that the derivatives of $\{C_F\}$ and $\{C_M\}$ with respect to α_{equiv} are achieved using the derivative information inherent in the spline-fit interpolation algorithms.

Appendix C

RLBA Engineering Report 00-02 (Rev. A)

2.5 Propulsion Characteristics

2.5.1 Laser Beam Transmission Characteristics

The overriding parameter that determines the propulsion of the Lightcraft is the (time-averaged) power that gets delivered to the Lightcraft, P_{ave} . This in turn is determined by the time-averaged power density output from the laser, Φ_{LB} . The beam cross-section area, S_{LB} , and the attenuation factor for the beam due to atmospheric conditions, Ξ_{LB} . The power output is determined by the pulsed power output and impulse rate and is therefore considered herein to be a form of rating of the source laser. This time-averaged power output is the appropriate input for the **LITE_DYN** computer code.

The attenuation characteristics, however, are determined by the downrange distance and zenith angle of the target point (i.e., the Lightcraft). Ultimately the attenuation characteristics must depend in part on the altitude of the Lightcraft as well as the distance of the Lightcraft from the laser. The functionality of Ξ_{LB} can be assumed to be first, a function of zenith angle and secondarily a function of range, which is, in turn, a function of zenith angle. The attenuation function is therefore modeled as follows:

$$\Xi_{LB}(range, \gamma_{LB}) = f_1(range(\gamma_{LB})) \quad (43)$$

The implementation of the attenuation coefficient in the **LITE_DYN** computer code is based on the input of tabular values the attenuation factor with dependency in terms of specified ranges for each selected value of zenith angle. [Note that, as with the implementation of the interpolation of the tabulated airloads, all the propulsion-related tabulated functions use the spline-fit interpolation techniques, as presented in Ref. 3, in the **LITE_DYN** computer code.] The power that ultimately reaches the Lightcraft is then expressed simply as a product of the average power density, the attenuation factor and the laser cross-section area.

The power that actually gets *utilized* by the Lightcraft is determined by how much of the Lightcraft's silhouette area is immersed in the laser beam. Thus the power that actually gets converted to thrust should be adjusted by an efficiency factor, η_{LB} , based on the Lightcraft's silhouette area in relation to the beam's area:

$$\bar{P} = P_{ave} = \Phi_{LB} \Xi_{LB} S_{LB} \eta_{LB} \quad (44)$$

where η_{LSD} may be roughly approximated by:

$$\eta_{LB} = \begin{cases} S_{ref} / S_{LB} \rightarrow S_{ref} < S_{LB} \\ 1 \rightarrow S_{ref} \geq S_{LB} \end{cases} \quad (45)$$

Appendix C

RLBA Engineering Report 00-02 (Rev. A)

where S_{ref} is the cross-section area of the Lightcraft, as is also used to define the vehicle's aerodynamic characteristics.

2.5.2 Gross Coupling Coefficient and Thrust Characteristics

Once the power impacting on the Lightcraft has been determined, the resulting thrust can then be determined. The thrust is determined using an experimentally determined *gross coupling coefficient* factor, C_C , that relates the thrust produced to the laser power actually being utilized by Lightcraft. The thrust is nominally just the product of the coupling coefficient and the utilized power and, without any attenuation factors, is denoted the *gross* thrust. Ref. 1 presents analytical predictions of the coupling coefficient as a function of Mach no. and altitude. These results have been incorporated in the LITE_DYN computer code as default values for C_C . These analytical results are presented in Fig. 3.

Two factors that have been found to attenuate the gross thrust, $F_{LOS}^{(t)}$, and $F_{AOS}^{(t)}$, are those due to *linear offset* and *angular offset* Δr and $\Delta \xi$, respectively. When these factors are included the final averaged thrust can be written as:

$$\bar{T} = T_{ave.} = C_C P_{ave.} F_{LOS}^{(t)}(\Delta \bar{r}) F_{AOS}^{(t)}(\Delta \xi) - C_{D_{RAM}} q S_{ref} = F_x^{(p)} \quad (46)$$

Note that in Eq. 46 the linear offset has been normalized by the maximum radius, r_{max} ($= l_{ref}$)

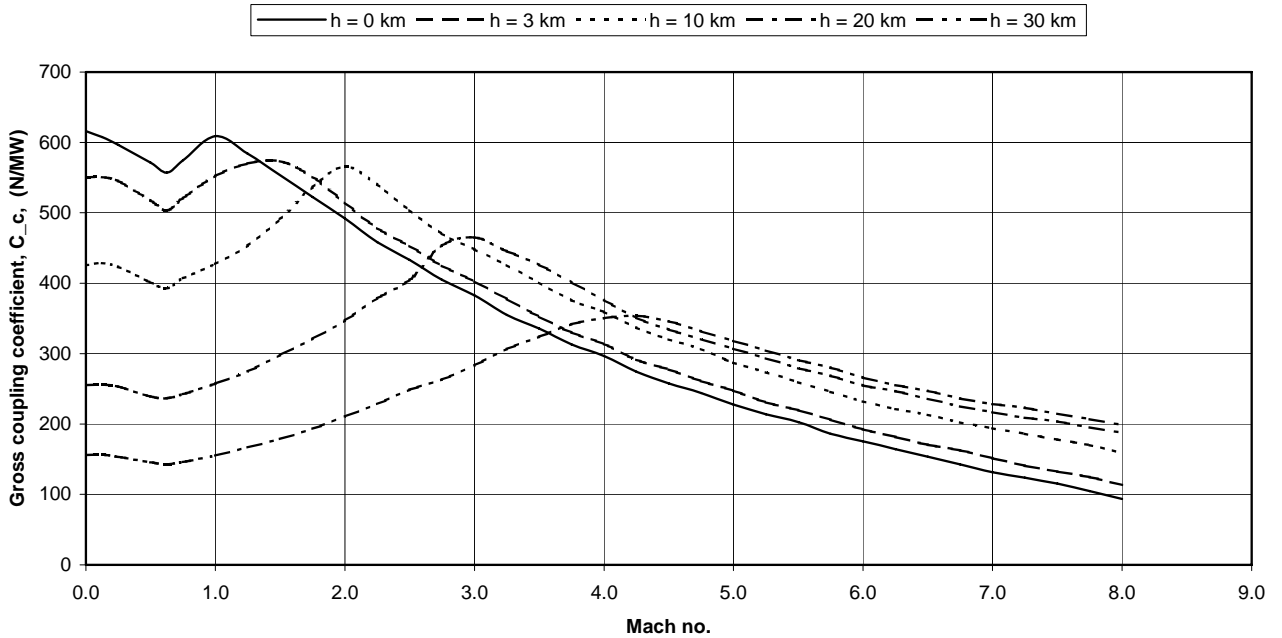


Fig. 3 Gross coupling coefficient vs Mach no. and altitude

Appendix C

RLBA Engineering Report 00-02 (Rev. A)

Using what limited experimental data that exists, tabulated curves for $F^{(t)}_{LOS}$, and $F^{(t)}_{AOS}$ have been prepared and are presented in Figures 4 and 5. Note that consistent with Eq. 46, the linear offset curve has been normalized by the Lightcraft maximum radius, r_{max} ($= l_{ref}$):

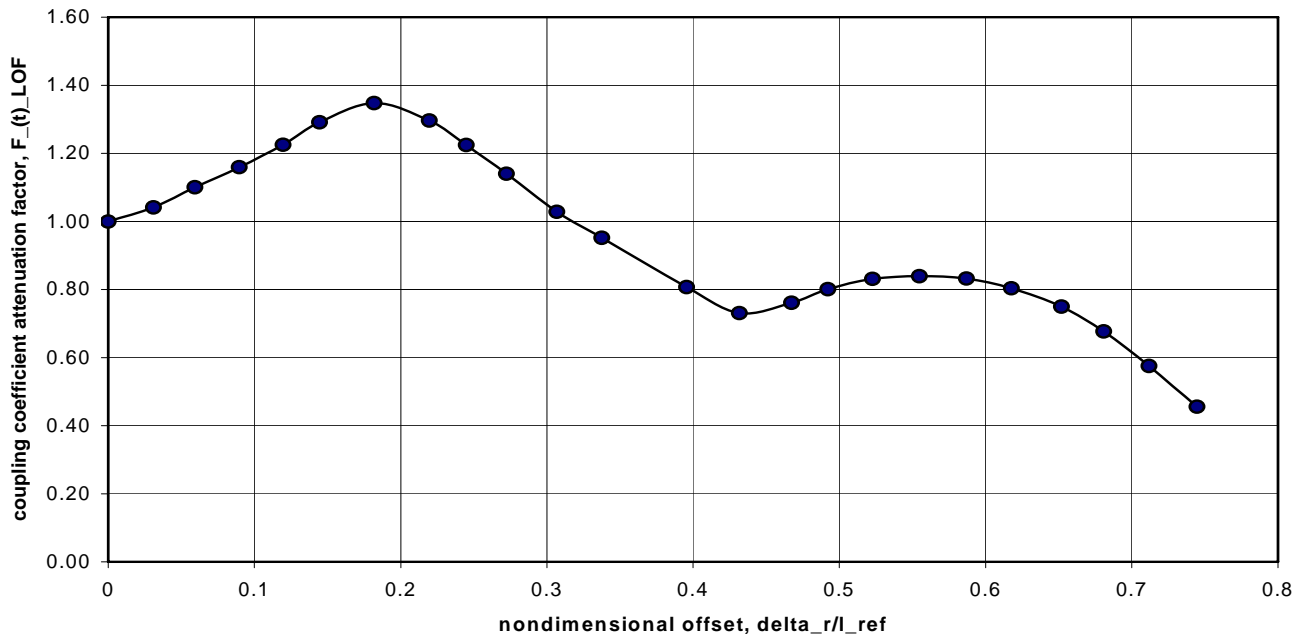


Fig. 4 Coupling coefficient attenuation factor due to linear offset

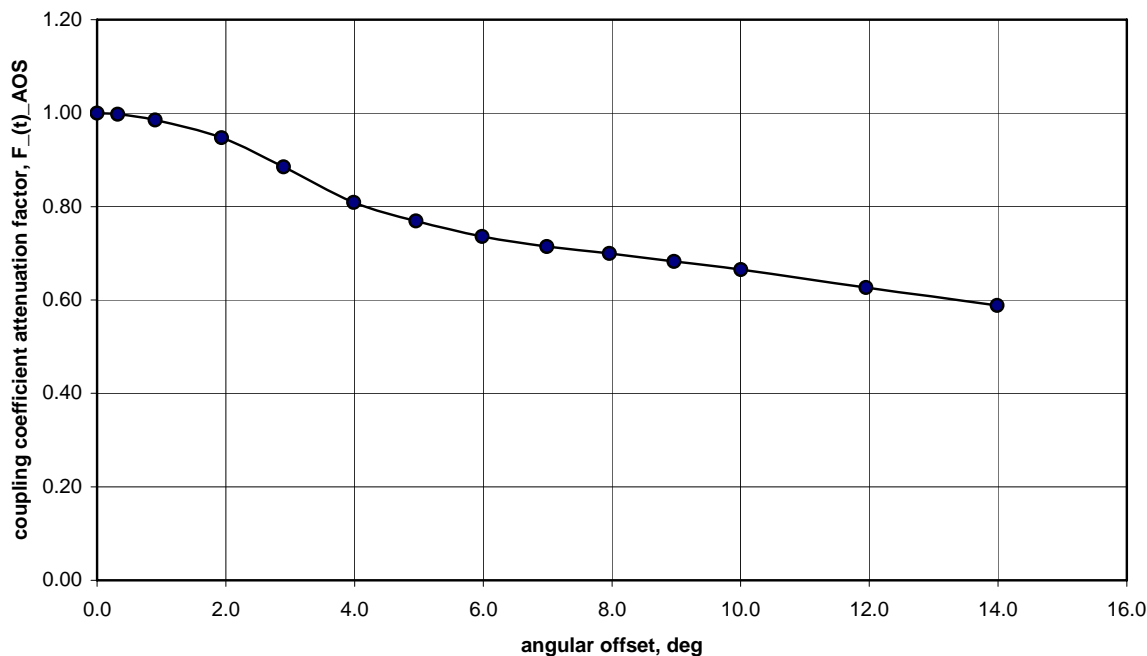


Fig. 5 Coupling coefficient attenuation factor due to angular offset

Appendix C

RLBA Engineering Report 00-02 (Rev. A)

2.5.3 Side Force and Moment Coupling

The same offsets, both linear and angular, used for modeling the propulsive thrust, can similarly be used to advantage in defining the time-averaged side force and moment:

Side Force:

$$\bar{F}_S^{(p)} = C_C P_{avg} \left(F_{LOS}^{(s)} + F_{AOS}^{(s)} \right) = C_C P_{avg} \left(F_{LOS}^{(s)} (\Delta \bar{r}) + F_{AOS}^{(s)} (\Delta \xi) \right) \quad (47)$$

Pitching Moments: In the case of moments resulting from the laser propulsive forces, two effects can be identified: a pure couple and a moment arising from the side force acting on a moment arm:

$$\bar{M}^{(p)} = \left(FS_{pc} - FS_{cg} \right) \bar{F}_S^{(p)} + C_C P_{avg} l_{ref} \left(F_{LOS}^{(m)} (\Delta \bar{r}) + F_{AOS}^{(m)} (\Delta \xi) \right) \quad (48)$$

where FS_{pc} is the fuselage station of the propulsive center, and $\Delta \bar{r}$ and $\Delta \xi$ are, respectively, the amplitudes of linear and angular offset. Note that:

$$\Delta \bar{r} = \Delta r / l_{ref} \quad (49)$$

The sign convention used for force and moment due to lateral offset and angular offset are given in Fig. 6:

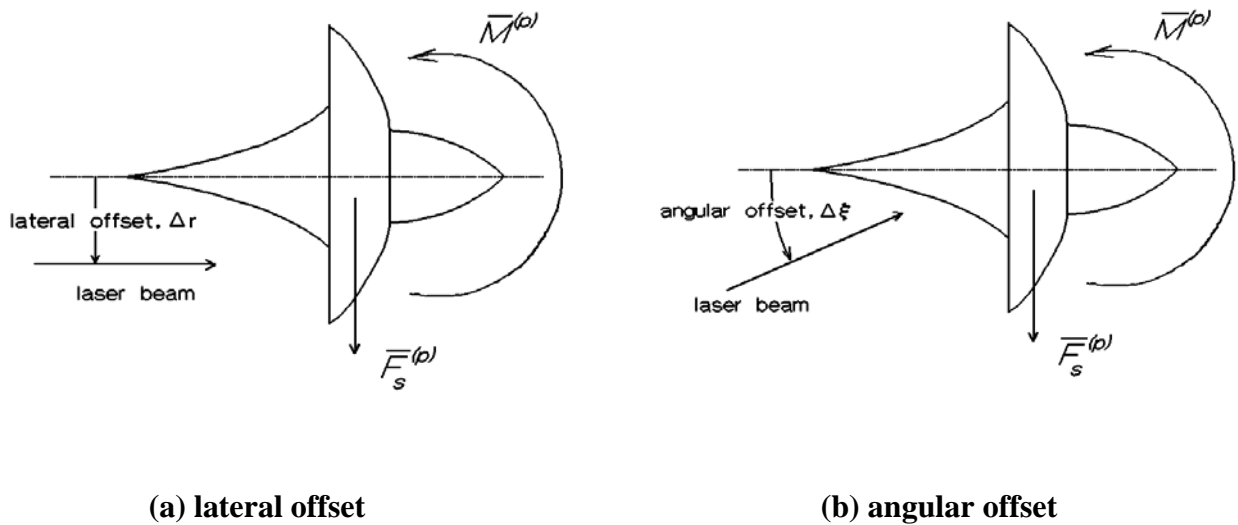


Fig. 6 Sign conventions for lateral force and transverse moment due to linear and angular offsets

Appendix C

RLBA Engineering Report 00-02 (Rev. A)

Of all the coupling coefficient factors defined in Eqs. 47 & 48, only the side force coupling coefficient factor due to linear offset has been experimentally evaluated. These data are shown in Figure 7:

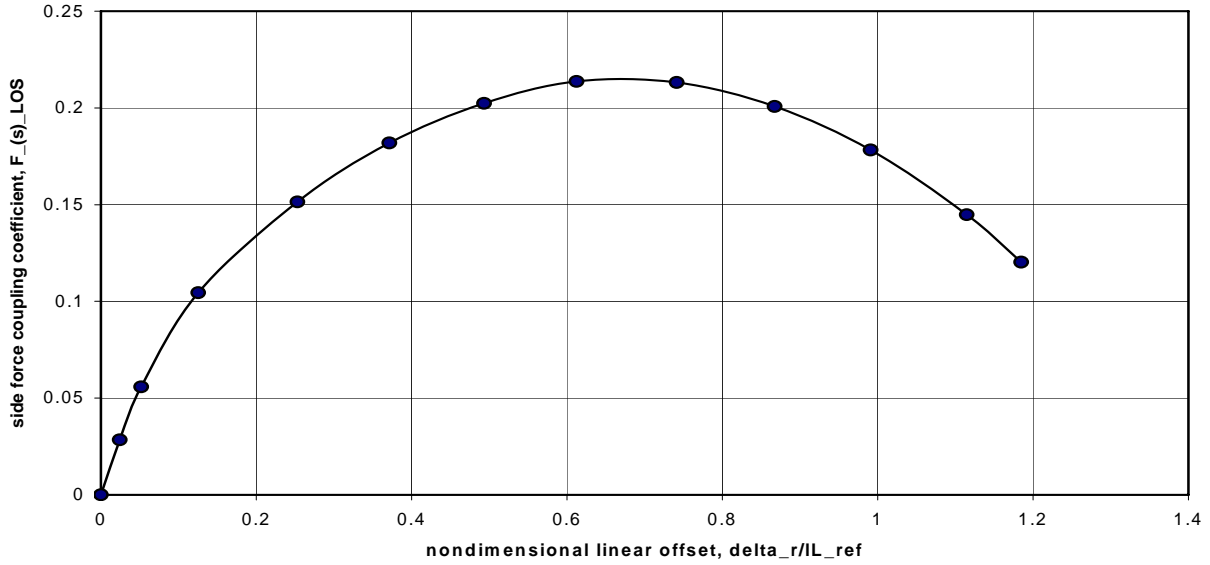


Fig. 7 Side force coupling coefficient factor due to linear offset

2.5.4 Laser Pointer System

Before the components of propulsive force and moment can be defined, the equations relating to linear and angular offset must be formulated. To this end two Earth-fixed coordinate systems, along with their mutual transformation matrix, must be considered: the local system attached to the launch point (i_1, j_1, k_1 system), and the local system of the Lightcraft, as defined by the vehicle's altitude, latitude and longitude (i_2, j_2, k_2). Figure 8 presented below, depicts these two coordinate systems in relation to the geosynchronous system (I, J, K). Note that the $(\dots)_2$ system is rotationally displaced from the $(\dots)_1$ system by the change in longitude, $\Psi_L (= L_2 - L_1)$, and the difference in latitude ($\Theta_2 - \Theta_1$):

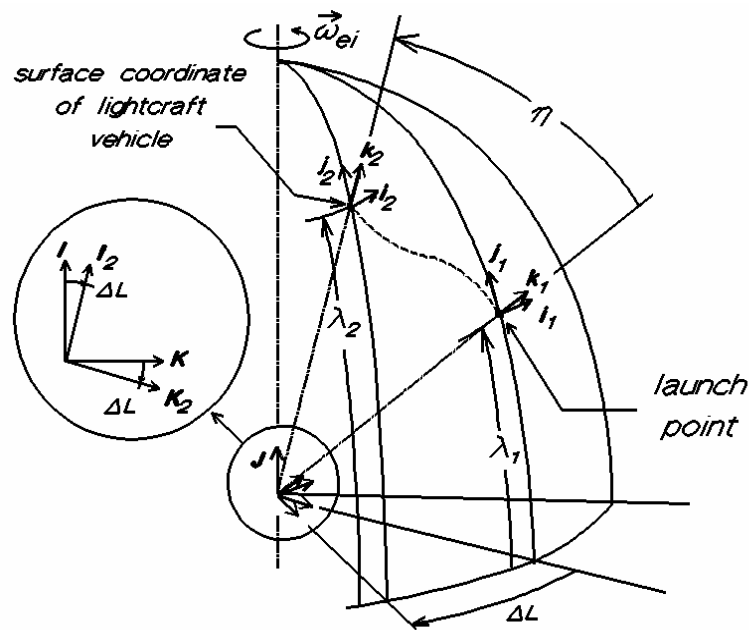


Fig. 8 Vehicle and launch point local Earth-fixed coordinate systems

2.5.4.1 Coordinate System Transformations: The $(\dots)_1$ coordinate system is related to the geosynchronous system as follows:

$$\left\{ \begin{matrix} \vec{i}_1 \\ \vec{j}_1 \\ \vec{k}_1 \end{matrix} \right\} = \begin{bmatrix} 1 & 0 & 0 \\ 0 & \cos \lambda_1 & -\sin \lambda_1 \\ 0 & \sin \lambda_1 & \cos \lambda_1 \end{bmatrix} \left\{ \begin{matrix} \vec{I} \\ \vec{J} \\ \vec{K} \end{matrix} \right\} \quad (50)$$

The $(\dots)_2$ coordinate is similarly related to the geosynchronous system:

$$\begin{Bmatrix} \vec{i}_2 \\ \vec{j}_2 \\ \vec{k}_2 \end{Bmatrix} = \begin{bmatrix} 1 & 0 & 0 \\ 0 & \cos \lambda_2 & -\sin \lambda_2 \\ 0 & \sin \lambda_2 & \cos \lambda_2 \end{bmatrix} \begin{bmatrix} \cos \Delta L & 0 & \sin \Delta L \\ 0 & 1 & 0 \\ -\sin \Delta L & 0 & \cos \Delta L \end{bmatrix} \begin{Bmatrix} \vec{I} \\ \vec{J} \\ \vec{K} \end{Bmatrix} \quad (51)$$

These two equations can then be used to relate the $(\dots)_1$ system to the $(\dots)_2$ system:

$$\begin{Bmatrix} \ddot{i}_2 \\ \ddot{j}_2 \\ \ddot{k}_2 \end{Bmatrix} = \begin{bmatrix} \cos \Delta L & -\sin \Delta L \sin \lambda_1 & \sin \Delta L \cos \lambda_1 \\ \sin \Delta L \sin \lambda_2 & (\cos \Delta L \sin \lambda_1 \sin \lambda_2 + \cos \lambda_1 \cos \lambda_2) & (-\cos \Delta L \sin \lambda_2 \cos \lambda_1 + \cos \lambda_2 \sin \lambda_1) \\ -\sin \Delta L \cos \lambda_2 & (-\cos \Delta L \sin \lambda_1 \cos \lambda_2 + \cos \lambda_1 \sin \lambda_2) & (\cos \Delta L \cos \lambda_1 \cos \lambda_2 + \sin \lambda_1 \sin \lambda_2) \end{bmatrix} \begin{Bmatrix} \ddot{i}_1 \\ \ddot{j}_1 \\ \ddot{k}_1 \end{Bmatrix} = [T_{1 \rightarrow 2}] \begin{Bmatrix} \ddot{i}_1 \\ \ddot{j}_1 \\ \ddot{k}_1 \end{Bmatrix} \quad (52)$$

Appendix C

RLBA Engineering Report 00-02 (Rev. A)

$$\begin{Bmatrix} \vec{i}_1 \\ \vec{j}_1 \\ \vec{k}_1 \end{Bmatrix} = [T_{2 \rightarrow 1}] \begin{Bmatrix} \vec{i}_2 \\ \vec{j}_2 \\ \vec{k}_2 \end{Bmatrix} \quad (53)$$

where: $[T_{2 \rightarrow 1}] = [T_{1 \rightarrow 2}]^{-1} = [T_{1 \rightarrow 2}]^T$. Note also that, for both the $(\dots)_1$ and $(\dots)_2$ systems:

$$\begin{Bmatrix} \vec{i} \\ \vec{j} \\ \vec{k} \end{Bmatrix} \equiv \begin{Bmatrix} east \\ north \\ up \end{Bmatrix} \quad (54)$$

2.5.4.2 Range Distance: Eq. 52 can be used to determine the Lightcraft's position in the $(\dots)_1$ coordinate system:

$$\begin{aligned} \vec{R}_{LC} = R_{gc_{LC}} \vec{k}_2 = R_{gc_{LC}} \begin{bmatrix} 0 & 0 & 1 \end{bmatrix} \begin{Bmatrix} \vec{i}_2 \\ \vec{j}_2 \\ \vec{k}_2 \end{Bmatrix} = R_{gc_{LC}} \bullet \\ \begin{bmatrix} -\sin \Delta L \cos \lambda_2, & (-\cos \Delta L \sin \lambda_1 \cos \lambda_2 + \cos \lambda_1 \sin \lambda_2), & (\cos \Delta L \cos \lambda_2 \cos \lambda_1 + \sin \lambda_1 \sin \lambda_2) \end{bmatrix} \begin{Bmatrix} \vec{i}_1 \\ \vec{j}_1 \\ \vec{k}_1 \end{Bmatrix} \end{aligned} \quad (55a)$$

where:

$$R_{gc_{LC}} = R_{gc_{launch}} + \Delta R_{gc} \quad (55b)$$

The vector defining the launch point in the $(\dots)_1$ system is simply described as:

$$\vec{R}_{launch} = R_{gc_{launch}} \vec{k}_1 \quad (56)$$

[Note that the geocentric radius of the launch site is determined by the launch altitude, h_{launch} , and the geodetic latitude (see Appendix B).]

The vector dot product of these two vectors will yield the down range angle of the Lightcraft vehicle relative to the launch point:

$$\begin{aligned} \eta &= \cos^{-1} \left[\vec{R}_{LC} \bullet \vec{R}_{launch} / R_{gc_{LC}} R_{gc_{launch}} \right] \\ &= \cos^{-1} (\cos \Delta L \cos \lambda_1 \cos \lambda_2 + \sin \lambda_1 \sin \lambda_2) \end{aligned} \quad (57)$$

Appendix C

RLBA Engineering Report 00-02 (Rev. A)

With this angle and the use of the law of cosines, the range can be determined:

$$\begin{aligned}
 S &= \sqrt{R_{gc_{launch}}^2 + R_{gc_{LC}}^2 - 2R_{gc_{launch}} R_{gc_{LC}} \cos \eta} \\
 &= \sqrt{\Delta R_{gc}^2 + 2R_{gc_{launch}} (R_{gc_{launch}} + \Delta R_{gc})(1 - \cos \eta)}
 \end{aligned}
 \tag{58a}$$

The Lightcraft's range "vector" can also be formed using Eqs. 55 and 56:

$$\begin{aligned}
 \vec{S}_{LC} &= \vec{R}_{LC} - \vec{R}_{launch} = R_{gc_{LC}} \vec{k}_2 - R_{gc_{launch}} \vec{k}_1 = \\
 &\left[-R_{gc_{LC}} \sin \Delta L \cos \lambda_2, R_{gc_{LC}} (-\cos \Delta L \sin \lambda_1 \cos \lambda_2 + \cos \lambda_1 \sin \lambda_2), \left(R_{gc_{LC}} (\cos \Delta L \cos \lambda_1 \cos \lambda_2 + \sin \lambda_1 \sin \lambda_2) - R_{gc_{launch}} \right) \right] \begin{Bmatrix} \vec{i}_1 \\ \vec{j}_1 \\ \vec{k}_1 \end{Bmatrix}
 \end{aligned}
 \tag{58b}$$

Although Eq. 58b is exact, it is computationally impractical due to the multiplication of "large" numbers with "small" numbers and the difference between "large" numbers. As was introduced in Section 2.3.4 the components of the Lightcraft range vector are most efficiently calculated using the solutions of their differential equations:

$$\begin{aligned}
 \dot{S}_{x_{LC}}^{(1)} &= \frac{d}{dt} (-R_{gc_{LC}} \sin \Delta L \cos \lambda_2) = -V_z \sin \Delta L \cos \lambda_2 \\
 &\quad + V_t (\cos \Delta L \cos \lambda_2 \sin \chi + \sin \Delta L \sin \lambda_2 \cos \chi)
 \end{aligned}
 \tag{58c}$$

$$\begin{aligned}
 \dot{S}_{y_{LC}}^{(1)} &= \frac{d}{dt} [R_{gc_{LC}} (-\cos \Delta L \sin \lambda_1 \cos \lambda_2 + \cos \lambda_1 \sin \lambda_2)] = \\
 &\quad V_t [\cos \chi (\cos \Delta L \sin \lambda_1 \sin \lambda_2 + \cos \lambda_1 \cos \lambda_2) - \sin \chi \sin \Delta L \sin \lambda_1 \cos \lambda_2] \\
 &\quad + V_z (\cos \lambda_1 \sin \lambda_2 - \cos \Delta L \sin \lambda_1 \cos \lambda_2)
 \end{aligned}
 \tag{58d}$$

$$\begin{aligned}
 \dot{S}_{z_{LC}}^{(1)} &= \frac{d}{dt} [R_{gc_{LC}} (\cos \Delta L \cos \lambda_1 \cos \lambda_2 + \sin \lambda_1 \sin \lambda_2) - R_{gc_{launch}}] = \\
 &\quad V_t [\cos \chi (\sin \lambda_1 \cos \lambda_2 - \cos \Delta L \cos \lambda_1 \sin \lambda_2) + \sin \chi \sin \Delta L \cos \lambda_1 \sin \lambda_2] \\
 &\quad + V_z (\cos \Delta L \cos \lambda_1 \cos \lambda_2 + \sin \lambda_1 \sin \lambda_2)
 \end{aligned}
 \tag{58e}$$

Appendix C

RLBA Engineering Report 00-02 (Rev. A)

2.5.4.3 Laser Beam Offsets: The offsets can be calculated by combining the vehicle's range position (Eq. 58b) with the laser focus center range position vector (as determined by the laser pointing zenith angle, γ_{LP}), and bearing angle, χ_{LP} . In the $(\dots)_1$ coordinate system, this vector is expressed as:

$$\vec{S}_{FC} = S \begin{bmatrix} \sin \gamma_{LP} \sin \chi_{LP}, & \sin \gamma_{LP} \cos \chi_{LP}, & \cos \gamma_{LP} \end{bmatrix} \begin{Bmatrix} \vec{i}_1 \\ \vec{j}_1 \\ \vec{k}_1 \end{Bmatrix} \quad (59)$$

Or, in terms of the $(\dots)_2$ coordinate system:

$$\vec{S}_{FC} = S \begin{bmatrix} \sin \gamma_{LP} \sin \chi_{LP}, & \sin \gamma_{LP} \cos \chi_{LP}, & \cos \gamma_{LP} \end{bmatrix} [T_{2 \rightarrow 1}] \begin{Bmatrix} \vec{i}_2 \\ \vec{j}_2 \\ \vec{k}_2 \end{Bmatrix} = \begin{bmatrix} \hat{S}_{FC_x} & \hat{S}_{FC_y} & \hat{S}_{FC_z} \end{bmatrix} \begin{Bmatrix} \vec{i}_2 \\ \vec{j}_2 \\ \vec{k}_2 \end{Bmatrix} \quad (60a)$$

One simplification that will prove useful is to define the unit laser focus center range position vector. (Computationally, this is useful for start-up conditions wherein the range is zero.):

$$\begin{aligned} \vec{1}_{FC} &= \vec{S} / S = \begin{bmatrix} \sin \gamma_{LP} \sin \chi_{LP}, & \sin \gamma_{LP} \cos \chi_{LP}, & \cos \gamma_{LP} \end{bmatrix} [T_{2 \rightarrow 1}] \begin{Bmatrix} \vec{i}_2 \\ \vec{j}_2 \\ \vec{k}_2 \end{Bmatrix} \\ &\equiv \begin{bmatrix} \hat{S}_{FC_x} & \hat{S}_{FC_y} & \hat{S}_{FC_z} \end{bmatrix} \begin{Bmatrix} \vec{i}_2 \\ \vec{j}_2 \\ \vec{k}_2 \end{Bmatrix} \end{aligned} \quad (60b)$$

The **(normalized) linear lateral offset** can then be easily calculated from the difference between the focus center vector and the vehicle position vector, as normalized by the reference length. But first the “2” coordinate system must be related to the “3” coordinate system, which is attached to the Lightcraft (the body-fixed) coordinate system. Relative to the “2” coordinate system this coordinate system is defined by the vehicle's heading angle, ψ , and the pitch angle, θ .

$$\begin{Bmatrix} \vec{i}_2 \\ \vec{j}_2 \\ \vec{k}_2 \end{Bmatrix} = \begin{Bmatrix} east \\ north \\ up \end{Bmatrix} = \begin{bmatrix} \sin \psi & \cos \psi & 0 \\ \cos \psi & -\sin \psi & 0 \\ 0 & 0 & 1 \end{bmatrix} \begin{bmatrix} \cos \theta & 0 & \sin \theta \\ 0 & 1 & 0 \\ \sin \theta & 0 & -\cos \theta \end{bmatrix} \begin{Bmatrix} \vec{i}_3 \\ \vec{j}_3 \\ \vec{k}_3 \end{Bmatrix} = [T_{3 \rightarrow 2}] \begin{Bmatrix} \vec{i}_3 \\ \vec{j}_3 \\ \vec{k}_3 \end{Bmatrix} \quad (61)$$

Appendix C

RLBA Engineering Report 00-02 (Rev. A)

The lateral offset vector can then be defined as follows:

$$\begin{aligned}\Delta \vec{r} &= (\vec{S}_{FC} - \vec{S}_{LC}) = \begin{bmatrix} \Delta \hat{r}_x & \Delta \hat{r}_y & \Delta \hat{r}_z \end{bmatrix} \begin{Bmatrix} \vec{i}_2 \\ \vec{j}_2 \\ \vec{k}_2 \end{Bmatrix} \\ &= \begin{bmatrix} \Delta \hat{r}_x & \Delta \hat{r}_y & \Delta \hat{r}_z \end{bmatrix} [T_{3 \rightarrow 2}] \begin{Bmatrix} \vec{i}_3 \\ \vec{j}_3 \\ \vec{k}_3 \end{Bmatrix} = \begin{bmatrix} \Delta \tilde{r}_x & \Delta \tilde{r}_y & \Delta \tilde{r}_z \end{bmatrix} \begin{Bmatrix} \vec{i}_3 \\ \vec{j}_3 \\ \vec{k}_3 \end{Bmatrix}\end{aligned}\quad (62)$$

Note that the x -component of offset is not a consideration and is not used. The total (normalized) lateral offset is then obtained from the y_2 - and z_2 - components of the \vec{r} vector:

$$\Delta \bar{r} = \sqrt{\Delta \tilde{r}_y^2 + \Delta \tilde{r}_z^2} / l_{ref} \quad (63)$$

This is then the value of lateral offset required for Eqs. 47 & 48.

The **angular offset angle** can be calculated by again considering the unit laser focus center range position vector. Use of Eq. 61 enables this vector to be expressed in the “3” coordinate system:

$$\vec{1}_{FC} = \begin{bmatrix} \hat{s}_{FC_x} & \hat{s}_{FC_y} & \hat{s}_{FC_z} \end{bmatrix} [T_{3 \rightarrow 2}] \begin{Bmatrix} \vec{i}_3 \\ \vec{j}_3 \\ \vec{k}_3 \end{Bmatrix} = \begin{bmatrix} \tilde{s}_{FC_x} & \tilde{s}_{FC_y} & \tilde{s}_{FC_z} \end{bmatrix} \begin{Bmatrix} \vec{i}_3 \\ \vec{j}_3 \\ \vec{k}_3 \end{Bmatrix} \quad (64)$$

The magnitude of the angular offset can be determined using the dot product of this unit vector with the \vec{i}_3 (unit) vector:

$$\Delta \xi = \cos^{-1}(\vec{i}_3 \bullet \vec{1}_{FC}) = \cos^{-1}(\tilde{s}_{FC_x}) \quad (65a)$$

Eq. 65 then defines the magnitude of the angular offset to be used in Eqs. 47 & 48. In order to obtain the projections of the offset angles on the i_3 - j_3 plane and i_3 - k_3 planes, as well as to resolve loads into their appropriate components, we use the cross product of the two unit vectors:

$$\vec{i}_3 \times \vec{1}_{FC} = \begin{vmatrix} \vec{i}_3 & \vec{j}_3 & \vec{k}_3 \\ 1 & 0 & 0 \\ \tilde{s}_{FC_x} & \tilde{s}_{FC_y} & \tilde{s}_{FC_z} \end{vmatrix} = \begin{pmatrix} -\tilde{s}_{FC_z} \vec{j}_3 + \tilde{s}_{FC_y} \vec{k}_3 \end{pmatrix} \quad (65b)$$

Appendix C

RLBA Engineering Report 00-02 (Rev. A)

Reference to Figure 9 shows that the projections of the $\Delta\xi$ angle onto the Lightcraft's longitudinal and horizontal planes, $\Delta\xi_y$ and $\Delta\xi_z$, respectively, are expressible as:

$$\Delta\xi_y = \sin^{-1}\left(\frac{-\tilde{s}_{FC_z}}{\sqrt{\tilde{s}_{FC_x}^2 + \tilde{s}_{FC_z}^2}}\right); \quad \Delta\xi_z = \sin^{-1}\left(\frac{\tilde{s}_{FC_y}}{\sqrt{\tilde{s}_{FC_x}^2 + \tilde{s}_{FC_y}^2}}\right) \quad (66a)$$

and that, using Eq. 65b, the angle μ is expressible as:

$$\mu = \tan^{-1}\left(\tilde{s}_{FC_y} / -\tilde{s}_{FC_z}\right) = \sin^{-1}\left(\tilde{s}_{FC_y} / \tilde{s}_{FC_{yz}}\right) \quad (66b)$$

where:

$$\tilde{s}_{FC_{yz}} = \sqrt{\tilde{s}_{FC_y}^2 + \tilde{s}_{FC_z}^2} \quad (66c)$$

2.5.4.4 Body Force and Moment Components: The remaining issue is to resolve the forces and moments arising from lateral and angular offset into the y_3 - and z_3 -components. Figure 9 serves as a guide to making this determination:

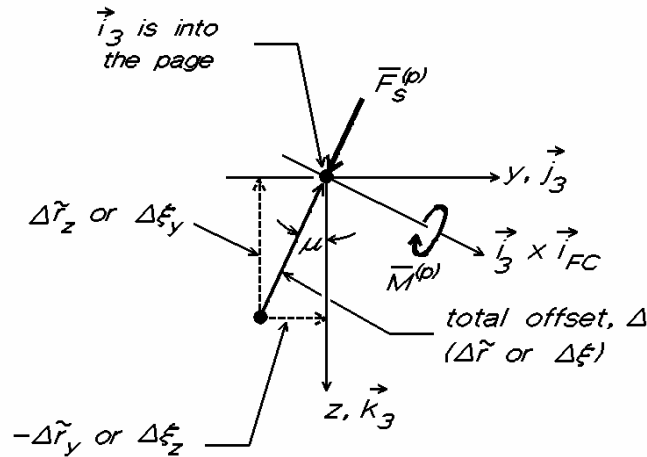


Fig. 9 Geometry defining decomposition of propulsive side forces and moments due to lateral and angular offsets

Appendix C

RLBA Engineering Report 00-02 (Rev. A)

Thus, the components of propulsive side force can then be expressed as follows:

$$\begin{Bmatrix} F_{S_y}^{(p)} \\ F_{S_z}^{(p)} \end{Bmatrix} = C_C P_{avg} \left[F_{LOS}^{(s)}(\Delta \bar{r}) \begin{Bmatrix} \Delta \tilde{r}_y / \Delta r \\ \Delta \tilde{r}_z / \Delta r \end{Bmatrix} - F_{AOS}^{(s)}(\Delta \xi) \begin{Bmatrix} \tilde{S}_{FC_y} / \tilde{S}_{FC_{yz}} \\ \tilde{S}_{FC_z} / \tilde{S}_{FC_{yz}} \end{Bmatrix} \right] \quad (67)$$

Similarly, the components of propulsive moments can be expressed as:

$$\begin{Bmatrix} \bar{M}_y^{(p)} \\ \bar{M}_z^{(p)} \end{Bmatrix} = (FS_{pc} - FS_{cg}) \begin{Bmatrix} -\bar{F}_{S_z}^{(p)} \\ \bar{F}_{S_y}^{(p)} \end{Bmatrix} + C_C P_{avg} l_{ref} \left[F_{LOS}^{(m)}(\Delta \bar{r}) \begin{Bmatrix} \Delta \tilde{r}_z / \Delta r \\ -\Delta \tilde{r}_y / \Delta r \end{Bmatrix} + F_{AOS}^{(m)}(\Delta \xi) \begin{Bmatrix} -\tilde{S}_{FC_z} / \tilde{S}_{FC_{yz}} \\ \tilde{S}_{FC_y} / \tilde{S}_{FC_{yz}} \end{Bmatrix} \right] \quad (68)$$

2.5.5 Perturbational Propulsive Forces and Moments

For purposes of inclusion of the perturbational propulsive forces and moments, the perturbational variables of interest are the perturbational lateral and angular offsets, \mathfrak{R}_y & \mathfrak{R}_z , and \mathfrak{R}_{θ_y} & \mathfrak{R}_{θ_z} , respectively. To facilitate the calculations of the partial derivatives of the force and moment components defined by Eqs. 65 and 66, the intermediary expressions and partial derivatives that follow are required.

Perturbations in lateral offset: First off, the expressions for the components of lateral offset must include the perturbations \mathfrak{R}_y & \mathfrak{R}_z in the following manner:

$$\Delta r = \sqrt{(\Delta \tilde{r}_y - \delta y)^2 + (\Delta \tilde{r}_z - \delta z)^2} \quad (69)$$

Thus:

$$\frac{\partial \Delta r}{\partial \delta y} = \frac{-\Delta \tilde{r}_y}{\sqrt{\Delta \tilde{r}_y^2 + \Delta \tilde{r}_z^2}}; \quad \frac{\partial \Delta r}{\partial \delta z} = \frac{-\Delta \tilde{r}_z}{\sqrt{\Delta \tilde{r}_y^2 + \Delta \tilde{r}_z^2}} \quad (70a\&b)$$

Note that for instances wherein both the numerator and denominator are equal to zero, these expressions become:

$$\frac{\partial \Delta r}{\partial \delta y} = -1; \quad \frac{\partial \Delta r}{\partial \delta z} = -1 \quad (71a,b)$$

Appendix C

RLBA Engineering Report 00-02 (Rev. A)

Subsequently:

$$\begin{aligned} \left(\frac{\Delta \tilde{r}_y}{\Delta r} \right) \frac{\partial \Delta r}{\partial \delta y} &= \frac{-\Delta \tilde{r}_y^2}{\Delta \tilde{r}_y^2 + \Delta \tilde{r}_z^2}; & \left(\frac{\Delta \tilde{r}_z}{\Delta r} \right) \frac{\partial \Delta r}{\partial \delta z} &= \frac{-\Delta \tilde{r}_z^2}{\Delta \tilde{r}_y^2 + \Delta \tilde{r}_z^2}; \\ \left(\frac{\Delta \tilde{r}_y}{\Delta r} \right) \frac{\partial \Delta r}{\partial \delta z} &= \left(\frac{\Delta \tilde{r}_z}{\Delta r} \right) \frac{\partial \Delta r}{\partial \delta y} = \frac{-\Delta \tilde{r}_y \Delta \tilde{r}_z}{\Delta \tilde{r}_y^2 + \Delta \tilde{r}_z^2} \end{aligned}$$

(72a,b,c&d)

where, again, if the components of Ψr are both equal to zero:

$$\begin{aligned} \left(\frac{\Delta \tilde{r}_y}{\Delta r} \right) \frac{\partial \Delta r}{\partial \delta y} &= \left(\frac{\Delta \tilde{r}_z}{\Delta r} \right) \frac{\partial \Delta r}{\partial \delta z} = -1; \\ \left(\frac{\Delta \tilde{r}_y}{\Delta r} \right) \frac{\partial \Delta r}{\partial \delta z} &= \left(\frac{\Delta \tilde{r}_z}{\Delta r} \right) \frac{\partial \Delta r}{\partial \delta y} = 0 \end{aligned}$$

(73a,b,c&d)

Continuing:

$$\begin{aligned} \frac{\partial}{\partial \delta y} \left(\frac{\Delta \tilde{r}_y}{\Delta r} \right) &= \frac{-\Delta \tilde{r}_z^2}{\left[\Delta \tilde{r}_y^2 + \Delta \tilde{r}_z^2 \right]^{3/2}}; & \frac{\partial}{\partial \delta z} \left(\frac{\Delta \tilde{r}_z}{\Delta r} \right) &= \frac{-\Delta \tilde{r}_y^2}{\left[\Delta \tilde{r}_y^2 + \Delta \tilde{r}_z^2 \right]^{3/2}}; \\ \frac{\partial}{\partial \delta y} \left(\frac{\Delta \tilde{r}_z}{\Delta r} \right) &= \frac{\partial}{\partial \delta z} \left(\frac{\Delta \tilde{r}_y}{\Delta r} \right) = \frac{\Delta \tilde{r}_y \Delta \tilde{r}_z}{\left[\Delta \tilde{r}_y^2 + \Delta \tilde{r}_z^2 \right]^{3/2}} \end{aligned}$$

(74a,b,c&d)

If the components of Ψr are both equal to zero:

$$\frac{\Delta \tilde{r}_y}{\Delta r} \rightarrow 1; \quad \frac{\Delta \tilde{r}_z}{\Delta r} \rightarrow 1$$

Hence, for this case:

$$\frac{\partial}{\partial \delta y} \left(\frac{\Delta \tilde{r}_y}{\Delta r} \right) = \frac{\partial}{\partial \delta z} \left(\frac{\Delta \tilde{r}_z}{\Delta r} \right) = \frac{\partial}{\partial \delta y} \left(\frac{\Delta \tilde{r}_z}{\Delta r} \right) = \frac{\partial}{\partial \delta z} \left(\frac{\Delta \tilde{r}_y}{\Delta r} \right) = 0$$

(75a,b,c&d)

The direct (approximate) derivatives of the side force and pitching moment (due to lateral offset), $(F^{(s)})_{LOS}$, and $(F^{(m)})_{LOS}$, with respect to Ψr , respectively, are inherently obtainable by virtue of the spline-fit interpolation scheme used on the numerical data defining the side force (Fig. 7, e.g.) and pitching moment.

Appendix C

RLBA Engineering Report 00-02 (Rev. A)

$$\begin{aligned}
 \frac{\partial F_{LOS}^{(s)}(\Delta \bar{r})}{\partial \delta y} &= \frac{1}{l_{ref}} \frac{\partial F_{LOS}^{(s)}}{\partial \Delta \bar{r}} \frac{\partial \Delta r}{\partial \delta y} = \frac{1}{l_{ref}} F_{LOS}^{'(s)} \frac{\partial \Delta r}{\partial \delta y}; \\
 \frac{\partial F_{LOS}^{(s)}(\Delta \bar{r})}{\partial \delta z} &= \frac{1}{l_{ref}} \frac{\partial F_{LOS}^{(s)}}{\partial \Delta \bar{r}} \frac{\partial \Delta r}{\partial \delta z} = \frac{1}{l_{ref}} F_{LOS}^{'(s)} \frac{\partial \Delta r}{\partial \delta z} \\
 \frac{\partial F_{LOS}^{(m)}(\Delta \bar{r})}{\partial \delta y} &= \frac{1}{l_{ref}} \frac{\partial F_{LOS}^{(m)}}{\partial \Delta \bar{r}} \frac{\partial \Delta r}{\partial \delta y} = \frac{1}{l_{ref}} F_{LOS}^{'(m)} \frac{\partial \Delta r}{\partial \delta y}; \\
 \frac{\partial F_{LOS}^{(m)}(\Delta \bar{r})}{\partial \delta z} &= \frac{1}{l_{ref}} \frac{\partial F_{LOS}^{(m)}}{\partial \Delta \bar{r}} \frac{\partial \Delta r}{\partial \delta z} = \frac{1}{l_{ref}} F_{LOS}^{'(m)} \frac{\partial \Delta r}{\partial \delta z}
 \end{aligned}
 \tag{76a,b,c&d}$$

where the derivatives of Δr with respect to δy and δz are given by Eqs. 70a & b.

Perturbations in angular offset: Eq. 64b is the appropriate starting point for obtaining the derivatives of the side forces and moments with respect to the perturbational pitching and yawing angular deflections, $\delta \theta_y$ and $\delta \theta_z$, respectively, noting that only the $[T_{3 \rightarrow 2}]$ matrix depends on these variables. For purposes of obtaining the required form, we write θ_y in place of θ :

$$[T_{3 \rightarrow 2}] = \begin{bmatrix} \sin \psi \cos \theta_y & \cos \psi & \sin \psi \sin \theta_y \\ \cos \psi \cos \theta_y & -\sin \psi & \cos \psi \sin \theta_y \\ \sin \theta_y & 0 & -\cos \theta_y \end{bmatrix}
 \tag{77}$$

Then, upon noting that $\cos \psi = \cos \delta \theta_y \cos \delta \theta_z$, the partial derivatives of these matrices can be written as:

$$\frac{\partial}{\partial \theta_y} [T_{3 \rightarrow 2}] = \begin{bmatrix} -\sin \psi \sin \theta_y & 0 & \sin \psi \cos \theta_y \\ -\cos \psi \sin \theta_y & 0 & \cos \psi \cos \theta_y \\ \cos \theta_y & 0 & \sin \theta_y \end{bmatrix}
 \tag{78}$$

$$\frac{\partial}{\partial \theta_z} [T_{3 \rightarrow 2}] = \begin{bmatrix} \cos \psi \cos \theta_y & -\sin \psi & \cos \psi \sin \theta_y \\ -\sin \psi \cos \theta_y & -\cos \psi & -\sin \psi \sin \theta_y \\ 0 & 0 & 0 \end{bmatrix} \cos \theta_y
 \tag{79}$$

With these expressions the following derivatives can be written:

$$\frac{\partial}{\partial \theta_y} (\vec{s}_{FC}) = \begin{bmatrix} \hat{s}_{FC_x} & \hat{s}_{FC_y} & \hat{s}_{FC_z} \end{bmatrix} \left[\frac{\partial T_{3 \rightarrow 2}}{\partial \theta_y} \right] \begin{Bmatrix} \vec{i}_3 \\ \vec{j}_3 \\ \vec{k}_3 \end{Bmatrix}
 \tag{80}$$

Appendix C

RLBA Engineering Report 00-02 (Rev. A)

$$\frac{\partial}{\partial \theta_z} (\vec{s}_{FC}) = \begin{bmatrix} \hat{s}_{FC_x} & \hat{s}_{FC_y} & \hat{s}_{FC_z} \end{bmatrix} \left[\frac{\partial T_{3 \rightarrow 2}}{\partial \theta_z} \right] \begin{Bmatrix} \vec{i}_3 \\ \vec{j}_3 \\ \vec{k}_3 \end{Bmatrix} \quad (81)$$

Combining the Eqs. 78 & 79 with 80 & 81 yields:

$$\frac{\partial}{\partial \theta_y} (\tilde{s}_{FC_x}) = \begin{bmatrix} \hat{s}_{FC_x} & \hat{s}_{FC_y} & \hat{s}_{FC_z} \end{bmatrix} \begin{Bmatrix} -\sin \psi \sin \theta_y \\ -\cos \psi \sin \theta_y \\ \cos \theta_y \end{Bmatrix} \quad (82)$$

$$\frac{\partial}{\partial \theta_z} (\tilde{s}_{FC_x}) = \begin{bmatrix} \hat{s}_{FC_x} & \hat{s}_{FC_y} & \hat{s}_{FC_z} \end{bmatrix} \begin{Bmatrix} \cos \psi \cos \theta_y \\ -\sin \psi \cos \theta_y \\ 0 \end{Bmatrix} \cos \theta_y \quad (83)$$

$$\frac{\partial}{\partial \theta_y} (\tilde{s}_{FC_y}) = \begin{bmatrix} \hat{s}_{FC_x} & \hat{s}_{FC_y} & \hat{s}_{FC_z} \end{bmatrix} \begin{Bmatrix} 0 \\ 0 \\ 0 \end{Bmatrix} = 0 \quad (84)$$

$$\frac{\partial}{\partial \theta_z} (\tilde{s}_{FC_y}) = \begin{bmatrix} \hat{s}_{FC_x} & \hat{s}_{FC_y} & \hat{s}_{FC_z} \end{bmatrix} \begin{Bmatrix} -\sin \psi \\ -\cos \psi \\ 0 \end{Bmatrix} \cos \theta_y \quad (85)$$

$$\frac{\partial}{\partial \theta_y} (\tilde{s}_{FC_z}) = \begin{bmatrix} \hat{s}_{FC_x} & \hat{s}_{FC_y} & \hat{s}_{FC_z} \end{bmatrix} \begin{Bmatrix} \sin \psi \cos \theta_y \\ \cos \psi \cos \theta_y \\ \sin \theta_y \end{Bmatrix} \quad (86)$$

$$\frac{\partial}{\partial \theta_z} (\tilde{s}_{FC_z}) = \begin{bmatrix} \hat{s}_{FC_x} & \hat{s}_{FC_y} & \hat{s}_{FC_z} \end{bmatrix} \begin{Bmatrix} \cos \psi \sin \theta_y \\ -\sin \psi \sin \theta_y \\ 0 \end{Bmatrix} \cos \theta_y \quad (87)$$

Appendix C

RLBA Engineering Report 00-02 (Rev. A)

Similar to the development of Eqs. 76, the direct (approximate) derivatives of the side force and pitching moment (due to *angular* offset), $(F^{(s)})_{AOS}$, and $(F^{(m)})_{AOS}$, with respect to Ψ_{\odot} , respectively, are inherently obtainable by virtue of the spline-fit interpolation scheme:

side force:

$$\begin{aligned}\frac{\partial F_{AOS}^{(s)}(\Delta \xi)}{\partial \theta_y} &= \frac{\partial F_{AOS}^{(s)}}{\partial \Delta \xi} \frac{\partial \Delta \xi}{\partial \theta_y} = F_{AOS}'^{(s)} \frac{\partial \Delta \xi}{\partial \theta_y}; \\ \frac{\partial F_{AOS}^{(s)}(\Delta \xi)}{\partial \theta_z} &= \frac{\partial F_{LOS}^{(s)}}{\partial \Delta \xi} \frac{\partial \Delta \xi}{\partial \theta_z} = F_{AOS}'^{(s)} \frac{\partial \Delta \xi}{\partial \theta_z}\end{aligned}\tag{88}$$

moment:

$$\begin{aligned}\frac{\partial F_{AOS}^{(m)}(\Delta \xi)}{\partial \theta_y} &= \frac{\partial F_{AOS}^{(m)}}{\partial \Delta \xi} \frac{\partial \Delta \xi}{\partial \theta_y} = F_{AOS}'^{(m)} \frac{\partial \Delta \xi}{\partial \theta_y}; \\ \frac{\partial F_{AOS}^{(m)}(\Delta \xi)}{\partial \theta_z} &= \frac{\partial F_{LOS}^{(m)}}{\partial \Delta \xi} \frac{\partial \Delta \xi}{\partial \theta_z} = F_{AOS}'^{(m)} \frac{\partial \Delta \xi}{\partial \theta_z}\end{aligned}\tag{89}$$

Using Eq. 65, one can easily obtain the partial derivatives of Ψ_{\odot} with respect to Ψ_y and Ψ_z :

$$\frac{\partial \Delta \xi}{\partial \theta_y} = \frac{\partial}{\partial \theta_y} \cos^{-1}(\tilde{s}_{FC_x}) = -\frac{1}{\sqrt{\tilde{s}_{FC_y}^2 + \tilde{s}_{FC_z}^2}} \frac{\partial \tilde{s}_{FC_x}}{\partial \theta_y}\tag{90}$$

$$\frac{\partial \Delta \xi}{\partial \theta_z} = \frac{\partial}{\partial \theta_z} \cos^{-1}(\tilde{s}_{FC_x}) = -\frac{1}{\sqrt{\tilde{s}_{FC_y}^2 + \tilde{s}_{FC_z}^2}} \frac{\partial \tilde{s}_{FC_x}}{\partial \theta_z}\tag{91}$$

With these equations all the necessary terms are available to form the final partial derivatives of the thrust, side force and moment components. Starting with Eqs. 46, 67 and 68 the following expressions can be formed:

$$\begin{Bmatrix} \delta F_{S_x}^{(p)} \\ \delta F_{S_y}^{(p)} \\ \delta F_{S_z}^{(p)} \end{Bmatrix} = \left\{ U_{v_x}^{(f)} \right\} \delta v_x + \left[U_{LOS}^{(f)} \right] \begin{Bmatrix} \delta y \\ \delta z \end{Bmatrix} + \left[U_{AOS}^{(f)} \right] \begin{Bmatrix} \delta \theta_y \\ \delta \theta_z \end{Bmatrix}\tag{92}$$

Appendix C

RLBA Engineering Report 00-02 (Rev. A)

$$\begin{aligned} \begin{Bmatrix} \delta \overline{M}_y^{(p)} \\ \delta \overline{M}_z^{(p)} \end{Bmatrix} &= \left(FS_{pc} - FS_{cg} \right) \begin{Bmatrix} -\delta \overline{F}_{S_z}^{(p)} \\ \delta \overline{F}_{S_y}^{(p)} \end{Bmatrix} + \\ &\quad \left\{ U_{v_x}^{(m)} \right\} \delta v_x + \left[U_{LOS}^{(m)} \right] \begin{Bmatrix} \delta y \\ \delta z \end{Bmatrix} + \left[U_{AOS}^{(m)} \right] \begin{Bmatrix} \delta \theta_y \\ \delta \theta_z \end{Bmatrix} \end{aligned} \quad (93)$$

where:

$$\left\{ U_{v_x}^{(f)} \right\} = \left\{ \begin{aligned} &\frac{1}{a_\infty} \left[\frac{\partial \mathcal{C}_C}{\partial M} P_{avg} F_{LOS}^{(t)} F_{AOS}^{(t)} - \frac{\partial \mathcal{C}_{D_{RAM}}}{\partial M} S_{ref} q_\infty \right] - C_{D_{RAM}} S_{ref} \rho_\infty v_x \\ &\frac{1}{a_\infty} \frac{\partial \mathcal{C}_C}{\partial M} P_{avg} \left[F_{LOS}^{(s)} (\Delta \tilde{r}_y / \Delta r) - F_{AOS}^{(s)} (\tilde{s}_{FC_y} / \tilde{s}_{FC_{yz}}) \right] \\ &\frac{1}{a_\infty} \frac{\partial \mathcal{C}_C}{\partial M} P_{avg} \left[F_{LOS}^{(s)} (\Delta \tilde{r}_z / \Delta r) - F_{AOS}^{(s)} (\tilde{s}_{FC_z} / \tilde{s}_{FC_{yz}}) \right] \end{aligned} \right\} \quad (94a)$$

$$\left[U_{LOS}^{(f)} \right] = \left[\frac{C_C P_{avg} F_{LOS}'^{(t)} (\Delta \tilde{r}) F_{AOS}^{(t)}}{l_{ref}} \left[\frac{\partial \Delta r}{\partial \delta y}, \frac{\partial \Delta r}{\partial \delta z} \right] \right] \quad (94b)$$

$$\begin{aligned} \left[U_{LOS}^{(s)} \right] &= C_C P_{avg} \left[\frac{F_{LOS}'^{(s)}}{l_{ref}} \begin{bmatrix} (\Delta \tilde{r}_y / \Delta r) \frac{\partial \Delta r}{\partial \delta y} & (\Delta \tilde{r}_y / \Delta r) \frac{\partial \Delta r}{\partial \delta z} \\ (\Delta \tilde{r}_z / \Delta r) \frac{\partial \Delta r}{\partial \delta y} & (\Delta \tilde{r}_z / \Delta r) \frac{\partial \Delta r}{\partial \delta z} \end{bmatrix} \right. \\ &\quad \left. + F_{LOS}^{(s)} \begin{bmatrix} \frac{\partial}{\partial \delta y} (\Delta \tilde{r}_y / \Delta r) & \frac{\partial}{\partial \delta z} (\Delta \tilde{r}_y / \Delta r) \\ \frac{\partial}{\partial \delta y} (\Delta \tilde{r}_z / \Delta r) & \frac{\partial}{\partial \delta z} (\Delta \tilde{r}_z / \Delta r) \end{bmatrix} \right] \end{aligned} \quad (94c)$$

$$\left[U_{AOS}^{(f)} \right] = \left[\frac{C_C P_{avg} F_{LOS}^{(t)} F_{AOS}'^{(t)} (\Delta \xi)}{-\left[U_{AOS}^{(s)} \right]} \left[\frac{\partial \Delta \xi}{\partial \theta_y}, \frac{\partial \Delta \xi}{\partial \theta_z} \right] \right] \quad (94d)$$

Appendix C

RLBA Engineering Report 00-02 (Rev. A)

$$\begin{aligned} \left[U_{AOS}^{(s)} \right] = C_C P_{avg} & \left[F_{AOS}'^{(s)} \begin{bmatrix} \left(\tilde{s}_{FC_y} / \tilde{s}_{FC_{yz}} \right) \frac{\partial \Delta \xi}{\partial \theta_y} & \left(\tilde{s}_{FC_y} / \tilde{s}_{FC_{yz}} \right) \frac{\partial \Delta \xi}{\partial \theta_z} \\ \left(\tilde{s}_{FC_z} / \tilde{s}_{FC_{yz}} \right) \frac{\partial \Delta \xi}{\partial \theta_y} & \left(\tilde{s}_{FC_z} / \tilde{s}_{FC_{yz}} \right) \frac{\partial \Delta \xi}{\partial \theta_z} \end{bmatrix} \right. \\ & \left. + F_{AOS}^{(s)} \begin{bmatrix} \frac{\partial}{\partial \theta_y} \left(\tilde{s}_{FC_y} / \tilde{s}_{FC_{yz}} \right) & \frac{\partial}{\partial \theta_z} \left(\tilde{s}_{FC_y} / \tilde{s}_{FC_{yz}} \right) \\ \frac{\partial}{\partial \theta_y} \left(\tilde{s}_{FC_z} / \tilde{s}_{FC_{yz}} \right) & \frac{\partial}{\partial \theta_z} \left(\tilde{s}_{FC_z} / \tilde{s}_{FC_{yz}} \right) \end{bmatrix} \right] \end{aligned} \quad (94e)$$

and where:

$$\left\{ U_{v_x}^{(m)} \right\} = \frac{1}{a_\infty} \frac{\partial C_C}{\partial M} P_{avg} l_{ref} \left\{ \begin{aligned} & \left(F_{LOS}^{(m)} (\Delta \tilde{r}_z / \Delta r) + F_{AOS}^{(m)} \left(-\tilde{s}_{FC_z} / \tilde{s}_{FC_{yz}} \right) \right) \\ & \left(F_{LOS}^{(m)} (-\Delta \tilde{r}_y / \Delta r) + F_{AOS}^{(m)} \left(\tilde{s}_{FC_z} / \tilde{s}_{FC_{yz}} \right) \right) \end{aligned} \right\} \quad (95a)$$

$$\begin{aligned} \left[U_{LOS}^{(m)} \right] = C_C P_{avg} & \left[F_{LOS}'^{(m)} \begin{bmatrix} (\Delta \tilde{r}_z / \Delta r) \frac{\partial \Delta r}{\partial \delta_y} & (\Delta \tilde{r}_z / \Delta r) \frac{\partial \Delta r}{\partial \delta_z} \\ -(\Delta \tilde{r}_y / \Delta r) \frac{\partial \Delta r}{\partial \delta_y} & -(\Delta \tilde{r}_y / \Delta r) \frac{\partial \Delta r}{\partial \delta_z} \end{bmatrix} \right. \\ & \left. + l_{ref} F_{LOS}^{(m)} \begin{bmatrix} \frac{\partial}{\partial y} (\Delta \tilde{r}_z / \Delta r) & \frac{\partial}{\partial z} (\Delta \tilde{r}_z / \Delta r) \\ -\frac{\partial}{\partial y} (\Delta \tilde{r}_y / \Delta r) & -\frac{\partial}{\partial z} (\Delta \tilde{r}_y / \Delta r) \end{bmatrix} \right] \end{aligned} \quad (95b)$$

$$\begin{aligned} \left[U_{AOS}^{(m)} \right] = C_C P_{avg} l_{ref} & \left[F_{AOS}'^{(m)} \begin{bmatrix} -\left(\tilde{s}_{FC_z} / \tilde{s}_{FC_{yz}} \right) \frac{\partial \Delta \xi}{\partial \theta_y} & -\left(\tilde{s}_{FC_z} / \tilde{s}_{FC_{yz}} \right) \frac{\partial \Delta \xi}{\partial \theta_z} \\ \left(\tilde{s}_{FC_y} / \tilde{s}_{FC_{yz}} \right) \frac{\partial \Delta \xi}{\partial \theta_y} & \left(\tilde{s}_{FC_y} / \tilde{s}_{FC_{yz}} \right) \frac{\partial \Delta \xi}{\partial \theta_z} \end{bmatrix} \right. \\ & \left. + F_{AOS}^{(m)} \begin{bmatrix} -\frac{\partial}{\partial \theta_y} \left(\tilde{s}_{FC_z} / \tilde{s}_{FC_{yz}} \right) & -\frac{\partial}{\partial \theta_z} \left(\tilde{s}_{FC_z} / \tilde{s}_{FC_{yz}} \right) \\ \frac{\partial}{\partial \theta_y} \left(\tilde{s}_{FC_y} / \tilde{s}_{FC_{yz}} \right) & \frac{\partial}{\partial \theta_z} \left(\tilde{s}_{FC_y} / \tilde{s}_{FC_{yz}} \right) \end{bmatrix} \right] \end{aligned} \quad (95c)$$

Appendix C

RLBA Engineering Report 00-02 (Rev. A)

The partial derivatives in Eqs. 94e and 95c are calculable using the following expressions:

$$\begin{aligned}\frac{\partial}{\partial \theta_q} \left(\tilde{s}_{FC_y} / \tilde{s}_{FC_{yz}} \right) &= \frac{\tilde{s}_{FC_z}}{\tilde{s}_{FC_{yz}}^3} \left(\tilde{s}_{FC_z} \frac{\partial \tilde{s}_{FC_y}}{\partial \theta_q} - \tilde{s}_{FC_y} \frac{\partial \tilde{s}_{FC_z}}{\partial \theta_q} \right) \\ \frac{\partial}{\partial \theta_q} \left(\tilde{s}_{FC_z} / \tilde{s}_{FC_{yz}} \right) &= \frac{\tilde{s}_{FC_y}}{\tilde{s}_{FC_{yz}}^3} \left(-\tilde{s}_{FC_z} \frac{\partial \tilde{s}_{FC_y}}{\partial \theta_q} + \tilde{s}_{FC_y} \frac{\partial \tilde{s}_{FC_z}}{\partial \theta_q} \right)\end{aligned}\tag{96, 97}$$

and where $\theta_q = \theta_y$ or θ_z , as appropriate.

2.6 Gravity Forces

The gravitational force components are determined by the scalar value of the gravitational acceleration and its directional vector relative to the axes of the Lightcraft. Because of the assumption that the roll angle of the Lightcraft is zero, the gravity forces would normally be assumed to impact only on the x - and z - force equations. For this assumption, these components would be determined solely by the pitch attitude angle, θ_y , the geocentric radius, R , the Earth equatorial R_{gc} , and Earth latitude, $\textcircled{2}$, all defined in the *geocentric* coordinate system. However, it is further assumed that, while the value of the gravitational acceleration is determined by the geocentric latitude, the direction of the acceleration is normal to the Earth ellipsoidal surface, *as defined by the geodetic latitude*, λ_{gd} . See Appendix B for the development of the difference between these two latitudes, $\Delta\lambda$, ($= \lambda_{gd} - \lambda_{gc}$). Thus, all three components of the gravitational acceleration will generally be non-zero.

2.6.1 Gravitational Acceleration

The standard spherical harmonic expansion for the Earth's gravitational field potential (Refs. 7 & 8, e.g.) is the starting point for determining the gravitational acceleration:

$$U(r, L) = \frac{\mu}{R} \left[-1 + \sum_{n=2}^{\infty} \left(\frac{R_E}{R} \right)^n J_n P_n(\sin \lambda) \right]\tag{98}$$

where P_n are the Legendre polynomials, and the Earth physical properties are taken from Refs. (9-13)

$$\begin{aligned}\textcircled{3} &= 3.986004418 \% 10^5 \text{ km}^3/\text{sec}^2 \\ R_E &= 6,378.1363 \text{ km.} \\ J_2 &= 1082.269256 \% 10^{-6} \\ J_3 &= -2.532307819 \% 10^{-6} \\ J_4 &= -1.62042999 \% 10^{-6} \\ J_5 &= -0.23 \% 10^{-6} \\ J_6 &= 0.54 \% 10^{-6}\end{aligned}$$

Appendix C

RLBA Engineering Report 00-02 (Rev. A)

The partial derivative of Eq. 98 with respect to the radial position, r , then yields the required expression for the gravitational acceleration:

$$g(R, \lambda) = \frac{\partial}{\partial R} U = \frac{\mu}{R^2} \left[1 - \frac{3}{2} J_2 \left(\frac{R_E}{R} \right)^2 (3 \sin^2 \lambda - 1) - 2 J_3 \left(\frac{R_E}{R} \right)^3 (5 \sin^3 \lambda - 3 \sin \lambda) \right. \\ \left. - \frac{5}{8} J_4 \left(\frac{R_E}{R} \right)^4 (35 \sin^4 \lambda - 30 \sin^2 \lambda + 3) \right. \\ \left. - \frac{3}{4} J_5 \left(\frac{R_E}{R} \right)^5 (63 \sin^5 \lambda - 70 \sin^3 \lambda + 15 \sin \lambda) \right. \\ \left. - \frac{7}{16} J_6 \left(\frac{R_E}{R} \right)^6 (231 \sin^6 \lambda - 315 \sin^4 \lambda + 105 \sin^2 \lambda - 5) \right] \quad (99a)$$

where herein, $R = R_{gc}$.

The gravitational vector is then defined in the “2” coordinate system as:

$$\vec{g} = g \begin{bmatrix} 0, & -\sin \Delta\lambda, & -\cos \Delta\lambda \end{bmatrix} \begin{Bmatrix} \vec{i}_2 \\ \vec{j}_2 \\ \vec{k}_2 \end{Bmatrix} = g \begin{bmatrix} 0, & -\sin \Delta\lambda, & -\cos \Delta\lambda \end{bmatrix} [T_{3 \rightarrow 2}] \begin{Bmatrix} \vec{i}_3 \\ \vec{j}_3 \\ \vec{k}_3 \end{Bmatrix} \quad (99b)$$

2.6.2 Total Gravity Loads

Use of Eqs 99a & 99b then yields the final components of the gravitational acceleration and thence the gravity loads:

$$F_x^{(g)} = -mg(\sin \Delta\lambda \cos \psi \cos \theta_y + \cos \Delta\lambda \sin \theta_y); \\ F_y^{(g)} = mg \sin \Delta\lambda \sin \psi \\ F_z^{(g)} = mg(-\sin \Delta\lambda \cos \psi \sin \theta_y + \cos \Delta\lambda \cos \theta_y) \quad (99c,d\&e)$$

Appendix C

RLBA Engineering Report 00-02 (Rev. A)

2.6.3 Perturbational Gravity Loads

Any perturbational variation in the gravity loads arising from the variations in the gravitational potential itself can safely be assumed to be negligible. The perturbational gravity loads can be ascertained by effecting a perturbational coordinate system from the “3” system to a perturbational one, “4”, as defined by the perturbational angles, $\delta\theta_y$ & $\delta\theta_z$:

$$\begin{Bmatrix} \vec{i}_4 \\ \vec{j}_4 \\ \vec{k}_4 \end{Bmatrix} = \begin{bmatrix} 1 & \delta\theta_z & -\delta\theta_y \\ -\delta\theta_z & 1 & 0 \\ \delta\theta_y & 0 & 1 \end{bmatrix} \begin{Bmatrix} \vec{i}_3 \\ \vec{j}_3 \\ \vec{k}_3 \end{Bmatrix}; \quad \begin{Bmatrix} \vec{i}_3 \\ \vec{j}_3 \\ \vec{k}_3 \end{Bmatrix} = \begin{bmatrix} 1 & -\delta\theta_z & \delta\theta_y \\ \delta\theta_z & 1 & 0 \\ -\delta\theta_y & 0 & 1 \end{bmatrix} \begin{Bmatrix} \vec{i}_4 \\ \vec{j}_4 \\ \vec{k}_4 \end{Bmatrix} \quad (100a,b)$$

Combining the results of Eq. 99b with Eq. 100b yields the components of the perturbational gravity loads:

$$\delta \begin{Bmatrix} F_x^{(g)} \\ F_y^{(g)} \\ F_z^{(g)} \end{Bmatrix} = mg \begin{bmatrix} (\sin\Delta\lambda \cos\psi \sin\theta_y - \cos\Delta\lambda \cos\theta_y) & (\sin\Delta\lambda \sin\psi) \\ 0 & (\sin\Delta\lambda \cos\psi \cos\theta_y + \cos\Delta\lambda \sin\theta_y) \\ -(\sin\Delta\lambda \cos\psi \cos\theta_y + \cos\Delta\lambda \sin\theta_y) & 0 \end{bmatrix} \begin{Bmatrix} \delta\theta_y \\ \delta\theta_z \end{Bmatrix} \quad (100)$$

[Note that the ψ dependency only occurs in the presence of the latitude difference, $\Delta\lambda$, as would be expected using the more simplified assumption that excludes this quantity.]

The above derivations complete all the formulations required for the complete dynamic nonlinear analysis of the basic configuration as well as the linearizations required for the eigenvalue solution, which is treated in the following section.

Appendix C

RLBA Engineering Report 00-02 (Rev. A)

3.0 Eigenvalue Solution

Although the non-linearity of the above described equation set (eq. 22), generally requires a time-history solution, by appropriate linearization, an eigenvalue solution can also be obtained. The rationale for implementing an eigenvalue solution is to enable the evaluation of the stability at regularly spaced instances in time throughout the entire time-history solution at a randomly selectable time interval.

3.1 Linearization of the Mechanical Terms

3.1.1 Assumptions

- a) The complete (nonlinear) description of the Lightcraft vehicle flight dynamics entails not only the equations of motion (involving the direct dynamic variables), Eq. 11, but also the subsidiary dynamics (instantaneous mass depletion rate, ground track, movement of the laser beam, changes in atmospheric properties, etc.). *The principal assumption is that the time scale, for which the eigensolution is intended to give meaningful results, is short enough that the subsidiary dynamics can be considered to be quasi-static.*
- b.) The perturbational external airloads and propulsion characteristics are to be linearized by taking perturbations about the instantaneous conditions (see previous sections).
- c.) All linearizations are formed by taking perturbations of the appropriate dynamic variables about values defined at each of the regularly spaced instances of time, $t = T_N$. The values about which the perturbations are then taken are denoted with an “N” subscript.
- d.) The inertial, body-fixed translational and rotational velocities will be taken to be the time derivatives of the lateral and angular offsets due to vehicle motion relative to the laser beam.
- e.) The basic set of perturbation variables is taken to be:

$$\{\delta X\} = \begin{Bmatrix} \delta v_x \\ \delta y \\ \delta z \\ \delta \theta_y \\ \delta \theta_z \end{Bmatrix} \quad (101)$$

Note that the fore and aft *displacement*, δx , is not included in the perturbation vector as there is no definable force proportional to it. Hence, only the fore and aft *velocity*, v_x , is included.

Appendix C

RLBA Engineering Report 00-02 (Rev. A)

3.1.2 Basic Linearized Equations of Motion:

The starting point for the formulation of the eigensolution equations is the basic equation set given earlier (Eq. 10), which can be written the following form:

$$\begin{aligned}
 m \left[\delta \ddot{v}_x + (Q_{ie} + q_N) \delta \dot{z} + v_{z_N} \delta \dot{\theta}_y - (R_{ie} + r_N) \delta \dot{y} - v_{y_N} \delta \dot{\theta}_z \right] \\
 = \sum \delta F_x = \delta F_x^{(a)} + \delta F_x^{(p)} + \delta F_x^{(g)} \\
 m \left[\delta \ddot{y} + (R_{ie} + r_N) \delta v_x + v_{x_N} \delta \dot{\theta}_z \right] = \sum \delta F_y = \delta F_y^{(a)} + \delta F_y^{(p)} + \delta F_y^{(g)} \\
 m \left[\delta \ddot{z} - (Q_{ie} + q_N) \delta v_x - v_{x_N} \delta \dot{\theta}_y \right] = \sum \delta F_z = \delta F_z^{(a)} + \delta F_z^{(p)} + \delta F_z^{(g)} \\
 I_d \delta \ddot{\theta}_y + J \Omega \delta \dot{\theta}_z = \sum \delta M_y = \delta M_{y_0}^{(a)} + \delta M_y^{(p)} + \delta M_{y_0}^{(c)} \\
 I_d \delta \ddot{\theta}_z - J \Omega \delta \dot{\theta}_y = \sum \delta M_z = \delta M_{z_0}^{(a)} + \delta M_z^{(p)} + \delta M_{z_0}^{(c)}
 \end{aligned} \tag{102a,b,c,d\&e}$$

where the perturbational forces and moments on the right-hand sides are respectively due to external airloads, $(\dots)^{(a)}$, propulsion characteristics, $(\dots)^{(p)}$, and gravity, $(\dots)^{(g)}$, as they are developed in Sections 2.4.5, 2.5.5, and 2.6.3, respectively. The perturbational control moments, $(\dots)^{(c)}$ are developed in a subsequent chapter.

3.2 Inclusion of Perturbational External Aerodynamics, Propulsion Offset Characteristics, and Gravity Loads

3.2.1 Perturbational Airloads

As developed in Section 2.4.5, the perturbational (external) airloads are functions only of the perturbational velocities:

perturbational external forces:

$$\begin{Bmatrix} \delta F_x^{(a)} \\ \delta F_y^{(a)} \\ \delta F_z^{(a)} \end{Bmatrix} = \begin{bmatrix} \frac{\partial F_x^{(a)}}{\partial v_x} & \frac{\partial F_x^{(a)}}{\partial v_y} & \frac{\partial F_x^{(a)}}{\partial v_z} \\ \frac{\partial F_y^{(a)}}{\partial v_x} & \frac{\partial F_y^{(a)}}{\partial v_y} & \frac{\partial F_y^{(a)}}{\partial v_z} \\ \frac{\partial F_z^{(a)}}{\partial v_x} & \frac{\partial F_z^{(a)}}{\partial v_y} & \frac{\partial F_z^{(a)}}{\partial v_z} \end{bmatrix}_{BF} \begin{Bmatrix} \delta v_x \\ \delta \dot{y} \\ \delta \dot{z} \end{Bmatrix} \tag{103}$$

Appendix C

RLBA Engineering Report 00-02 (Rev. A)

perturbational external moments:

$$\begin{Bmatrix} \delta M_{y_0}^{(a)} \\ \delta M_{z_0}^{(a)} \end{Bmatrix} = \begin{bmatrix} \frac{\partial M_{y_0}^{(a)}}{\partial v_x} & \frac{\partial M_{y_0}^{(a)}}{\partial v_y} & \frac{\partial M_{y_0}^{(a)}}{\partial v_z} \\ \frac{\partial M_{z_0}^{(a)}}{\partial v_x} & \frac{\partial M_{z_0}^{(a)}}{\partial v_y} & \frac{\partial M_{z_0}^{(a)}}{\partial v_z} \end{bmatrix}_{BF} \begin{Bmatrix} \delta v_x \\ \delta \dot{y} \\ \delta \dot{z} \end{Bmatrix} \quad (104)$$

3.2.2 Perturbational Propulsive Loads and Moments

Section 2.5.5 presents the detailed equations for the calculations of the required partial derivatives needed to form the following partial derivative matrices relating perturbational thrust, side forces and moments due to perturbations in longitudinal velocity and propulsive offsets:

perturbational forces:

$$\begin{Bmatrix} \delta F_{S_x}^{(p)} \\ \delta F_{S_y}^{(p)} \\ \delta F_{S_z}^{(p)} \end{Bmatrix} = \begin{bmatrix} \frac{\partial F_{S_x}^{(p)}}{\partial v_x} & \frac{\partial F_{S_x}^{(p)}}{\partial \delta y} & \frac{\partial F_{S_x}^{(p)}}{\partial \delta z} & \frac{\partial F_{S_x}^{(p)}}{\partial \theta_y} & \frac{\partial F_{S_x}^{(p)}}{\partial \theta_z} \\ \frac{\partial F_{S_y}^{(p)}}{\partial v_x} & \frac{\partial F_{S_y}^{(p)}}{\partial \delta y} & \frac{\partial F_{S_y}^{(p)}}{\partial \delta z} & \frac{\partial F_{S_y}^{(p)}}{\partial \theta_y} & \frac{\partial F_{S_y}^{(p)}}{\partial \theta_z} \\ \frac{\partial F_{S_z}^{(p)}}{\partial v_x} & \frac{\partial F_{S_z}^{(p)}}{\partial \delta y} & \frac{\partial F_{S_z}^{(p)}}{\partial \delta z} & \frac{\partial F_{S_z}^{(p)}}{\partial \theta_y} & \frac{\partial F_{S_z}^{(p)}}{\partial \theta_z} \end{bmatrix} \begin{Bmatrix} \delta v_x \\ \delta y \\ \delta z \\ \delta \theta_y \\ \delta \theta_z \end{Bmatrix} \quad (105)$$

perturbational moments:

$$\begin{Bmatrix} \delta M_y^{(p)} \\ \delta M_z^{(p)} \end{Bmatrix} = \begin{bmatrix} \frac{\partial M_y^{(p)}}{\partial v_x} & \frac{\partial M_y^{(p)}}{\partial \delta y} & \frac{\partial M_y^{(p)}}{\partial \delta z} & \frac{\partial M_y^{(p)}}{\partial \theta_y} & \frac{\partial M_y^{(p)}}{\partial \theta_z} \\ \frac{\partial M_z^{(p)}}{\partial v_x} & \frac{\partial M_z^{(p)}}{\partial \delta y} & \frac{\partial M_z^{(p)}}{\partial \delta z} & \frac{\partial M_z^{(p)}}{\partial \theta_y} & \frac{\partial M_z^{(p)}}{\partial \theta_z} \end{bmatrix} \begin{Bmatrix} \delta v_x \\ \delta y \\ \delta z \\ \delta \theta_y \\ \delta \theta_z \end{Bmatrix} \quad (106)$$

Appendix C

RLBA Engineering Report 00-02 (Rev. A)

3.2.3 Perturbational Gravity Forces

As presented in Section 2.6.3, the perturbational gravity forces are given by:

$$\begin{aligned} \delta \begin{Bmatrix} F_x^{(g)} \\ F_y^{(g)} \\ F_z^{(g)} \end{Bmatrix} &= \begin{bmatrix} \frac{\mathcal{F}_x^{(g)}}{\partial y} & \frac{\mathcal{F}_x^{(g)}}{\partial z} \\ 0 & \frac{\mathcal{F}_y^{(g)}}{\partial z} \\ \frac{\mathcal{F}_z^{(g)}}{\partial y} & 0 \end{bmatrix} \begin{Bmatrix} \delta \theta_y \\ \delta \theta_z \end{Bmatrix} \\ &= mg \begin{bmatrix} (\sin \Delta \lambda \cos \psi \sin \theta_y - \cos \Delta \lambda \cos \theta_y) & (\sin \Delta \lambda \sin \psi) \\ 0 & (\sin \Delta \lambda \cos \psi \cos \theta_y + \cos \Delta \lambda \sin \theta_y) \\ -(\sin \Delta \lambda \cos \psi \cos \theta_y + \cos \Delta \lambda \sin \theta_y) & 0 \end{bmatrix} \begin{Bmatrix} \delta \theta_y \\ \delta \theta_z \end{Bmatrix} \end{aligned} \quad (107)$$

3.3 Canonical Form of Equations Required for Typical Solution

As required for typical matrix eigenvalue solutions the matrix equation must be cast in the appropriate canonical form:

$$\lambda [I] \{\delta \Psi\} = [C] \{\delta \Psi\}; \quad \text{or, alternatively:} \quad \lambda [I] \{\delta \Psi\} - [C] \{\delta \Psi\} = 0$$

Where the eigenvalue, λ , is complex: $\lambda = \alpha + i \beta = -\frac{\omega}{2} + i \beta$. It should be noted that in the present context the $[C]$ matrix is nonsymmetric. In order to achieve this canonical form, the perturbational equations must first be put into the form:

$$[A] \{\delta \dot{Z}\} - [B] \{\delta Z\} = 0 \quad (108)$$

where:

$$\{\delta Z\} = \begin{Bmatrix} \delta v_x \\ \delta \dot{y} \\ \delta \dot{z} \\ \delta \dot{\theta}_y \\ \delta \dot{\theta}_z \\ \delta y \\ \delta z \\ \delta \theta_y \\ \delta \theta_z \end{Bmatrix} \quad (109)$$

Appendix C

RLBA Engineering Report 00-02 (Rev. A)

$$[A] = \begin{bmatrix} m & 0 & 0 \\ 0 & M & 0 \\ 0 & 0 & I_4 \end{bmatrix}; \quad [B] = \begin{bmatrix} b_{11} & B_{12} & B_{13} \\ B_{21} & B_{22} & B_{23} \\ 0 & I_4 & 0 \end{bmatrix} \quad (110, 111)$$

The component submatrices comprising the implied matrix partitioning of $[A]$ and $[B]$ are defined as follows:

$$[M] = \begin{bmatrix} m & 0 & 0 & 0 \\ & m & 0 & 0 \\ & (S) & I_d & 0 \\ & & & I_d \end{bmatrix} \quad (112)$$

$$b_{11} = \frac{\partial F_x^{(a)}}{\partial v_x} + \frac{\partial F_x^{(p)}}{\partial v_x} \quad (113)$$

$$[B_{12}] = \left[m(R_{ie} + r_N) + \frac{\partial F_x^{(a)}}{\partial v_y}, \quad -m(Q_{ie} + q_N) + \frac{\partial F_x^{(a)}}{\partial v_z}, \quad -mv_{z_N}, \quad mv_{y_N} \right] \quad (114)$$

$$[B_{13}] = \left[\frac{\partial F_x^{(p)}}{\partial \delta y}, \quad \frac{\partial F_x^{(p)}}{\partial \delta z}, \quad \left(\frac{\partial F_x^{(p)}}{\partial \theta_y} + \frac{\partial F_x^{(g)}}{\partial \theta_y} \right), \quad \left(\frac{\partial F_x^{(p)}}{\partial \theta_z} + \frac{\partial F_x^{(g)}}{\partial \theta_z} \right) \right] \quad (115)$$

$$\{B_{21}\} = \left\{ \begin{array}{l} \left(\frac{\partial F_y^{(a)}}{\partial v_x} + \frac{\partial F_y^{(p)}}{\partial v_x} - mR_{ie} \right) \\ \left(\frac{\partial F_z^{(a)}}{\partial v_x} + \frac{\partial F_z^{(p)}}{\partial v_x} + mQ_{ie} \right) \\ \left(\frac{\partial M_y^{(a)}}{\partial v_x} + \frac{\partial M_y^{(p)}}{\partial v_x} \right) \\ \left(\frac{\partial M_z^{(a)}}{\partial v_x} + \frac{\partial M_z^{(p)}}{\partial v_x} \right) \end{array} \right\} \quad (116)$$

Appendix C

RLBA Engineering Report 00-02 (Rev. A)

$$[B_{22}] = \begin{bmatrix} \frac{\partial F_y^{(a)}}{\partial v_y} & \frac{\partial F_y^{(a)}}{\partial v_z} & 0 & -mv_{x_N} \\ \frac{\partial F_z^{(a)}}{\partial v_y} & \frac{\partial F_z^{(a)}}{\partial v_z} & mv_{x_N} & 0 \\ \frac{\partial M_y^{(a)}}{\partial v_y} & \frac{\partial M_y^{(a)}}{\partial v_z} & 0 & -J\Omega \\ \frac{\partial M_z^{(a)}}{\partial v_y} & \frac{\partial M_z^{(a)}}{\partial v_z} & J\Omega & 0 \end{bmatrix} \quad (117)$$

$$[B_{23}] = \begin{bmatrix} \frac{\partial F_{S_y}^{(p)}}{\partial \delta y} & \frac{\partial F_{S_y}^{(p)}}{\partial \delta z} & \frac{\partial F_{S_y}^{(p)}}{\partial \theta_y} & \left(\frac{\partial F_{S_y}^{(p)}}{\partial \theta_z} + \frac{\partial F_y^{(g)}}{\partial \theta_z} \right) \\ \frac{\partial F_{S_z}^{(p)}}{\partial \delta y} & \frac{\partial F_{S_z}^{(p)}}{\partial \delta z} & \left(\frac{\partial F_{S_z}^{(p)}}{\partial \theta_y} + \frac{\partial F_z^{(g)}}{\partial \theta_y} \right) & \frac{\partial F_{S_z}^{(p)}}{\partial \theta_z} \\ \frac{\partial M_y^{(p)}}{\partial \delta y} & \frac{\partial M_y^{(p)}}{\partial \delta z} & \frac{\partial M_y^{(p)}}{\partial \theta_y} & \frac{\partial M_y^{(p)}}{\partial \theta_z} \\ \frac{\partial M_z^{(p)}}{\partial \delta y} & \frac{\partial M_z^{(p)}}{\partial \delta z} & \frac{\partial M_z^{(p)}}{\partial \theta_y} & \frac{\partial M_z^{(p)}}{\partial \theta_z} \end{bmatrix} \quad (118)$$

The final step is to invert the $[A]$ matrix and form the required $[C]$ matrix by premultiplying that inverse with the $[B]$ matrix:

$$[C] = [A]^{-1}[B] = \left[\begin{array}{c|c|c} \left(b_{11}/m \right) & \left(1/m \right) [B_{12}] & \left(1/m \right) [B_{13}] \\ \hline [M]^{-1} \{B_{21}\} & [M]^{-1} [B_{22}] & [M]^{-1} [B_{23}] \\ \hline \{0\} & [I_4] & [0] \end{array} \right] \quad (119)$$

Appendix C

RLBA Engineering Report 00-02 (Rev. A)

Eq. 119 then represents the matrix to be used in the usual canonical matrix eigenvalue solution. Since the $[C]$ matrix is 9×9 , there will be nine eigenvalues. It is to be expected that there will generally be one aperiodic root associated with the longitudinal velocity, and four complex pairs, although any or some of the complex pairs may degenerate into a pair of aperiodic roots.

The development of this section represents the basic approach to forming the eigenvalue solution, as well as presenting the actual terms associated with the simplest Lightcraft configuration. In the following chapters developments are presented for the inclusion of the dynamics associated with a gimbaled, dual-spin configuration, as well as the coupling afforded by the use of a general feed-back control system.

4.0 Dual-spin Configuration

Initial experiments with the Lightcraft models must necessarily be dynamically simple and have involved using spin-stabilized configurations. This configuration is the basis of the developments in the previous chapters. However, as the concept develops and matures, the vehicle will undoubtedly be designed for manned flight. For such a vehicle the use of spin-stabilization for the entire vehicle, including the crew compartment, will be unacceptable. For manned vehicles, as well as other designs that require a non-spinning environment for a portion of the vehicle, the vehicle must have a dual-spin capability. With a dual-spin configuration the aft, propulsion-directed part of the vehicle can and should assume the presence of a spinning environment. The forward part of the vehicle would then constitute the non-spinning part of the vehicle. The two portions of the Lightcraft would then require a bearing connection with some form of (active) application of torque to overcome the bearing drag and provide a method of roll control for the forward (non-spin) portion of the Lightcraft.

4.1 *Supplementary Assumptions*

4.1.1 General

- a) The previously developed equations of motion (defining force and moment equilibrium) still apply to the dual-spin configuration, as long as they are defined relative to the Lightcraft's actual (instantaneous) center of gravity.
- b) The dual-spin configuration realistically requires the recognition that any bearing support structure will introduce angular (bending) flexibilities into the Lightcraft structure such that the forward (non-spin) portion of the Lightcraft will have deflection angles in pitch and yaw relative to the aft (spin) portion of the Lightcraft (see the accompanying figure):

Appendix C

RLBA Engineering Report 00-02 (Rev. A)

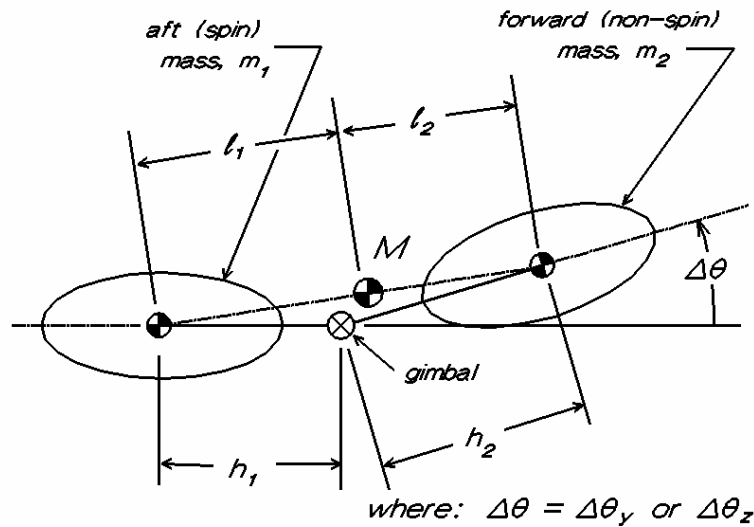


Fig. 10 Basic kinematics of dual-spin configuration

Note that due to deflections of the bearing structure ($\neq \theta_y$ and/or $\neq \theta_z \neq 0$) the total mass center can migrate off the vehicle's centerline.

- c) While the aft (spin) portion of the Lightcraft is still defined with an identically zero value of "roll" degree of freedom, the upper (non-spin) portion can now assume a non-zero value, in the usual definition of roll.

4.1.2 Mechanical System (continuing)

- d) Both deflection angles, ($\neq \theta_y$ and $\neq \theta_z$), are "small". Consequently, nonlinear combinations of these deflections with the roll degree of freedom of the forward non-spin portion, θ_{NS} , are neglected.
- e) The bearing attachment structure can be idealized as a gimbal with angular springs representing the bending flexibilities about the gimbal. Furthermore, these springs are isotropic (i.e., equal values in the pitch and yaw directions).
- f) The previously formulated external aerodynamic and propulsive loads are applied only to the total Lightcraft equilibrium equations, with the exception that the drag load is assumed to apply to the forward non-spin portion. This assumption leads to a formulation of the axial thrust that the bearings must support.
- g) Control moments are applied to both the total Lightcraft moments and the upper non-spin mass. The control moments are aligned with the non-spin section of the Lightcraft which has a "roll" degree of freedom. Consequently, the control moments, as applied to the total Lightcraft, must be resolved into components aligned with the spin section degrees of freedom.
- h) When it occurs (in rocket mode), the mass depletion occurs in the aft, spin body only.

Appendix C

RLBA Engineering Report 00-02 (Rev. A)

4.1.3 Action of Thrust and Drag

The action of the propulsive thrust, which acts on the aft spin mass, must be reconciled with the drag, which acts on the forward non-spin mass. The following figure depicts the interaction of the three axial loads:

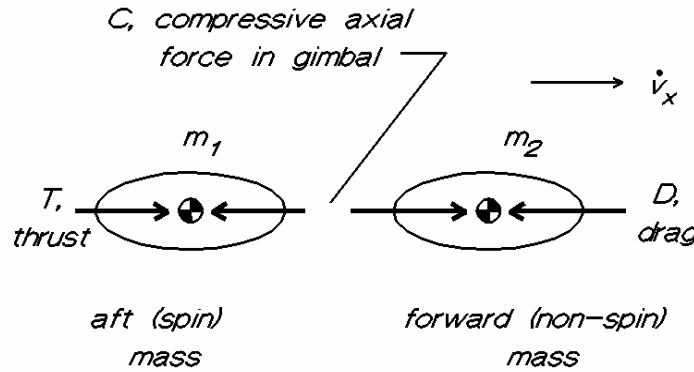


Fig. 11 Interaction of thrust and drag on bearing structure compressive load

Thus, with the total mass denoted as m , the following expressions can be written:

mass 1:

$$(T - C) = m_1 \dot{v}_x = \frac{m_1}{m} (T - D) \quad (120a)$$

mass 2:

$$(C - D) = m_2 \dot{v}_x = \frac{m_2}{m} (T - D) \quad (120b)$$

total mass:

$$(T - D) = m \dot{v}_x \quad (120c)$$

These equations can be used to eliminate $d\dot{v}_x/dt$, to give the following expression for the thrust loading across the bearing structure:

$$C = \left(1 - \frac{m_1}{m}\right) T + \frac{m_1}{m} D \quad (121)$$

Appendix C

RLBA Engineering Report 00-02 (Rev. A)

4.2 Supplemental Equations of Motion

Lagrange's equations were selected as the tool for identifying the additional terms to be added to the existing (basic) equations, as well as for deriving outright the equations needed for the dynamics of the bending deflections of the forward mass about the the gimbal, relative to the undeformed positions.

4.2.1 Revised Augmented State Vector and Supplementary Equations:

With the inclusion of the articulation about the gimbal and the lack of spin on the forward mass, three additional independent degrees of freedom are defined: the pitching and yawing angular deflections of the forward mass about the gimbal, $\Delta\theta_y$ and $\Delta\theta_z$, respectively, and the roll deflection angle of the forward (non-spin) mass, ϕ_{NS} . The augmented state vector then becomes:

$$\{Y\}_{augmented} \equiv \left\{ \begin{array}{c} v_x \\ v_y \\ v_z \\ q \\ r \\ \Delta\dot{\theta}_y \\ \Delta\dot{\theta}_z \\ p_{NS} \\ \Delta\theta_y \\ \Delta\theta_z \\ \frac{\phi_{NS}}{m} \\ \Delta R_{gc} \\ \lambda \\ L \\ \psi \\ \theta_y \end{array} \right\} \quad (122)$$

where the center partition contains the additional terms relating to the forward mass equilibrium equations.

Appendix C

RLBA Engineering Report 00-02 (Rev. A)

4.2.2 Kinetic Energy

For purposes of using Lagrange's equations the kinetic energy for the two-mass system (excluding the gyroscopic terms) is given by the following expression:

$$\begin{aligned}
 T = & \left(\frac{1}{2} \right) \left\langle m_1 \left[v_x^2 + (v_y - l_1 \dot{\theta}_z)^2 + (v_z + l_1 \dot{\theta}_y)^2 \right] \right. \\
 & + m_2 \left\{ v_x^2 + \left[v_y + l_2 \dot{\theta}_z + h_2 (\sin \phi \Delta \dot{\theta}_y + \cos \phi \Delta \dot{\theta}_z) \right]^2 \right. \\
 & \quad \left. \left[v_z - l_2 \dot{\theta}_y - h_2 (\cos \phi \Delta \dot{\theta}_y - \sin \phi \Delta \dot{\theta}_z) \right]^2 \right\} \\
 & + m_1 (l_1^2 + k_1^2) (q^2 + r^2) + J_2 p_{NS}^2 \\
 & + m_2 (l_2^2 + k_2^2) \left[(q + \cos \phi \Delta \dot{\theta}_y - \sin \phi \Delta \dot{\theta}_z)^2 + \right. \\
 & \quad \left. (r + \cos \phi \Delta \dot{\theta}_z + \sin \phi \Delta \dot{\theta}_y)^2 \right] \Bigg\rangle
 \end{aligned} \tag{123}$$

where m_1 & m_2 are the masses, respectively, of the spin aft section and of the non-spin forward section. The radii of gyration, k_1 and k_2 refer to the moments of inertia of m_1 and m_2 , respectively, about transverse axes through the respective mass centers. Finally J_2 is the polar moment of inertia of the non-spin forward mass about the x-axis centerline.

4.2.3 Potential Energy and Generalized Forces

The potential energy relating to the equivalent gimbal springs and the angular articulation about the gimbal of the non-spin forward mass is given simply by:

$$V = \frac{1}{2} K_{gimbal} (\Delta \theta_y^2 + \Delta \theta_z^2) \tag{124}$$

The generalized forces relating to the forward mass degrees of freedom arise from thrust effects, centripetal acceleration, gravity and control moments. The total virtual work relating to the basic as well as the additional degrees of freedom is expressible as:

$$\begin{aligned}
 \delta W = & \Xi_{v_x} \delta v_x + \Xi_y \delta y + \Xi_z \delta z + \Xi_{\theta_y} \delta \theta_y + \Xi_{\theta_z} \delta \theta_z \\
 & + \Xi_{\Delta \theta_y} \delta \Delta \theta_y + \Xi_{\Delta \theta_z} \delta \Delta \theta_z + \Xi_{\phi_{NS}} \delta \phi_{NS}
 \end{aligned} \tag{125}$$

Appendix C

RLBA Engineering Report 00-02 (Rev. A)

wherein those generalized forces that are incremented by the non-spin degrees of freedom are given by:

$$\begin{aligned}\Xi_{\theta_y} = & M_y^{(a)} + M_y^{(p)} + \cos \phi_{NS} M_y^{(c)} - \sin \phi_{NS} M_z^{(c)} + \\ & (T - D) \frac{m_2 h_2}{m} (\cos \phi_{NS} \Delta \theta_y - \sin \phi_{NS} \Delta \theta_z)\end{aligned}\quad (126)$$

$$\begin{aligned}\Xi_{\theta_z} = & M_z^{(a)} + M_z^{(p)} + \sin \phi_{NS} M_y^{(c)} + \cos \phi_{NS} M_z^{(c)} + \\ & (T - D) \frac{m_2 h_2}{m} (\sin \phi_{NS} \Delta \theta_y + \cos \phi_{NS} \Delta \theta_z)\end{aligned}\quad (127)$$

$$\begin{aligned}\Xi_{\Delta \theta_y} = & h_2 \left\langle \left[T \left(1 - \frac{m_1}{m} \right) + D \frac{m_1}{m} \right] \Delta \theta_y - \right. \\ & m_2 \left\{ g \left[\left(-\sin \Delta \lambda \cos \psi \sin \Theta_y + \cos \Delta \lambda \cos \Theta_y \right) \cos \phi_{NS} - \right. \right. \\ & \left. \left. (\sin \Delta \lambda \sin \psi) \sin \phi_{NS} \right] + \right. \\ & \left. \left[(Q_{ie} + q) \cos \phi_{NS} + (R_{ie} + r) \sin \phi_{NS} \right] v_x \right\} \rangle + M_y^{(c)}\end{aligned}\quad (128)$$

$$\begin{aligned}\Xi_{\Delta \theta_z} = & h_2 \left\langle \left[T \left(1 - \frac{m_1}{m} \right) + D \frac{m_1}{m} \right] \Delta \theta_z + \right. \\ & m_2 \left\{ g \left[\left(-\sin \Delta \lambda \cos \psi \sin \Theta_y + \cos \Delta \lambda \cos \Theta_y \right) \sin \phi_{NS} + \right. \right. \\ & \left. \left. (\sin \Delta \lambda \sin \psi) \cos \phi_{NS} \right] + \right. \\ & \left. \left[(Q_{ie} + q) \cos \phi_{NS} + (R_{ie} + r) \sin \phi_{NS} \right] v_x \right\} \rangle + M_y^{(c)}\end{aligned}\quad (129a)$$

where:

$$\Theta_y = \theta_y + \Delta \theta_y \cos \phi_{NS} - \Delta \theta_z \sin \phi_{NS}\quad (129b)$$

$$\Xi_{\phi_{NS}} = M_x^{(c)}\quad (130)$$

Appendix C

RLBA Engineering Report 00-02 (Rev. A)

4.2.4 Final Form of Dynamic Equations

With a standard application of Lagrange's equations, the above formulations lead to the following final form of the equations of motion:

X-force equilibrium: [unchanged from previous formulation, but reproduced here for completeness]:

$$m\dot{v}_x = -m[(Q_{ie} + q)v_z - (R_{ie} + r)v_y] + F_x^{(a)} + F_x^{(p)} + F_x^{(g)} \quad (131)$$

Y-force equilibrium:

$$m\dot{v}_y + m_2 h_2 (\sin \phi_{NS} \Delta \ddot{\theta}_y + \cos \phi_{NS} \Delta \ddot{\theta}_z) = -m(R_{ie} + r)v_x + F_y^{(a)} + F_y^{(p)} + F_y^{(g)} \quad (132)$$

Z-force equilibrium:

$$m\dot{v}_z + m_2 h_2 (-\cos \phi_{NS} \Delta \ddot{\theta}_y + \sin \phi_{NS} \Delta \ddot{\theta}_z) = m(Q_{ie} + q)v_x + F_z^{(a)} + F_z^{(p)} + F_z^{(g)} \quad (133)$$

Total vehicle (pitch) y-axis Moment equilibrium:

$$I_d \dot{q} + m_2 (h_2 l_2 + k_2^2) (\cos \phi_{NS} \Delta \ddot{\theta}_y - \sin \phi_{NS} \Delta \ddot{\theta}_z) = \cos \phi_{NS} M_y^{(c)} - \sin \phi_{NS} M_z^{(c)} - I_d \dot{Q}_{ie} - J_{spin} \Omega (R_{ie} + r) + (T - D) \frac{m_2 h_2}{m} (\cos \phi_{NS} \Delta \theta_y - \sin \phi_{NS} \Delta \theta_z) + M_y^{(a)} + M_y^{(p)} \quad (134)$$

Total vehicle (yaw) z-axis Moment equilibrium:

$$I_d \dot{r} + m_2 (h_2 l_2 + k_2^2) (\sin \phi_{NS} \Delta \ddot{\theta}_y + \cos \phi_{NS} \Delta \ddot{\theta}_z) = \sin \phi_{NS} M_y^{(c)} + \cos \phi_{NS} M_z^{(c)} - I_d \dot{R}_{ie} + J_{spin} \Omega (Q_{ie} + q) + (T - D) \frac{m_2 h_2}{m} (\sin \phi_{NS} \Delta \theta_y + \cos \phi_{NS} \Delta \theta_z) + M_z^{(a)} + M_z^{(p)} \quad (135)$$

Appendix C

RLBA Engineering Report 00-02 (Rev. A)

Non-spin mass (pitch) y-axis Moment equilibrium:

$$\begin{aligned}
 & m_2 h_2 (\sin \phi_{NS} \dot{v}_y - \cos \phi_{NS} \dot{v}_z) + m_2 (h_2 l_2 + k_2^2) (\cos \phi_{NS} \dot{q} + \sin \phi_{NS} \dot{r}) + \\
 & m_2 (l_2^2 + k_2^2) \Delta \ddot{\theta}_y = M_y^{(c)} + h_2 \left[T \left(1 - \frac{m_l}{m} \right) + D \frac{m_l}{m} \right] \Delta \theta_y - K_{gimbal} \Delta \theta_y \\
 & - m_2 h_2 \left\{ g \left[(-\sin \Delta \lambda \cos \psi \sin \Theta_y + \cos \Delta \lambda \cos \Theta_y) \cos \phi_{NS} - (\sin \Delta \lambda \sin \psi) \sin \phi_{NS} \right] \right. \\
 & \quad \left. + [(Q_{ie} + q) \cos \phi_{NS} + (R_{ie} + r) \sin \phi_{NS}] v_x \right\}
 \end{aligned} \tag{136}$$

Non-spin mass (yaw) z-axis Moment equilibrium:

$$\begin{aligned}
 & m_2 h_2 (\cos \phi_{NS} \dot{v}_y + \sin \phi_{NS} \dot{v}_z) + m_2 (h_2 l_2 + k_2^2) (-\sin \phi_{NS} \dot{q} + \cos \phi_{NS} \dot{r}) + \\
 & m_2 (l_2^2 + k_2^2) \Delta \ddot{\theta}_z = M_z^{(c)} + h_2 \left[T \left(1 - \frac{m_l}{m} \right) - D \frac{m_l}{m} \right] \Delta \theta_z - K_{gimbal} \Delta \theta_z \\
 & + m_2 h_2 \left\{ g \left[(-\sin \Delta \lambda \cos \psi \sin \Theta_y + \cos \Delta \lambda \cos \Theta_y) \sin \phi_{NS} + (\sin \Delta \lambda \sin \psi) \cos \phi_{NS} \right] \right. \\
 & \quad \left. + [(Q_{ie} + q) \sin \phi_{NS} - (R_{ie} + r) \cos \phi_{NS}] v_x \right\}
 \end{aligned} \tag{137}$$

Non-spin Roll Equation:

$$J_{NS} \dot{P}_{NS} = M_x^{(c)} \tag{138}$$

The above equation set constitutes a reasonably complete nonlinear formulation of the dynamics. Relative to the basic equation set, the time-history solution of this new equation set is complicated by the fact that there is now inertia coupling. Thus, the coupled equation set, using the augmented state vector defined by Eq. 122, becomes:

$$[A] \{ \dot{Y} \}_{augmented} = \{ F(t, Y) \} \tag{139}$$

where:

$$[A] = \begin{bmatrix} A_{11} & A_{12} & 0 & 0 \\ \dots & A_{22} & 0 & 0 \\ 0 & 0 & I_3 & 0 \\ (S) & 0 & 0 & I_8 \end{bmatrix} \tag{140}$$

Appendix C

RLBA Engineering Report 00-02 (Rev. A)

$$[A_{11}] = \begin{bmatrix} m & & & \\ & m & & 0 \\ & & m & \\ & 0 & & I_d \\ & & & & I_d \end{bmatrix} \quad (141)$$

$$[A_{12}] = \begin{bmatrix} 0 & 0 & 0 \\ m_2 h_2 \sin \phi_{NS} & m_2 h_2 \cos \phi_{NS} & 0 \\ -m_2 h_2 \cos \phi_{NS} & m_2 h_2 \sin \phi_{NS} & 0 \\ m_2 (h_2 l_2 + k_2^2) \cos \phi_{NS} & -m_2 (h_2 l_2 + k_2^2) \sin \phi_{NS} & 0 \\ m_2 (h_2 l_2 + k_2^2) \sin \phi_{NS} & m_2 (h_2 l_2 + k_2^2) \cos \phi_{NS} & 0 \end{bmatrix} \quad (142)$$

$$[A_{22}] = \begin{bmatrix} m_2 (k_2^2 + l_2^2) & 0 & 0 \\ 0 & m_2 (k_2^2 + l_2^2) & 0 \\ 0 & 0 & J_{NS} \end{bmatrix} \quad (143)$$

Using standard partitioning methods Eq.136 can be inverted to the form required for an application of the Runge-Kutta solution methodology:

$$\{\dot{Y}\}_{augmented} = [A]^{-1} \{F(t, Y)\} \quad (144)$$

4.2.5 Eigenvalue Solution Considerations

The perturbational forms of Eqs. 131 thru 138 should, for strict consistency, contain the perturbational forms of the control moments, $M^{(c)}$. [i.e., $(\mathfrak{R} M^{(c)})_{x,y,z}$]. However, the development of these moments is deferred to a subsequent chapter. The expansion of the basic eigenvalue formulation and solution to include the dual-spin, two-body dynamics begins with a redefinition of the perturbational state vector. The $\{\mathfrak{R}Z\}$ vector previously defined in Eq. 109, now becomes:

Appendix C

RLBA Engineering Report 00-02 (Rev. A)

$$\begin{bmatrix} \delta Z \end{bmatrix} = \begin{bmatrix} \delta Z_1 & | & \delta Z_2 & | & \delta Z_3 & | & \delta Z_4 & | & \delta Z_5 \end{bmatrix} \quad (145)$$

where:

$$\begin{aligned} \begin{bmatrix} \delta Z_1 \end{bmatrix} &= \delta v_x \\ \begin{bmatrix} \delta Z_2 \end{bmatrix} &= \begin{bmatrix} \delta \dot{y} & \delta \dot{z} & \delta \dot{\theta}_y & \delta \dot{\theta}_z \end{bmatrix} \\ \begin{bmatrix} \delta Z_3 \end{bmatrix} &= \begin{bmatrix} \delta y & \delta z & \delta \theta_y & \delta \theta_z \end{bmatrix} \\ \begin{bmatrix} \delta Z_4 \end{bmatrix} &= \begin{bmatrix} \delta \Delta \dot{\theta}_y & \delta \Delta \dot{\theta}_z & \delta \dot{\phi}_{NS} \end{bmatrix} \\ \begin{bmatrix} \delta Z_5 \end{bmatrix} &= \begin{bmatrix} \delta \Delta \theta_y & \delta \Delta \theta_z & \delta \phi_{NS} \end{bmatrix} \end{aligned} \quad (146b)$$

and where the $[A]$ and $[B]$ matrices defining the eigenvalue problem (Eq. 108) are commensurately expanded to include additional partitions:

$$[A] = \begin{bmatrix} m & 0 & 0 & 0 & 0 \\ \dots & M & 0 & \hat{A}_{24} & 0 \\ \dots & \dots & I_4 & 0 & 0 \\ \dots & (S) & \dots & M_{NS} & 0 \\ \dots & \dots & \dots & \dots & I_3 \end{bmatrix} \quad (147)$$

and

$$[B] = \begin{bmatrix} b_{11} & B_{12} & B_{13} & 0 & 0 \\ B_{21} & B_{22} & B_{23} & 0 & B_{25} \\ 0 & I_4 & 0 & 0 & 0 \\ B_{41} & B_{42} & B_{43} & 0 & B_{45} \\ 0 & 0 & 0 & I_3 & 0 \end{bmatrix} \quad (148)$$

Appendix C

RLBA Engineering Report 00-02 (Rev. A)

where:

$$[M_{NS}] = \begin{bmatrix} m_2(l_2^2 + k_2^2) & 0 & 0 \\ 0 & m_2(l_2^2 + k_2^2) & 0 \\ 0 & 0 & J_{NS} \end{bmatrix} \quad (= [A_{22}]) \quad (149)$$

$$[\hat{A}_{24}] = \begin{bmatrix} m_2 h_2 \sin \phi_{NS} & m_2 h_2 \cos \phi_{NS} & 0 \\ -m_2 h_2 \cos \phi_{NS} & m_2 h_2 \sin \phi_{NS} & 0 \\ m_2(h_2 l_2 + k_2^2) \cos \phi_{NS} & -m_2(h_2 l_2 + k_2^2) \sin \phi_{NS} & 0 \\ m_2(h_2 l_2 + k_2^2) \sin \phi_{NS} & m_2(h_2 l_2 + k_2^2) \cos \phi_{NS} & 0 \end{bmatrix} \quad (150)$$

$$[B_{25}] = \begin{bmatrix} 0 & 0 & 0 \\ 0 & 0 & 0 \\ (T-D) \frac{m_2 h_2}{m} \cos \phi_{NS} & -(T-D) \frac{m_2 h_2}{m} \sin \phi_{NS} & 0 \\ (T-D) \frac{m_2 h_2}{m} \sin \phi_{NS} & (T-D) \frac{m_2 h_2}{m} \cos \phi_{NS} & 0 \end{bmatrix} \quad (151)$$

$$\{B_{41}\} = \begin{Bmatrix} -m_2 h_2 [(Q_{ie} + q_N) \cos \phi_{NS} + (R_{ie} + r_N) \sin \phi_{NS}] \\ m_2 h_2 [(Q_{ie} + q_N) \sin \phi_{NS} - (R_{ie} + r_N) \cos \phi_{NS}] \\ 0 \end{Bmatrix} \quad (152)$$

$$[B_{42}] = \begin{bmatrix} 0 & 0 & -m_2 h_2 v_{x_N} \cos \phi_{NS} & -m_2 h_2 v_{x_N} \sin \phi_{NS} \\ 0 & 0 & m_2 h_2 v_{x_N} \sin \phi_{NS} & -m_2 h_2 v_{x_N} \cos \phi_{NS} \\ 0 & 0 & 0 & 0 \end{bmatrix} \quad (153)$$

Appendix C

RLBA Engineering Report 00-02 (Rev. A)

$$[B_{43}] = \begin{bmatrix} 0 & 0 & (m_2 h_2 g \Gamma_{\Delta 1} \cos \phi_{NS}) & (m_2 h_2 g \Gamma_{\Delta 1} \sin \phi_{NS}) \\ 0 & 0 & (-m_2 h_2 g \Gamma_{\Delta 1} \sin \phi_{NS}) & (m_2 h_2 g \Gamma_{\Delta 1} \cos \phi_{NS}) \\ 0 & 0 & 0 & 0 \end{bmatrix} \quad (154)$$

$$[B_{45}] = \begin{bmatrix} \begin{pmatrix} -K_{gimbal} + \Gamma_{TD} + \\ m_2 h_2 g \Gamma_{\Delta 1} \end{pmatrix} & 0 & \Gamma_{y\phi} \\ 0 & \begin{pmatrix} -K_{gimbal} + \Gamma_{TD} + \\ m_2 h_2 g \Gamma_{\Delta 1} \end{pmatrix} & \Gamma_{z\phi} \\ 0 & 0 & 0 \end{bmatrix} \quad (155)$$

where:

$$\Gamma_{TD} = h_2 \left[T \left(1 - \frac{m_1}{m} \right) + D \frac{m_1}{m} \right] \quad (156a)$$

$$\Gamma_{\Delta 1} = \sin \Delta \lambda \cos \psi \cos \Theta_y + \cos \Delta \lambda \sin \Theta_y$$

$$\Gamma_{\Delta 2} = -\sin \Delta \lambda \cos \psi \sin \Theta_y + \cos \Delta \lambda \cos \Theta_y$$

$$\Gamma_{\Delta 3} = \sin \Delta \lambda \sin \psi$$

(156b,c,d)

$$\Gamma_{y\phi} = m_2 h_2 \left\{ g(\Gamma_{\Delta 2} \sin \phi_{NS} + \Gamma_{\Delta 3} \cos \phi_{NS}) + [(Q_e + q) \sin \phi_{NS} - (R_e + r) \cos \phi_{NS}] v_x \right\}_N \quad (156e)$$

$$\Gamma_{z\phi} = m_2 h_2 \left\{ g(\Gamma_{\Delta 2} \cos \phi_{NS} - \Gamma_{\Delta 3} \sin \phi_{NS}) + [(Q_e + q) \cos \phi_{NS} + (R_e + r) \sin \phi_{NS}] v_x \right\}_N \quad (156f)$$

With the exclusion of the perturbational control loads, the perturbational roll equation can be seen to have no terms other than the inertia term. Hence, this mode would have an identically zero eigenvalue, and would not be of much interest to the simulation. Hence, for a complete description of the dynamics of the forward non-spin portion of the Lightcraft, a statement of the control dynamics must be included. This development is provided in the following section.

Appendix C

RLBA Engineering Report 00-02 (Rev. A)

5.0 Attitude Control Characteristics

The guidance and control of the Lightcraft is complicated by the fact that, to a large degree, the Lightcraft is guided by the time history of the ground-based laser pointing system. As such, this does not define an autonomous control scenario, unless the pointer descriptors, i.e., the laser zenith and bearing angles, can be controlled by the Lightcraft itself. While this is theoretically possible, it would involve significant telemetric processes that are not yet practical. Thus, as far as the laser pointing characteristics are concerned, the dynamic simulation developed herein adopts only an open-loop capability, as is described in a previous section.

One problem that such an open-loop scenario poses is that it does not account for the fact that the Lightcraft must maintain an optimum orientation with the laser beam. This situation thus creates a requirement for some form of attitude control. The problem is further complicated in that the Lightcraft is a highly gyroscopic body and, therefore, will experience significant cross coupling between pitch and yaw.

In the development to follow the details of the actual moment producing mechanisms (attitude thrusters, gyro wheels, etc.) are not considered. All of the control system dynamics have *control moments* as the final output to the airframe.

5.1 Modeling Considerations

5.1.1 Physical Considerations

Two types of control can be applied to the Lightcraft: open-loop and multi-variant feedback, and both are included in this flight dynamic simulation. Furthermore, each of these control types is assumed to consist exclusively of the three components of control *moment* (i.e., no control forces are considered):

a. “roll” control, $(M_x)^{(c)}$, wherein this control moment is applied only to the non-spin component if the dual-spin modeling is activated. Note that the non-spin roll degree of freedom can realistically exist only by providing a bearing to allow for the dual-spin operation. Such a bearing will generally have some degree of friction resulting in a source of damping about that axis. This defines the requirement for providing some form of compensating torque (a motor or externally provided torque) to the non-spin component of the Lightcraft, to keep it from eventually spinning along with the aft spin component. This torque requirement must, therefore, be included with the *actual* implementation of the roll control. From a simulation standpoint, however, it is assumed that the torque compensation is present and equilibrates the friction torque to achieve a constant roll angle in the non-spin component of the Lightcraft. Thus, only the variations from the torque compensation value are considered. Even the variations from the steady value must account for the effective damping resulting from the friction in the bearing.

b. “pitch” control, $(M_y)^{(c)}$, which is applied to both the total Lightcraft and the non-spin fore-body component. Since this control moment can realistically be applied only to the non-spin component, it will be aligned with the roll angle of the non-spin component. This characteristic has already been addressed in the previous section.

Appendix C

RLBA Engineering Report 00-02 (Rev. A)

c. “yaw” control, $(M_z)^{(c)}$, which is also applied to both the total Lightcraft and the non-spin component, and subject to the same considerations.

The control system is assumed to be driven by combinations of the following (input) dynamic variables:

- 1) Direct open-loop (specified time histories of) moments, $M_x(t)_{OL}$, $M_y(t)_{OL}$, $M_z(t)_{OL}$,
- 2) Vehicle angular rates about the Lightcraft’s principal axes, p , q , and r (feed-back variables)
- 3) Specified open-loop time histories of commanded values of the Lightcraft’s Euler angles, θ , Θ_y , and Θ_{NS} (i.e., heading, pitch attitude and roll of the non-spin component).
- 4) Actual (internally measured) values of the Lightcraft’s Euler angles (feedback variables).
- 5) Total angular offset angles, Θ_y and Θ_z , (includes pitch and yaw deflections of the non-spin fore-body) relating the orientation of the laser beam to the center line of the Lightcraft (feedback variables). [The actual practical implementation of a scheme for measuring these angles is a design problem outside the scope of the present report and an issue to be solved in the future.]

Additionally, all three components of control moment (arising from the sums of direct input values and those due to feedback) that are actively applied to the Lightcraft are subject to limiters.

5.1.2 Basic Control Law Strategies

It is assumed that the eventual design of a satisfactory control system for the Lightcraft will necessarily be a multi-variable one with multi-variable inputs and outputs. Besides being multi-variant, the system is assumed to consist of only proportional and integrator elements. However, because the state vector to be implemented includes rate terms, the system is inherently a PID system. The exact selection of gains in any particular design is beyond the current knowledge of the Lightcraft’s dynamics and thus, a wide range of possible inputs has been assumed. *It is to be stressed that the principal objective of the present analysis is to provide the tools for enabling the systematic selection of these gains.* Fig. 12 summarizes the structure and strategies assumed for a “generic” Lightcraft control system:

Appendix C

RLBA Engineering Report 00-02 (Rev. A)

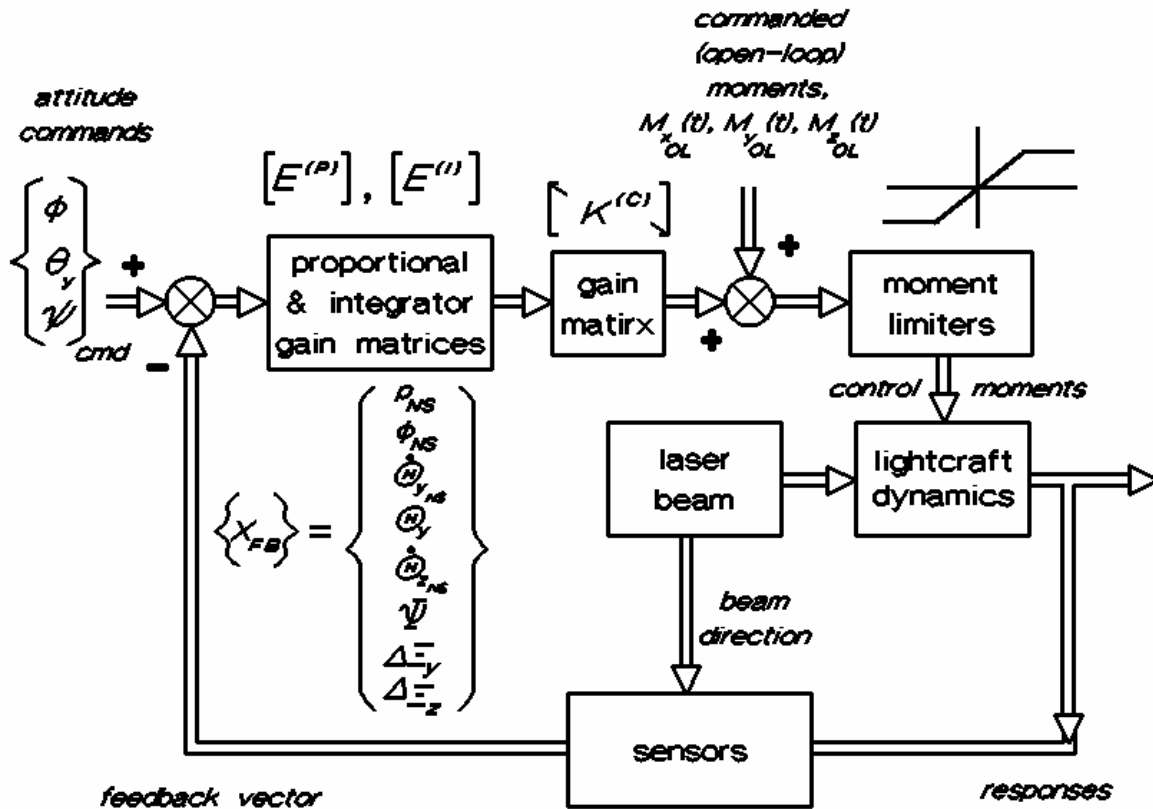


Fig. 12 Schematic of Generic Lightcraft Control System

5.2 Implementations of Moment Control Mechanisms

5.2.1 Feed Back Moment Description

As Fig. 12 indicates, the control system is multi-variant wherein the three components of control moment are each a combination of a commanded (open-loop) moment and a moment arising from the feedback function. In Laplace operator notation these combined moments can be expressed as:

Appendix C

RLBA Engineering Report 00-02 (Rev. A)

$$\begin{Bmatrix} M_x^{(c)} \\ M_y^{(c)} \\ M_z^{(c)} \end{Bmatrix} = [L(s)] \left\{ \begin{Bmatrix} M_{xOL} \\ M_{yOL} \\ M_{zOL} \end{Bmatrix} + [K^{(c)}] \left[[E^{(I)}] \frac{1}{s} + [E^{(P)}] \right] \begin{Bmatrix} -p_{NS} \\ \phi_{cmd} - \phi_{NS} \\ -\dot{\Theta}_{y_{NS}} \\ \theta_{y_{cmd}} - \Theta_y \\ -\dot{\Theta}_{z_{NS}} \\ \psi_{cmd} - \Psi \\ -\Delta \Xi_y \\ -\Delta \Xi_z \end{Bmatrix} \right\} \quad (157a)$$

or, alternatively:

$$\begin{Bmatrix} M_x^{(c)} \\ M_x^{(c)} \\ M_x^{(c)} \end{Bmatrix} = [L(s)] \left\{ \begin{Bmatrix} M(s)_{xOL} \\ M(s)_{yOL} \\ M(s)_{zOL} \end{Bmatrix} + [K^{(c)}] \left[[E^{(I)}] \frac{1}{s} + [E^{(P)}] \right] \{ X_{cmd}^{(c)} - X_{FB}^{(c)} \} \right\} \quad (157b)$$

where $[L(s)]$ is a diagonal matrix and represents the action of the moment limiters. In the time domain this matrix is given by:

$$[L(t)] = \begin{bmatrix} L_{M_X} & 0 & 0 \\ 0 & L_{M_Y} & 0 \\ 0 & 0 & L_{M_Z} \end{bmatrix} \quad (158)$$

where L_{Mq} represents a unit gain for the “ q th” component of moment (i.e., $q = x, y$, or z) if the absolute value of that moment is less than the saturation value, M_{qmax} , and is equal to the saturation value (% sign of M_q) if the absolute value of the moment is greater than the saturation value. The proportional and integrator coupling matrices have the following partitioned forms:

Appendix C

RLBA Engineering Report 00-02 (Rev. A)

$$\begin{aligned} \left[E^{(P)} \right] &= \left[\begin{array}{cc|cccccc} k_{X,p}^{(P)} & k_{X,\phi}^{(P)} & & & & & & \\ & & & & & & & 0 \\ \hline & 0 & k_{Y,q}^{(P)} & k_{Y,\theta_Y}^{(P)} & k_{Y,r}^{(P)} & k_{Y,\psi}^{(P)} & k_{Y,\Delta\xi_Y}^{(P)} & k_{Y,\Delta\xi_Z}^{(P)} \\ & & k_{Z,q}^{(P)} & k_{Z,\theta_Y}^{(P)} & k_{Z,r}^{(P)} & k_{Z,\psi}^{(P)} & k_{Z,\Delta\xi_Y}^{(P)} & k_{Z,\Delta\xi_Z}^{(P)} \end{array} \right] \\ &= \left[\begin{array}{c|c} E_{11}^{(P)} & 0 \\ \hline 0 & E_{22}^{(P)} \end{array} \right] \end{aligned} \quad (159)$$

$$\begin{aligned} \left[E^{(I)} \right] &= \left[\begin{array}{cc|cccccc} k_{X,p}^{(I)} & k_{X,\phi}^{(I)} & & & & & & \\ & & & & & & & 0 \\ \hline & 0 & k_{Y,q}^{(I)} & k_{Y,\theta_Y}^{(I)} & k_{Y,r}^{(I)} & k_{Y,\psi}^{(I)} & k_{Y,\Delta\xi_Y}^{(I)} & k_{Y,\Delta\xi_Z}^{(I)} \\ & & k_{Z,q}^{(I)} & k_{Z,\theta_Y}^{(I)} & k_{Z,r}^{(I)} & k_{Z,\psi}^{(I)} & k_{Z,\Delta\xi_Y}^{(I)} & k_{Z,\Delta\xi_Z}^{(I)} \end{array} \right] \\ &= \left[\begin{array}{c|c} E_{11}^{(I)} & 0 \\ \hline 0 & E_{22}^{(I)} \end{array} \right] \end{aligned} \quad (160)$$

The moment gain matrix is simply a diagonal matrix containing the gains appropriate to the three axes:

$$\left[K^{(c)} \right] = \begin{bmatrix} K_{M_X} & 0 & 0 \\ 0 & K_{M_Y} & 0 \\ 0 & 0 & K_{M_Z} \end{bmatrix} \quad (161)$$

[Note that lack of control axis activation (see Appendix A) is implemented by setting the gain appropriate to the component of moment control not being activated, to zero.]

5.2.2 Details of the Error Vector

The error vector given in Eqs. 157a&b is comprised of the commanded attitude angles, the sensed angular rates about the major axes (in the non-spin portion of the Lightcraft) and the angular offsets of the laser beam vis-à-vis the longitudinal axis of the Lightcraft. In particular:

$$\Delta \tilde{\theta}_y = \theta_{y_{cmd}} - \Theta_y = \theta_{y_{cmd}} - \left(\theta_y + \Delta \theta_y \cos \phi_{NS} - \Delta \theta_z \sin \phi_{NS} \right) \quad (162a)$$

Appendix C

RLBA Engineering Report 00-02 (Rev. A)

$$\begin{aligned}\Delta\tilde{\Psi} &= \Psi_{cmd} - \Psi = \Psi_{cmd} - \left[\Psi + \cos\Theta_y \left(\Delta\theta_y \sin\phi_{NS} + \Delta\theta_z \cos\phi_{NS} \right) \right] \\ &= \Psi_{cmd} - \cos\Theta_y \left[\theta_z + \sin\phi_{NS} \Delta\theta_y + \cos\phi_{NS} \Delta\theta_z \right]\end{aligned}\quad (162b)$$

where the time variations of θ_y and θ_z are, respectively, governed by Eqs. 18 & 19. The response variables associated with the dual-spin configuration, θ_y and θ_z are determined by the time-history solution of the coupled system, as described in the section 4.0. The (total) offset error angles Θ_y and Θ_z are governed by developments presented in Section 2.5.4.2 and include the angular deflections of the non-spin fore-body. In particular:

$$\begin{aligned}\Delta\Xi_y &= \Delta\xi_y - \left(\cos\phi_{NS} \Delta\theta_y - \sin\phi_{NS} \Delta\theta_z \right) \\ \Delta\Xi_z &= \Delta\xi_z - \left(\sin\phi_{NS} \Delta\theta_y + \cos\phi_{NS} \Delta\theta_z \right)\end{aligned}\quad (163a,b)$$

where:

$$\Delta\xi_y = -\sin^{-1} \left(\frac{\tilde{s}_{FC_z}}{\sqrt{\tilde{s}_{FC_x}^2 + \tilde{s}_{FC_z}^2}} \right) \quad ; \quad \Delta\xi_z = \sin^{-1} \left(\frac{\tilde{s}_{FC_y}}{\sqrt{\tilde{s}_{FC_x}^2 + \tilde{s}_{FC_y}^2}} \right)\quad (162c,d)$$

Note that the portions of the angular offsets that do not include the deflections of the non-spin fore-body (Eqs. 162c&d) also implicitly produce side forces and moments due to propulsive characteristics (see Section 2.5.4.2). Nevertheless, these offsets are explicitly included in the moment control system to provide the wherewithal for modifying these characteristics if they prove to be inadequate (i.e., too weak or conducive to unstable operation).

The feedback state vector, as would be measured in the non-spin component of the Lightcraft, can be represented in terms of the vehicle state vector components:

$$\left\{ X_{FB}^{(c)} \right\} = \left\{ \begin{array}{c} p_{NS} \\ \phi_{NS} \\ \Delta\dot{\theta}_y + q \cos\phi_{NS} + r \sin\phi_{NS} \\ \theta_y + \Delta\theta_y \cos\phi_{NS} - \Delta\theta_z \sin\phi_{NS} \\ \Delta\dot{\theta}_z - q \sin\phi_{NS} + r \cos\phi_{NS} \\ \Psi + \cos\Theta_y \left(\Delta\theta_y \sin\phi_{NS} + \Delta\theta_z \cos\phi_{NS} \right) \\ \Delta\Xi_y \\ \Delta\Xi_z \end{array} \right\}\quad (164)$$

Appendix C

RLBA Engineering Report 00-02 (Rev. A)

5.3 Incorporating the Control System Simulation into the Nonlinear Equation Set

The presence of integrator terms in the control moment dynamics requires that a set of equations be used to solve for the control moments and that the equations be incorporated into the general equations set (that is solved by the Runge-Kutta method). To this end an auxiliary control state vector is defined using the control state vector, $\{X^{(c)}\}$, defined in Eq. 157:

$$\left\{ Y^{(c)} \right\} = \int_0^t \left\{ X^{(c)} \right\} dt \quad (165)$$

Thus, Eq. 153 can be rewritten as:

$$\begin{Bmatrix} M_x^{(c)} \\ M_y^{(c)} \\ M_z^{(c)} \end{Bmatrix} = [L(t)] \begin{Bmatrix} M(s)_{xOL} \\ M(s)_{yOL} \\ M(s)_{zOL} \end{Bmatrix} + [K^{(c)}] \left\{ [E^{(I)}] \left\{ Y^{(c)} \right\} + [E^{(P)}] \left\{ X^{(c)} \right\} \right\} \quad (166)$$

And the augmented state vector then becomes:

$$\{Y\}_{augmented} \equiv \begin{Bmatrix} v_x \\ v_y \\ v_z \\ q \\ r \\ \hline \Delta \dot{\theta}_y \\ \Delta \dot{\theta}_z \\ p_{NS} \\ \Delta \theta_y \\ \Delta \theta_z \\ \hline \phi_{NS} \\ \{Y^{(c)}\} \\ \hline m \\ R_{gc} \\ \lambda \\ L \\ \psi \\ \theta_y \end{Bmatrix} \quad (167)$$

Appendix C

RLBA Engineering Report 00-02 (Rev. A)

where the required entry in the time derivative of the augmented state vector is simply:

$$\{\dot{Y}\}_{augmented} = \begin{Bmatrix} \vdots \\ \hline \dot{Y}^{(c)} \\ \hline \vdots \end{Bmatrix} = \begin{Bmatrix} \vdots \\ \hline X^{(c)} \\ \hline \vdots \end{Bmatrix} \quad (168)$$

5.4 Supplement to Eigenvalue Solution:

In the development of Section 4.2.5 the inclusion of the control moments was omitted pending the development of the present section. With the inclusion of the perturbational control loads, the perturbational form of the dual-spin equations of motion can be represented as:

$$[A]\{\delta\dot{Z}\} = [B]\{\delta Z\} + \left\{ \begin{array}{c} 0 \\ \hline 0 \\ 0 \\ \cos \phi_{NS} \delta M_y^{(c)} + \sin \phi_{NS} \delta M_z^{(c)} \\ - \sin \phi_{NS} \delta M_y^{(c)} + \cos \phi_{NS} \delta M_z^{(c)} \\ \hline 0 \\ 0 \\ 0 \\ 0 \\ \hline \delta M_y^{(c)} \\ \delta M_z^{(c)} \\ \delta M_x^{(c)} \\ \hline 0 \\ 0 \\ 0 \end{array} \right\} = [B]\{\delta Z\} + [U] \begin{Bmatrix} \delta M_x^{(c)} \\ \delta M_y^{(c)} \\ \delta M_z^{(c)} \end{Bmatrix} \quad (169)$$

Appendix C

RLBA Engineering Report 00-02 (Rev. A)

where:

$$[U] = \begin{bmatrix} 0 & 0 & 0 \\ 0 & 0 & 0 \\ 0 & 0 & 0 \\ 0 & \cos \phi_{NS} & \sin \phi_{NS} \\ 0 & -\sin \phi_{NS} & \cos \phi_{NS} \\ 0 & 0 & 0 \\ 0 & 0 & 0 \\ 0 & 0 & 0 \\ 0 & 0 & 0 \\ 0 & 1 & 0 \\ 0 & 0 & 1 \\ 1 & 0 & 0 \\ 0 & 0 & 0 \\ 0 & 0 & 0 \\ 0 & 0 & 0 \end{bmatrix}$$

(170)

Using formulations from Section 2.5.5, and in particular, Eqs. 84, 85 & 86, the perturbational form of the feedback state vector can be expressed as:

$$\delta \left\{ X_{FB}^{(c)} \right\} = \begin{bmatrix} 0 & H_2 & H_3 & H_4 & H_5 \end{bmatrix} \left\{ \begin{array}{c} \delta Z_1 \\ \delta Z_2 \\ \delta Z_3 \\ \delta Z_4 \\ \delta Z_5 \end{array} \right\} = [H] \left\{ \begin{array}{c} \delta Z_1 \\ \vdots \\ \delta Z_5 \end{array} \right\}$$

(171)

where:

$$[H_2] = \begin{bmatrix} 0 & \dots & 0 \\ 0 & \dots & 0 \\ 0 & 0 & \cos \phi_{NS} & \sin \phi_{NS} \\ 0 & 0 & 0 & 0 \\ 0 & 0 & -\sin \phi_{NS} & \cos \phi_{NS} \\ 0 & \dots & 0 \\ 0 & \dots & 0 \\ 0 & \dots & 0 \end{bmatrix}$$

(172)

Appendix C

RLBA Engineering Report 00-02 (Rev. A)

$$[H_3] = \begin{bmatrix} 0 & \dots & & 0 \\ 0 & \dots & & 0 \\ 0 & \dots & & 0 \\ 0 & 0 & 1 & 0 \\ 0 & \dots & & 0 \\ 0 & 0 & 0 & \cos \theta_{y_N} \\ 0 & 0 & \frac{\partial(\Delta \xi_y)_N}{\partial \theta_y} & \frac{\partial(\Delta \xi_y)_N}{\partial \theta_z} \\ 0 & 0 & \frac{\partial(\Delta \xi_z)_N}{\partial \theta_y} & \frac{\partial(\Delta \xi_z)_N}{\partial \theta_z} \end{bmatrix}$$

(173)

$$[H_4] = \begin{bmatrix} 0 & 0 & 1 \\ 0 & 0 & 0 \\ 1 & 0 & 0 \\ 0 & 0 & 0 \\ 0 & 1 & 0 \\ 0 & \dots & 0 \\ \vdots & \dots & \vdots \\ 0 & \dots & 0 \end{bmatrix}$$

(174)

$$[H_5] = \begin{bmatrix} 0 & 0 & 0 \\ 0 & 0 & 1 \\ 0 & 0 & 0 \\ \cos \phi_{NS} & -\sin \phi_{NS} & 0 \\ 0 & 0 & 0 \\ \cos \Theta_{y_N} \sin \phi_{NS} & \cos \Theta_{y_N} \cos \phi_{NS} & 0 \\ -\cos \phi_{NS} & \sin \phi_{NS} & 0 \\ -\sin \phi_{NS} & -\cos \phi_{NS} & 0 \end{bmatrix}$$

(175)

Appendix C

RLBA Engineering Report 00-02 (Rev. A)

5.4.1 Expansion of Perturbational State Vector:

With the inclusion of the control system response variables, the perturbational state vector needs to be expanded to include these variables. Thus, the perturbational state vector previously defined by Eqs. 146a&b can then be written as:

$$\begin{bmatrix} \delta \tilde{Z} \end{bmatrix} = \begin{bmatrix} \delta Z_1 & \delta Z_2 & \delta Z_3 & \delta Z_4 & \delta Z_5 & \delta Z_6 \end{bmatrix} \quad (176)$$

where δZ_1 thru δZ_5 are as defined by Eqs. 146b, and δZ_6 is defined by:

$$\left\{ \delta \dot{Z}_6 \right\} = \left\{ \delta X_{FB}^{(c)} \right\} = \begin{bmatrix} 0 & H_2 & H_3 & H_4 & H_5 & 0 \end{bmatrix} \begin{Bmatrix} \delta Z_1 \\ \vdots \\ \delta Z_5 \\ \delta Z_6 \end{Bmatrix} \quad (177)$$

5.4.2 Effect of the Moment Limiters

For the perturbational moments, the effect of the moment limiters is to reduce the perturbational moments to zero if the saturation condition is reached. Thus, the limiter matrix for the eigenvalue solution is defined as follows:

$$\begin{bmatrix} L^* \end{bmatrix} = \begin{bmatrix} L_{M_X}^* & 0 & 0 \\ 0 & L_{M_Y}^* & 0 \\ 0 & 0 & L_{M_Z}^* \end{bmatrix} \quad (178)$$

where $L_{M_q}^*$ is either unity, if the moment at the linearization condition “N” is less than or equal to the saturation (limiting) moment, and zero if the moment exceeds that value.

Appendix C

RLBA Engineering Report 00-02 (Rev. A)

5.4.3 Final Form of Eigenvalue Problem

The inclusion of the control dynamics in the eigenvalue problem is implemented by including the αZ_6 ($\alpha Y_{FB}^{(c)}$) vector. This inclusion requires that the dimension of the matrices must increase from 15 to 23. The resulting (modified) $[A]$ and $[B]$ matrices then become:

$$[\tilde{A}] = \left[\begin{array}{c|c} [A] & 0 \\ \hline 0 & I_8 \end{array} \right] \quad (179)$$

$$[\tilde{B}] = \left[\begin{array}{c|c} [B] - [U][L^*][K^{(c)}][E^{(P)}][H] & -[U][L^*][K^{(c)}][E^{(I)}] \\ \hline [H] & 0 \end{array} \right] \quad (180)$$

The eigenvalue problem of the complete dynamic system with the dual-spin configuration and the generic control system then has the following form:

$$\left[\lambda [\tilde{A}] - [\tilde{B}] \right] \begin{Bmatrix} \delta Z_1 \\ \vdots \\ \delta Z_5 \\ \delta Z_6 \end{Bmatrix} = \left[\lambda [\tilde{A}] - [\tilde{B}] \right] \{ \delta \tilde{Z} \} = \{ 0 \} \quad (181)$$

where the $[A]$ and $[B]$ matrices are defined by Eqs. 147 and 148. This completes the development of the equations of motion for the Lightcraft flight dynamic simulation.

Appendix C

RLBA Engineering Report 00-02 (Rev. A)

6.0 Summary of Results and Recommendations

6.1 Summary

The equations of motion for the flight dynamics of the laser Lightcraft have been formulated to form a comprehensive analysis tool for the eventual development of this flight concept. In addition to addressing the basic open-loop flight configurations that have been tested currently, the analysis includes next-generation configuration modeling configurations: the dual-spin configuration, which will eventually be required for both sophisticatedly instrumented unmanned and manned flights. Additionally, the coupling required for a generic feedback control system, which would require a non-spin component of the Lightcraft for both state sensing and control moment application, has also been comprehensively formulated. While no explicit feedback gains were identified, the control system amounts to a multi-variant PID feedback system. Additionally, the concurrent application of time histories of open-loop control moments has been included in the analysis.

Lastly, the analysis development has included the use of a constrained-minimization calculation resource to enable the identification of specific feedback gains and other system parameters to produce an optimized control scheme. While the constrained minimization resource (CONMIN) is one that is more or less standard within the contemporary technology base, the analysis was configured in such a way as to utilize the resource in a variety of ways and thus, enable the user to uniquely define his/her own optimization criterion.

6.2 Recommendations

During the development of the analysis several deficiencies in the Lightcraft technology base were identified. It is therefore recommended that:

1. Considerably more aerodynamic data should be experimentally obtained, especially with regard to a finer and wider mesh of angles of attack. Of equal importance, tests at higher Mach numbers and Reynolds numbers should also be undertaken.
2. Analyses should be performed to model the aerodynamic pitching damping characteristics of the Lightcraft for inclusion in the herein analytical simulation.
3. More tests should be performed to ascertain the effects of lateral (linear) offsets and angular offsets on both the coupling coefficient as well as on the side force and moment characteristics.
4. Practical schemes should be developed for applying control moments to the Lightcraft.
5. A practical method for implementing the dual-spin configuration should be developed, along with an estimation of typical elasto-mechanical characteristics, preferably with appropriate scaling characteristics.
6. The FORTRAN implementation of the analysis developed herein (LITE_DYN) should be subjected to a rigorous validation effort with as much experimental data as is available.

Appendix C

RLBA Engineering Report 00-02 (Rev. A)

7. As more substantiated laser and external aerodynamic characteristics (as discussed above) become available, the LITE_DYN code should be upgraded to include these data in the form of default data.
9. As realistic control systems evolve for the Lightcraft more details should be included in the analysis. One such refinement would be the inclusion of rate limiters on the rate feedback functions.
10. A laser beam pointing system that would enable insertion into Earth orbit (multiple lasers, e.g.) should be brought to practicality and its salient features should be included in the LITE_DYN code, along with provision for orbital specifications.
11. The constrained minimization resource should be exercised with a variety of minimization schemes to establish the basic types of control laws that are appropriate to and/or required for this type of flight vehicle.
12. The basic LITE_DYN computer code, as developed using the herein analytical development (and described in Appendix A), should be subjected to a thorough program of check-out and correlation.

Appendix C

RLBA Engineering Report 00-02 (Rev. A)

7.0 References

1. Myrabo, L. N., "Transatmospheric Laser Propulsion, Final Technical Report," SDIO Laser Propulsion Program, (contract no. 2073803), Rensselaer Polytechnic Institute, June, 1989.
2. McCormick, B. W., *Aerodynamics, Aeronautics and Flight Mechanics, second edition*, John Wiley & Sons, New York, 1995.
3. Press, W. H., Flannery, B. P., Teukolsky, S. A., Vetterling, W. T., *Numerical Recipes*, Cambridge University Press, Cambridge, 1986.
4. Wrigley, W., & Hollister, W. M., *Gyroscopic Theory, Design and Instrumentation*, M.I.T. Press, Cambridge, MA, 1969.
5. Ralston, A. & Wilf, H.S., *Mathematical Methods for Digital Computers*, Wiley, New York, 1960.
6. Panetta, A. D., et al., "Low Speed Wind Tunnel Testing of a Laser Propelled Vehicle," Final Report (contract no. F0470098M4128), Edwards Research Site, Air Force Office of Scientific Research, Rensselaer Polytechnic Institute, July, 1999.
7. Bate, R.R., Mueller, D.D., & White, J.E., *Fundamentals of Astrodynamics*, Dover, New York, 1971.
8. Fortescue, P., & Stark, J., *Spacecraft Systems Engineering*, Wiley & Sons, New York, 1999.
9. Cox, A.N. ed., *Astrophysical Quantities*, Springer-Verlag, New York, 1999.
10. Seidelmann, P.K., ed., *The Explanatory Supplement to the Astronomical Almanac*, USNO, University Science Books, Mill Valley, CA, 1992.
11. Zee, C-H, *Theory of Geostationary Satellites*, Kluwer, Netherlands.
12. McCarthy, D.D., "IERS Conventions," IERS Technical Note 21, USNO, 1996.
13. Lerch, F. J., et al., NASA Tech. Memo 104555, 1992.
14. Wertz, J.R., & Larsen, W.J. (eds), *Space Mission Analysis and Design, Third Edition*, Space Technology Library (Microcosm Press, Torrance, CA & Kluwer Academic Publishers, Boston), 1999.
15. Vanderplaats, G. N., "CONMIN – a FORTRAN Program for Constrained Function Minimization - User's Manual," NASA TMX-62,282, Ames Research Center, Moffett Field, CA, 1973.
16. Zoutendijk, G., *Methods of Feasible Directions*, Elsevier Publishing Co., Amsterdam, 1960.

Appendix C

RLBA Engineering Report 00-02 (Rev. A)

17. Vanderplaats, G. N., "Structural Optimization by Methods of Feasible Directions," National Symposium on Computerized Structural Analysis and Design, Washington, D.C., 1972.
18. Fletcher, R., and Reeves, C.M., "Function Minimization by Conjugate Gradients," British Computer Journal, Vol. 7, no. 2, 1964.

Appendix C

RLBA Engineering Report 00-02 (Rev. A)

Nomenclature

Scalars:

C	=	longitudinal compression between the two components of the vehicle, N
C_C	=	laser gross coupling factor, N/MW
$C_L, C_D \text{ \& } C_y$	=	aerodynamic lift, drag and side force coefficients, respectively.
C_m, C_n	=	aerodynamic pitching and yawing moments, respectively
D	=	drag, N
$F_x, F_y \text{ \& } F_z$	=	applied forces along the vehicle's principal axes, N
$F^{(p)}_s$	=	propulsive side force due to laser beam offsets, N
$F^{(t)}_{AOS}, F^{(s)}_{AOS}$ & $F^{(m)}_{AOS}$	=	thrust, side force and moment coupling factors, respectively, due to angular offsets, deg ⁻¹
$F^{(t)}_{LOS}, F^{(s)}_{LOS}$ & $F^{(m)}_{LOS}$	=	thrust, side force and moment coupling factors, respectively, due to (non-dimensional) linear offsets
FS	=	fuselage station, as measured from the vehicle's nose, m
FS_{arc}	=	fuselage station of external aerodynamic center, m
FS_{cg}	=	fuselage station of mass center, m
FS_{pc}	=	fuselage station of propulsion center, m
g	=	gravitational acceleration, m/s ²
H_{ns}	=	non-spin angular momentum, kg-m ² /s
H_{spin}	=	spin angular momentum, kg-m ² /s
h	=	(geodetic) altitude, km
h_1, h_2	=	distances the respective mass centers of the aft (spin) and forward (non-spin) portions of the vehicle are from the effective gimbal point, m
I_d	=	moment of inertia about transverse axis through the mass center, kg-m ²
$\mathbf{I}, \mathbf{J}, \mathbf{K}$	=	unit vectors in the geosynchronous system (see Fig 8)
$\mathbf{i}_q, \mathbf{j}_q, \mathbf{k}_q$	=	unit vectors in the "qth" coordinate system
J	=	polar moment of inertia about the longitudinal axis, kg-m ²
J_1, \dots, J_6	=	constants defining the gravitational potential.
K_{gimbal}	=	rotational spring rate of (effective) rotation spring about the gimbal point, Nm/rad
k_1, k_2	=	radii of gyration of the m_1 and m_2 masses about transverse axes through their respective mass centers, m
L	=	Earth (west) longitude, deg.
l_{ref}	=	reference length for determination of Reynold's no. (= radius of S_{ref}), km
l_1, l_2	=	distances the respective mass centers of the aft (spin) and forward (non-spin) portions of the vehicle are from the total vehicle mass center, m
$M^{(p)}_s$	=	pitching moment due to laser beam offsets, N-m
$M_x, M_y \text{ \& } M_z$	=	applied moments about the principal axes, N-m
m	=	mass of the (total) vehicle, kg
m_1, m_2	=	masses of the aft spin and forward non-spin portions of the vehicle, kg
P_{avg}	=	(averaged) output power of the laser, kJ
$p, q \text{ \& } r$	=	vehicle angular velocities about the principal axes, rad/s
Q, R	=	total vehicle (inertial) pitch and yaw response rates, respectively, rad/sec

Appendix C

RLBA Engineering Report 00-02 (Rev. A)

Q_{ie}, R_{ie}	=	components of Earth rotation rate about the y- & z- axes, rad/s
q_{∞}	=	ambient dynamic pressure, kN/m ²
R_E	=	Earth equatorial radius, km
R_{FC}	=	amplitude of vector of the laser beam's focus center, km
R_P	=	Earth polar radius, km
R_{gc}	=	geocentric radius (from the Earth's center) of vehicle's position, km
Rn	=	Reynold's number
\mathbf{r}	=	laser beam linear offset, m (typically normalized by the characteristic length, l_{ref})
$\mathbf{r}_y, \mathbf{r}_z$	=	components of \mathbf{r} in the y- and z- directions, respectively
S	=	range distance of vehicle from the laser, m
S_{LB}	=	cross section area of laser beam, m ²
S_{ref}	=	reference area for definition of aerodynamic coefficients, (= maximum cross sectional area = πl_{ref}^2), m ²
$s_x, s_y \text{ \& } s_z$	=	components of the unit vector in the "range" direction, m ²
T	=	thrust, N, or kinetic energy, kg-m ² /s ²
T_N	=	time at which the eigenvalue solution is linearized about, s
t	=	time, s
V	=	vehicle flight speed, m/s
V_t	=	projection of the flight speed in the local horizontal plane, km/s
V_z	=	(geocentric) radial component of the flight speed, km/s
y, z	=	translational responses in the y- and z-directions, respectively, m
$v_x, v_y \text{ \& } v_z$	=	translational velocities in the x-, y- & z- directions, respectively, (see Fig 1), m/s
α	=	angle of attack, deg
α_{equ}	=	total (equivalent) angle of attack, deg.
β	=	vehicle side-slip angle, deg.
θ	=	zenith angle, deg
$\mathfrak{A}(\dots)$	=	denotes the perturbational form of a variable
ζ	=	critical damping ratio
\mathcal{L}_{LB}	=	efficiency factor of laser beam
$\mathcal{L}^{(n)}$	=	aerodynamic coefficient curve-fitting factors for nth exponent of α
\mathcal{K}_y	=	total pitch angle of the forward mass about the y- axis, deg.
φ_y, φ_z	=	rotation angles of total vehicle about the y- and z- axes, deg.
$\mathbf{\varphi}_y, \mathbf{\varphi}_z$	=	angular pitch and yaw angular deflection, respectively of the forward (non-spin) portion of the vehicle about the effective gimbal point, rad.
κ	=	orientation angle between α and β , deg

Appendix C

RLBA Engineering Report 00-02 (Rev. A)

$\textcircled{2}$	=	alternatively, Earth geocentric latitude, deg, or eigenvalue, [$\textcircled{2} = \textcircled{9} ! i \textcircled{6} = -\textcircled{6}_n ! i \textcircled{6}_d$], as appropriate
μ	=	orientation angle between components of (linear or angular) beam offsets, also Earth gravitational parameter, m^3/s^2 , as appropriate.
$\textcircled{4}$	=	kinematic viscosity of ambient air, m^2/s
\textcircled{Q}_{LB}	=	attenuation factor of laser beam
\textcircled{Q}_q	=	generalized forces for the “ q th” degree of freedom.
$\textcircled{5}$	=	laser beam angular offset angle from the vehicle longitudinal axis, deg.
$\textcircled{5}_y, \textcircled{5}_z$	=	$\textcircled{5}_y, \textcircled{5}_z$ wherein the non-spin fore-body angular deflections are included, deg
$\textcircled{5}_y, \textcircled{5}_z$	=	projections of $\textcircled{5}$ onto the $x_3\text{-}z_3$ and $x_3\text{-}y_3$ planes, respectively, deg.
$\textcircled{8}$	=	ambient air density, kg/m^3
$\textcircled{9}$	=	flight path elevation angle, deg.
$\textcircled{9}_{LB}$	=	power area density of laser beam, MW/m^2
$\textcircled{2}_{NS}$	=	roll angle of the forward non-spin portion of the vehicle, rad..
$\textcircled{4}$	=	(compass) bearing angle, deg
\textcircled{er}	=	heading angle of the non-spin, fore-body (includes the angular deflections of the fore-body), deg.
$\textcircled{5}$	=	(compass) heading angle, deg.
$\textcircled{\omega}$	=	spin rate of the vehicle about the x -axis, rad/s
$\textcircled{6}_d, \textcircled{6}_n$	=	damped and undamped (natural) frequencies, respectively, rad/s

Matrices:

$[A], [B]$	=	matrices defining the general eignvalue problem
$[A_{mn}]$	=	the m,n th partition of $[A]$
$[B_{mn}]$	=	the m,n th partition of $[B]$
$[E^{(P)}],$ $[E^{(I)}]$	=	gain matrices for proportional and integral control feedback coupling
$[E_{mn}]$	=	indicates the m,n th partitioning of one of the $[E]$ matrices
$[H]$	=	feedback vector distribution matrix
$[H_q]$	=	the “ q ” th partition of the $[H]$ matrix
$[I_n]$	=	denotes an identity matrix of dimension “ n ”
$[K^{(c)}]$	=	the (diagonal) control moment gain matrix
$[L], [L^*]$	=	(diagonal) matrices representing the control moment limiting function
$[M]$	=	mass matrix
$[T_{WA\delta_3}]$	=	coordinate transformation matrix converting wind axes to the “3” system
$[T_{2\delta_I}]$	=	coordinate transformation matrix converting from the “2” to the “1” system
$[T_{3\delta_2}]$	=	coordinate transformation matrix converting from the “3” to the “2” system
$[U]$	=	moment distribution matrix
$\{U^{(f)}_{vx}\},$ $\{U^{(m)}_{vx}\},$	=	vectors relating perturbations of longitudinal velocity to propulsive (total) force and moment, respectively.

Appendix C

RLBA Engineering Report 00-02 (Rev. A)

$[U^{(f)}_{AOS}]$, $[U^{(s)}_{AOS}]$ & $[U^{(m)}_{AOS}]$	=	matrices relating components of angular offset to components of total force, side force and moment, respectively
$[U^{(f)}_{LOS}]$, $[U^{(s)}_{LOS}]$ & $[U^{(m)}_{LOS}]$	=	matrices relating components of linear offset to components of total force, side force and moment, respectively
$\{X^{(c)}\}$	=	the vector of feedback variables for the control system
$\{Y\}$	=	state vector of degrees of freedom
$\{Y\}_{aug}$	=	augmented state vectors to include dependent variables
$\{\mathfrak{A}Z\}$	=	the perturbational vector defining the eigenvalue problem
$\{\mathfrak{A}Z_q\}$	=	the “ q ” the partition of $\{\mathfrak{A}Z\}$

Subscripts:

$()_{arc}$	=	aerodynamic reference center
$()_{BF}$	=	body fixed
$()_{cmd}$	=	commanded values
$()_{FB}$	=	feedback
$()_{FC}$	=	focus center
$()_{gc}$	=	geocentric
$()_{gd}$	=	geodetic
$()_{ie}$	=	Earth to inertial space
$()_{int}$	=	integrator feedback related
$()_{LB}$	=	laser beam
$()_{LC}$	=	lightcraft
$()_{LP}$	=	laser pointing system
$()_{launch}$	=	launch point
$()_N$	=	conditions at the N th time step for linearization for the eigensolution
$()_{NS}$	=	non-spin
$()_{non-spin}$	=	those components that have no spin
$()_{OL}$	=	open loop
$()_{pc}$	=	propulsion (reference) center
$()_{prp}$	=	proportional feedback related
$()_{spin}$	=	those components that have spin associated with \odot
$()_{WA}$	=	wind axis
$()_0$	=	at the center of gravity
$()_1$	=	alternatively, the geocentric launch point coordinate system, and the aft spin component of the vehicle, as appropriate
$()_2$	=	alternatively, the geocentric vehicle position coordinate system, and the forward non-spin component of the vehicle, as appropriate
$()_3$	=	the body-fixed flight axis coordinate system (see Fig. 1)

Appendix C

RLBA Engineering Report 00-02 (Rev. A)

Superscripts:

$()^{(a)}$	=	relating to external aerodynamic forces and moments
$()^{(c)}$	=	relating to moment control
$()^{(g)}$	=	relating to gravitational forces
$()^{(p)}$	=	relating to the propulsive forces and moments
$()^{(0)}, ()^{(1)}$	=	relating to the coefficients defining the aerodynamic coefficients
$()^{(2)}$	=	multiplying exponents of angle of attack of 0, 1 and 2, respectively.
$()^{(I)}$	=	integrator feedback
$()^{(P)}$	=	proportional feedback
$()^{\square}$	=	nondimensionalized value
$()^{\phi}$	=	geodetically defined
$()^N$	=	measured in the “2” coordinate system
$()^{\sim}$	=	measured in the “3” coordinate system

RLBA Engineering Report 00-02 (Rev. A)

This appendix documents the usage of the PC-configured FORTRAN Program, LITE_DYN, which simulates the dynamic response and eigenvalue characteristics of laser lightcraft vehicles. The appendix is divided into sections relating to general operation of the program, file inputs, and structure of the input data file.

The program is generally run with the program in the DOS mode. Once in the DOS mode the user can initiate the program by typing in:

Input and output with the program is accomplished using appropriate files. The next section describes the operations with the input files. A subsequent appendix describes the outputs and their appropriate files.

A.2.1 File Operations

Once the program is initiated the user is queried as to the identifications of the pertinent input and output files. There are five basic files that need to be identified. In operation the user will be queried as follows (with the user's responses indicated by bold face items):

File name for TERMINATION STATE VECTOR to be saved;

Appendix C

RLBA Engineering Report 00-02 (Rev. A)

[* ENTER for Scratch Buffer File] ? <File Name 6>

(enter)

File name for CONMIN RESULTS to be saved;
[* ENTER for Scratch Buffer File] ? <File Name 7>

(enter)

The first file to be identified, <File Name 1>, contains all the input quantities to be used by the program. The structure of this file is given in a subsequent section of this appendix. <File Name 2> is used for documenting the inputs that are contained in <File Name 1>, but in a narrative format along with appropriate units. <File Name 3> is used only for debugging selected portions of the program during program development. <File Name 4> & <File Name 5> contain the response results from the programs calculations; these files are described in a subsequent appendix. Finally, <File Name 6> is a file that contains the (time-history) state vector at the selected termination of the time-history, so that the calculation can be continued with another run of the program, if so desired. Note that the program will test all these files for availability and /or duplication or ambiguity. If any of the various file names is unavailable or being duplicated, the program will query the user for another name.

If an asterisk (*) is input for <File Name 1>, further program operation will be terminated. Case control and scheduled program termination also is addressed in a subsequent section. If an asterisk (*) is input for any of the subsequent files, the program will instead assign the indicated output to a scratch buffer file that will not generally be available. All of the output information that is output to the designated output files is also output to the screen, however. Therefore, if the program is run with the output screen file assignment option invoked (i.e., >filename after typing LITE_DYN), all of the program output can alternatively be saved to file.

A.2.2 Structure of the Loader Input File

The input file, <File Name 1>, is structured with data grouped generically in specific blocks (i.e., A, C, D, F, O, P, S & V). Within each data block the data items are then assigned specific locations, into which the data must be input. The data is input, several items to a line, each line dedicated to a specific data block. This is achieved by using the following format for each line of input data:

XX, NN, LL, DATA(LL), DATA(LL +1), DATA(LL +2), . . . , DATA(LL-1+NN)

where the data items are input in “free format”, with a non-alphameric character (i.e., “space”, “,” , “/”, etc.) separating each item, and where:

XX is the letter (A, C, D, F, O, P, S or V) denoting which data block the items from this line should be input.

NN is the number of data items to be read from the current line of input data

LL is the starting location within the data block (XX) that the remaining data within the Line must be sequentially input.

Appendix C

RLBA Engineering Report 00-02 (Rev. A)

DATA(ii) are the data items to be entered into the XX data block, where ii varies from LL to LL-1+NN

Note that the use of any character for XX other than (A, C, D, F, O, P, S & V) will be treated as follows: If the character is an asterisk (*) then the line will be treated as a character string and used as an identifier to be output appropriately along with the standard output results, for run identification purposes. If the character is a negative sign, (-), it will be used for case termination purposes (to be described in the following section). For all other characters the input line will be ignored and can be used for including comments within the data file for documentation, etc. Also, note that NN is limited to a maximum of 10 per line.

A.2.3 Case Termination

Once the input of all data defining a given case has been completed, the input of data for that case must be terminated. The method for terminating the input of data for the case makes use of data location S(99), i.e., location 99 within the “S” data block. This data item should be the last data entry for the given case and can alternatively be input with an “S” data block identifier, or a “-” identifier (i.e., either as {S, 1, 99, <data>}, or as {-, 1, 99, <data>}. The sole data item in the line, <data>, is then either a “+1.” or “-1.” The use of a “+1.” input value tells the program that there are additional cases to follow, and that further loading of data from the input file, <File Name 1>, is to done after the current case is completed. On the other hand, the use of a “-1.” input value tells the program that there are no more case to follow and that the program will terminate running any more data from the input file following the calculation for the current case. Thus, the last line of data for any given case that is *not the last case* would be:

-, 1, 99, 1.

Whereas the last line of data within the data file *must* be:

-, 1, 99, -1.

After the termination of this “last” case the program will then return to the start of the program which consists of a query as to the file name for the next set of cases. At this point, if no further calculations are to be made, the file name should be an asterisk (*), to terminate further operation of the program.

A.2.4 Description of Data Items within Each Data Block

The following descriptions define the detailed input quantities, their input blocks and locations within the block. [Note that in the following descriptions the appropriate units given. Where the units are parenthetically defined they are with respect to either of the two alternative unit systems available in LITE_DYN: the SI (metric) system or the English system. The appropriate unit system to be used is that elected by the user via input location 1 in the S Block. The system will be either the SI or English system, as input to that location is “0.”, or “1.”, respectively. *Thus, the default system would be the SI system.*] In the material to follow the appropriate alternate SI and English system units are respectively denoted by: (XX||YY).

Appendix C

RLBA Engineering Report 00-02 (Rev. A)

(A) Block Data (External Aerodynamic Data)

(If the *External Aerodynamics Table* is null or flawed. TM default values will be used.).

Location in block

1	no of angles of attack in input table, n_{α}	(maximum = 5)
2	no of ND rotation speeds in input table, n_{Ω}	(maximum = 6)
3	maximum Reynold's no. used in input table	
4	angle of attack, no 1, $\alpha(1)$	deg
5	ND rotation speed no. 1, for $\alpha(1)$, $\Omega_B(1,1)$	(ND)

Lift coefficient inputs:

6	$C_{Lo}(1,1)$
7	$\eta_{1L}(1,1)$
8	$\eta_{2L}(1,1)$
9	$\eta_{3L}(1,1)$

Drag coefficient inputs:

10	$C_{Do}(1,1)$
11	$\eta_{1D}(1,1)$
12	$\eta_{2D}(1,1)$
13	$\eta_{3D}(1,1)$

Y-Force coefficient inputs:

14-17	$C_{Y0}(1,1)$
-------	---------------

...

Pitching moment coefficient inputs:

18-21	$C_{Mo}(1,1)$
-------	---------------

...

Yawing moment coefficient inputs:

22-25	$C_{No}(1,1)$
-------	---------------

...

35	$\Omega_B(1,2)$	(ND)
----	-----------------	------

36-39	$C_{Lo}(1,2)$
-------	---------------

...

40-43	$C_{Do}(1,2)$
-------	---------------

...

44-47	$C_{Y0}(1,2)$
-------	---------------

...

48-51	$C_{Mo}(1,2)$
-------	---------------

...

52-55	$C_{No}(1,2)$
-------	---------------

...

The sequence is repeated for each non-dimensional rotation speed for the first angle of angle of attack, wherein each such sub-block location is incremented by 30. The next angle of

Appendix C

RLBA Engineering Report 00-02 (Rev. A)

attack block of data begins with the new angle of attack input at location defined by what would be the start of the next rotation speed sub-block minus one (1).

[4 + 30% n_{\odot}] angle of attack, no 2, $\alpha(2)$ deg
 [5 + 30% n_{\odot}] ND rotation speed no. 1, for $\alpha(2)$, $\Omega_B(2,1)$
 ...

(C) Block Data (Flight Control Parameters)

Location in block

1.)	1	flight control type:	(open loop moment inputs only =
			(feed-back control network only =
2.)			(both of the above = 3.)
1.)	2	control axis activation code:	(start with 0., then: for pitch, add
			for yaw, add
2.)			for roll, add
4.)			
	3	roll (x-axis) control power gain	(N-m lb-ft)
	4	pitch (y-axis) control power gain	(N-m lb-ft)
	5	yaw (z-axis) control power gain	(N-m lb-ft)
	6	maximum roll (M_x) axis moment	(N-m lb-ft)
	7	maximum pitch (M_y) axis moment	(N-m lb-ft)
	8	maximum yaw (M_z) axis moment	(N-m lb-ft)
	20	no. of points in time-history descriptions of open-loop moments and/or attitude angle commands (maximum = 50)	

Open-Loop Control Moment Time-Histories:

	time (sec)	//	M_x	//	M_y	//	M_z	//
			(N-m lb-ft)		(N-m lb-ft)		(N-m lb-ft)	
21	...	71	...	121	...	171	...	
22	...	72	...	122	...	172	...	

Feed-Back Control Command Angle Time-Histories:

	time (sec)	//	Roll (deg)	//	Pitch (deg)	//	Heading (deg)	//
(21)	(same as		221	...	271	...	321	...
(22)	above)		222	...	272	...	322	...

Appendix C

RLBA Engineering Report 00-02 (Rev. A)

feed-network (integrator & proportional) error gains:

401, 402	$[eM_x/(-P)]_{int}, [eM_x/(-P)]_{prp}$	
	(sec ² /rad,sec/rad)	
403, 404	$[eM_x/(\Delta\phi)]_{int}, [eM_x/(\Delta\phi)]_{prp}$	(sec/rad, -
	/rad)	
405, 406	$[eM_y/(-Q)]_{int}, [eM_y/(-Q)]_{prp}$	
	(sec ² /rad,sec/rad)	
407, 408	$[eM_y/(\Delta\theta_y)]_{int}, [eM_y/(\Delta\theta_y)]_{prp}$	(sec/rad, -
	/rad)	
409, 410	$[eM_y/(-R)]_{int}, [eM_y/(-R)]_{prp}$	
	(sec ² /rad,sec/rad)	
411, 412	$[eM_y/(\Delta\psi)]_{int}, [eM_y/(\Delta\psi)]_{prp}$	(sec/rad, -
	/rad)	
413, 414	$[eM_y/(\Delta\odot_y)]_{int}, [eM_y/(\Delta\odot_y)]_{prp}$	
	(sec/rad, -/rad)	
415, 416	$[eM_y/(\Delta\odot_z)]_{int}, [eM_y/(\Delta\odot_z)]_{prp}$	(sec/rad, -
	/rad)	
417, 417	$[eM_z/(-Q)]_{int}, [eM_z/(-Q)]_{prp}$	
	(sec ² /rad,sec/rad)	
419, 420	$[eM_z/(\Delta\theta_y)]_{int}, [eM_z/(\Delta\theta_y)]_{prp}$	(sec/rad, -
	/rad)	
421, 422	$[eM_z/(-R)]_{int}, [eM_z/(-R)]_{prp}$	
	(sec ² /rad,sec/rad)	
423, 424	$[eM_z/(\Delta\psi)]_{int}, [eM_z/(\Delta\psi)]_{prp}$	(sec/rad, -
	/rad)	
425, 426	$[eM_z/(\Delta\odot_y)]_{int}, [eM_z/(\Delta\odot_y)]_{prp}$	(sec/rad, -
	/rad)	
427, 428	$[eM_z/(\Delta\odot_z)]_{int}, [eM_z/(\Delta\odot_z)]_{prp}$	(sec/rad, -
	/rad)	

(D) Block Data (Dynamic State Vector – solution continuation)

Location in block

1	time	sec
2	geocentric altitude (relative to launch geocentric radius)	(m ft)
3	Earth (geocentric) latitude, ②	deg(N)
4	Earth longitude, <i>L</i>	deg(W)
5	heading angle, ⑤	deg
6	(geocentric) pitch attitude angle, θ_y	deg


Appendix C

RLBA Engineering Report 00-02 (Rev. A)

7	$S_{LCx}^{(1)}$	
8	$S_{LCy}^{(1)}$	
9	$S_{LCz}^{(1)}$	
10-20	(intentionally blank)	
21	V_x	(m ft)/sec
22	V_y	(m ft)/sec
23	V_z	(m ft)/sec
24	pitch rate, q	rad/sec
25	yaw rate, r	rad/sec
26	$\Delta q_{non-spin}$	rad/sec
27	$\Delta r_{non-spin}$	rad/sec
28	$p_{non-spin}$	rad/sec
29	$\Delta \theta_y_{non-spin}$	rad
30	$\Delta \theta_z_{non-spin}$	rad
31	$\phi_{non-spin}$	rad
32	$y(1)_{control}$	
33	$y(2)_{control}$	
34	$y(3)_{control}$	
35	$y(4)_{control}$	
36	$y(5)_{control}$	
37	$y(6)_{control}$	
38	$y(7)_{control}$	
39	$y(8)_{control}$	
38,39	(intentionally blank)	
40	vehicle mass, M_V	(kg lb-s ² /ft)

(F) Block Data (Launch Flight and Orbital Insertion Parameters)

Location in block

1	launch (geodetic) altitude	(m ft)
2	temperature	deg. (C F)
3	(sea level) pressure (altimeter setting) [0. = standard conditions]	(cm in) Hg
4	(geodetic) latitude	deg (N)
5	longitude	deg (W)
6	(vehicle) geodetic heading angle	deg
7	(vehicle) geodetic pitch attitude angle	deg
8	(laser) geodetic off-zenith angle, θ_{LB0} (when constant)	deg
9	(laser) geodetic bearing angle, ψ_{LB0} ()	deg

Lateral wind characteristics (when constant w.r.t. altitude):

Appendix C



RLBA Engineering Report 00-02 (Rev. A)

10	wind direction	deg
11	wind velocity	kts
12-19	(intentionally blank)	


Appendix C

RLBA Engineering Report 00-02 (Rev. A)

Laser Pointer Time-history Description:

20	no. of points in time-history description of Laser Pointer orientation time-history, N_{LP} (maximum = 50)	
21	N_{LP} time values, t_j , $1 \leq j \leq N_{LP}$	sec
	...	
71	N_{LP} bearing angle values, ψ_{LPj} ()	deg
	...	
121	N_{LP} off-zenith angle values, γ_{LPj} ()	deg
	...	

Lateral Wind Vector Profile:

200	no. of points in (AGL) altitude variation of lateral wind, N_{LW} (maximum = 20)	
201	N_{LW} (AGL) altitude values	(m ft)
	...	
221	N_{LW} direction angle values, ψ_{wi} $1 \leq i \leq N_{LW}$	deg
	...	
241	N_{LW} wind velocity values, V_{wi} ()	kt
	...	

=

(O) Block Data (Optimization Parameters)

Location in block

Standard CONMIN input parameters:




1	<i>ITMAXL</i> ,	maximum no. of iterations	(default = 10.)
2	<i>IPRINT</i> ,	output level print control (= 0., 1., 2., ... 5.; where 0. = no	
printout)			
3	<i>NDV</i> ,	number of design variables (internally calculated, input not used)	
4	<i>NCON</i> ,	no of inequality constraints (internally calculated, input not used)	
5	<i>NSIDE</i> ,	side constraint parameter: (not use, use) side constraints = (0., 1.)	
6	<i>ICNDIR</i> ,	conjugate direction restart parameter (default value = $NDV + 1$)	
7	<i>NSCAL</i> ,	scaling control parameter:	
		(< 0., scale variable increments by internally calculated $SCAL(i)$	
		= 0., do not scale	
		> 0., scale every $NSCAL$ iterations by $abs(X)$)	
8	<i>NFDG</i> ,	gradient calculation control parameter:	
		(internally set to 0., TM uses finite difference	
		methods)	
9	<i>FDCH</i> ,	gradient scaling factor for ∇X_{DV}	(default value = 0.01)
10	<i>FDCHM</i> ,	minimum value for ∇X_{DV}	(default value = 0.01)
11	<i>CT</i> ,	constraint thickness parameter	(default value = -0.1)

Appendix C

RLBA Engineering Report 00-02 (Rev. A)

12	<i>CTMIN</i> ,	minimum absolute value of <i>CT</i>	(default value =
0.001)			
13	<i>CTL</i> ,	<i>CT</i> for linear and side constraints	(default value = -
0.01)			
14	<i>CTLMIN</i> ,	minimum absolute value of <i>CTL</i>	(default value = 0.001)
15	<i>THETA</i> ,	push-off parameter	(default value = 1.0)
16	<i>DELFUN</i> ,	relative convergence criterion on objective function	(default value =
0.000001)			
17	<i>DABFUN</i> ,	absolute convergence criterion on objective function	(default value =
0.0000001)			
18	<i>LINOBJ</i> ,	linear objective function identifier	(internally set to 0.)
19	<i>ITRM</i> ,	consecutive iterations to indicate convergence	(default value = 3.)

Lightcraft Flight-Specific Parameters:

21	objective function basis, = (1.,2.) as objective function is based on: (time history, eigenvalue) dynamics		
22	selected degree of freedom for time-history-based objective function		
23	selected eigenvalue (mode) for eigenvalue-based objective function		
	specifications on selected eigenvalue:		
24	critical damping ratio, $\zeta_{\text{specified}}$		(ND)
25	frequency, $f_{\text{specified}}$	hz	
26	number of inequality constraints for <i>X</i> values defined in the C Block, (max = 10)		
27	number of inequality constraints for <i>X</i> values defined in the F Block, ()		
28	number of inequality constraints for <i>X</i> values defined in the P Block, ()		
29	number of inequality constraints for <i>X</i> values defined in the V Block, ()		
31-50	indices within (C) block, n_j , defining <i>X</i> values from the C Block, X_{Cj}		
51-70	lower limit side constraints for X_{Cj}		
71-90	upper limit side constraints for X_{Cj}		
91-110	indices within (F) block, n_k , defining <i>X</i> values from the F Block, X_{Fk}		
111-130	lower limit side constraints for X_{Fk}		
131-150	upper limit side constraints for X_{Fk}		
151-170	indices within (P) block, n_m , defining <i>X</i> values from the P Block, X_{Pm}		
171-190	lower limit side constraints for X_{Pm}		
191-210	upper limit side constraints for X_{Pm}		
211-230	indices within (V) block, n_i , defining <i>X</i> values from the P Block, X_{Vi}		
231-250	lower limit side constraints for X_{Vi}		
251-270	upper limit side constraints for X_{Vi}		

Appendix C

RLBA Engineering Report 00-02 (Rev. A)

(P) Block Data (Propulsion Characteristics)

Location in block

1	nominal laser output power density	MW/m ²
2	beam cross-sectional area	m ²
3	altitude for air-breathing to rocket conversion	(m ft)
4	coupling coefficient in the rocket mode	N/MW
5	FS of thrust action center	(m ft)
6-10	(intentionally blank)	

Time-Averaged (Laser) Power Attenuation Characteristics:

(If *Time-Averaged (Laser) Power Attenuation Characteristics* are:
null or flawed. TM default values will be used.)

101	no. of zenith angle curves (maximum = 9)	
102	no. of range values (maximum = 19)	
103	scaling factor	
104	use log ₁₀ ordinate inputs (no,yes) TM (= 0.,1.)	
105	use log ₁₀ abscissa (range) inputs (no,yes) TM (= 0.,1.)	
106-109	(intentionally blank)	
110-128	range values	(m ft)
...		
130	off-zenith angle, $\gamma(1)$	(deg)
131	attenuation factor values (zenith angle no. 1) (variation with range)	
...		
151	beam area ratio values (zenith angle no. 1) (variation with range)	
...		
170	off-zenith angle, $\gamma(2)$	(deg)
171	attenuation factor values (zenith angle no. 2) (variation with range)	
...		
191	beam area ratio values (zenith angle no. 2) (variation with range)	
...		
...		
460- 489	data for off-zenith angle no. 9...	

Appendix C

RLBA Engineering Report 00-02 (Rev. A)

Gross coupling Coefficient Data:

(If *Gross Coupling Coefficient Data* is:

null or flawed. TM default values will be used.)

501	no. of altitude curves	(maximum = 6)
502	no. of Mach nos.	(maximum = 49)
503	scaling factor	(default = 1.)
504	use log ₁₀ ordinate inputs (no,yes) TM (= 0.,1.)	
505-509	(intentionally blank)	
510	Mach number values	
	...	
600	altitude(1)	(m ft)
601	coupling coefficient(1) (variation with Mach no.)	N/MW
	...	
650	altitude(2)	(m ft)
651	coupling coefficient(2) (variation with Mach no.)	N/MW
	...	
... - 899	...	

Ram Drag Coefficient vs. Mach no.:

(If *Ram Drag Coefficient vs. Mach no. Table* is:

null or flawed. TM default values will be used.)

900	no. of abscissa-ordinate pairs (maximum = 49)
901	use log ₁₀ ordinate inputs (no,yes) TM (= 0.,1.)
902	Mach no.(1)
903	drag coefficient entry(1)
904	Mach no. (2)
905	drag coefficient entry(2)
	...
... - 1099	...

Appendix C

RLBA Engineering Report 00-02 (Rev. A)

Coupling Coeff. Factor vs. (linear) offset:

(If *Coupling Coeff. Factor* vs. *Linear Offset Table* is:

null or flawed. TM default values will be used.)

1000	no. of abscissa-ordinate pairs (maximum = 49)
1001	use log ₁₀ ordinate inputs (no,yes) TM (= 0.,1.)
1002	ND (linear) offset(1)
1003	factor(1)
1004	ND (linear) offset(2)
1005	factor(2)
...	...
... - 1099	...

Coupling Coeff. Factor vs. (angular) offset:

(If *Coupling Coeff. Factor* vs. *Angular Offset Table* is:

null or flawed. TM default values will be used.)

1101	scaling value (default value = 1.)	
1102	angular offset(1)	deg
1103	factor(1)	
1104	angular offset(2)	deg
1105	factor(2)	
...	...	
... - 1199	...	

Side Force Coupling Coeff. Factor vs. (linear) offset:

(If *Side Force Coupling Coeff. Factor* vs. *Linear Offset Table* is:

null or flawed. TM default values will be used.).

1200	no. of abscissa-ordinate pairs (maximum = 49)
1201	scaling value (default value = 1.)
1202	ND (linear) offset(1)
1203	factor(1)
1204	ND (linear) offset(2)
1205	factor(2)
...	...
... - 1299	...

Appendix C

RLBA Engineering Report 00-02 (Rev. A)

Side Force Coupling Coeff. Factor vs. (angular) offset:

(If *Side Force Coupling Coeff. Factor vs. Angular Offset Table* is:

null or flawed. TM default values will be

used.).

1300	no. of abscissa-ordinate pairs (maximum = 49)	
1301	scaling value (default value = 1.)	
1302	angular offset(1)	deg
1303	factor(1)	
1304	angular offset(2)	deg
1305	factor(2)	
	...	
... - 1399	...	

Moment Coupling Coeff. Factor vs. (linear) offset:

(If *Moment Coupling Coeff. Factor vs. Linear Offset Table* is:

null or flawed. TM default values will be

used.).

1400	no. of abscissa-ordinate pairs (maximum = 49)	
1401	scaling value (default value = 1.)	
1402	ND (linear) offset(1)	
1403	factor(1)	
1404	ND (linear) offset(2)	
1405	factor(2)	
	...	
... - 1499	...	

Moment Coupling Coeff. Factor vs. (angular) offset:

(If *Moment Coupling Coeff. Factor vs. Angular Offset Table* is:

null or flawed. TM default values will be

used.).

1500	no. of abscissa-ordinate pairs (maximum = 49)	
1501	scaling value (default value = 1.)	
1502	angular offset(1)	deg
1503	factor(1)	
1504	angular offset(2)	deg
1505	factor(2)	
	...	
... - 1599	...	

Appendix C

RLBA Engineering Report 00-02 (Rev. A)

=====

=

(S) Block Data (Solution Control)

Location in block

1	Units Declaration = (0,1.) as unit system is (SI,English)	
2	(optional) run ID no.	
3	total flight time, T_{max}	sec
4	integration time step, Δt	sec
5	time-history output sampling time step	sec
6	eigenvalue solution sampling time step, Δt_{eigen}	sec
7	eigenvector output control: = (0,1.) to (suppress, include) eigenvector output	
10	restart control: = (0,1.) to (not use, use) the restart state vector	
99	END OF CASE CONTROL + or - 1.	

=====

=

(V) Block Data (Vehicle Mechanical Properties)

Location in block

1	initial (total) mass , M_{V0}	(kg lb-s ² /ft)
2	FS of mass center	(m in)
3	polar moment of inertia , J_0	(kg-m ² lb-s ² -
ft)		
4	pitch moment of inertia about mass center, I_{d0}	(kg-m ² lb-s ² -
ft)		
5	vehicle spin rate, Ω_{spin}	RPM
6	maximum diameter	(m ft)
7	(all-over) length	(m ft)
8	mass depletion rate (rocket mode only)	(kg/s lb-s/ft)
9	mass of (non-spin) forebody, $M_{non-spin}$	(kg lb-s ² /ft)
10	FS of non-spin mass center	(m in)
11	FS of gimbal location	(m in)
12	spring rate of gimbaling stiffness, K_{gimbal}	(Nm lb-ft)/rad
13	pitch moment of inertia about non-spin c.g., $I_{d non-spin}$	(kg-m ² lb-s ² -
ft)		
14	polar moment of inertia of non-spin mass, $J_{non-spin}$	(kg-m ² lb-s ² -
ft)		

Appendix C

RLBA Engineering Report 00-02 (Rev. A)

A.2.5 Supplemental Keyboard Data Input

As a convenience for inputting data, provision has been made for directly adding/modifying the input data from the keyboard after the data file has already been read. After all the file identifiers have been input, the user is queried as follows:

Do you wish to modify/supplement the input data, [y or n] ?: **<y or n> (enter)**

If the user's response to this query is yes (or YES, y or Y), then the user is further prompted:

*Input type the supplemental data line (in LOADER format),
[A single asterisk (*) entry will terminate this input]:* **<XX> (enter)**

In this mode of input the group identifier (i.e., A, C, D, etc.) is input with an immediate "rtn". If this entry is an asterisk (*), this will terminate the supplemental data entry, otherwise the appropriate input string is:

**<NN, LL, DATA(LL), DATA(LL+1), DATA(LL+2), . . . , DATA(LL-1+NN)>
(enter)**

As with the any of the lines of data entry within the input *file*, NN is limited to a maximum of 10. If the number of entries exceeds 10, or if the location LL is outside the range for the selected input data group, a message is output to the screen and the string of data must be reinput.

A.3 *Program Termination*

Once the program has run to completion and the output has been written to the appropriate selected files, the program will query the user as follows:

Do you wish to run another case (y or n) ?: **<y or n> (enter)**

Accordingly, if the response is affirmative (as exemplified above) then the program will restart as if it were a new case.

A.4 *Notes for Efficient Program Usage*

A.4.1 The Eigenvalue Solution

The eigenvalue solution is a useful tool not only for identifying predominately modes but also for establishing proper inputs for the time-history solution. The interpretation of the eigenvalue results is standard as far as quantifying the oscillatory modal frequencies, along with their stability levels (as determined by the real parts of the eigenvalues). Using Loader Input item **SBV(7)** the eigenvectors can be either omitted or output. The principal usefulness of these vectors is in identifying the principal degrees of freedom that constitute the motion of each respective mode.

Another use of the eigenvalue solution is in identifying the minimum time step needed for the time-history solution. The eigenvalues are always output with descending frequency

Appendix C

RLBA Engineering Report 00-02 (Rev. A)

content. Thus, the first oscillatory eigenvalue in the output list identifies the highest value of frequency that will be inherent in the Lightcraft transient dynamics (i.e. f_{max}). From this frequency a proper selection of integration time step can be determined, as is described in the following section.

A.4.2 The Time-history Solution

The selected integration scheme, the Runge-Kutta method, is a fairly robust one, but like all such integration schemes, there exists a maximum integration step size above which the method breaks down (i.e., numerical instability). With this method, a good rule of thumb is that there should be no fewer than eight (8) time steps within the period of the highest frequency, f_{max} , as is typically available from the eigenvalue solution. This relationship can be expressed as:

$$\Delta t \leq \frac{1}{8f_{max}}$$

While the above rule of thumb should produce numerically stable results, it is not enough to insure accuracy. It is, therefore, a generally a good practice to adjust the integration time step downward until negligible changes in the results are obtained.

When recording of the time histories onto the user-designated *DYNAMIC RESPONSE RESULTS* file a proper selection of the output sampling time step must be made. Although this selection doesn't impact on the accuracy of the results, it does impact on the frequency content of the responses, as perceived from these output results. Although the same Δt as used for the integration step size can certainly be used, a more coarse sampling time step is sometimes advisable to minimize the size of the data files for more efficient data storage and handing. This selection should be balanced against the bandwidth needed for correct usage of the response results.

Appendix C

RLBA Engineering Report 00-02 (Rev. A)

Appendix B – Earth Geodetic vs Geocentric Coordinate Conversions

The usual position parameters for topographical location, altitude, latitude angle and bearing angle are all defined in the geodetic frame of reference, i.e., relative to the normal to the Earth's surface. However, the equations of motion, including the most of the coordinate system transformations are best defined in the geocentric system. Because of the Earth's oblateness, however, the two systems are the same only at the equator and at the poles, and therefore, conversions between the two reference systems are required. This appendix presents the conversions required to go from one system to the other. In each case, the quantities to be converted are first, the latitude angle and the altitude (or distance from the Earth's center, as appropriate), and then the Euler angles, heading, ψ , and pitch, θ_y . The formulations are based on material from Refs. 7 & 13. Those quantities defined in the geodetic system are denoted as (\neq), whereas the similarly defined quantities in the geocentric system are denoted without any superscripting. Since the effect of Earth oblateness is not a function of longitude, the following figure illustrates the basic relationships involved in the primary conversions:

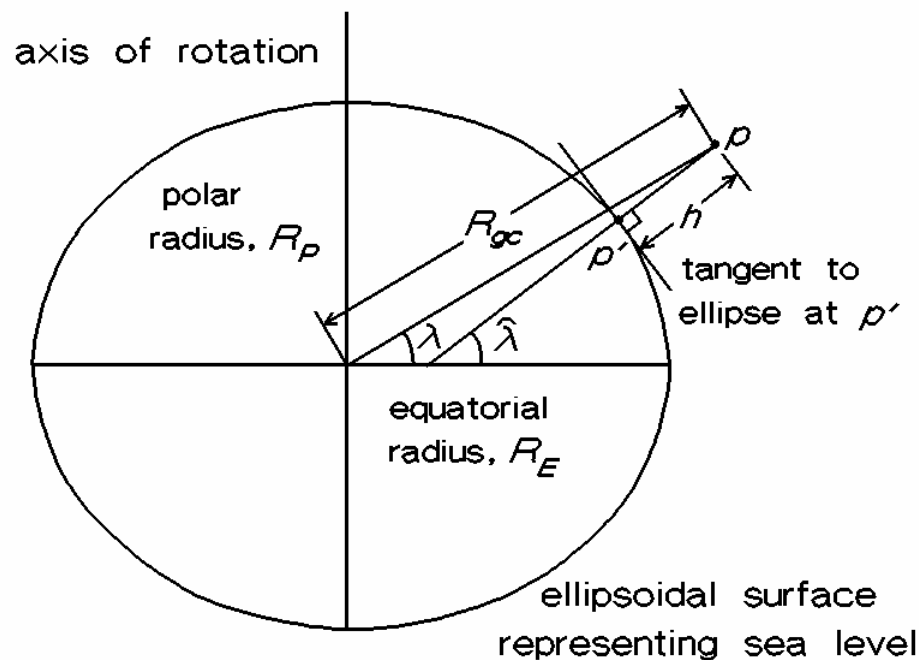


Fig B.1 Geocentric vs Geodetic Coordinates

The pertinent Earth data are as follows:

Polar radius,	$R_P (= b) = 6,356.7517 \text{ km}$
Equatorial radius,	$R_E (= a) = 6,378.1363 \text{ km}$
Eccentricity,	$e = 0.081819301$

Appendix C

RLBA Engineering Report 00-02 (Rev. A)

B.1 Geocentric Cartesian Coordinates

The geocentric cartesian coordinates of point p can be expressed using both the geodetic and geocentric coordinates:

$$\begin{Bmatrix} X \\ Y \\ Z \end{Bmatrix}_p = R_{gc} \begin{Bmatrix} \cos \lambda \\ 0 \\ \sin \lambda \end{Bmatrix} = \begin{Bmatrix} (N_\lambda + h) \cos \hat{\lambda} \\ 0 \\ \left[(1 - e^2) N_\lambda + h \right] \sin \hat{\lambda} \end{Bmatrix} \quad (\text{B.1})$$

where N_λ is the ellipsoidal radius of curvature in the meridian and is given by:

$$N_\lambda = R_E / \sqrt{1 - e^2 \sin^2 \hat{\lambda}} \quad (\text{B.2})$$

B.2 Geodetic to Geocentric Conversion

The distance from the Earth's center to the point p is obtained from the X and Z components using the Pythagorean theorem:

$$R_{gc} = \sqrt{X^2 + Z^2} = \sqrt{(N_\lambda + h)^2 - \left[(2e^2 - e^4) N_\lambda^2 + 2e^2 N_\lambda h \right] \sin^2 \hat{\lambda}} \quad (\text{B.3})$$

Then the geocentric latitude can be obtained:

$$\lambda = \sin^{-1} \left\{ \frac{\left[(1 - e^2) N_\lambda + h \right] \sin \hat{\lambda}}{R_{gc}} \right\} \quad (\text{B.4})$$

From the two latitude angles we can define the difference angle:

$$\Delta \lambda = \hat{\lambda} - \lambda \quad (\text{B.5})$$

Appendix C

RLBA Engineering Report 00-02 (Rev. A)

The secondary conversions relating to pitch angle and yaw (or bearing) angle can then be made by transforming the unit vector aligned with the longitudinal axis of the Lightcraft, i.e., the \hat{i}_3 vector, first into components in the “2” coordinate system and then into those of the geosynchronous system (using Eqs 51 and 77, with ΔL set to zero). This procedure is separately performed using the geodetic latitude and then the geocentric latitude. After the geosynchronous components for these two cases are equated the following expressions can be obtained:

(B.6)

$$\psi = \tan^{-1} \left(\frac{\sin \hat{\psi} \cos \hat{\theta}_y}{\cos \Delta \lambda \cos \hat{\psi} \cos \hat{\theta}_y + \sin \Delta \lambda \sin \hat{\theta}_y} \right)$$

$$\theta_y = \tan^{-1} \left(\frac{\cos \Delta \lambda \sin \hat{\theta}_y - \sin \Delta \lambda \cos \hat{\psi} \cos \hat{\theta}_y}{\sin \psi \sin \hat{\psi} \cos \hat{\theta}_y + \cos \psi (\cos \Delta \lambda \cos \hat{\psi} \cos \hat{\theta}_y + \sin \Delta \lambda \sin \hat{\theta}_y)} \right)$$

(B.7)

B.3 Geocentric to Geodetic Conversion

First off a number of intermediary variables must be calculated:

$$E = \left[bZ - (a^2 - b^2) \right] / aX$$

$$F = \left[bZ + (a^2 - b^2) \right] / aX$$

$$P = 4(EF + 1) / 3$$

$$Q = 2(E^2 - F^2)$$

$$D = \sqrt{P^3 + Q^2}$$

$$\nu = (D - Q)^{1/3} - (D + Q)^{1/3}$$

$$G = \frac{1}{2} \left[\sqrt{E^2 + \nu} + E \right]$$

$$t = \sqrt{G^2 + (F - \nu G) / (2G - E)} - G$$

(B.8a-h)

Appendix C

RLBA Engineering Report 00-02 (Rev. A)

Then the geodetic latitude and altitude can be calculated as follows:

$$\hat{\lambda} = \tan^{-1} \left[a(1 - t^2) / 2bt \right]$$

(B.9)

$$h = (X - at) \cos \hat{\lambda} + (Z - b) \sin \hat{\lambda}$$

(B.10)

where X and Z are given by the first part of Eq B.1

Similar to Eqs. B.6 & B.7, the secondary conversions relating to pitch angle and yaw (or bearing) angle can then be made:

$$\hat{\psi} = \tan^{-1} \left(\frac{\sin \psi \cos \theta_y}{\cos \Delta \lambda \cos \psi \cos \theta_y - \sin \Delta \lambda \sin \theta_y} \right)$$

(B.11)

$$\hat{\theta}_y = \tan^{-1} \left(\frac{\cos \Delta \lambda \sin \theta_y + \sin \Delta \lambda \cos \psi \cos \theta_y}{\sin \hat{\psi} \sin \psi \cos \theta_y + \cos \hat{\psi} (\cos \Delta \lambda \cos \psi \cos \theta_y - \sin \Delta \lambda \sin \theta_y)} \right)$$

(B.12)

Appendix C

RLBA Engineering Report 00-02 (Rev. A)

Appendix C – Default External Aerodynamic Loads Description

As is described in Section 2.4, and in particular Section 2.4.2, the external aerodynamic loads description requires a tabulation of the aerodynamic coefficients, C_L , C_Y , C_D , C_m and C_n in a form that gives has a power series description of the variation of the coefficients with Reynold's number. This selection of form was suggested in part by the experimental data presented in Ref. 7. Thus, each of the aerodynamic coefficients is assumed to have the form:

$$C_X = C_{X_0} \left(1 + \eta_{X_1}^{(0)} Rn + \eta_{X_2}^{(0)} Rn^2 + \eta_{X_3}^{(0)} Rn^3 \right) + \\ C_{X_\alpha} \alpha^n \left(1 + \eta_{X_1}^{(n)} Rn + \eta_{X_2}^{(n)} Rn^2 + \eta_{X_3}^{(n)} Rn^3 \right)$$

(C.1)

where n is equal to 2 for the drag coefficient, C_D , and 1 for all the other coefficients. A second reason for the selection of this form was that it streamlines the input of aerodynamic coefficient data if only a limited amount of Reynold's number variation, if any, is available. It should be noted that the data from Ref. 7, as described herein, has been included in the **LITE_DYN** computer code as a set of *default* data to be superseded, if other data is available for input.

The original results from Ref. 6 were subsequently nondimensionalized to accommodate other Reynold's numbers and nondimensional spin rates, as would arise from configurations other than exactly that which was tested. These data were also limited in scope and general usage as the tests were performed at zero α and only two values of yaw, Ψ (0 and , nominally, 25 deg.). Thus, in addition to the aforementioned nondimensionalization, the data were resolved to variations with respect to angle-of-attack, α , and the aerodynamic loads were translated to the nose of the lightcraft model. Lastly, the loads at zero angle-of-attack and yaw angle were used as "tare" values for wind tunnel corrections.

The remainder of this appendix presents the data that resulted from the operations identified herein. Note that although the angle of attack resulting from the tested value of yaw angle is nominally 25 deg., a value of 26.32 deg. was obtained using the actual measured dimensions of the nose of the model in the yawed configuration. Except for the drag coefficient results, all the data are only for the 26.32 deg. angle-of-attack case. Furthermore, the results for side force (C_Y) and yawing moment (C_n), do not have results for the zero spin case as these coefficients must be zero by reasons of symmetry.

Appendix C

RLBA Engineering Report 00-02 (Rev. A)

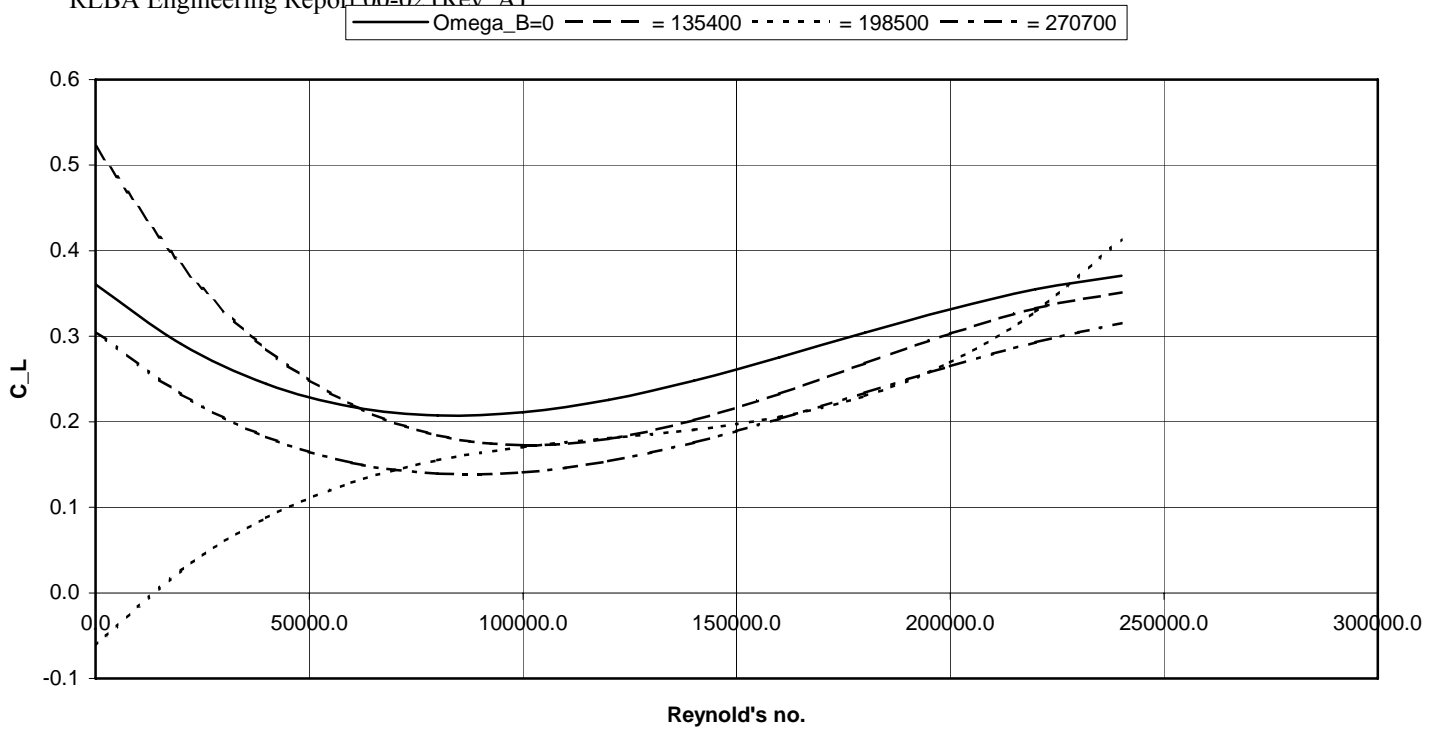


Fig. C.1 lift coefficient variation with Reynold's no. and spin rate, $\alpha = 26.32$ deg.

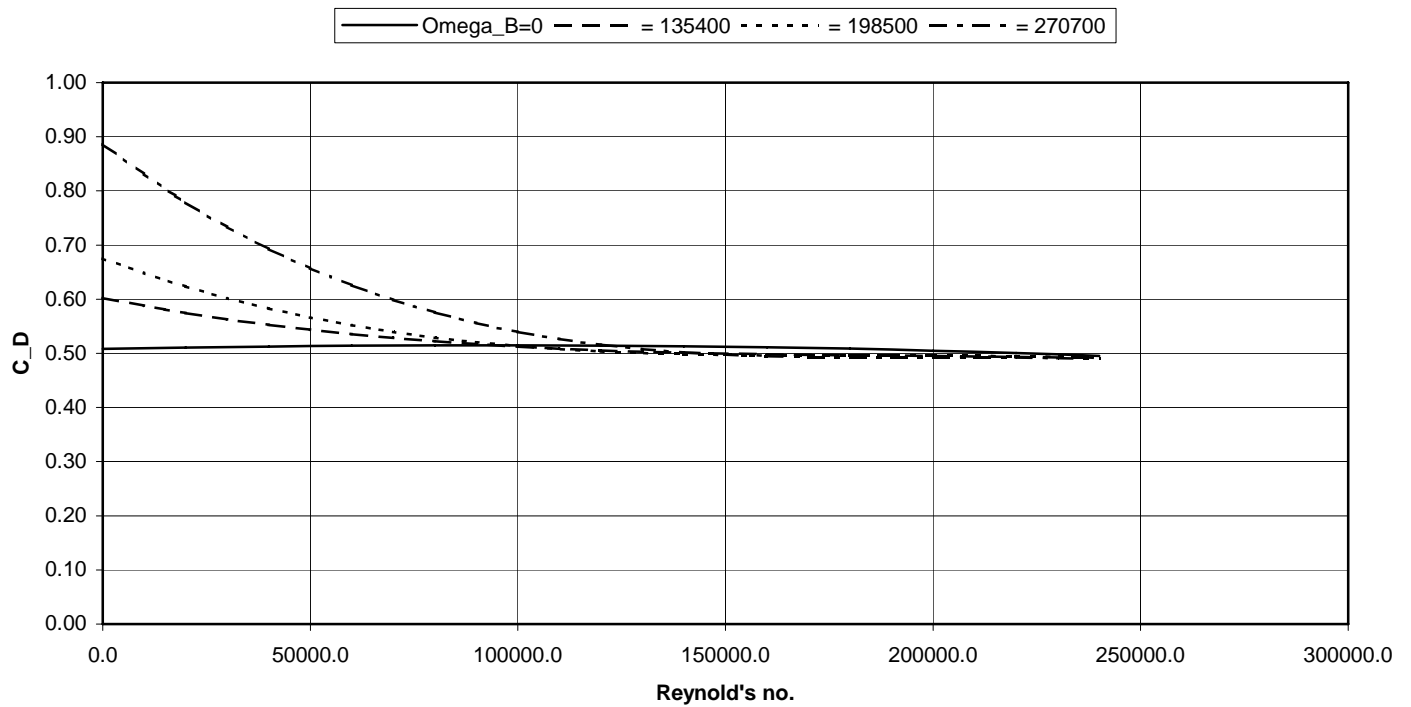


Fig C.2 drag coefficient variation with Reynold's no. and spin rate, $\alpha = 0$

Appendix C

RLBA Engineering Report 00-02 (Rev. A)

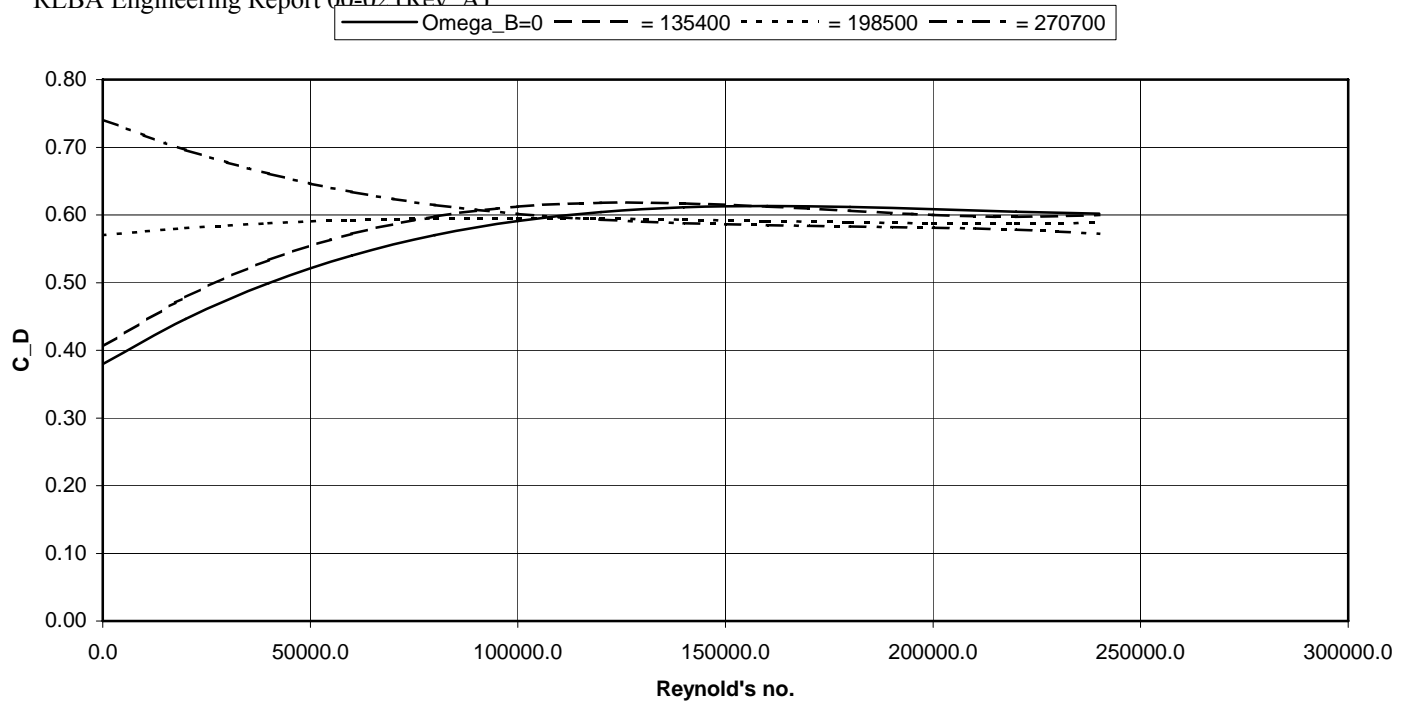


Fig. C.3 drag coefficient variation with Reynold's no. and spin rate, $\alpha = 26.32$ deg.

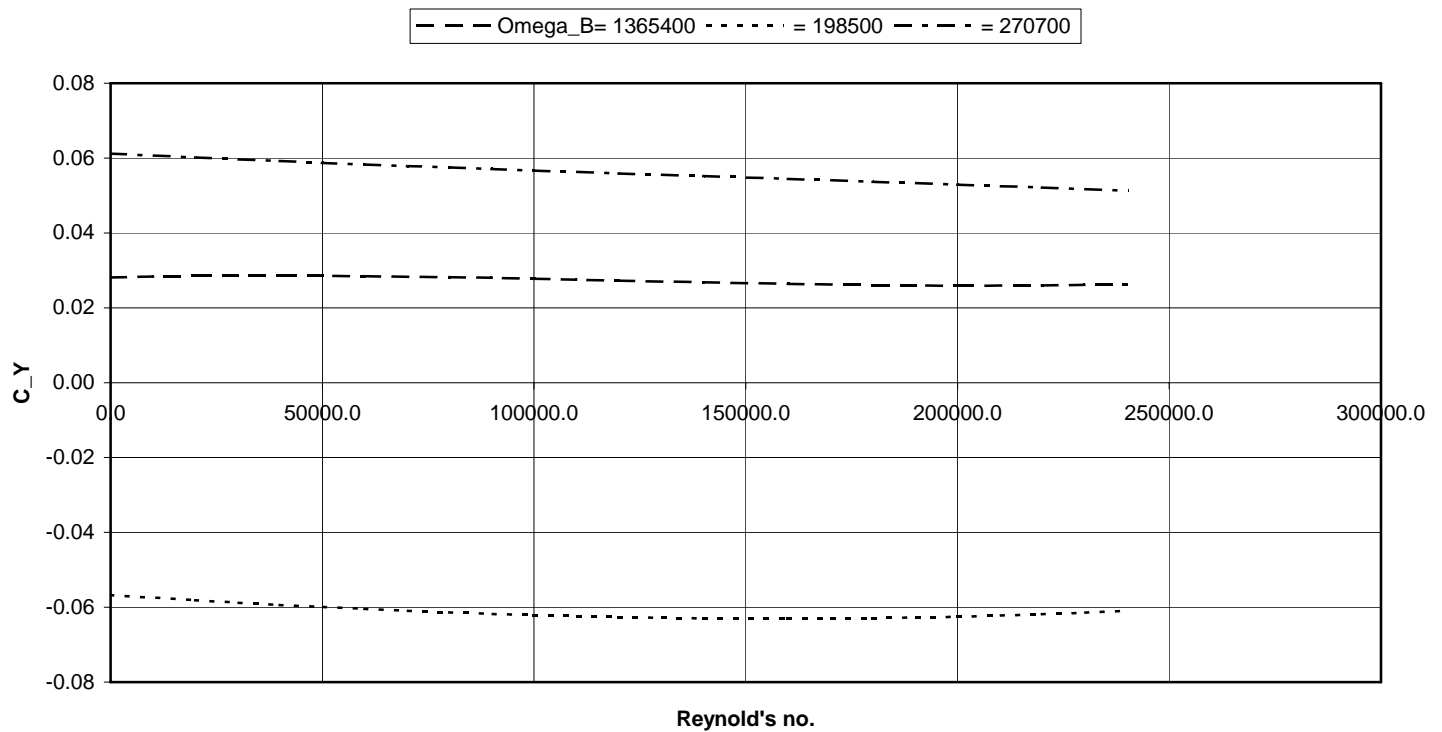


Fig. C.4 Y-force coefficient variation with Reynold's no. and spin rate, $\alpha = 26.32$ deg.

Appendix C

RLBA Engineering Report 00-02 (Rev. A)

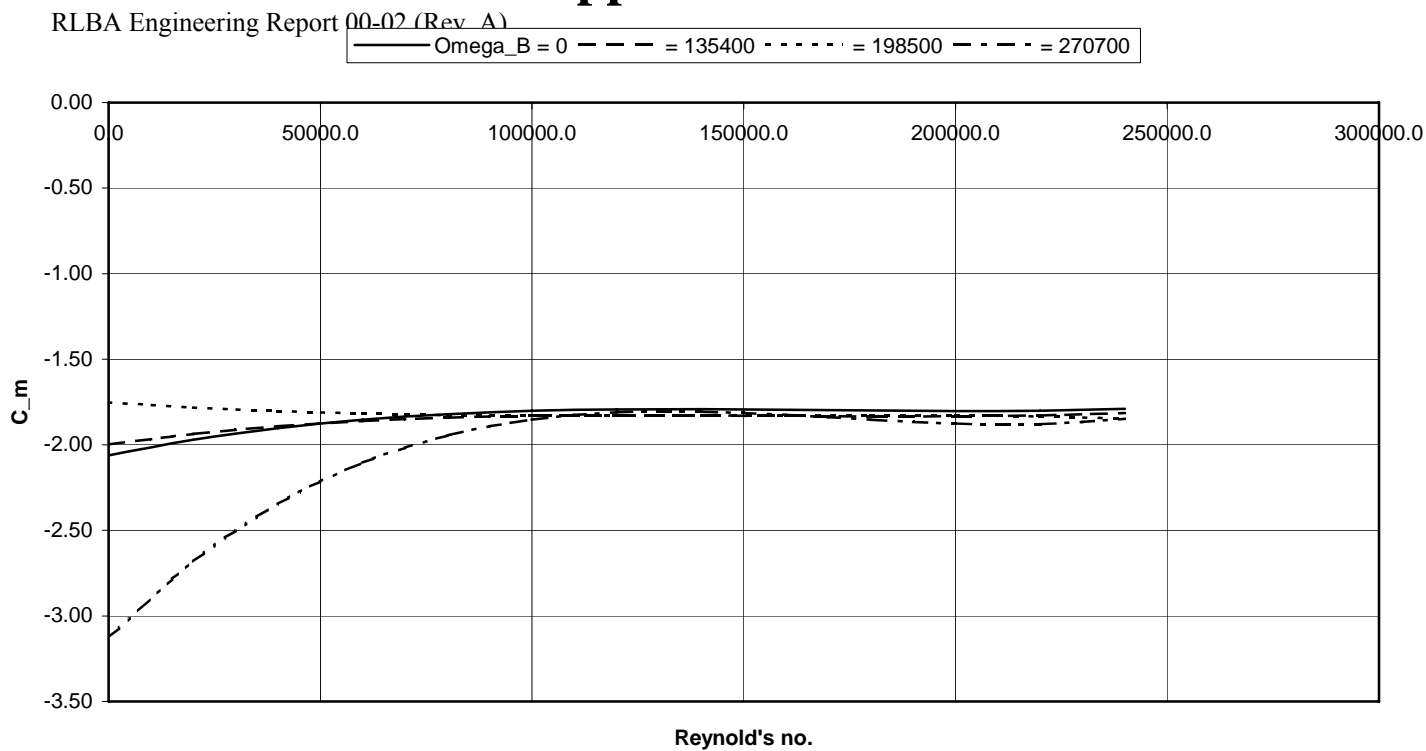


Fig. C.5 pitching moment coefficient variation with Reynold's no. and spin rate, $\alpha = 26.32$ deg.

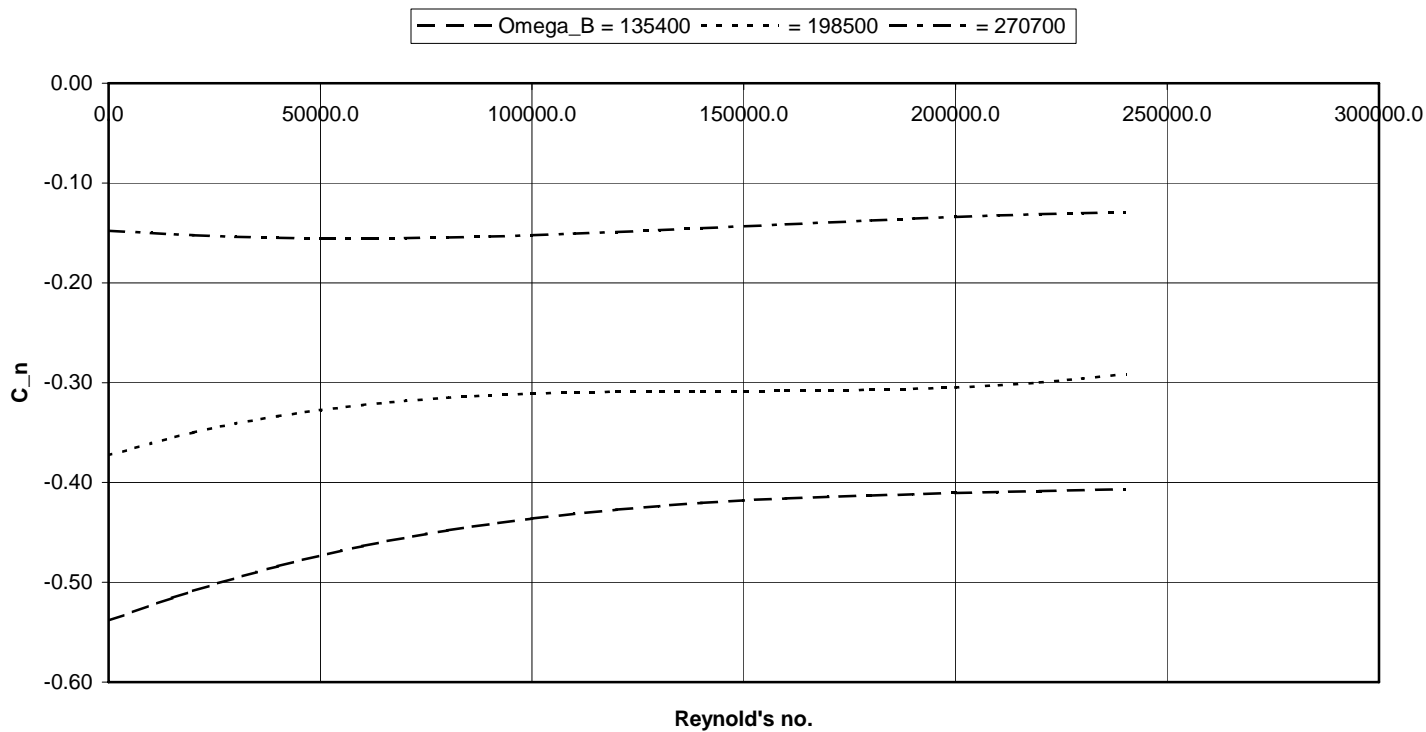


Fig. C.6 yawing moment coefficient variation with Reynold's no. and spin rate, $\alpha = 26.32$ deg.

Appendix C

RLBA Engineering Report 00-02 (Rev. A)

Appendix D – Implementation of the CONMIN Optimization Feature

The purpose of this appendix is to describe the implementation of the CONMIN algorithms that has been made, as well as providing an indication of how one would go about incorporating specific supplemental FORTRAN coding.

D.1 The CONMIN Program for Constrained Function Minimization

Ref. 15 describes the use of the CONMIN FORTRAN program for the general minimization of constrained functions. This code is a well-established analysis resource that has been used for many varied purposes. The intended use in the LITE_DYN analysis is to establish optimum modes of operation in the development of lightcraft flight. The CONMIN analysis is highly useful in that it enables the optimization of any function that can be numerically evaluated together with side constraints on the design (decision) variables along with a multiplicity of inequality constraints. Thus, the mathematical problem can be simply stated: Find values for the set of variables, X_i , that:

Minimize: $OBJ(X_i)$

Subject to:

- i) $G_j = G(X_i)_j \leq 0 \quad j = 1, \dots, NCON$
- ii) $VLB_i \leq X_i \leq VUB_i \quad i = 1, \dots, NDV$

where OBJ is a general function (*objective function*) of the variables X_i , referred to as decision variables. OBJ need not be a simple analytic function, and may be any function that can be numerically evaluated. G_j is the value of the j th *inequality constraint*, which is also a function of X_i . $NCON$ is the number of such constraints and can be zero. VLB_i and VUB_i are, respectively, the lower and upper bounds, or *side constraints* on the X_i variables. The reader is referred to Ref. 8 for a full description of the various standard inputs to the CONMIN algorithm and to Refs. 16, 17 and 18 for a description of the underlining theory. The principal drawback to the use of the CONMIN analysis tool is that, for any specific application, the evaluations of the objective function evaluation, as well as the inequality constraints, must be included in the **LITE_DYN** program as appropriate separate FORTRAN subroutines. Thus, complete use of the **LITE_DYN** code requires the ability to modify the source code and recompile it to obtain a new executable. Code.

D.2 Extent of Coding Incorporated in the LITE_DYN Code

The basic CONMIN FORTRAN coding, as described in Ref. 8, has been incorporated to the extent that the program will access the CONMIN algorithms in a structured manner. The following provisions have been made:

- 1) The user can select up to eighty (80) decision parameters from any of the inputs in the **C**, **F**, **P** or **V** input blocks, as described in Appendix A. Through appropriate inputs made to the **O** block, the desired decision parameters can be randomly selected. Provision has been made for inputting appropriate side constraints on the selected decision variables.

Appendix C

RLBA Engineering Report 00-02 (Rev. A)

- 2) Two alternative standard objective functions have been defined and programmed. The first is the mean-squared response of any of the several (again, randomly selectable) time-history response variables, $y_n(t)$. Thus:

$$OBJ = \frac{\sum_{k=1}^K t_k y_n^2(t_k)}{T_k}$$

(D.1)

where T_k is the time interval defined by the K time steps.

The second alternative objective function is provided by the eigenvalue solution of the linearized equation set. Here the definition of the objective function is based on the approach of driving one of the user-selectable eigenvalues (modes), $\zeta^{(k)}$, (as defined by its values of damping and frequency), to user-selectable values. The damping is expressed in terms of the linear critical damping ratio, $\zeta^{(k)}$, and undamped natural frequency, $f_n^{(k)}$, where $f_n^{(k)}$ is expressed in hz units. Thus:

$$OBJ = \kappa_1 \left(\zeta_{calc.}^{(k)} - \zeta_{required}^{(k)} \right)^2 + \kappa_2 \left(f_{n_{calc.}}^{(k)} - f_{n_{required}}^{(k)} \right)^2$$

(D.2)

where κ_1 and κ_2 are separately set to (0, .5, or 1) depending on whether the corresponding eigenvalue quantity (damping or frequency) was (not selected, jointly selected, or solely selected). While the time-history based objective function uses response values at every time, the eigenvalue-based function uses only the eigenvalues calculated at the last time instance. The subroutine resident in the LITE_DYN code that calculates the objective function is named **[object_func_calc]**.

- 3) No actual inequality constraints are included in the originating version of the LITE_DYN code, but the subroutine resident in the LITE_DYN code that has been provided for that purpose is named **[constraint_calc]**. Provision has been made for a total of forty (40) inequality constraints. For each of the **C**, **F**, **P** or **V** input blocks ten such constraints can be defined.

- 4) In the context of the flight dynamics of lightcraft, a great deal of latitude exists with regard to selections of both objective function and inequality constraints. While not actually programmed in the originating version of the LITE_DYN code, a combination the two above described alternative objective functions could be accomplished by defining the eigenvalue-based objectives as inequality constraints:

$$\zeta_{required}^{(k)} - \zeta_{calculated}^{(k)} \leq 0 \quad \left| f_{n_{calc.}}^{(k)} - f_{n_{required}}^{(k)} \right| - \varepsilon \leq 0$$

(D.3a,b)

Appendix C

RLBA Engineering Report 00-02 (Rev. A)

D.3 FORTRAN coding of CONMIN-related User-Defined Subroutines

The following FORTRAN (-90) listings present the basic (default) codes for those subroutines needed to define the objective function and the inequality constraints. While the subroutine **object_func_calc** does present alternative calculations for two basic objective functions, the subroutines, **constraint_calc** and **CFPV_constraints** are only in a form that defines the structure to the analysis without any actual constraints being defined. The subroutine *Preprocess_Data_CFPV* sets up the CONMIN-related parameters that relate to the D,F,P and V data blocks and does not need any user-definition.

```
!*****
      SUBROUTINE object_func_calc(OBJ)
!
!   Subroutine object_func_calc calculates the OBJECTIVE FUNCTION, OBJ.
!
      REAL*8 OBJ
!
      include 'v_arrays.inc'
      include 'v_mscmns.inc'
      include 'v_reslts.inc'
      Include 'v_conmin.inc'
!
      do 100 n = 1,NDV
      k = k_xindex(n)
      m = m_xindex(n)
      IF (K.EQ.1) CBV(IXINDEX(k,m)) = sngl(X_DV(NDV))
      IF (K.EQ.2) FBV(IXINDEX(k,m)) = sngl(X_DV(NDV))
      IF (K.EQ.3) PBV(IXINDEX(k,m)) = sngl(X_DV(NDV))
      IF (K.EQ.4) VBV(IXINDEX(k,m)) = sngl(X_DV(NDV))
100 CONTINUE
!
      CALL Preprocess_Data_CFPV
      CALL Initialize
      CALL DYNAMICS
!
!   Initialize the OBJECTIVE FUNCTION & Related variables
!
      OBJ = 0.
!
!   Form the OBJECTIVE FUNCTION
!
      if (i_use_conmin.eq.1) then
         XN_time = real(N_time)
!
         do 200 n = 1,N_time
            OBJ = OBJ + dble(float(n))*dble(YY(n,i_TH_DOF)**2)
200          continue
            OBJ = dsqrt(OBJ/dble(XN_time))
         else
            ww_n = sqrt(RTR(i_eigen_mode)**2 + RTI(i_eigen_mode)**2)
            actual_zeta = - RTR(i_eigen_mode)/ww_n
            actual_freq = 0.5*ww_n/(sqrt(1. - actual_zeta**2))*pi
!
            OBJ = dble(weight_zeta*(actual_zeta-specifd_zeta)**2 +
            &
            weight_freq*(actual_freq-specifd_freq)**2)
```

Appendix C

RLBA Engineering Report 00-02 (Rev. A)

```

        endif
        RETURN
!
2000    FORMAT(5X,'Intermittent values of design variables:',/
1      ,10(5X,5D12.6/))
        END
!*****
        SUBROUTINE constraint_calc
!
!      Subroutine constraint_calc calculates the CONSTRAINTS:
!
!              G(j) < 0., for j = 1,NCON
!
!      include 'v_arrays.inc'
!      include 'v_mscmns.inc'
!      include 'v_reslts.inc'
!      Include 'v_conmin.inc'
!
!      dimension G_CBV(10), G_FBV(10), G_PBV(10), G_VBV(10)
!      real*8 G_CBV, G_FBV, G_PBV, G_VBV
!
!      The above variables must be supplied by user in form of a separate
!      subroutine, <CFPV_constraints>
!
!      constraint_calc is called by the MAIN program.
!
!      PRINT*, 'START OF constraint_calc'
!
!      CALL CFPV_constraints (G_CBV, G_FBV, G_PBV, G_VBV)
!
!      do 100 n = 1,NCON
!      k = k_Gindex(n)
!      m = m_Gindex(n)
!      IF (K.EQ.1) then
!          G(n) = G_CBV(m)
!      IF (K.EQ.2) then
!          G(n) = G_FBV(m)
!      IF (K.EQ.3) then
!          G(n) = G_PBV(m)
!      IF (K.EQ.4) then
!          G(n) = G_VBV(m)
!      100 CONTINUE
!
!      PRINT*, 'LEAVING constraint_calc'
!
!      WRITE(18,FMT=*) ' Constraints = ', (G(I), I= 1,10)
!      RETURN
!
!      END
!*****

```

Appendix C

RLBA Engineering Report 00-02 (Rev. A)

```
!*****
      SUBROUTINE CFPV_constraints (G_CBV, G_FBV, G_PBV, G_VBV)
!
!   User-supplied Subroutine for inequality constraints on X_dv's
!   defined in the CBV, FBV, PBV, & VBV data blocks
!
      include 'v_arrays.inc'
      include 'v_mscmns.inc'
      include 'v_reslts.inc'
      Include 'v_conmin.inc'
!
      dimension G_CBV(10), G_FBV(10), G_PBV(10), G_VBV(10)
      real*8 G_CBV, G_FBV, G_PBV, G_VBV, blank
!
      blank = 0.
!
      do 100 n = 1,NCON
      do 200 m = 1,m_gindex(n)
!
         if (k_gindex(n).eq.1) G_CBV(m) = blank
         if (k_gindex(n).eq.2) G_FBV(m) = blank
         if (k_gindex(n).eq.3) G_PBV(m) = blank
         if (k_gindex(n).eq.4) G_VBV(m) = blank
200      continue
100      continue
!
      return
!
      end
!*****
```

Appendix C

RLBA Engineering Report 00-02 (Rev. A)

Appendix E – Descriptions of Standard Outputs

Appendix A briefly identifies the types of output file selection queries to which the user is required to respond, but concentrates on the required contents of the data file containing the input data. This appendix briefly describes the various types of output requiring distinct file names (to be provided by the user):

- 1.) *ECHO of LOADER DATA*
- 2.) *DEBUG RESULTS*
- 3.) *EIGENVALUE RESULTS, and*
- 4.) *DYNAMIC RESPONSE RESULTS*
- 5.) *TERMINATION STATE VECTOR*
- 6.) *CONMIN RESULTS*

The *Echo of the (Input) Loader Data* is intended as a method for documenting the runs made with the LITE_DYN Computer Code. The *DEBUG* outputs are generally intended only for developmental purposes. The two operationally important outputs are those giving the eigenvalue solution results and the time-history solution resulting from the Runge-Kutta integration of the fully nonlinear equations of motion.

E.1 Eigenvalue Results

The eigenvalue output results consist of three groups of data:

- 1.) The matrices forming the eigenvalue problem, reflecting the linearization of the actual equations of motion. (These matrices are normally provided only with the *DEBUG* outputs, however.)
- 2.) The eigenvalues, and
- 3.) The mode shapes.

The eigenvalues are, furthermore, arranged in descending order of frequency and are identified as to type (i.e., aperiodic, complex, etc.). The output of zero roots is suppressed. [Note that the eigenvalue solution is suppressed if a scratch file (*) is input for the eigenvalue results file name.]

E.2 Time-history Results

The time-history results are output as an ASCII file with each line representing the dynamic system state at each (k index) of the progressive values of time. The first item is the time value, *time(k)*, followed by the values of the (60) selected variables forming the internally named *YY* array. This file can then be used by any of a wide variety of plotting programs, such as Excel, etc. The following list identifies the variables comprising the *YY* array:

```
!      Following (23) variables ARE part of the Runge-Kutta solution
algorithm:
!
!      The following (11) variables define the direct body dynamics:
!          YY(k,1)      = v_x_k
!          YY(k,2)      = v_y_k
!          YY(k,3)      = v_z_k
```

Appendix C

RLBA Engineering Report 00-02 (Rev. A)

```

!               yy(k,4)      = qq_k
!               yy(k,5)      = rr_k
!-----
!       The following (6) variables are non-zero only when the dual-spin option
!       is invoked:
!
!               yy(k,6)      = del_thetayP_k      units = rad/sec
!               yy(k,7)      = del_thetazP_k      "
!               yy(k,8)      = pp_nspn_k          "
!               yy(k,9)      = del_thetay_k        units = deg
!               yy(k,10)     = del_thetaz_k        "
!               yy(k,11)     = phi_nspn_k          "
!-----
!       The following (6) variables describe the Earth-centered flight-path:
!
!               yy(k,12)     = vehicle_mass_k
!               yy(k,13)     = delta_R_geocentric_k
!               yy(k,14)     = geocentric_latitude_k units = deg
!               yy(k,15)     = longitude_k         "
!               yy(k,16)     = heading_k           "
!               yy(k,17)     = theta_k             "
!               yy(k,18)     = SS_LC_x1
!               yy(k,19)     = SS_LC_y1
!               yy(k,20)     = SS_LC_z1
!-----
!       Following variables are those associated with the feedback control
!       network:
!
!               yy(k,21)     = y1_control_k
!               yy(k,22)     = y2_control_k
!               yy(k,23)     = y3_control_k
!               yy(k,24)     = y4_control_k
!               yy(k,25)     = y5_control_k
!               yy(k,26)     = y6_control_k
!               yy(k,27)     = y7_control_k
!               yy(k,28)     = y8_control_k
!-----
!       Following variables ARE NOT part of the Runge-Kutta solution state
!       vector, but are derived from the above and are included for
!       completeness:
!
!               yy(k,29)     = x1_control_k
!               yy(k,30)     = x2_control_k
!               yy(k,31)     = x3_control_k
!               yy(k,32)     = x4_control_k
!               yy(k,33)     = x5_control_k
!               yy(k,34)     = x6_control_k
!               yy(k,35)     = x7_control_k
!               yy(k,36)     = x8_control_k
!-----
!               yy(k,37)     = geodetic_altitude_k
!               yy(k,38)     = geodetic_latitude_k units = deg
!               yy(k,39)     = bearing_k           units = deg!
!               yy(k,40)     = gamma_k
!               yy(k,41)     = Flt_Pth_phi_k
!               yy(k,42)     = Range_k
!-----
!               yy(k,43)     = bearing_LB_k        units = deg
!               yy(k,44)     = gamma_LB_k          "
!               yy(k,45)     = v_wind_k

```


Appendix C

RLBA Engineering Report 00-02 (Rev. A)

```

!                yy(k,46)    = psi_wind_k                units = deg
!-----
!-----
!                yy(k,47)    = offset_ND_lin_3(2) (Y-axis linear offset)
!                yy(k,48)    = offset_ND_lin_3(3) (Z-axis linear offset)
!                yy(k,49)    = offset_ang_3(2)      (Y-axis angular offset)
!                yy(k,50)    = offset_ang_3(3)      (Z-axis angular offset)
!-----
!                yy(k,51)    = vx3_wind
!                yy(k,52)    = vy3_wind
!                yy(k,53)    = vz3_wind
!-----
!                yy(k,54)    = M_x command
!                yy(k,55)    = M_y command
!                yy(k,56)    = M_z command
!-----
!                yy(k,57)    = roll    angle command units = deg
!                yy(k,58)    = pitch   angle command      "
!                yy(k,59)    = heading angle command      "
!                yy(k,60)    = net thrust
!-----

```

Note that if the feedback control variables [$yy(k, 18)$ thru $yy(k, 33)$] are not invoked, these components of the $yy(kk, i)$ array are deleted.

E.3 Termination State Vector

At the end of the time-history calculation the various state variables defining the dynamics are output to the *TERMINATION STATE VECTOR* named file. This file will contain the loader format data needed for the “D” input data block (see Section A.2.4) in order to continue the time-history. This file will have the following format:

```

D,9,1, .xxxxxxxExx, .xxxxxxxExx, .xxxxxxxExx, .xxxxxxxExx, ... , .xxxxxxxExx
D,5,21, .xxxxxxxExx, .xxxxxxxExx, .xxxxxxxExx, .xxxxxxxExx, .xxxxxxxExx
D,6,26, .xxxxxxxExx, .xxxxxxxExx, .xxxxxxxExx, .xxxxxxxExx, .xxxxxxxExx, .xxxxxxxExx
D,8,32, .xxxxxxxExx, .xxxxxxxExx, .xxxxxxxExx, .xxxxxxxExx, ... , .xxxxxxxExx
D,1,40, .xxxxxxxExx
F,1,1, .xxxxxxxExx
S,1,6, 1.0

```

E.4 CONMIN Results

This file will record the various iterations of the objective function and the design variables as the optimization process converges.

Appendix C

RLBA Engineering Report 00-02 (Rev. A)

Appendix D

Laser Propulsion Assessment

Dr. James P. Reilly

**Northeast Science and Technology, Inc.
117 North Shore Blvd
East Sandwich, Cape Cod, MA 02537**

**508-833-8980, fax 508-833-6657
ReillyNST@aol.com
ReillyNST@compuserve.com**

NST

Northeast Science and Technology, Inc

Table of Contents

Section A--	Basis of Analyses Laser Options Analysis Methodology Laser and Beam Director Cost Algorithms
Section B--	Low-Altitude Boost and Mid-Altitude Boost Phases Repped-Pulse Solid-State Laser & Beam Director Repped-Pulse Gas Lasers & Beam Directors CW Gas Lasers & Beam Directors
Section C--	High-Altitude Boost and All Vacuum Environments Repped-Pulse Solid-State Laser & Beam Director Repped-Pulse Gas Lasers & Beam Directors
Section D--	High-Altitude Boost and All Vacuum Environments CW Gas Lasers & Beam Directors
Section E--	Full analysis using four criteria for a system : Repped-Pulse Solid-State Laser & Beam Director Repped-Pulse Gas Lasers & Beam Directors CW Gas Lasers & Beam Directors
Section F--	Conclusions

Layout of Assessment Study :

Task

- | | | |
|----------|--|------------------|
| 1 | Thrust / Impulse Generator Laser Device | > 90 % |
| 2 | Quick-Look Optical System Capability | < 5 % |
| 3 | Quick-Look Propagation & Compatibility Analysis | < 5 % |

Section A--

Basis of Analyses

**Analyzed in this section : Repped-Pulse Solid-State Laser & Beam Director
Repped-Pulse Gas Lasers & Beam Directors
CW Gas Lasers & Beam Directors**

Generic Costs of Lasers & Beam Directors (From NASA "ORION" Study)

Outline of methodology to combine these into system costs under restraints of system requirements

NST

Northeast Science and Technology

High-Power Laser Technology Options for Operating Launch Systems

	Use Air Plasma as Thrust-Generator	Use Target Plasma as Thrust-Generator	Use Straight Ablation as Thrust-Generator
RP Waveform	required	required	NOT PRACTICAL
CW Waveform	NOT PRACTICAL	NOT PRACTICAL	O K
Low-Altitude Boost	YES	O K	O K
Mid-Altitude Boost	MAYBE	O K	O K
High-Altitude Boost / Orbit Insertion	-----	O K	O K
Orbit Change	-----	O K	O K

NST

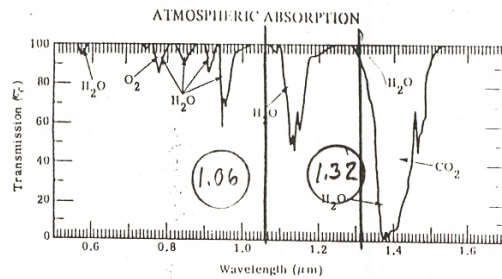
Laser Propagation Windows in the Atmosphere

Northeast Science and Technology, Inc

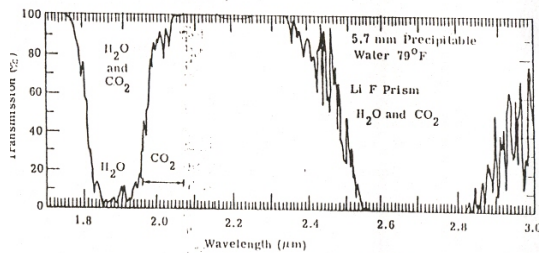
Linear Atmospheric Propagation is good for :

Laser Wavelength (microns)	High-Power Laser Technology
1 thru 1.1	Solid State Lasers
1.2 thru 1.3	Iodine Lasers
3.4 thru 4.15	CO-first overtone Lasers DF Chemical Lasers
8.5 thru 12	Standard CO2 Isotopic CO2

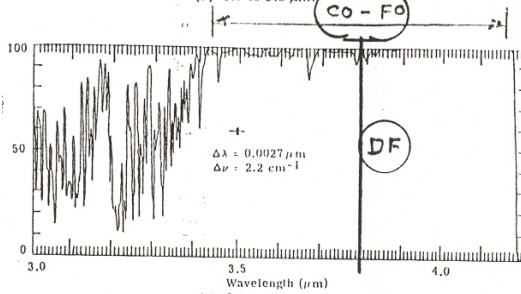
Linear Atmospheric Propagation is good for Certain High Power Lasers



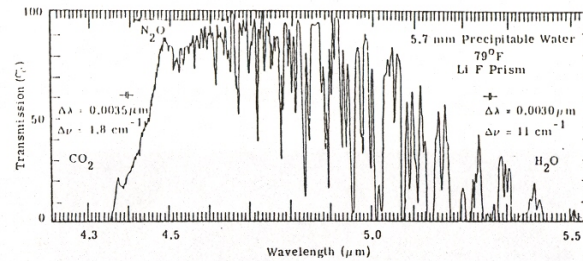
(a) 0.5 to 1.7 μm .



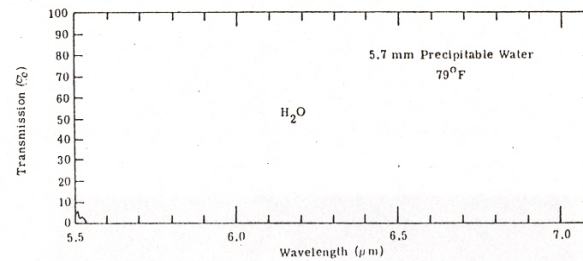
(b) 1.7 to 3.0 μm .



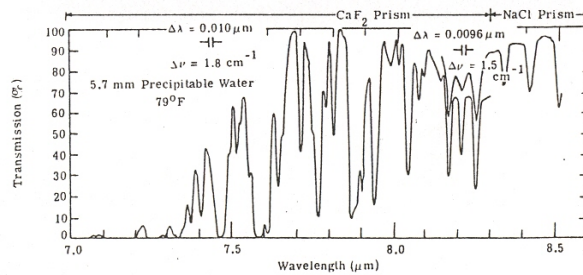
(c) 3.0 to 4.2 μm .



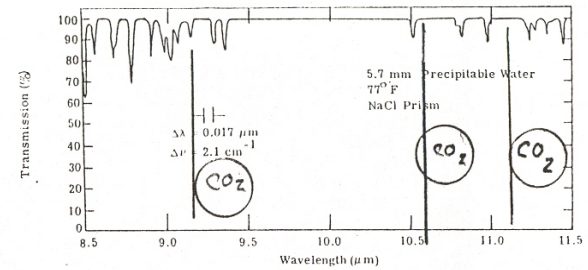
(d) 4.2 to 5.518 μm .



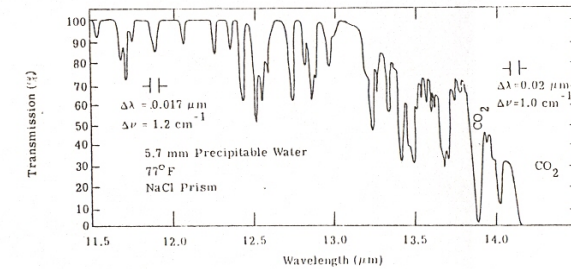
(e) 5.5 to 7.0 μm .



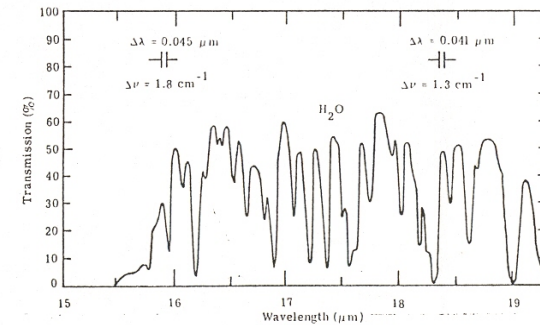
(f) 7.0 to 8.5 μm .



(g) 8.5 to 11.5 μm .



(h) 11.5 to 14.0 μm .



(i) 15.0 to 19.0 μm .

	CO2	CO	Chemical	Iodine	ND-Yag ND-Glass	Excimer
Wavelength	common 9, 10 μm alternative 11 μm	4-6 μm 2.5-3.5 μm	2.7 μm 3.5 μm	1.316 μm	1.06 μm 1.05 μm	0.35 to 0.55 μm
Waveform	RP & CW	RP & CW	RP & CW	RP & CW	RP & CW	RP only
Technologies	CW :GDL CW & RP: Electrical	GDL Electrical	Flashlamp- and E-beam- pumped	Flashlamp- pumped	Flashlamp- and Diode- pumped	Electrical
Open -vs- Closed Cycle	both	both	open cycle	open cycle	closed cycle	closed cycle
Gas vs Solid-State	gas	gas	gas	gas	solid-state	gas
Excitation Technology	electrical and combustion	electrical and combustion	chemical reaction	electrical	electrical	electrical
High Power Capability	classified	classified	classified	classified	classified	a few kW
Comments	Electric-powered Closed -cycle operation very attractive at CO Wavelengths	----- ----- as CO2 ----- -----	Not a player for high launch rates and long term usage	Potential for closed-cycle operation makes this a player	Lots of development req'd but possible (LLNL)	Not a Player -- only low power laser devices
	GDL technology very cheap to build & run (pollution a problem)	----- as CO2 ----- ----- -----				

Might be a
real long-term
contender,
depending on
costs

Appears as a
real long-term
contender as
electric laser,
at 3.5 microns

Appears as a
real long-term
contender

Appears as a
real long-term
contender

LONG-RANGE TARGET: Airey's Rule applied to laser device and technology selection

- Assume:**
- 1---careful System Design and Implimentation minimizes all Non-Linear Effects
 - 2--- existing Adaptive Optics Technology minimizes beam pointing and phase aberrations
 - 3---linear beam attenuation & scattering by atmosphere

$$\text{REAL peak centerline far field beam intensity} = \frac{\text{Power at Aperture} \times \text{Beam Area at Aperture}}{(\text{wavelength})^2 \times (\text{Range})^2 \times \text{Beam Degradation ratio}}$$

$$I = \frac{P_o \times A_o \times (\text{Transmission})}{(\lambda)^2 \times (Z)^2 \times SR_{tot}}$$

$$I = \frac{P_o \times A_o \times (T)}{(\lambda)^2 \times (Z)^2 \times \{ SR_{non-lin} \times [1 + (\theta_{jitter} / \theta_{dffrn})^2 + (\theta_{turb} / \theta_{dffrn})^2 + (\beta)^2] \}}$$

SHORT-RANGE TARGET: Minimum focussing required at low altitudes

$$I = \frac{P_o \times (T)}{\text{Beam Collector Area} \times \{ SR_{non-lin} \times [1 + (\theta_{jitter} / \theta_{dffrn})^2 + (\theta_{turb} / \theta_{dffrn})^2 + (\beta)^2] \}}$$

Laser System Req'ts depend on Beam Properties required by Target and on Mission Parameters

Peak Beam Intensity-----I peak
Avg Beam Intensity-----I avg
Waveform-----τ pulse, PRF, CW

Range Requirements-----Z
Angular Slew Rates-----Ω
Beam Director Optics Diameter-----D
Launch Rate

Laser System Capital Costs and Operating Costs depend Predominately on Laser Device and Pointer-Tracker

Thruster Requirement

Cost # 1 Cost # 2

Power at Aperture X Beam Area at Aperture

REAL peak centerline far field beam intensity =
$$\frac{\text{Power at Aperture} \times \text{Beam Area at Aperture}}{(\text{wavelength})^2 \times (\text{Range})^2 \times \text{Beam Degradation ratio}}$$

$$I = \frac{P_o \times A_o \times (\text{Transmission})}{(\lambda)^2 \times (Z)^2 \times SR_{tot}}$$

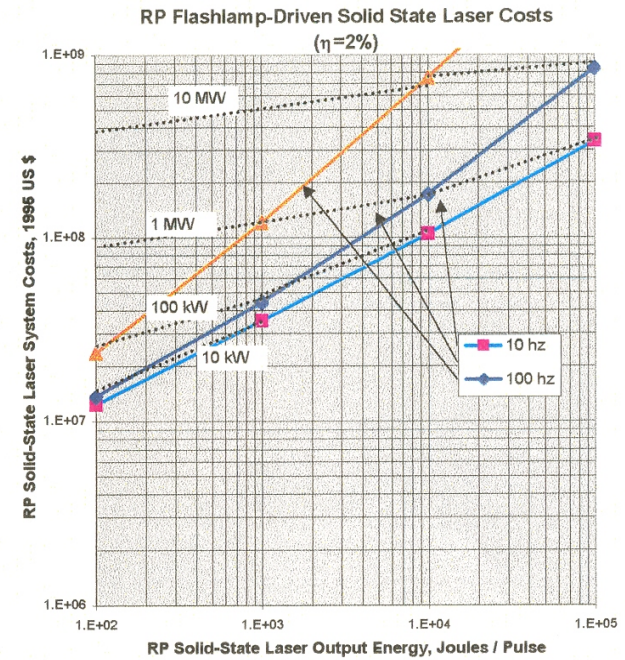
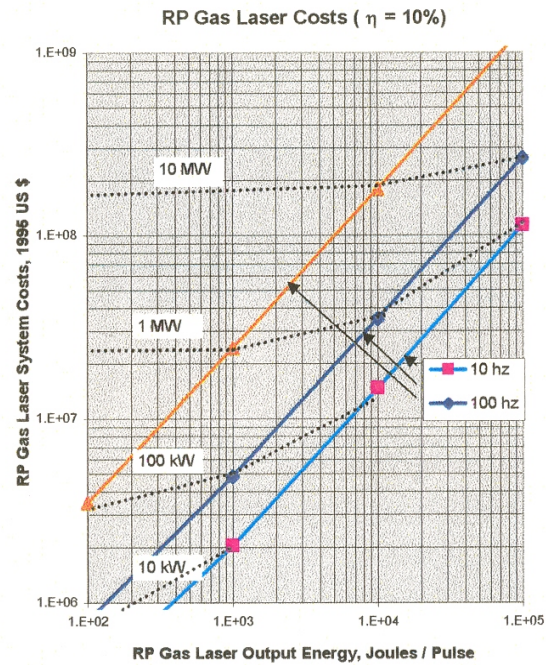
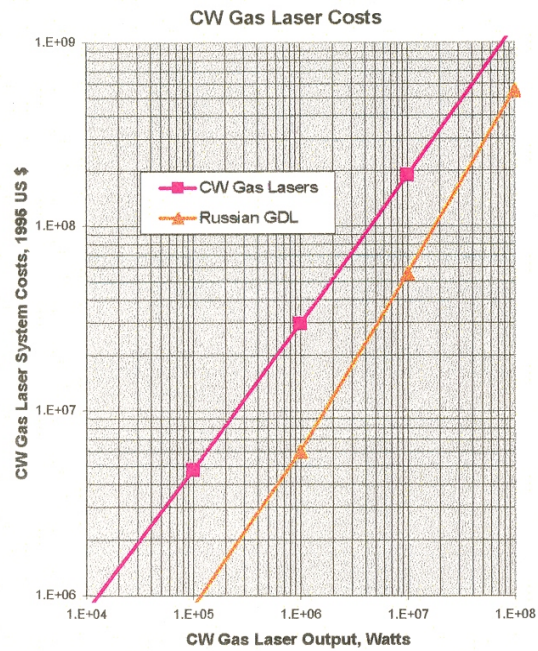
Thruster fixes I. Then mission profile brackets [(λ), (Z), SR_{tot}].

More laser power (Po) means more Laser cost, but less Pointer-Tracker cost (Ao).

Data on Laser Facility Costs and Telescope Facility costs obtained in NASA's ORION Program

NST

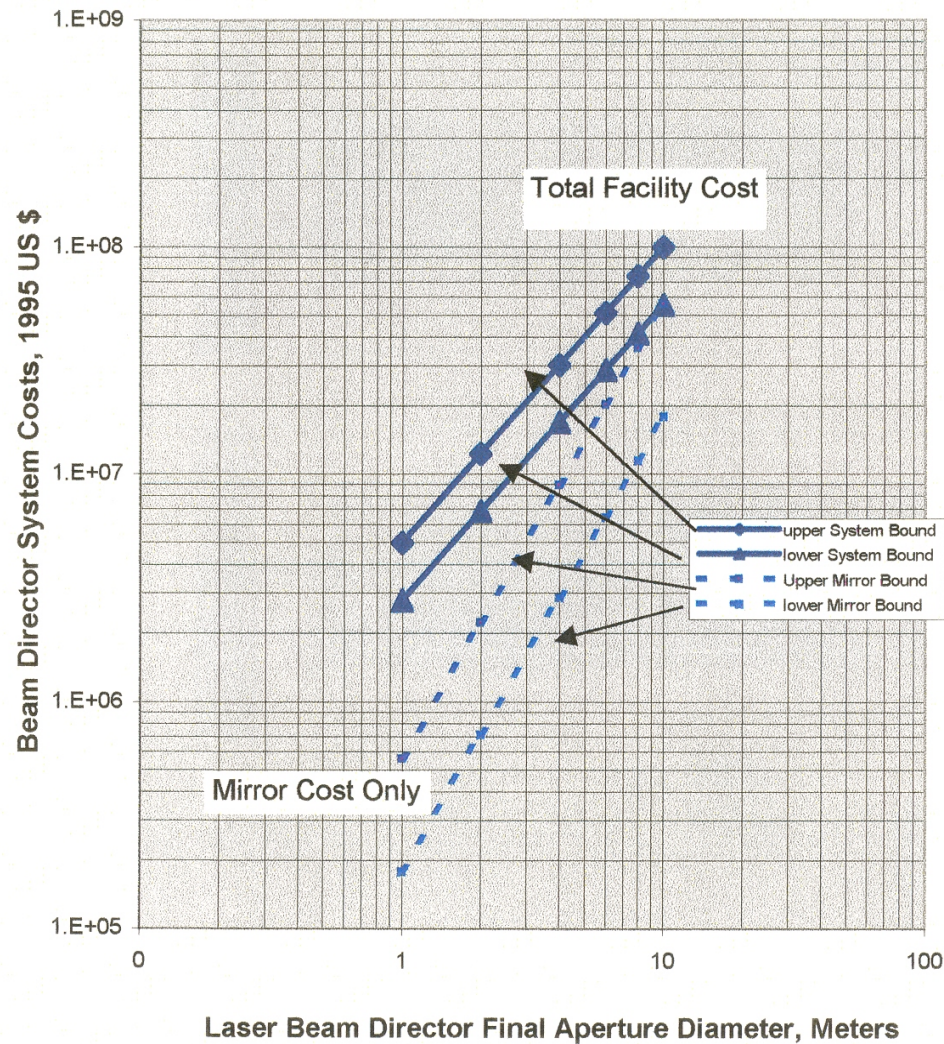
Northeast Science and Technology, Inc



NST

Northeast Science and Technology, Inc

Beam Director Cost Scaling



NST

Northeast Science and Technology

General Laser Technology Requirements

Impulse Coupling Coefficient is used to Compute both Pulsed-laser Impulse and CW laser Thrust Production

$$\text{Avg Thrust} = (\text{Impulse per pulse}) \times (\text{Pulse Repetition Freq.})$$

$$= (CC \times I_{\text{peak}} \times \text{pulse duration}) \times (\text{PRF})$$

$$\text{Avg Thrust} = (CC) \times I_{\text{avg}}$$

as well as : $\text{Peak Thrust} = (CC) \times I_{\text{peak}}$

Example: 5 lbs @ 5 g's

$$5\text{lb} \times 454 \text{ gr/lb} \times 5 \times 980 \text{ cm/sec}^2 = 1 \times 10^7 \text{ dynes}$$

-at Coupling Coeff of 10 dynes/ watt =10 dyne-sec/joule
requires

requires $1 \times 10^7 / 10 = 1 \text{ MW}$ on target average during entire flyout period

$$= 3 - 10 \text{ MW from ground-laser , time-averaged during flyout}$$

But in addition, thruster must receive :

Pulsed Lasers: a minimum centerline laser intensity to produce efficient vaporization and/or plasma production

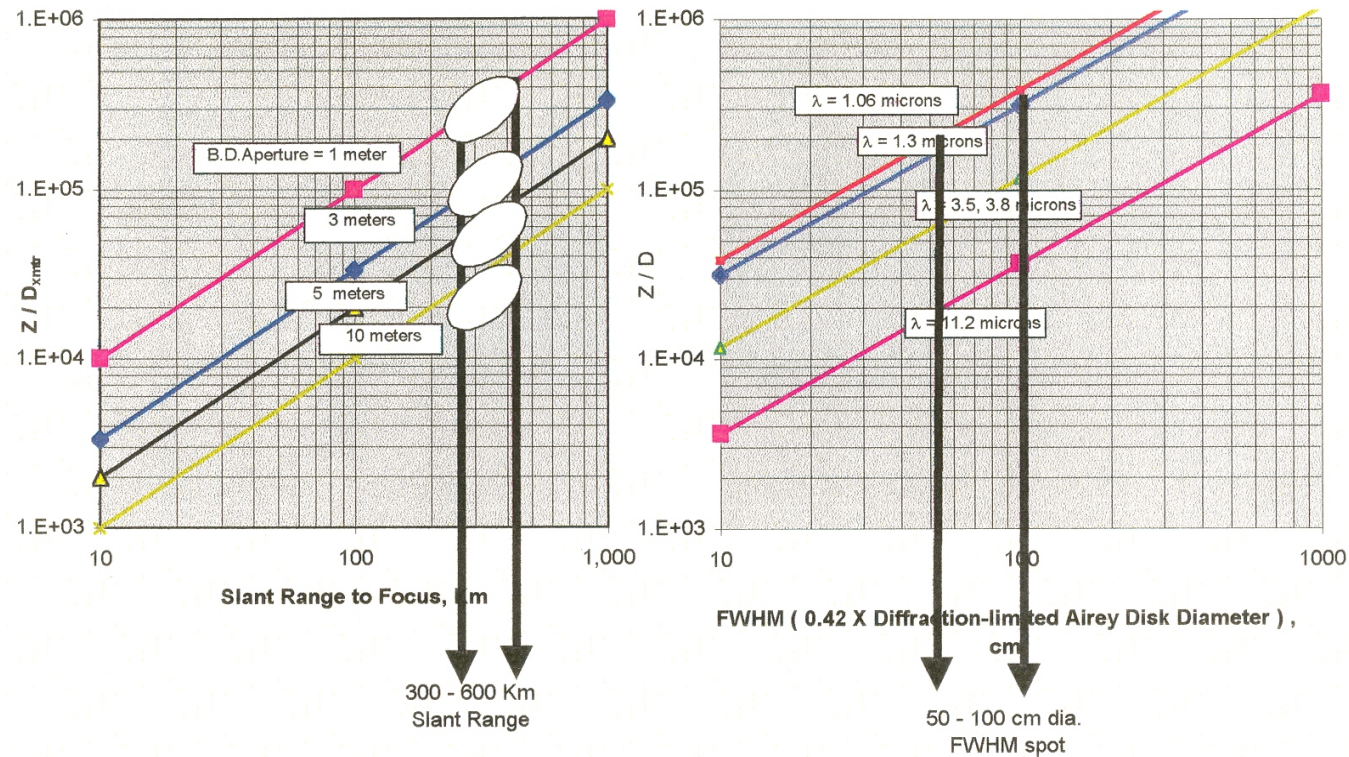
or

CW Lasers : a minimum centerline laser intensity to produce efficient vaporization

NST

Northeast Science Technology, Inc

Diffraction-Limited Spot Diameter at Range



Criteria : 50-100 cm FWHM spot diameter at 300 - 600 Km slant range

Requires :	λ microns	Beam Director Aperture Diameter meters
	1.06	1 - 2
	1.3	1.5 - 3
	3.5	3.5 - 8
	3.8	3.5 - 8
	10.6, 11.2	10 - 15

Section B--

Low-Altitude Boost and possibly Mid-Altitude Boost Phases

do not require bringing beam to focal point--only filling Beam Collection Optics

Can use any and all thrust-generation mechanisms-

Use Air Plasma

Use Target Plasma

Use Straight Ablation

Anayzed in this section :

Repped-Pulse Solid-State Laser & Beam Director

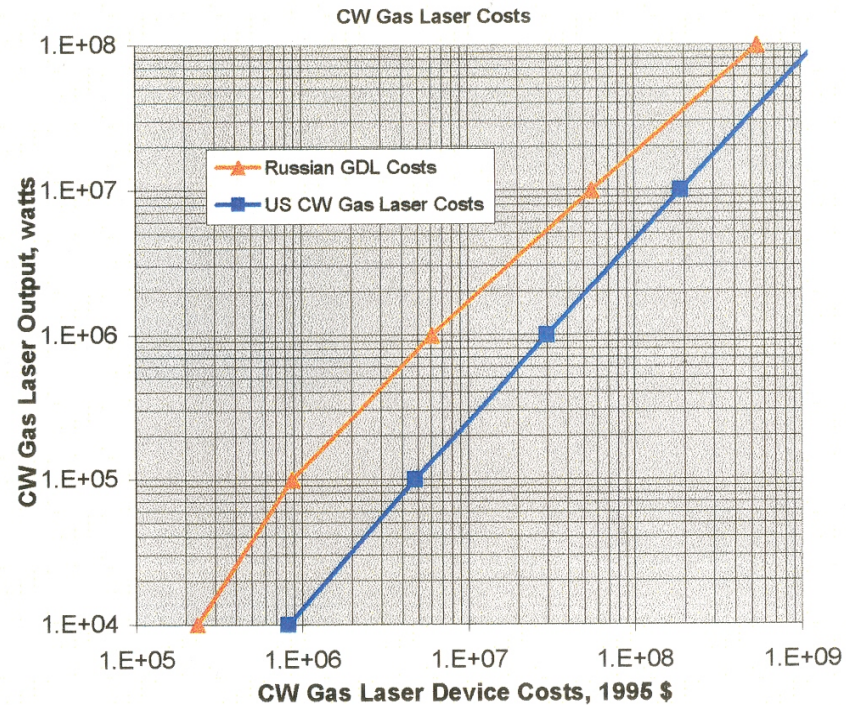
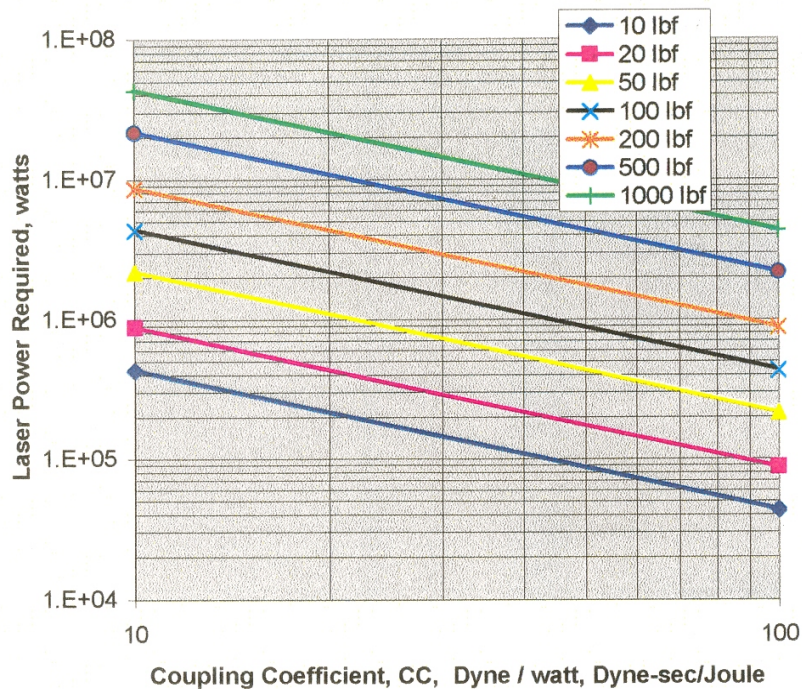
Repped-Pulse Gas Lasers & Beam Directors

CW Gas Lasers & Beam Directors

NST

Northeast Science and Technology, Inc

Low-Altitude Thrust Generation
Plasma or Straight Ablation
CW Gas Lasers



Standard Coupling Coefficients (CC=10 Dyne / Watt) require 400 Kw of on-target laser power to produce 10 lbf of thrust

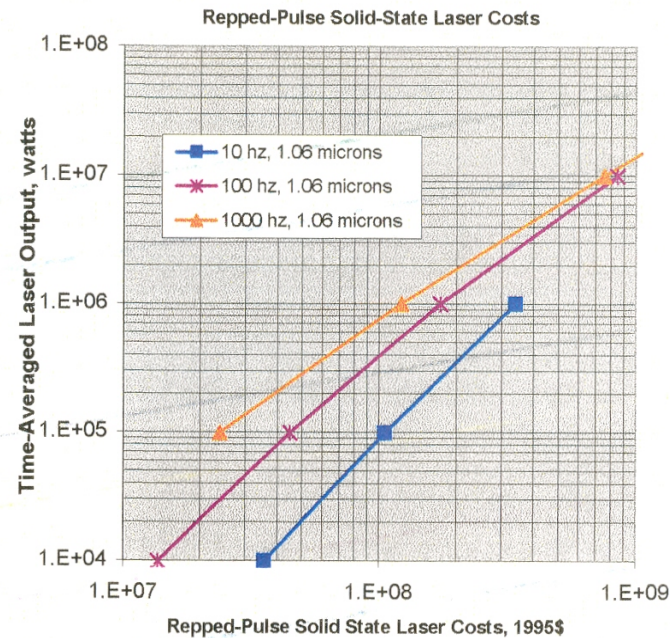
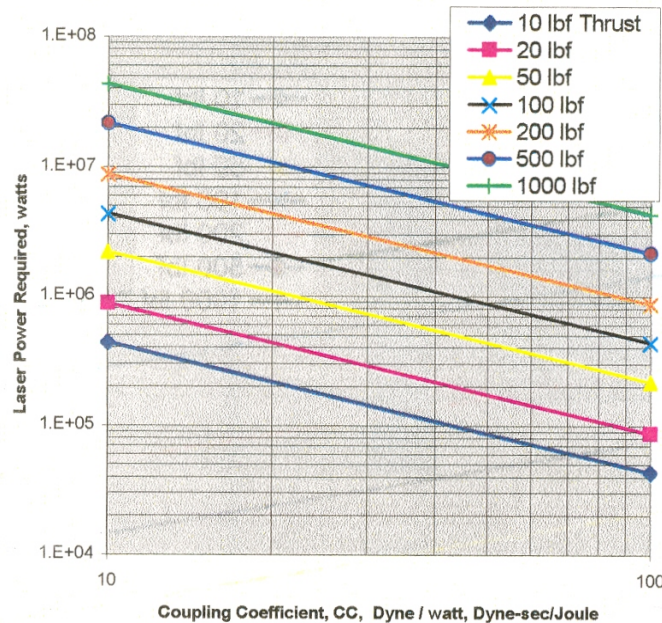
With this low CC, the laser alone would cost between a low \$4,000,000 (Russian GDL Technology) to a high of \$15,000,000 (US)

A new 2 meter Beam Director would add a cost of between a low of \$2,300,000 and a high of \$12,300,000

A new 8 meter Beam Director would add a cost of between a low of \$36,900,000 and a high of \$75,700,000

With a high CC (say, 60 Dyne/Watt), the laser cost would drop to between a low \$800,000 (Russian GDL Technology) to a high of \$4,000,000 (US)

Beam Director Costs would remain the same.



Standard Coupling Coefficients (CC=10 Dyne-sec / joule) require 400 Kw of on-target laser power to produce 10 lbf of thrust

With this low CC, the laser alone would cost between a low \$65,000,000 (1000 hz rep rate technology)
to a high of \$220,000,000 (10 hz rep rate technology)

A new 2 meter Beam Director would add a cost of between a low of \$2,300,000 and a high of \$12,300,000

A new 8 meter Beam Director would add a cost of between a low of \$36,900,000 and a high of \$75,700,000

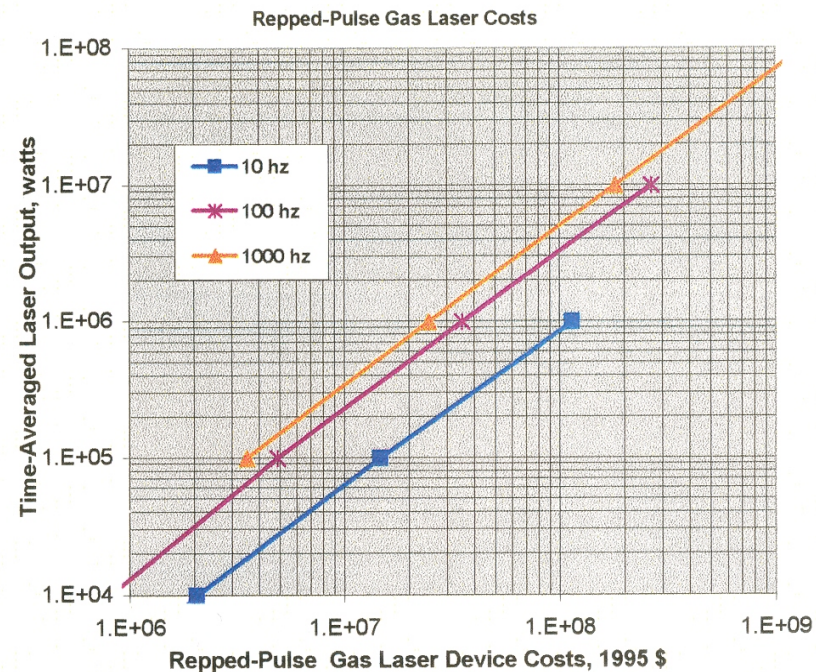
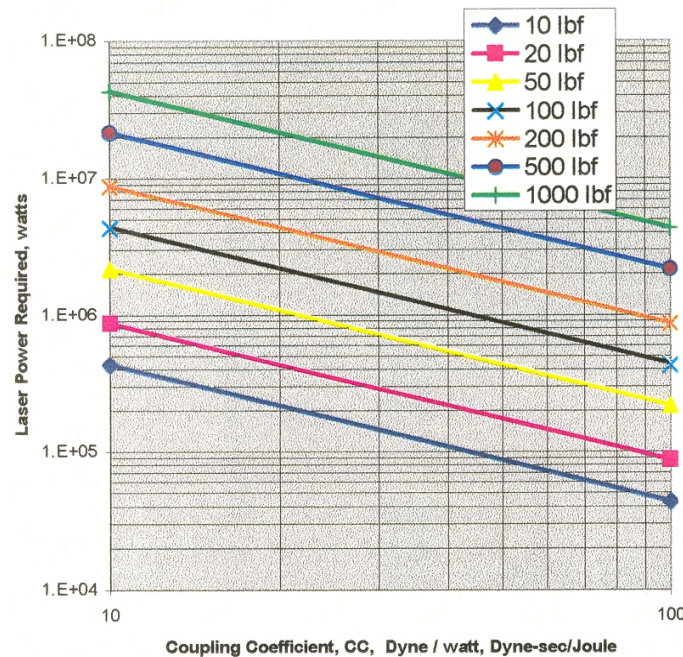
With a high CC (say 60 Dyne-sec/joule), the laser cost would drop to between a low of \$21,000,000 (1000 hz rep rate technology)
to a high of \$90,000,000 (10 hz rep rate technology)

Beam Director Costs would remain the same.

NST

Northeast Science and Technology, Inc

Low-Altitude Thrust Generation Plasma or Straight Ablation Repped-Pulse Gas Lasers



Standard Coupling Coefficients (CC=10 Dyne-sec / joule) require 400 Kw of on-target laser power to produce 10 lbf of thrust

With this low CC, the laser alone would cost between a low \$11,000,000 (1000 hz rep rate technology)
to a high of \$50,000,000 (10 hz rep rate technology)

A new 2 meter Beam Director would add a cost of between a low of \$2,300,000 and a high of \$12,300,000

A new 8 meter Beam Director would add a cost of between a low of \$36,900,000 and a high of \$75,700,000

With a high CC (say 60 Dyne-sec/joule), the laser cost would drop to between a low \$1,800,000 (1000 hz rep rate technology)
to a high of \$8,000,000 (10 hz rep rate technology)

Beam Director Costs would remain the same.

Section C--

High-Altitude Boost and All Vacuum Environments

Absolutely require bringing beam to focal point to fill Beam Collection Optics

Can use only two possible thrust-generation mechanisms-

**Target Plasma
Straight Ablation**

**Anayzed in this section : Repped-Pulse Solid-State Laser & Beam Director
Repped-Pulse Gas Lasers & Beam Directors**

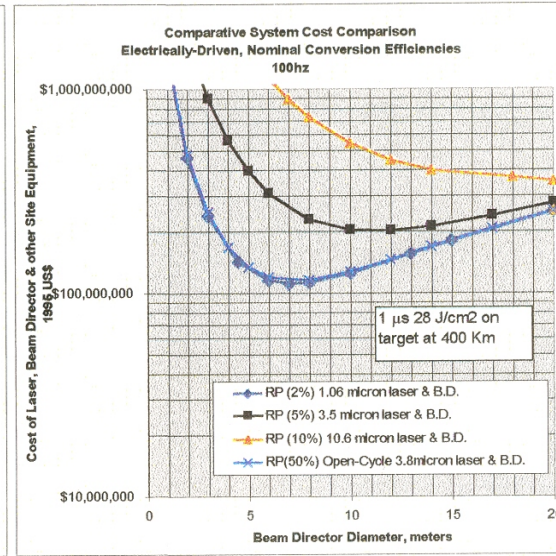
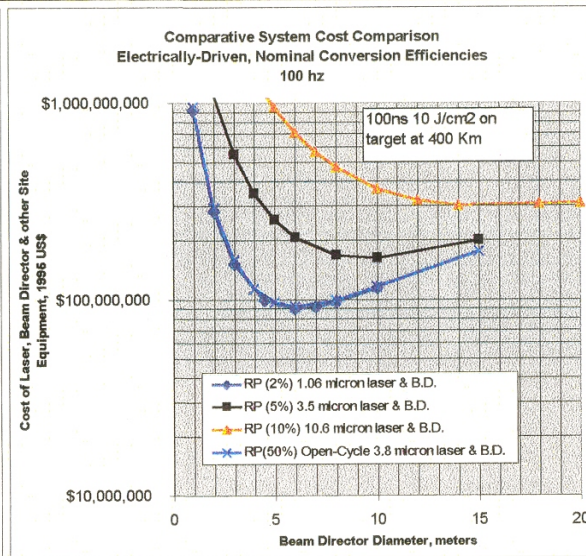
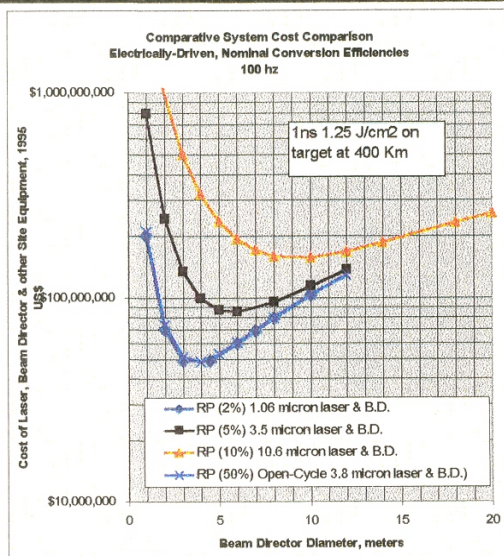
(both at near-optimum fluence at Focal Point)

(both at 100 hz and 500 hz repped operation)

NST

Northeast Science Technology, Inc

Relative Cost Comparison : Effect of Pulse Width on Laser Energy Req't Cost Laser-Plasma Thruster Design



System Cost is strongly influenced by choice of Laser pulse width : On-Target Fluence to achieve plasma Ignition on material surfaces in Vacuum

Wavelength 1 ns 100 ns 1 μs

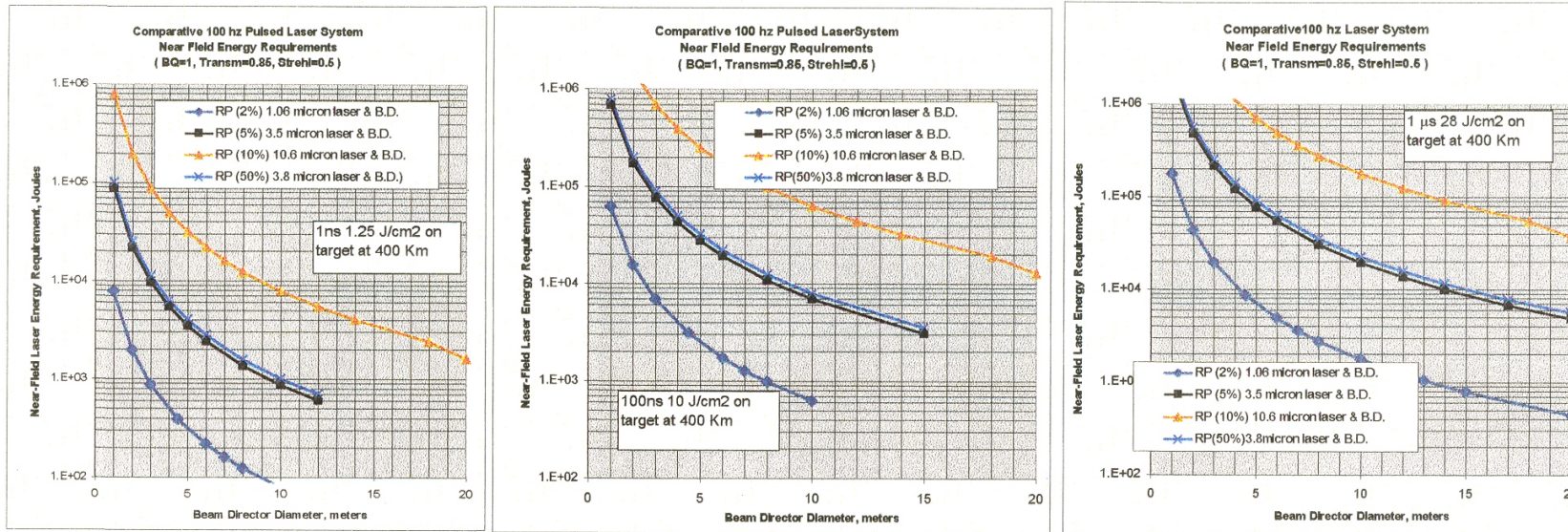
1.06 micron	1.25 J/cm ²	10 J/cm ²	28 J/cm ²
3.5 micron	1.25 J/cm ²	10 J/cm ²	28 J/cm ²
3.8 micron	1.25 J/cm ²	10 J/cm ²	28 J/cm ²
10.6 micron	1.25 J/cm ²	10 J/cm ²	28 J/cm ²

Choose Demonstrated Short-Pulse Laser Technology
to minimize risk, development time & cost

NST

Northeast Science Technology, Inc

Relative Cost Comparison : Effect of Pulse Width on Laser Energy Req't Cost Laser-Plasma Thruster Design



From the above, as wavelength increases, so does focal point spot size--requiring larger optics to bring focal point down in size.

For Plasma Impulse-reaction thrust generation, 1-30 Joule/cm2 is minimum (note pulse-length dependency)--
-2X or 3X is more robust, requiring more raw energy into same focal point.

Note : The above Laser and Beam Director Systems are sized with only a single criteria, that of achieving an irradiance (watt/cm2 or joule/cm2) to achieve near maximum coupling coefficient within the FWHM of the Far Field focal point.

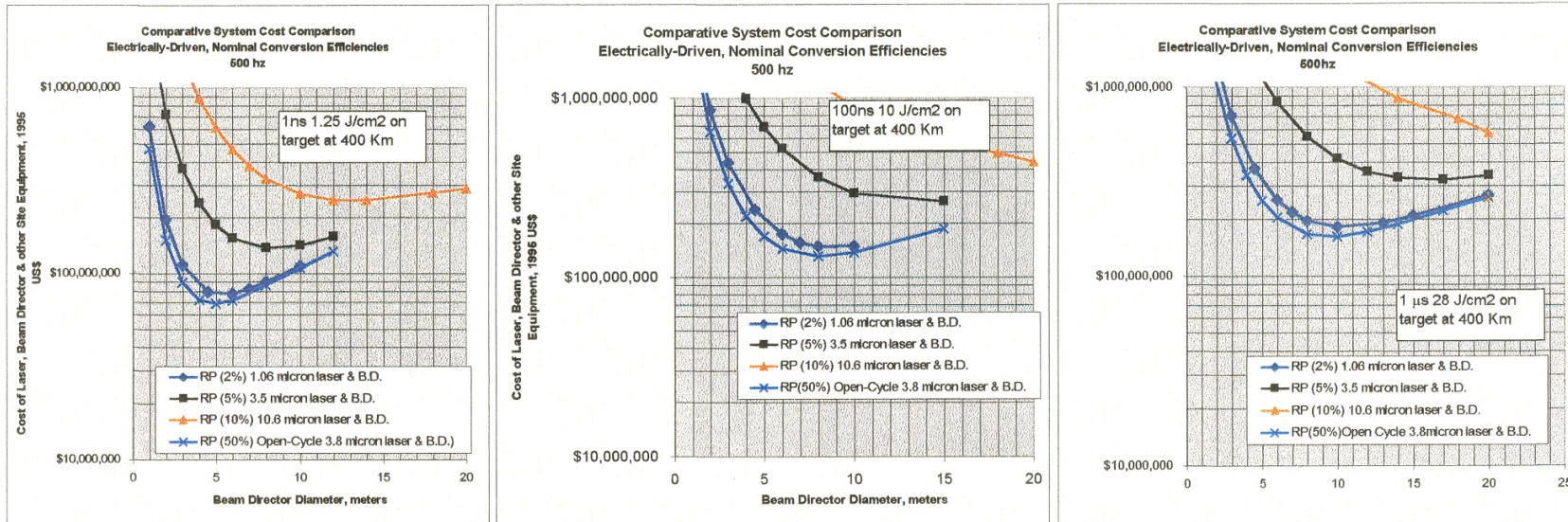
- However :**
- 1 The FWHM spot size in the above MAY NOT BE CONSISTANT with the payload's beam collector
 - 2 The laser power level in the above MAY NOT BE CONSISTANT with the required thrust level

Hence : The details of the payload design are required (FWHM beam size, thrust level required and coupling coefficient), as are the characteristics of the beam path (slant range) and of the beam itself (Strehl ratio including all effects of the phase and amplitude distribution in the outgoing beam, Beam Director jitter and phase errors, beam jitter and spread caused by atmospheric turbulence

NST

Northeast Science Technology, Inc

Relative Cost Comparison : Effect of Pulse Width on Laser Energy Req't Cost Laser-Plasma Thruster Design



System Cost is strongly influenced by choice of Laser pulse width : On-Target Fluence to achieve plasma Ignition on material surfaces in Vacuum

Wavelength	1 ns	100 ns	1 μs
	(2 Amp MOPA)	(MOPA)	(natural)
1.06 micron	1.25 J/cm ²	10 J/cm ²	28 J/cm ²
3.5 micron	1.25 J/cm ²	10 J/cm ²	28 J/cm ²
3.8 micron	1.25 J/cm ²	10 J/cm ²	28 J/cm ²
10.6 micron	1.25 J/cm ²	10 J/cm ²	28 J/cm ²

Choose Demonstrated Short-Pulse Laser Technology
to minimize risk, development time & cost

NST

Northeast Science Technology, Inc

Complete Constraint of System Analysis leads to Long-Wavelength Gas Lasers as choice for R.P.-Laser Launch System

Example-1 : 60 hz/ 100ns R.P. 5 MW Laser device comparison with 50 cm FWHM, peak CC on axis

wavelength lamda cm	Mirror Dia cm	η Elec-to Laser conversion Effic	Beam Director System 1995 US\$ (High Side)	Laser Device C _{ost} (incl 10% margin and ampl multiplier) 1995 US\$	US laser scaling Total Laser & B.D. Station (incl 10% margin)
1.06E-04	87	2%	\$ 4,172,007	\$ 910,248,156	\$ 914,420,163
1.30E-04	105	2%	\$ 5,327,410	\$ 914,747,690	\$ 920,075,100
3.50E-04	285	5%	\$ 19,510,497	\$ 437,940,278	\$ 457,450,775
1.06E-03	865	10%	\$ 82,621,095	\$ 267,656,093	\$ 350,277,187

Example-2 : 60 hz/ 100ns R.P. 5 MW Laser device comparison with 50 cm FWHM, peak CC on axis

wavelength lamda cm	Mirror Dia cm	η Elec-to Laser conversion Effic	Beam Director System 1995 US\$ (High Side)	Laser Device C _{ost} (incl 10% margin and ampl multiplier) 1995 US\$	US laser scaling Total Laser & B.D. Station (incl 10% margin)
1.06E-04	87	2%	\$ 4,172,007	\$ 1,052,812,952	\$ 1,056,984,959
1.30E-04	105	2%	\$ 5,327,410	\$ 1,076,983,740	\$ 1,082,311,150
3.50E-04	285	5%	\$ 19,510,497	\$ 507,224,518	\$ 526,735,015
1.06E-03	865	10%	\$ 82,621,095	\$ 303,769,250	\$ 386,390,344

Observations :

- 1 Solid State Laser technology appears too costly (beam director savings more-than-offset by laser device costs)
- 2 Pulsed Coil technology appears too costly (beam director savings more-than-offset by laser device costs)
- 3 CO Overtone technology appears most inexpensive, but consumables will eat up savings
- 4 RP CO₂ Laser technology appears least expensive option

NST

Northeast Science Technology, Inc

Complete Constraint of System Analysis
leads to Inexpensive CO2 GDL Gas Lasers
as choice
for CW-Laser Launch System

Example : CW 5 MW Laser device comparison with 50 cm FWHM, peak CC on axis

wavelength lamda cm	Mirror Dia meters	η Elec-to Laser Conversion Effic	Total Laser Device C _{tot} (incl 10% margin) 1995 US\$	Beam Director System 1995 US\$ (High Side) 1995 US\$	Total Laser & B.D. Station (incl 10% margin) 1995 US\$
1.30E-04	1.05	ABL COIL technology	\$ 170,622,633	\$ 5,327,410	\$ 175,950,043 US technology
3.50E-04	2.9	11%	\$ 163,730,508	\$ 19,956,639	\$ 183,687,147 US technology
1.06E-03	8.5	10%	\$ 172,622,856	\$ 80,763,403	\$ 253,386,258 US technology
1.06E-03	8.5	20%	\$ 156,457,041	\$ 80,763,403	\$ 237,220,444 US technology
1.06E-03	8.5	Russian GDL	\$ 45,875,249	\$ 80,763,403	\$ 126,638,652 Russian GDL

Observations :

- 1 Coil technology appears a strong contender (USAF program underway for ABL)
- 2 CO Overtone technology appears a strong contender (unproven at high powers)
- 3 Russian CO2 GDL technology is so cheap that beam director dominates cost
(even a factor of 2 cost increase makes it a choice)

Section D--

High-Altitude Boost and All Vacuum Environments

Absolutely require bringing beam to focal point to fill Beam Collection Optics

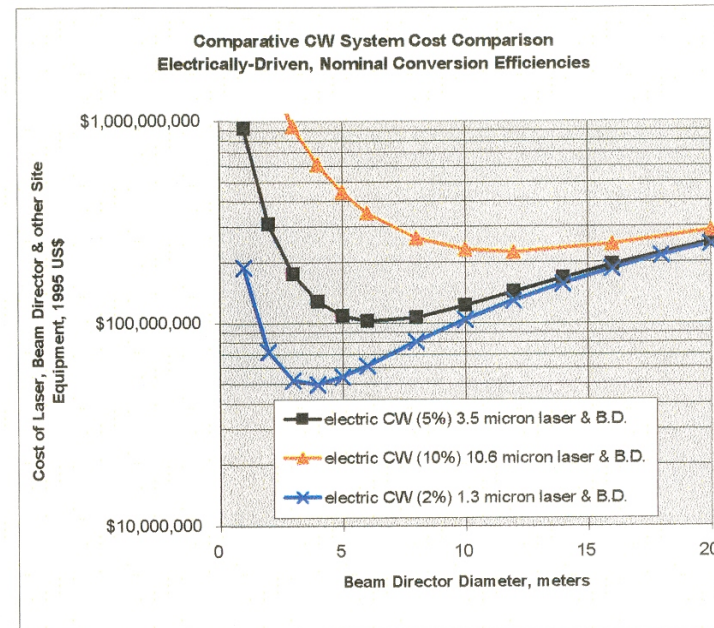
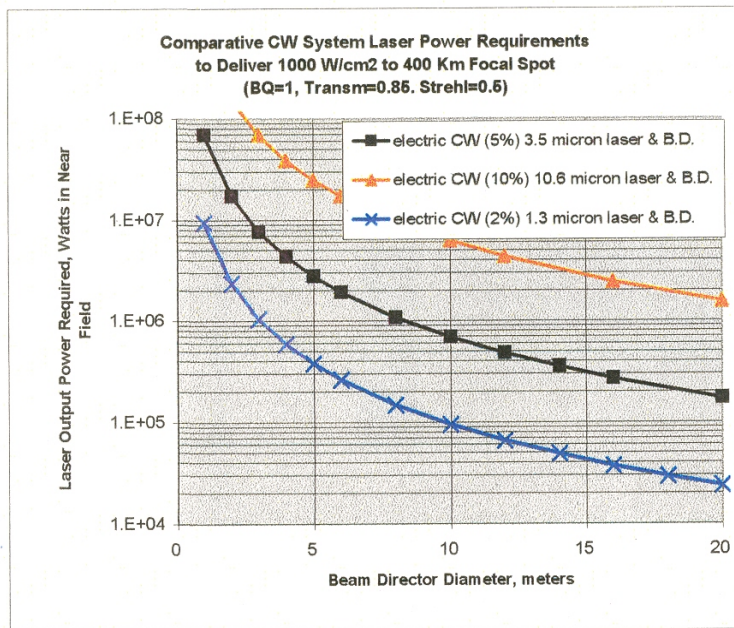
Analyzed in this section : CW Gas Lasers & Beam Directors

Can use only one possible thrust-generation mechanism-

Straight Ablation

(at near-optimum irradiance at Focal Point --used 1000 w/cm²)

(both U.S Electric Discharge and Russian GDL technology)



- 1 From the above, as wavelength increases, so does focal point spot size--requiring larger optics to bring focal point down in size.
- 2 For straight ablation-reaction thrust generation, 1000 w/cm² is minimum--
-2000 or 3000 w/cm² is more robust, requiring more raw power into same focal point.
- 3 **Note :** The above Laser and Beam Director Systems are sized with only a single criteria, that of achieving an irradiance (watt/cm² or joule/cm²) to achieve near maximum coupling coefficient within the FWHM of the Far Field focal point.

However : 1 The FWHM spot size in the above MAY NOT BE CONSISTANT with the payload's beam collector

2 The laser power level in the above MAY NOT BE CONSISTANT with the required thrust level

Hence : The details of the payload design are required (FWHM beam size, thrust level required and coupling coefficient), as are the characteristics of the beam path (slant range) and of the beam itself (Strehl ratio including all effects of the phase and amplitude distribution in the outgoing beam, Beam Director jitter and phase errors, beam jitter and spread caused by atmospheric turbulence

Section E--

Full analysis using four criteria for a system :

- 1 fix collector optics diameter on payload : 50 cm diameter
- 2 fill collector optics on payload at irradiance for max Coupling Coefficient:
CW beams : 1000 w / cm²
RP beams : 10 - 30 J / cm², depending on pulse duration
- 3 fix laser power 5 Megawatt out of laser
- 4 fix slant range to payload : 400 Km
(High-Altitude Boost
and All Vacuum Environments)

Absolutely require bringing beam to focal point to fill Beam Collection Optics

Anayzed in this section :

Repped-Pulse Solid-State Laser	(1.06 microns)
Repped-Pulse Gas Lasers	(1.3, 3.5, 3.8, 10.6 microns)
CW Gas Lasers	(1.3, 3.5, 3.8, US & Russian 10.6 microns)
Beam Directors	(Upper Cost Bound used)

Section F--

Conclusions

- 1 Reasonable choices of payload mass (5 - 50 lb.) and reasonable coupling coefficients (20 - 40) result in reasonable levels of required minimum laser power levels (200 kW - 5 Mw)
- 2 A number of propagation windows in the atmosphere allow consideration of five laser technology options (solid state, Iodine, Carbon Monoxide, Deuterium Fluoride & Carbon Dioxide) which can easily produce these levels of average power.
- 3 Constraints must be set on the laser system to produce self-consistent overall system designs:
 - a- The beam delivered to the payload must always match to its collection optics
 - b- The irradiance delivered to the payload must be above the threshold for efficient thrust production with high coupling coefficient
 - c- The minimum power required at the thruster is this average irradiance times the thruster's collection optics times a factor 2.7 for optimal matching between beam and collection optic when the thruster is far enough from the Beam Director to require operation at the focal plane
 - d- The additional power required from the laser is sized by the mid-altitude, high-altitude and insertion phases of boost because of atmospheric transmission losses, inherent beam Strehl Ratio losses, beam director jitter and atmospheric turbulence (blur and jitter)
 - e- The beam director is sized by the mid-altitude, high-altitude and insertion phases of boost
——the low-altitude segment of boost phase requires it merely fill the thruster's collection optic
- 4 Under these constraints, the laser and beam director system designed for the last phases of boost EASILY performs the low-altitude boost function
- 5 Under these constraints, the projected very high costs of solid-state lasers are NOT compensated for by reduced beam director sizes and costs. Rather, the costing analysis performed under this brief study indicates that longer wavelength lasers (1.3 micron, 3.5 - 3.8 micron, and 10 - 11 micron) lasers are far more cost effective.
- 6 For repetitive-pulse lasers, the CO overtone and standard CO2 laser are closed-cycle lasers which appear as feasible choices for the laser-propulsion function.
- 7 For CW lasers, the very inexpensive CO2 GDL technology appears as a surprisingly attractive economic choice for a system, even though its beam director is so large. The USAF COIL technology is also an attractive option, since its technology will be available in 1-2 years and beam directors with the proper characteristics already exist.

Appendix E

Conceptual Design of a 100 kW TEA CO₂ Laser with Spark Preionization

by

**John A. Nilson
John A. Nilson & Associates
1778 Gilbert Ave.
Ottawa, ON
Canada K2C 1A4**

**Final Report
20 Aug 1999**

Appendix E

TABLE OF CONTENTS

Section	Page
1. INTRODUCTION	1
2. LASER DESIGN	1
2.1 Laser Configuration	1
2.2. Optical specification	2
2.3 Protection and monitoring	4
2.4 Design Spreadsheet.	4
3. PREIONIZA TION	4
3.1 Ultraviolet (UV) Preionization with an Array of Sparks	4
3.2 Barrier discharge	5
3.3 Electron beam	6
3.4 Radio frequency discharge	6
4. ELECTRODES	6
5. OPTICAL CAVITY DESIGN	6
5.1 Cavity Design	6
5.2 Front optic mounting options	7
5.3 Rear optic	7
5.4 Optical damage to the output window	8
5.5 Space Frame	8
5.6 Clear Aperture	8
5.7 Rotating beam combining mirror	9
6. LASER AND LIGHT CRAFT INTERACTION	9
6.1 Optimum optical pulse shape for Lightcraft propulsion	9

Appendix E

6.2	Optical pulse shapes	9
6.3	Optical feedback between the lightcraft and the laser.	10
6.4	Lightcraft interactions in the near and far fields	10
7.	LASER GAS	11
8.	VESSEL	11
9.	ELECTRICAL PULSER	11
10.	GAS FLOW AND ACOUSTIC DAMPING	12
11.	DESIGN EVALUATION TEST BEDS	13
11.1	Low pulse rate laser module test bed	13
11.2	High pulse rate switch and capacitor test bed	14
11.3	Preionization test bed	14
11.4	Flow test bed	14
12.	THOUGHTS FOR A MEGA WATT SYSTEM	14
13.	OTHER POSSIBLE ASSISTANCE	14
14.	CONCLUSIONS	14
	REFERENCES	15
	APPENDIX A - Calculations for a 50 kW Laser Module for the Conceptual Design of a 100 kW CO ₂ Laser with Spark Preionization	A-I
	APPENDIX B - Summary of Discussion on the Lightcraft Project with Russian Scientist Professor Victor Apollonov	B-1

Appendix E

GLOSSARY

ASE	amplified stimulated emission
C	Equivalent Capacitor carbon
CO ₂	dioxide
D	output aperture
diffraction limit	the smallest beam divergence possible, which is limited by diffraction
far-field	far from the laser where the beam intensity profile remains constant
FFCL	far-field central lobe
FWHM	full width at half maximum
g ₀	small signal gain
L	equivalent Inductance
L _g	length of the gain medium
Lightcraft	proposed space module, see reference 1
MOPA	master oscillator and power amplifier combination
near-field	close to the laser where the beam intensity profile is changing
R _c	Equivalent critically damped resistance of the discharge
R _t	threshold reflectivity for lasing
SDI	Strategic Defense Initiative
UV	ultraviolet (preionization)
TEA	transversely excited atmospheric
λ	the laser wavelength = 10.6 μm

Appendix E

1. INTRODUCTION

This study was performed by J.A. Nilson & Associates (JAN) for the Air Force Research Laboratory's (AFRL) Propulsion Sciences and Advanced Concepts Division. The laser is to be used for the evaluation of the propulsion of satellites into space using the Lightcraft concept¹. The evaluation requires a laser delivering microsecond pulses at a nominal 200 Hz pulse rate to deliver 100 kW average power. This power has to be in the far-field central lobe of a diffraction limited beam to be useful over the large distances involved. The following conceptual design study is based on transversely excited atmospheric (TEA), carbon dioxide (CO₂) laser technology. Several optical configurations and methods of preionization for the discharge are considered. Spreadsheet calculations for particular designs are given in Appendix A.

In the past 25 years, large laser systems of the appropriate energy capability were designed in support of laser fusion, Strategic Defense Initiative (SDI) and other military and scientific programs. As well, there are many examples of lower power TEA lasers operating at high repetition rates. The challenge is to produce a reliable laser combining high energy, high peak power, and high repetition rate, while producing a good quality low divergence beam.

2. LASER DESIGN

The following design is for a 100 kW TEA CO₂ laser to operate at a nominal 200 Hz pulse rate with a microsecond pulse length. It generates a beam of which the far-field central lobe is close to the diffraction limit. When the Lightcraft is in the near-field of the laser beam, it will receive 150 kW or more power.

2.1 Laser Configuration

To stay within reasonable extrapolations from existing laser designs, it is recommended that two completely independent 50 kW laser modules be made and configured in one or more of the four options outlined below. The optimal configuration used will depend on which is found to be best for Lightcraft propulsion, since the average power difference between the configurations is not expected to be large. This evaluation would also provide useful design information for extending the technology to a 1 MW laser and beyond. Any of the oscillators described below could also be operated as a regenerative oscillator, generating nanosecond pulses (see Section 6.2 c).

- 1) Two laser modules are mounted optically in series, in a master oscillator power amplifier (MOPA) configuration. The oscillator module would have an optical cavity in an unstable resonator configuration. The amplifier module would have tilted anti-reflection windows to avoid reflecting energy into the oscillator. The pulse shape to be modified by controlling the relative firing of the oscillator and amplifier modules to allow the preferential amplification of the initial spike or the tail (see Section 2.2 note I).
- 2) Two laser modules can be mounted optically in series and pulsed synchronously in a single unstable resonator oscillator cavity. The unstable resonator magnification would be higher than the above.

Appendix E

- 3) Two laser modules can be mounted optically in series but with an unstable resonator magnification as in option 1, so that each module can be alternately pulsed. This will provide half the energy at double the repetition rate of the above configurations.
- 4) The beams from two alternately pulsed laser modules are fed into a rotating beam combining mirror. This produces a beam of half the energy and double the repetition rate of the MOP A.

A comparison of the laser configuration options.

- 1) The MOP A configuration has the most possibilities for pulse variation, but as the unstable resonator magnification is lower than option 2, there will be a smaller fraction of energy in the far-field central lobe of the beam. There will likely be more possibilities for optical feedback problems (see Section 6.4) than the other options because the amplifier module will be at full gain before the beam from the oscillator saturates it.
- 2) The two module synchronously pulsed oscillator configuration, should produce more energy than the MOP A, because oscillators are more efficient in extracting energy from the active medium than amplifiers, but may have less peak power because to the timing possibilities of the MOP A. It will have fewer problems with optical feed back problems than the MOP A, but not as low as options 3 and 4 since the magnification is higher.
- 3) The configuration of single optical cavity built around two alternately firing modules would, like option 4, have lower feedback than options 1 and 2. However, the advantage of not requiring a rotating mirror may be outweighed by the possibility of the gas in the non-pulsing unit causing optical disturbance for the lasing module thus requiring a higher gas flow. It would also have double the average power optical flux on the laser optics as option 4.
- 4) This option is the simplest from a laser viewpoint, but does require two sets of laser optics and a rotating beam combining optic. The power on the laser optics is half that of options 1 and 2, and the feedback problem is also that of a single laser module. It would be a useful prototype for making a megawatt power laser system by the combination of beams using a rotating mirror.

2.2. Optical specification

Table 1 gives a suggested optical specification for the far-field central lobe laser beam based on design #2 of Appendix A.

--..

Appendix E

Table 1. Optical Output Specification for a 100 kW TEA CO₂ Laser

Average Power	100 kW	
Pulsing Mode	Synchronous	Alternating
Pulse Rate	222 Hz	444 Hz
Energy Per Pulse	450J	225 J
Pulse to Pulse Variation	+/- 10 %, peak to peak	
Nominal Pulse Length (1)	0.5 to 1.5 μ s	
Operating Burst Length	5 minutes	
Time Between Bursts	60 minutes	
Beam Size (2)	15 cm, square	
FWHM Beam Divergence (3)	170 μ R, or 1.2 X diffraction limit	
Beam Pointing Accuracy	+/- 16 μ R, or +/- 0.1 X FWHM Beam Angle	
Pulses between maintenance (4)	6 megapulses	

Notes:

- 1) A typical TEA laser with a microsecond pulse ($CO_2/N_2 = 3/1$) and a 3 X magnification unstable resonator has an initial spike with energy typically one-third to one half of the total, and a FWHM of 50 to 60 ns. Following this, the energy then falls close to zero and is followed by a tail that rises again in 100 to 200 ns to a low shoulder that then decays exponentially with a time constant less than one microsecond. This makes it difficult to specify pulse length in a single number. It is suggested that the overall pulse length be measured from the time when the power initially rises above the half height of the shoulder of the tail to when it again falls below that value.
- 2) If the laser output is rectangular it is possible to reshape it using cylindrical optics in a one dimensional beam expander.
- 3) The far-field beam from a 2 X magnification unstable resonator is similar to the Airy diffraction pattern from a 50 % centrally obscured aperture. The beam pattern consists of a central lobe surrounded by concentric rings, and for this application the primary interest is energy and divergence of the central lobe. The central lobe beam divergence is near the diffraction limit, and it typically contains roughly one-half to two-thirds the total energy. The concentric rings have relatively low intensity compared to the central lobe and are not expected to contribute to the Lightcraft propulsion in the far-field. The beam from an unstable resonator beam in the far-field has a full width at half maximum (FWHM) beam divergence of $2/\lambda d$ where λ is the laser wavelength (10.6 micron) and d is the beam output diameter (for simplicity use the electrode spacing). For example, if $d = 150$ mm and $\lambda = 10.6$ μ m the diffraction limited FWHM beam divergence is 141 μ R.
- 4) Maintenance is defined as any planned repair or replacement needed, such as changing spark gaps or optics, which could require opening the laser head or pulser tank.

Appendix E

2.3 Protection and monitoring

The laser control systems provide protection and monitoring for the benefit of the personnel, the Lightcraft, and the laser itself. Some suggestions follow.

- 1) The use of warnings and interlocks would limit access to the high voltage and beam area to qualified personnel.
 - a) Restart after Missed Pulse Group: It may be useful for the control to shut down and try again after a set time (i.e., 1/10 second, or 20 missed pulses) to avoid having to abort the Lightcraft launch.
 - b) Charge Voltage Low at Fire: This can be used to monitor the power supply charging rate, check for shorts and flash-over, and to stop efforts to operate above the set pulse rate.
 - a) Maximum Pulse Rate: The allowable maximum pulse rate should be set in hardware (i.e., 10 Hz above normal program rate) to protect the system.
- 2) The beam pulse energy, and power, as well as the optical beam quality should be continuously monitored and logged to perform the following.
 - a) Lightcraft Performance Analysis: This data can be directly related to the Lightcraft performance.
 - b) Power Programming: Within the stability region of the laser, the pulse energy and pulse rate can be adjusted to maintain a pre-programmed power profile.

2.4 Design Spreadsheet.

The design spreadsheet "50 kW Laser Module for Lightcraft Demonstration Laser - Four Conceptual Designs" lists the laser module design parameters. Two modules would be combined to deliver the required power, as discussed in Section 2.1.

3. PREIONIZATION

A self-sustained discharge in a TEA CO₂ laser is obtained by preionizing the gas before the main current pulse is applied to the laser electrodes. Four of these methods are discussed below.

3.1 Ultraviolet (UV) Preionization with an Array of Sparks

- 1) Method: An Array of Sparks close to the main discharge volume is pulsed a microsecond or so before the discharge voltage is applied. This is done to create a low density of electrons in the main discharge volume. In large aperture low repetition rate lasers³ an array of sparks in a series/parallel arrangement (flash board) is used to create the UV. This is mounted behind a screen electrode and driven with a single capacitor and triggered switch. The concept of mounting an array of sparks on the upstream and downstream sides of the was considered. This was abandoned because it was not practical to get the sparks sufficiently close to the main discharge volume.

Appendix E

- 2) Typical mechanical configuration: The rows of sparks are separated by 1.5 cm, and the individual sparks are also separated by 1.5 cm. For low pulse rate lasers, the individual electrodes for these sparks and the return current path running on a line underneath are etched from a dielectric printed circuit board. This is not expected to be satisfactory for this laser because the high pulse rates required will dissipate high powers in the preionization structure. This could result in both overheating and a short lifetime. Therefore, an alternative method is provided below.
- 3) Suggested mechanical configuration: In small high pulse rate lasers good operation and lifetime is achieved when the preionization occurs over ceramic spacers, or "trackers" (to ensure reliable sparking). These are mounted in the gas flow for cooling. The concept of ceramic trackers can be combined with the flash board concept by making an array of water-cooled "flash rods" from ceramic tubes. The individual metallic electrodes should be a millimeter or so thick to have long life, and could be bonded to metalized sections on the tubes, or mechanically fitted to grooves machined in the ceramic tubes. The array could be cooled in either of the following ways:
 - a) the ceramic tubes can be internally metalized to serve as the ground return and the watercooling channel,
 - b) the ceramic tubes could be closely fitted over water-cooled electrically grounded metal.
- 4) Electrical circuit: For discharge lengths up to one meter, the flash board is usually powered by a single capacitor. However due to the long length of the discharge volume, it may be better to use two sections of flash rods, each with an energy storage capacitor. Both capacitors could be driven with one switch.
- 5) Testing: It is suggested that the basic flash rod structure be evaluated at low pulse rates at full energy. Following this it should be operated in a high pulse rate test bed to obtain operating life data.

3.2 Barrier discharge

Similar to UV preionization this also uses an array of spark discharges mounted behind a screen electrode that is the cathode for the discharge. However, in this method this array of sparks is used as one electrode to form a plasma by applying an electrical field between it and the screen electrode. This plasma is then used as a source of electrons which are drifted from the plasma into the main interelectrode space. This is done by an electric field applied between the screen cathode and anode at a voltage below the laser gas break-down. The field is applied for a time long enough (a few microseconds) to allow the electrons to drift completely across the inter-electrode space. This fills the space with drifted electrons rather than creating the electrons by the ionization of impurities with UV preionization as in Sec. 3.1. Although a little more complex than UV preionization, it may result in a more robust system because the electrons are made in a more direct process. The resulting space charge also shields the electrodes and allows the creation of a uniform discharge even with poorly profiled electrodes. This is not possible with UV preionization since the non-uniform field at the electrodes leads to arc formation. Several systems have been made^{4,5} with the most recent work being done in Russia⁶ (see Appendix B). This appears to be a promising alternative, and it is suggested that a low pulse rate prototype be made to develop the mechanical structure and the electrical circuit. If sufficiently promising, it should then be operated in a full power test bed to obtain reliability data. In the design spreadsheet in Appendix A it is assumed that the pulse energy to drive the flash rods would be similar to UV preionization.

Appendix E

3.3 Electron beam

In this design an electron gun, similar to that used for long pulse (typically tens of microseconds) "sustained" discharges, is used a source of electrons to fill the inter-electrode space. However, for a self-sustained discharge it is only operated long enough (a microsecond or so) to provide the required background of electrons for preionization. Although more complex, since it is required to only operate at one-tenth the duty cycle of a sustained laser, it could prove to be very reliable, justifying the complexity. Because the author has no experience with this technology it will not be discussed further.

3.4 Radio frequency discharge

This has been used recently with an excimer laser⁷ and looks interesting. There is very little detail in this paper, and it is not clear how well it would work with a large volume TEA CO₂ laser. However, it does have the advantage of being much cleaner (generating less dust) than the UV preionization and barrier discharge. More research is required to determine if it is worth considering for the 100 kW laser.

4. ELECTRODES

To accommodate any of the possible preionization schemes, the high voltage electrode should have a profile to operate with a flat ground electrode. This profile can be developed when the overall size and configuration of the laser are determined. The surface of the electrode should have low optical reflectivity or fine surface roughness to be optically scattering to avoid amplified stimulated emission (ASE) or non-controlled lasing. ASE can be a problem with high magnification unstable resonators and amplifiers. A plasma sprayed surface of nickel has been found to work well and also have long life. These electrodes should be evaluated in a low-pulse-rate test bed.

5. OPTICAL CAVITY DESIGN

With careful optical cavity design, the far-field central lobe energy of large, short pulse, single shot lasers is typically close to calculated values. The challenges for this laser design relate to high pulse rates and high average power, in particular, the high optical flux on the optical elements.

5.1 Cavity Design

Points to consider in the design of the optical cavity are listed below.

- a) It is assumed that a "standard" positive branch unstable resonator will be used.
- b) For a single 50 kW unit with a cavity gain of 4 the magnification of the unstable resonator can be 2 to 3. For two 50 kW units in the same optical cavity, there is no benefit in going beyond a magnification of 4 or 5 since the loss due to the obscuration becomes small. It is also important that the optical feedback be greater than that from spurious reflections.
- c) All flat surfaces within the laser that could possibly allow ASE should be covered with a rough optically absorbing surface, such as raw woven fiber glass, to reduce spurious reflections.

Appendix E

5.2 Front optic mounting options

Four options for the front optic design are given below, followed by recommendations.

Options:

- 1) The front optic is can be mounted on a stalk on the output window. This appears to be the only way to avoid shadows (and resulting diffraction patterns in the beam) from mounting hardware while having symmetric edge diffraction. This diffraction helps to detennine the optical axis and gives good pointing stability. The output window can have an anti-reflection coating and be mounted at a small angle (i.e., 5 mR) to the laser axis to avoid feedback. If the absorption of the front optic is sufficiently low so that it does not require water cooling, then this is a very simple method. It would be possible to cool the front optic using a heat pipe, in the shadow of the front optic. This could carry the heat through the output window to be cooled with an air flow. However, if it must be water cooled, one of the following methods should be used.
- 2) The front optic can be placed before the output window and mounted it on a "spider" (similar to large telescopes) which can also carry cooling water. This is a well proven design, the front optic and window are separate simple elements, and the increase in diffraction losses should be acceptable.
- 3) The output beam can be coupled out of the cavity by a 45 degree mirror placed before the front mirror. The shape of the central hole determines the size and shape of the beam that is returned back into the cavity. The output window is mounted at 90 degrees to the optic axis. This method has not been used by this author because of the concern that the skimming mirror does not give the same symmetric diffraction feedback as a free-standing mirror. This symmetric diffraction also assists in determining the optical axis. Experience should be sought from others who have used this method. Here water cooling should be no problem.
- 4) A more challenging option is to create a front optic on a output window that has a convex radius on the inside appropriate for the unstable resonator magnification. This is done by depositing a partially transparent dielectric coating (e.g. 50 % reflectivity) in the center on the inside of the mirror. The central partial reflector is surrounded by an antireflection coating. This uses only a single optic for the front optic and window. The inside surface of the window has a radius of curvature to make a window having zero optical power. Because there is some output through the partially transparent front mirror, the magnification of the unstable resonator is reduced to give the required optical feedback. The center of the beam has a significant intensity so there is less diffraction loss than from a totally reflective mirror. The intensity variations in the near-field are lower, and the fraction of the energy in the far field central lobe is higher. It would be possible to surface cool this optic with high gas flow between it and a second window. This option would create the best beam, but the optics would be expensive and be prone to damage particularly in the antireflection-dielectric interface.

Recommendations: Option 2 is chosen as the best alternative because it is a well proven design, and is inexpensive, simple and robust. The small diffraction losses in the far-field from the mounting spider can be made up with an increase in total output power.

5.3 Rear optic

This can be a diamond turned concave metal mirror that is water cooled and carefully mounted to avoid distortion. To minimize loss it can be coated with gold and a dielectric overlay. It is very useful to have a small (1 mm) central hole in the mirror. This can be used to inject a HeNe alignment beam into the

Appendix E

optical cavity to assist in aligning the cavity optics and help to determine the beam path. The hole can also be used to inject a mode-locking beam or extract a sample of the pulse.

5.4 Optical damage to the output window

Optical damage can be separated into damage due to high average power, and high energy density.

- 1) Damage due to high average power loading is a consequence of absorption in the optic and coatings. This can cause high temperature gradients resulting in optical distortion and optic breakage. The total power on the output window loading for two lasers in series for design #2 of Appendix A is 150 kW. This is far above a commonly accepted limit of 10 kW for edge cooled optics. There are several possible solutions.
 - a) The output window can be face cooled by rapidly flowing cool gas over the external surface, or for more control, flowing cool gas between two windows.
 - b) A reflective beam expanding telescope can be placed inside the laser chamber after the output coupler and before the output window to reduce the power density of the beam. This would make face cooling of the window easier.
 - c) Large lasers have been built with a gas-dynamic window separating the laser gas and the atmosphere, but the author has no experience with these.
- 2) Design #2 of Appendix A gives an optical energy density of 3 J/cm² for two lasers operating in series. At these energy densities optical damage is severe if the laser gas in contact with the optic is not free of dust. However, the author has experience with small high repetition rate lasers operating at these energy densities where the optics are kept dust free. This has shown that they can operate with insignificant damage for over 1 billion (10⁹) pulses. Therefore, it is recommended that a flow of filtered laser gas is provided to the laser optics.

5.5 Space Frame

A vibration-isolated, stable and rigid space-frame should be used to keep the cavity optics and the resulting beam well aligned. This has to withstand the forces of full vacuum, and alignment should be adjustable and maintainable at fixed pressures from 0.5 to 1 atmosphere, in case sub-atmospheric operation is desired. The length of the optical cavity is used in the design of the unstable resonator optics and is not critical unless the laser is to be actively mode-locked. The angular stability of the cavity is critical. For an optic of diameter $d = 150$ mm, the angular stability should be $17.7 \sim \text{rad}$. This is calculated by assuming the allowable misalignment is $1/4$ of the half-angle-diffraction-limited beam divergence, given by λ/d . The alignment should be adjustable to within $8.8 \sim \text{rad}$ (one-half of the above).

5.6 Clear Aperture

To make the most use efficient use of the laser power, all the beam handling optics must transmit the full laser as defined by the unstable optics. Any obstruction of the beam as it passes through the extra-cavity optics and out the telescope because any obstruction will cause diffraction from the central lobe. For a square output beam from a laser with 15 cm electrode separation, and allowing a margin of 1 cm at the corners, a clear aperture of 23.2 cm is required. External cylindrical optics can be used to square a rectangular beam.

Appendix E

5.7 Rotating beam combining mirror

A rotating mirror is required if a decision is made to combine the outputs of two alternately pulsed lasers into one beam. As discussed in Section 2.1.2, this gives a pulse rate double that of the individual lasers. The mirror must rotate at the pulse rate of the individual laser (i.e., 222 Hz or 13,200 rpm, for a 444 Hz beam output) while maintaining the beam quality and pointing accuracy within the system specification.. The rotating mirror will need to be water cooled, as it will receive the combined 150 kW power from both lasers.

6. LASER AND LIGHTCRAFT INTERACTION

6.1 Optimum optical pulse shape for Lightcraft propulsion

It is not yet clear what the best pulse shape (energy and pulse shape of the initial spike and tail) would be for Lightcraft propulsion. Following are some questions and comments that may assist in determining how to optimize both the laser and Lightcraft.

- a) Does the initial air breakdown provide the majority of the impulse thus favoring a pulse length less than one microsecond?
- b) Can the optimum pulse shape be reached by changes in gas composition within the limits of optical reflectivity of an unstable resonator?
- c) Is plasma heating after the initial breakdown an important factor, making the pulse tail important?
- d) What is the contribution of the tail of the pulse to the heating the Lightcraft shroud?
- e) Would a well-controlled nanosecond pulse train be beneficial? It will be partially self mode-locked by varying degrees pulse to pulse in any case (see 6.2 c)).
- f) The laser design should be versatile enough to help address the above and other questions. This information can then be integrated into possible upgrades future designs.

6.2 Optical pulse shapes

A range of pulse shapes is readily obtainable from a TEA C02 laser with an unstable resonator. Some of these are listed below.

- a) A TEA C02 laser with an unstable resonator normally produces a microsecond pulse as described in Table 1, Note 1
- b) The ratio of energy in the spike relative to the tail can be lowered by a limited degree by reducing the ratio of C02 to N2 from the optimum ratio of 3: 1 for highest energy in the spike. It can be lowered until the unstable resonator no longer has sufficient feedback to be efficient. This ratio will depend upon the overall optical gain of the oscillator and may have to be evaluated experimentally. Note that the discharge stability improves with decreasing ratio of C02 to N2.
- c) The laser pulse can be changed into a reproducible train of nanosecond pulses by using the laser cavity as a regenerative amplifier for an injected nanosecond pulse. There is no loss of pulse energy, and the peak powers of the nanosecond pulses are much higher. This has been suggested by many including Professor Apollonov, (see Appendix B).

Appendix E

6.3 Optical feedback between the Lightcraft and the laser.

The Lightcraft module is likely to exhibit considerable retro-reflectivity because it receives thrust from the laser beam by means of highly reflective optics. These reflections back into the laser can be amplified by passing through the full length of the gain medium to the rear mirror and back to the reflector. This can only occur early in the launch when the optical round-trip time from the laser to the Lightcraft module is such that the laser is still exhibiting gain. For example, if the laser gain is high for two microseconds, which may be the case for an amplifier, the interaction can occur up to a laser to Lightcraft separation distance of 300 m. Such optical feedback can modify the laser modes and cause lasing in spurious directions.

For an amplifier module, the single pass gain for light passing through an unsaturated gain medium of length L_g , is $g_0 L_g$, with an amplification factor of $\exp(g_0 L_g)$, where g_0 is the small signal gain. Laser amplifiers are normally stable and remain under optical control for gains below a threshold given by $g_0 L_g = 5$. For the single module designs in Appendix A, the single pass gain $g_0 L_g = 4$, which indicates that a single amplifier stage should normally stay under control. The threshold level of reflectivity where feedback may cause problems can be calculated by setting the product of the double pass amplification times the reflectivity equal to one. This gives the threshold reflectivity

$$R_t = 1/\exp(2 g_0 L_g). \quad (1)$$

For $g_0 L_g = 4$, $R_t = 3.36 \times 10^{-4}$. This is a very low level of reflectivity, and the reflectivity of the Lightcraft is very likely to be above this value, particularly when a breakdown plasma is formed.

To keep an oscillator module under control, the reflectivity of the Lightcraft module should be lower than the reflectivity of the front optic of the unstable resonator. For an unstable resonator with magnification set at $M = 5$, the effective reflectivity is only 2.5%. This is also a low value.

Therefore it is expected that in the first few hundred meters that the laser beam may be modified by feedback from the Lightcraft module. It is possible that the cavity that includes the Lightcraft as a mirror could concentrate the energy in unexpected locations causing damage and/or unexpected Lightcraft operation. It would be very useful to have continuous monitoring of the laser output beam quality throughout the launch to evaluate the effect of Lightcraft feedback. This could be done by using a beam sampling mirror placed near the laser output.

All the above interactions occur in the near field of the laser (see Section 6.4). Here the Lightcraft module is subject to the whole laser output, which may be 50 % more than the far field power. It would be possible to reduce the effect of these problems, by limiting the laser power (possibly even turning off one of the laser modules) until the Lightcraft is sufficiently far away.

6.4 Lightcraft interactions in the near and far fields

The distance to the far field (where the beam no longer changes in intensity profile) is usually given as the distance where the beam diameter becomes twice the output aperture, d . For a diffraction limited beam this distance is given by $d^2/t.$, where $t.$ is the wavelength. For a 20 cm diameter beam $d^2/\lambda = 4$ km. If a variable-focus, beam-expanding telescope is used, the problem becomes more complex, and these simple concepts are no longer valid. Computer modeling and experimentation will be required to determine the beam intensity profile at the Lightcraft module.

Appendix E

The Lightcraft will thus spend considerable time in the near field and will be subject to rather large intensity variations across the beam. Close to the output of an unstable resonator as the central hole in the unstable resonator fills in, a very intense diffraction spot (spot of Arago) appears on axis. This can be a serious problem for optics in the beam path (it can drill holes in optics) and possibly for the Lightcraft module. A model of a diffraction limited beam with an obscured aperture, representing the unstable resonator should be made to determine the seriousness of this problem.

7. LASER GAS

The laser gas can be mixed using bottled gases of helium, carbon dioxide, nitrogen and carbon monoxide, or it can be obtained premixed in bottles. It is assumed that the laser will operate at atmospheric pressure, although the laser operation may be more stable at lower pressures. The following addresses some of the laser gas issues.

- 1) Composition: To obtain reliable operation with microsecond pulses, the ratio of $\text{CO}_2/(\text{N}_2 + \text{CO})$ should be roughly 3:1. The molecular content ($\text{CO}_2 + \text{N}_2 + \text{CO}$) should be roughly 30 %, with the remainder He.
- 2) Gas Life: Using the relatively high CO_2 concentrations required for a microsecond optical pulse causes O_2 buildup. Depending on the overall stability of the system, this can quickly lead to short term failure due to arcing and long term failure due to electrode oxidation. The O_2 can be maintained within stability limits by recirculating laser gas through a catalytic converter⁹. This can be assisted by the addition of CO (e.g., 4%). The amount of flow may depend on the preionization scheme used. This rate can be determined in the low pulse rate test bed.
- 3) Additives: Although low ionization additives (doping) have been used to provide more stable operation⁶, these should be avoided at high pulse rates because contamination build-up from discharge decomposition products would be expected.

8. VESSEL

It is assumed that an existing laser vessel will be modified for this laser. The following should be considered.

- 1) Vacuum enclosure: It should be possible for it to be pumped to a low pressure for rapid laser gas changes, and also allow the possibility of sub-atmospheric laser operation.
- 2) Preionization port: The design of this opening should be made to evaluate any of the preionization schemes.

9. ELECTRICAL PULSER

The design issues given below consider the matching of the electrical pulser to laser, and not the design of electrical pulser, which is a major task in itself. The basic parameters of the pulser for the laser module are given in the spreadsheet in Appendix A, and depend upon the particular design chosen.

Appendix E

- 1) Inductance: To drive the microsecond self-sustained discharge, a source inductance of $1 \sim$ or less is required. It will be a challenge to maintain this low value while also maintaining insulation at a high voltage approaching 300 kV and also accommodating space for gas flow.
- 2) Preionization: The preionization circuit has to be separately timed to fire (e.g., $2 \mu\text{s}$) before the main discharge. The rise time should be rapid and clean to ensure a uniform discharge is formed, and the energy should have sufficient margin to reliably initiate a discharge. The discharge impedance of a self-sustained discharge once it is formed, is primarily determined by the pulsed voltage, the impedance of the driver, and the gas mix.
- 3) Spark Gaps: The operating parameters for the spark gap switches in the Marx bank are challenging. It is suggested that a single stage of the Marx bank be made to pre-test and evaluate both the capacitor and spark gap designs. This should be operated at full repetition rate into a dummy load having the expected impedance. This evaluation would provide an estimate for the expected operating life of these components to allow scheduling of preventative maintenance, thus reducing the possible failures and gas resulting down-time of the complete system. The results of this development and testing would also provide design information for future Marx bank designs.
- 4) Source impedance: When the source impedance of the electrical pulser matches the discharge, this results in a close-to critically damped wave-form having little or no voltage reversal. This improves the lifetime of the components and reduces the incidence of the laser arcing. This matching can be obtained by adjusting the gas mix and charging voltage. The switching components still must be able to withstand the occasional arc fault, and the control should stop the laser before serious damage occurs.

10. GAS FLOW AND ACOUSTIC DAMPING

The calculations in Appendix A indicate that the required gas flow velocity is well below sonic speed, therefore, conventional blowers can be used. It will also be necessary to have damp the acoustic energy in the discharge pulse in order to achieve an optically uniform gain medium. Two alternative flow systems are considered below.

- 1) Constrained "wind-tunnel" flow: In this design, the gas from the blower and cooler enters a plenum upstream of the laser electrodes. The area is then reduced by a factor of 3 or 4, and a smooth flow transition is made to the electrodes. Attached to the electrodes at the outlet is an expansion diffuser with an initially low, but increasing, angle of expansion. This is to avoid flow separation and provide a smooth flow transition from the electrodes to the low pressure plenum. The gas re-enters the blower and cooler to repeat the circuit. Some issues related to this design are listed below.
 - a) The wall from the nozzle and the diffuser to the high voltage electrode must be made of insulating material.
 - b) The acoustic energy is constrained to a channel that increases relatively slowly up and down stream from the discharge. The acoustic energy is not rapidly attenuated by expansion and has to be damped in the channel close to the source.
- 2) Unconstrained "nozzle flow": In this design the gas from the blower and cooler flows into a plenum and then through a nozzle. This nozzle is not in contact with the electrodes, but is

Appendix E

sufficiently far away to avoid electrical breakdown. The nozzle outlet is similar in size to the electrode gap and provides a smooth flow a few nozzle diameters from the outlet. The flow is only required to be well behaved until it has passed through the discharge volume. There is no outlet diffuser except for the electrode profile. The gas is allowed to freely expand both up and downstream into the laser volume and find its own way back to the cooler and blower for the next pulse. Some design issues are listed below.

- a) In this design there is no physical contact between the flow system and the high voltage electrode. No walls of insulating materials are required, and the flow ducting can be made of metal, making a cleaner design.
- b) The area of the flow channel expands rapidly both up and down stream of the electrodes rapidly attenuating the acoustic intensity. Acoustic damping can be put in low velocity areas of the chamber to avoid reflections.
- c) To the authors knowledge this has not been evaluated in a large high pulse rate system.

11. DESIGN EVALUATION TEST BEDS

Early in the development cycle of the 50 kW laser module it would be very beneficial to use "Test Beds" to prove concepts and determine reliability of the subsystem. These are discussed in more detail below.

11.1 Low pulse rate laser module test bed

This test bed would in the final configuration but with no fast gas flow, and would be used to evaluate all the discharge and optical parameters. Some design considerations are listed below.

- a) Laser chamber: The chamber vessel should withstand pumping to a low pressure to allow sub atmospheric testing and allow quick gas changes. The chamber should accommodate any of the preionization schemes to be evaluated.
- b) Electrical driver: This should have the same electrical parameters as the high repetition rate design, but it can use low pulse rate components. It can be used to verify the electrical high voltage design, and measure inductances, etc.
- c) Preionization schemes: Prototypes should be made of uv, e-beam and barrier discharge preionization configurations, so the discharge stability can be measured to assist in determining the most appropriate scheme for the laser module.
- d) Electrode configuration: The electrode profiles and surface structure can be tested and modified if required before several laser modules are made.
- e) Optical Beam: The output beam can be characterized and the design of optical resonator can be optimized. The optical output specification can be verified by measuring the beam energy, pulse shape, and stability in the central lobe in the far field (at the focus of a mirror). The stability of the beam can be tested in the far field as a function of delay after the pulse to measure the space frame stability. Beam shaping and expansion schemes can also be tested.
- f) Lightcraft impulse: Single shot Impulse measurements can be made on Lightcraft modules to check for optical feedback and the effect of pulse shape on the impulse. This should be done in the near field and as far away as reasonable

Appendix E

11.2 High pulse rate switch and capacitor test bed

This would test and evaluate the critical components of the electrical pulser, in particular the capacitor and spark gap. It would consist of a single stage of the Marx bank operating at full power loading into a dummy load.

11.3 Preionization test bed

This is required to life test the basic components of the preionization schemes at high average power by making a sub-section of preionization configuration and operating it at full pulse rate.

11.4 Flow test bed

The flow test bed can be used to evaluate both nozzle and wind-tunnel flow. The Nozzle Flow configuration will use a subset of the Wind-tunnel flow system. The nozzle can be spaced a sufficient distance from the electrodes to avoid electrical breakdown. Acoustic damping should be applied to low flow regions as required.

12. THOUGHTS FOR A MEGAWATT SYSTEM

After a review of the issues associated with the design of a 100 kW laser, a megawatt laser appears to be a challenging task. If the 100 kW laser is built, it would provide a much better understanding of the issues of scaling it up by ten-times. Assuming a beam pulsing at a few kHz is appropriate for Lightcraft propulsion, the most direct method would appear to be to combine the beams from ten 100 kW lasers by using a rotating mirror.

13. OTHER POSSIBLE ASSISTANCE

During this study an opportunity developed to discuss this project with a well-recognized Russian scientist, Professor Victor Apollonov of the Russian Academy of Sciences. After he discussed the Lightcraft concept with Professor Leik Myrabo at the Lasers '98 conference he traveled to Ottawa Canada where the author met with him. A summary of these discussions is given in Appendix B.

14. CONCLUSIONS

- 1) The most serious problem arising from the conceptual design appears to be the power and energy density loading on the output window, even for the individual 50 kW modules. This may make the series configuration, at twice the flux, unrealistic. Placing a convex mirror after the output coupler and within the laser gas envelope to expand the beam before it reaches the output window would reduce this flux. Building a reliable laser, although challenging, appears to be feasible, providing a solution to high flux on the output window can be found.
- 2) The more challenging components of the laser design should be evaluated as prototypes in (Test Bed's) to reduce the design uncertainty and prove the reliability. This should be done before large expenditures are made to manufacture duplicate parts.

Appendix E

- 3) The efficiency of the interaction with the Lightcraft module is key to the success of this program. A versatile 100 kW laser would allow this, and also obtain operating experience.
- 4) This design was developed assuming existing laser modules that can accommodate a 15 cm electrode gap would be used. If a new laser enclosure were designed, a 20 cm or larger gap would be attractive because of the greater design freedom, and reduced energy density in the discharge and flux on the optics.

REFERENCES

- 1 Leik N. Myrabo et al, Transatmospheric Laser Propulsion (Lightcraft, Technology Demonstrator), Final Technical Report, prepared under Contract no. 2073803 for the Lawrence Livermore National Laboratory and the SDIO Laser Propulsion Program, June 30, 1989, by Rensselaer Polytechnic Institute.
- 2 A.E. Siegman, Appl. Opt. 13, 353, (1974).
- 3 M.C. Richardson et al., Large Aperture CO₂ Laser Discharges, IEEE, J. Quantum Electronics, 1973, QE-9, No.9, p 34; K.O Tan, DJ James and J.A. Nilson, Compact 0.1 TW CO₂ Laser System, Rev Sci Instrum v51 # (6) p. 776, 1980.
- 4 R. Dumachin et al. Augmentation de l'energie et de la puissance par unite de volume d'un laser CO₂ en regime pulse. C.R.Academie de Science (Paris), 1969, v. 269B, No. 18, p 916-917.
- 5 M. John Yoder et al, Surface Discharge Preionized CO₂ Laser Development, Laser's '82
- 6 V. V. Apollonov et al., Small Signal Gain of CO₂ Lasers Pumped by a Volume Discharge, Intl' conf. "Lasers- '87, Lake Tahoe, 1987.
- 7 T. Enami et al, High Spectral Purity and High Durability kHz Excimer Laser. SPIE Vol. 3334 pp1034 - 1039.
- 8 R.F. Haglund et al, IEEE J. Quantum Electron. , vol QE-17, No 9, pp 1799-1808, (1981).
- 9 C. Willis and J .C. Purdon, Catalytic control of the gas chemistry of sealed TEA CO₂ lasers, J. Appl. Phys. vol. 50, p 2539, 1979.

Appendix E

Appendix A

Calculations for a 50 kW Laser Module for the Conceptual Design of a 100 kW CO₂ Laser with Spark Preionization

Two such modules will be used to obtain 100 kW in the far-field central lobe (FFCL) – see Section 2.1.

In the spreadsheet, ":" and underlines indicate input data, and "=" calculated data.

Concept #1 is a conservative design for a 15-cm square beam, #2 is more aggressive, #3 is the same as #2, except for a 15-cm X 20-cm rectangular beam, and #4 is similar to #2 except with a 20 cm square beam.

Conceptual Design for Module	#1	#2	#3	#4
Optical Output				
FFCL Power, W:	<u>50,000</u>	<u>50,000</u>	<u>50,000</u>	<u>50,000</u>
Ratio: Total Beam/FFCL (1):	<u>2</u>	<u>1.5</u>	<u>1.5</u>	<u>1.5</u>
Total Beam Power, W =	100,000	75,000	75,000	75,000
Repetition Rate, Hz (2) =	296	222	167	167
FFCL Energy, J=	169	225	300	300
Total Beam Energy, J=	337	337	450	450
Electrical Power				
Electrical Efficiency of Total Beam Power:	<u>7.5%</u>	<u>7.5%</u>	<u>7.5%</u>	<u>7.5%</u>
Electrical Energy Stored, kJ =	4.50	4.50	6.00	6.00
Pulsed Electrical Power, MW =	1.33	1.00	1.00	1.00
Burst Time, minutes:	<u>5</u>	<u>5</u>	<u>5</u>	<u>5</u>
Burst Interval, minutes:	<u>60</u>	<u>60</u>	<u>60</u>	<u>60</u>
Duty Cycle =	8.3%	8.3%	8.3%	8.3%
Average Electrical Power Input, kW =	11	8	8	8
Beam Characteristics				
Interelectrode Aperture, cm:	<u>15</u>	<u>15</u>	<u>15</u>	<u>20</u>
Flow Direction Aperture. Cm:	<u>15</u>	<u>15</u>	<u>20</u>	<u>20</u>
Output Area, cm ² =	225	225	300	400
FFCL Energy Flux, J/cm ² =	0.75	1.00	1.00	0.75
Total Beam Energy Flux, J/cm ² =	1.50	1.50	1.50	1.13
FFCL Power Flux, W/cm ² =	222	222	167	125
Total Beam Power Flux, W /cm ² =	444	333	250	188
Main Discharge				
Electrical Energy Density, J/I:	<u>133.33</u>	<u>133.33</u>	133.33	100.00
Discharge Length, cm:	<u>150</u>	<u>150</u>	<u>150</u>	<u>150</u>
Discharge Volume, Lg =	33.75	33.75	45.00	60.00

Appendix E

Optical gain and threshold reflectivity

Small Signal Gain, g_0 , m-I (3) =	2.7	2.7	2.7	2.0
Single Pass Gain X Discharge Length =	4.00	4.00	4.00	3.00
Threshold Reflectivity R_t =	3.36E-04	3.36E-04	3.36E-04	2.48E-03

Flow (4)

Flow Clearing Ratio (4):	<u>2.5</u>	<u>2</u>	<u>2</u>	<u>2</u>
Flow overfill (over the discharge length):	<u>1:2</u>	<u>1:1</u>	<u>1:1</u>	<u>1:1</u>
Total Flow, l/s =	30,001	16,500	16,500	22,000
Velocity m/s =	111	67	67	67

Behind Screen uv Preionization (5)

Row Spacing, cm:	<u>1.50</u>	<u>1.50</u>	<u>1.50</u>	<u>1.50</u>
Spark spacing, cm:	<u>1.50</u>	<u>1.50</u>	<u>1.50</u>	<u>1.50</u>
Energy/spark, mJ:	<u>170.00</u>	150.00	150.00	150.00
Charge Voltage, kV:	<u>32</u>	<u>32</u>	<u>32</u>	<u>32</u>

Preionization requirements Per module

Aperture V (Gap), cm =	15	15	15	20
# Rows (6) =	11	11	14	14
# Sparks in row (6) =	102	102	102	102
# Sparks =	1122	1122	1428	1428
Total Preionization Energy, J =	191	168	214	214
Capacitor size, mF A90=	0.37	0.33	0.42	0.42
Preionization power, kW =	56.5	37.4	35.7	35.7

Pulsed Power

Electric Field, kV/cm:	<u>17.00</u>	<u>17.00</u>	<u>17.00</u>	<u>17.00</u>
Pulse Voltage, kV =	255.00	255.00	255.00	340.00
Equivalent Capacitor (C), μ F =	0.138	0.138	0.185	0.104
Number of Stages:	<u>3</u>	<u>3</u>	<u>3</u>	<u>4</u>
Charge Voltage, kV =	85.00	85.00	85.00	85.00
Stage Capacitor, μ F =	0.046	0.046	0.062	0.026
Equivalent Inductance L, μ H:	<u>0.80</u>	<u>0.80</u>	<u>0.80</u>	<u>0.80</u>
One Half Period, μ s (7) =	1.05	1.05	1.21	0.91
Equivalent Resistance R_c , Ohm (8) =	4.81	4.81	4.16	5.55
Peak Current (9) kA =	47.43	47.43	54.77	54.77

Appendix E

Notes.

1. FFCL refers to the far-field central lobe of the laser beam.
2. The repetition rate and discharge energy density were adjusted to keep the module length 150 cm.
3. A gain of 4 mot is typical for alms pulse at 200 J/ electrical energy density. Assuming a linear relationship for lower energy densities, this gives a specific gain $g_o = 2.0E-5 \text{ m}^2/\text{J}$.
4. The flow assumes 'nozzle' or 'plug' flow with high flow over the discharge area only. The clearing ratio is the ratio of the gas velocity to the product of the discharge width and the pulse rate. Note that Mach 1 is approximately 700 m/s in a 32 % molecular gas mix typical for a TEA laser.
5. This data is typical for a TEA laser such as the Lumonics (R) TEA 620. The e-drift methods may use more power. Electron beam preionization has not been considered.
6. # Rows = [Width/Row Spacing] + 1, and # Sparks = [Length/Spark Spacing] + 2.
7. One-half the 'ringing' period into a short circuit = $p.\text{sqrt}(LC)$
8. The impedance of good discharges are close to the critically damped value $R_c^2 = 4L/C$.
9. The peak current when critically damped case is $V/\text{sqrt}(5L/C)$, and when shorted, it is 2.2 X larger

Conclusions.

1. Two of these modules are required to provide 100 kW, so if they are mounted in series, the output optical flux will be double the above values, making the parallel configuration look more attractive.
2. Laser concept #1, due to the multiplying effect of conservative design parameters, requires more power and gas flow and has significantly higher power density on the optics.
3. Concepts #2 and #3 are less conservative, but are still well within the design envelope of the discharge energy density of low pulse rate lasers.
4. Designs #1, #2, and to a lesser extent #3, have very high optical power densities on the optic.
5. Design #4 is given to show that a larger aperture would allow more design freedom, allowing the discharge energy density to be reduced to a similar value used in small high pulse rate lasers. The energy density on the output window is also more reasonable.
6. For a single module, a total beam power of 75 to 100 kW is a very high power loading for the output window, and for two modules in series it doubles to 150 to 200 kW which is a potentially serious problem.

Appendix E

APPENDIX B:

Summary of Discussion on the Lightcraft Project with Russian Scientist Professor Victor Apollonov

During this study an opportunity developed to discuss this project with a well-recognized Russian scientist, Professor Victor Apollonov of the Russian Academy of Sciences. After he met with Professor Leik Myrabo at the Lasers '98 conference to discuss the Lightcraft concept he traveled to Ottawa Canada, where the author met with him. A wide range of issues was discussed, and he showed great interest in the Lightcraft program. It became clear he and his colleagues would have useful input to all aspects of the program. They have experience with large kilo-joule energy systems using the electron drift (also called barrier discharge, or dynamic profiling) preionization method and have compared this method to other preionization techniques. The following is a summary of the discussion between Professor Apollonov and the author.

1. Large lasers.

Professor Apollonov and his group have performed research on large lasers and have demonstrated TEA CO₂ laser discharges at 1.5 m inter-electrode gaps with a very homogenous discharges medium. Apollonov stated that they have produced diffraction limited beams in these apertures for pulse lengths less than 1.5 microsecond. They have found: a) that longer pulse lengths, such as those obtained from an electron beam sustained laser, result in higher divergence, and b) to obtain good beam quality a self-sustained discharge must be used. These limitations are independent of the method of preionization used. He feels that a 15 to 20 cm beam size is appropriate for a high repetition rate laser, although he did not indicate they had experience at high repetition rates for long periods.

His group has delivered several large TEA CO₂ lasers using unstable resonator optical cavities to Japan. These have been used for attracting lightning by creating 100's of meters of ionization channels in the atmosphere.

2. Electron drift preionization

This method utilizes a plasma at the cathode surface or behind a screen cathode for a source of electrons. These electrons are drawn into the discharge space under an electrical field to create preionization. When they have drifted completely across the electrode gap, the main ionization pulse is applied, which creates a uniform discharge. This preionization method can be used with volume-efficient 'sharp' edged electrodes, which would cause an arc when using UV preionization. This explains why it is also called the barrier discharge, or dynamic profiling preionization method. However where space is not a premium, it works better with well-profiled electrodes. Apollonov's group has a lot of experience with this method in large, low pulse rate, lasers. He mentioned using a carbon fiber composite as a base for the plasma source, but the author is doubtful that it would survive high pulse rates.

3. Nano-second pulses train

For the Lightcraft application, Apollonov is keen on using a burst (or "train") of nanosecond pulses from a regenerative oscillator, and may have actual experience with their interaction on targets. The individual pulses have widths of a few nanoseconds and an inter-pulse spacing of the cavity round-trip time (typically tens of nanoseconds). This train of pulses can be created by injecting nanosecond pulses from a small mode locked laser into a large laser. This can be done through a small hole in the rear

Appendix E

mirror. The resulting train of equally spaced pulses has an envelope of amplitudes that follow shape of the normal TEA laser pulse shape. They also have an integrated energy similar to, or possibly higher than, a normal TEA laser pulse. Note that a pulse from a non-actively-mode-locked laser typically displays self-modelocking with a large pulse-to-pulse variation in the degree of modulation. Apollonov also said:

- It is very reliable, and gives more consistent results than the normal self-mode-locked pulse.
- To a certain degree one can control the energy in the individual pulses.
- It may be possible to extract more energy from the laser by using widely spaced pulses having very high peak power. The energy extraction is more efficient because there is more time for the gain to re-build between pulses.
- Because there is more time for radiative cooling between pulses widely spaced pulses create less atmospheric distortion from thermal effects.
- The interaction with the target may be a stronger and efficient because of the high peak power.

4. Related work

Professor Apollonov and his colleagues have interest in assisting with the design of the whole system. This includes the beam delivery from the laser through the adaptive optics, transmission through the atmosphere (100 km beam path), and the optical and propulsion interaction with Lightcraft. The author assumes they have done theoretical and experimental work on SDI type laser damage in the atmosphere since. More comments follow.

- They made beam measurements over long distances, and did not simply measure the near-field energy and use assumptions regarding beam propagation.
- He said that the Lightcraft requirement is basically no different from a military system. You have to get energy to a distant target in the real atmosphere. That is the challenge. The laser is relatively easy.

They could assist in:

- optimizing the mechanical pulse created by the air breakdown,
- optimizing the plasma impulse including its expansion around to the front of the Lightcraft module, • optimizing the air-breathing phase of Lightcraft propulsion,
- designing fluid flows to enhance interaction with the target at higher altitudes,
- dealing with shock wave interactions,
- designing the laser, including the modification of an existing of an existing system,
- making parts, and assisting in the assembly, testing and evaluation.

They also have interest and knowledge in many other laser systems including HF and DF lasers that emit in the 3 to 5 μm wavelength range, and N_2O with wavelengths beyond 10 μm . These lasers have advantages of higher atmospheric transmission, and may be considered for the future. However, Apollonov stated that CO_2 lasers are well known and should be used for this phase.

AFRL-PR-ED-TR-2007-0078

Primary Distribution of this Report:

AFRL/PRSP (15 CD)
Dr. Frank Mead
10 E. Saturn Blvd
Edwards AFB CA 93524-7680

AFRL/PRSA (1 CD)
Dr. Jean-Luc Cambier
10 E. Saturn Blvd.
Edwards AFB CA 93524-7680

AFRL/PR (1 CD)
Dr. Alan Garscadden
1950 Fifth Street, Building 18
Wright-Patterson AFB, OH 45433-7251

AFRL/PR Technical Library (2 CD + 1 HC)
6 Draco Drive
Edwards AFB CA 93524-7130

Chemical Propulsion Information Agency (1 CD)
Attn: Tech Lib (Dottie Becker)
10630 Little Patuxent Parkway, Suite 202
Columbia MD 21044-3200

Dr. Adrian Alden (1 CD)
Communications Research Centre
3701 Carling Ave., P.O. Box 11490, Station H
Ottawa, Ontario, K2H 8S2
CANADA

Dr. Victor Apollonov (1 CD)
General Physics Institute
Vavilov St., 38
Moscow, 119991
RUSSIA

Dr. Young Bae (1 CD)
Bae Institute
1101 Bryan Ave., Suite C
Tustin CA 92780

Dr. Willy Bohn (1 CD)
DLR Institute of Technical Physics
Pfaffenwaldring 38-40
Stuttgart, D-70569
GERMANY

Defense Technical Information Center
(1 Electronic Submission via STINT)
Attn: DTIC-ACQS (Pat Mawby)
8725 John J. Kingman Road, Suite 94
Ft. Belvoir VA 22060-6218

Dr. James Benford (1 CD)
Microwave Sciences, Inc.
1041 Los Arabis Ln.
Lafayette, CA 94549

Dr. Gary L. Bennett (1 CD)
5000 Butte Road
Emmett ID 83617-9500

Dr. Mitat Birkan (1 CD)
875 North Randolph Street, Suite 325
Arlington, VA 22203

Dr. David Chenault (1 CD)
Polaris Sensor Technologies, Inc.
200 Westside Square, Suite 320
Huntsville AL 35801

Mr. John Cole (5 CD)
TD-15, Bldg 4203, Rm 4401
NASA/Marshall Space Flight Center
Huntsville AL 35812

Mr. Joung Cook (1 CD)
J. Cook & Associates
1450 Emerson Avenue, Suite 202
McLean VA 22101

Dr. Leo Christodoulou (1 CD)
DARPA/DSO
3701 North Fairfax Drive
Arlington VA 22203

Dr. James Degnan (1 CD)
AFRL/DEHP
Kirtland AFB, NM 87117

Dr. Eric Davis (3 CD)
Institute for Advanced Studies
11855 Research Blvd.
Austin TX 78759

Dr. Tim Easler (1 CD)
ATK COI Ceramics
9617 Distribution Avenue
San Diego CA 92121

Mr. Ken Edwards (3 CD)
AFRL/MNAV
101 Eglin Blvd., Ste 342
Eglin AFB FL 32542-6810

Mr. Terry Finley (1 CD)
Miltec Corp.
678 Discovery Dr.
Huntsville AL 35806

Dr. Robert Frisbee (1 CD)
JPL, MS 125-109
4800 Oak Grove Dr.
Pasadena, CA 91109

Mr. H. David Froning (1 CD)
Flight Unlimited
P.O. Box 180
Gumeracha SA 5233
Australia

Maj Peter A. Garretson (3 CD)
HQ USAF/XPXC 5C169
1070 Air Force Pentagon
Washington DC 20330-1070

Dr. Ken Goretta (1 CD)
AOARD
7-23-17 Roppongi, Minato-ku
Tokoyo 106-0032
JAPAN

Dr. C. C. Green (1 CD)
50723 Harbourview Dr., South
New Baltimore MI 48047

Mr. John Harchenko (3 CD)
Polaris Sensor Technologies, Inc.
200 Westside Square, Suite 320
Huntsville AL 35801

Prof. Hideyuki Horisawa (3 CD)
Tokai University
1117 Kitakaname
Hiratsuka, Kanagawa, 259-1292
JAPAN

Dr. Andrey Ionin (1 CD)
Institute of Quantum Radiophysics
P.N. Lebedev Physical Institute
Leninsky pr., 53 Moscow
119991, GSP-1 RUSSIA

Prof. In-Seuck Jeung (1 CD)
Seoul National University
Dept. of Aerospace Eng., Kwanak-Ku
Seoul, 151-744
KOREA

Mr. Mike Kaiserman (1 CD)
Raytheon Missile Systems Company
Bldg 805, M/S C3
Tucson AZ 85734

Dr. Jordan Kare (2 CD)
Intellectual Ventures
1600 132nd Ave. NE, Suite 100
Bellevue WA 98004

Mr. Ron Kita (1 CD)
Chiral Material Research
87 Shady Springs Dr.
Doylestown PA 18901

Prof. Kimiya Komurasaki (3 CD)
University of Tokyo
Kashiwanoha 5-1-5, Kiban 304
Kashiwa-shi, Chiba 277-8561
JAPAN

Mr. Sean Knecht (1 CD)
4746 11th Ave. N.E., Apt. 309
Seattle WA 98105

Dr. Timothy Knowles (1 CD)
ESLI
6888 Nancy Ridge Dr.
San Diego CA 92121

Dr. C. William Larson (1 CD)
AFRL/RZSS
1 Ara Road
Edwards AFB CA 93524-7013

Mr. Michael Libeau (1 CD)
NSWCDD Attn: Code G23 Libeau
17320 Dahlgren Rd.
Dalgren VA 22448

LtC Timothy Lawrence (3 CD)
Hdqtrs USAFA, Suite 1M 147
2354 Fairchild Dr.
USAF Academy CO 80840

Mr. Kevin Mahaffy (2 CD)
Exquadrum, Inc.
12130 Rancho Road
Adelanto CA 92301

Mr. Greg Meholic (1 CD)
The Aerospace Corp.
P.O. Box 92957 – M4/970
Los Angeles CA 90009-2957

Dr. Don Messitt (1 CD)
1145 Galston Dr.
Folsom CA 95630

Dr. Sheldon Meth (1 CD)
DARPA
Tactical Technology Office
3701 N. Fairfax Dr.
Arlington VA 22203

Dr. Michael M. Micci (1 CD)
Prof. of Aerospace Engineering
2333 E. Hammond Bldg.
University Park PA 16802

Mr. Marc Millis (1 CD)
NASA/Glenn Research Center
MS 86-2
21000 Brookpark Rd.
Cleveland OH 44135

Mr. Yoshinari Minami (1 CD)
Advanced Space Propulsion Research Project
35-13, Higashikubo-Cho, Nishi-ku
Yokohama 220-0062
JAPAN

Dr. Marco Minucci (3 CD)
Institute for Advanced Studies
Rodovia dos Tamoios, km 5.5
CEP 12228-01
Sao Jose dos Campos, SP, BRAZIL

Mr. Paul Murad (1 CD)
Sr. Analyst, Director for Intel Production
Missile & Space Intel Center
Defense Intelligence Agency
Washington DC 20340-6054

Dr. Leik Myrabo (3 CD)
Rensselaer Polytechnic Institute
4004 Jonsson Engineering Center
Troy NY 12180

Dr. Takashi Nakamura (1 CD)
PSI
2110 Omega Rd., Suite D
San Ramon CA 94583

Mr. Kimio Nishino (1 CD)
Toyota Motor Corp.
23-22 Izumi 1-Chome
Higashi-Ku, Nagoya, 461-8711
JAPAN

Dr. Andrew Pakhomov (10 CD)
American Institute of Beamed Energy Propulsion
P.O. Box 1907
Madison AL 35758

Dr. Claude Phipps (1 CD)
Photonic Associates
200A Ojo de la Vaca Rd.
Santa Fe NM 87505

Dr. Alan Pike (2 CD)
DSAS
1988 Crescent Park Drive
Reston VA 20190

Dr. Harold Puthoff (1 CD)
Institute for Advanced Studies
11855 Research Blvd.
Austin TX 78759

Dr. James Reilly (1 CD)
Northeast Science & Technology, Inc.
117 North Shore blvd.
Cape Cod MA 02537

Dr. Yuri Rezunkov (1 CD)
Research Institute for Complex Testing of
Optic-electronic Devices
Sosnovy Bor, Leningrad Region, 188540
RUSSIA

Dr. Eric Rice (1 CD)
Orbital Technologies Corp.
Space Center
1212 Fourier Drive
Madison WI 53717

Dr. Stanley Rosen (1 CD)
Association for Strategic Planning
12021 Wilshire Blvd., Suite 286
Los Angeles CA 90025-1200

Prof. Akihiro Sasoh (3 CD)
Nagoya University Furo-cho
Department of Aerospace Engineering
Chikusa-ku, Nagoya 464-8603
JAPAN

Mr. Stefan Scharring (1 CD)
Institute of Technical Physics
Pfaffenwaldring 38-40
70569 Stuttgart
GERMANY

Dr. Thomas Lippert (1 CD)
Paul Scherrer Institute
CH-5232 Villigen PSI
SWITZERLAND

Dr. Vladimir Sherstobitov (1 CD)
Institute for Laser Physics
12Birzhevaya Line
199034, St-Petersburg
RUSSIA

Dr. Robert Sierakowski (1 CD)
AFRL/MN, Chief Scientist
101 W. Eglin Blvd., Suite 105
Eglin AFB FL 32542-6810

Mr. John Sinko (1 CD)
229 Queensbury Dr., #14
Huntsville AL 35802

Mr. Steve Squires (5 CD)
Directorate of Applied Technology
Test and Simulation
STEWS-DATTS-OO
White Sands Missile Range NM 88002

Dr. Martin Tajmar (1 CD)
ARC Seibersdorf Research GmbH
A-2444 Seibersdorf
AUSTRIA

Dr. Zhiping Tang (1 CD)
University of Science and Technology of China
Department of Modern Mechanics
Hefei, Anhui 230026
P.R. CHINA

Prof. Shigeaki Uchida (3 CD)
Tokyo Institute of Technology
2-12-1 O-okayama, Meguro-ku
Tokyo 152-8552
JAPAN

Prof. Takashi Yabe (3 CD)
Tokyo Institute of Technology
2-12-1 O-okayama, Meguro-ku
Tokyo 152-8552
JAPAN

Dr. Hiroshi Yamakawa (1 CD)
Research Institute for Sustainable Humanosphere
Kyoto University
Gokasho, Uji,
Kyoto 611-0011 JAPAN

Dr. Thomas York (1 CD)
1215 Inverary Pl.
State College PA 16801

Dr. Ingrid Wysong (1 CD)
AFRL/RZSA
10 E. Saturn Blvd.
Edwards AFB CA 93524-7680